Effect of Surface Nitridation on the Growth of GaN Films on c-Sapphire, Si(111) and Si(100) Surfaces

A Thesis
Submitted for the Degree of

Doctor of Philosophy

by

Satish Shetty

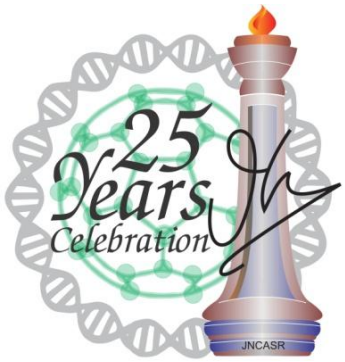

Chemistry and Physics of Materials Unit

Jawaharlal Nehru Centre for Advanced Scientific Research

(A Deemed University)

Bangalore-560064 (INDIA)

June, 2014.

DEDICATED TO

MY PARENTS

DECLARATION

I hereby declare that this thesis entitled **"Effect of Surface Nitridation on the Growth of GaN Films on c-Sapphire, Si(111) and Si(100) surfaces"** is an authentic record of the research work carried out by me under the supervision of **Prof. S. M. Shivaprasad** at the Chemistry and Physics of Materials Unit, Jawaharlal Nehru Centre for Advanced Scientific Research, Bangalore, India, and it has not been submitted elsewhere for the award of any degree or diploma.

In keeping with the general practice of reporting scientific observations, due acknowledgement has been made whenever work described here has been based on the findings of other investigators. Any omission that might have occurred due to oversight or error in judgment is regretted.

Date: **Satish Shetty**

Place: Bangalore, India (PhD Student)

CERTIFICATE

Certified that the work described in this thesis entitled **"Effect of Surface Nitridation on the Growth of GaN Films on c-Sapphire, Si(111) and Si(100) surfaces"** has been carried out by **Satish Shetty** at the Chemistry and Physics of Materials Unit, Jawaharlal Nehru Centre for Advanced Scientific Research, Bangalore, India under my supervision and that it has not been submitted elsewhere for the award of any degree or diploma.

Date: Prof. S. M. Shivaprasad

Place: Bangalore, India (Research Supervisor)

ACKNOWLEDGEMENTS

First and foremost, I would like to thank my research supervisor, **Prof. S.M. Shivaprasad** for his invaluable guidance throughout this research journey. I am extremely grateful to him for suggesting the research projects as well as propelling it in the right direction. His optimistic and imaginative approach in scientific research is awe-inspiring. I am indebted to him for the acquired skills in several instrumental techniques. His methodical approach with the instruments and his creative ideas has helped in the efficient use of them. I thank **Mrs. Anupama Shivaprasad**, Sharvani and Umesh for their warmth and hospitality.

Prof. C. N. R. Rao's presence is a motivation for performing scientific research. I am fortunate to be on this campus, and to listen to encouraging words about research by the legend. I am grateful to him for being a source of inspiration to all of us with his boundless enthusiasm, up-to date knowledge, dedication and commitment to science.

I am grateful to the past and present chairmen of CPMU, Prof. C.N.R. Rao, **Prof. G.U.Kulkarni** and **Prof. Balasubramanian** for their constant support and encouragement in various ways. I express my sincere thanks to my various collaborators during the research work, Prof. Chandrabhas Narayana and Dr. Ranjan Datta. I also thank all the faculty members of CPMU, TSU and NCU for their cordiality, especially my course work teachers, Prof. S. Ranganathan, Prof. Shobana Narasimhan, Prof. G.U Kulkarni, Dr. A. Govindaraj and Dr. N. S. Vidhyadhiraja for the courses and useful discussions.

I would like to thank all my teachers, who have guided me till now, especially **Dr. N.S. Kini** who prompted me to take up research as a career. I am grateful to my labmates, Dr. Praveen, Dr. Manoj, Dr. Jithesh, Varun, Malli, Darshana, Sreedhar, Arpan, Sanjay Kumar Nayak, Shivakumar D.T, Sandheep and Dr. K. K. Nagaraja for discussions and cheerful atmosphere.

Timely and ready assistance and also friendly attitude from technical staff, Mr. Srinath and Mr. Somashekar is acknowledged. I am highly thankful to Mr. Mahesh

(SEM), Mr. Prajwal & Mr. Jagadish(FE-SEM), Mr. Vasu (UV, IR, PL), Dr. Jay Ghatak (TEM), Mrs. Selvi (FESEM) and Dr. S. Basavaraja (AFM), Mr. Anil (XRD), Mr. Kishore (XPS), Mr. Kishore Upadhyaya, Dr. Karthik (FIB), Dr. Partha (Raman) and Mr. A. Srinivasa Rao for their invaluable technical assistance. Mr. Suresh, Mr. Mune Gowda and Mr. Michael are acknowledged for their help in various lab activities.

I thank the staff of academic and administrative section in JNC for their assistance, especially Mr. A.N. Jayachandra, Dr. Princy and Mr. Sachin Belavadi for their advice and friendly nature. I also thank the library and computer lab staff for their help. Financial assistance from JNCASR is acknowledged. I thank all JNC colleagues for a memorable and joyous JNC life. I also thank my friends at JNCASR, and there are no words to express my gratitude to my family members. This thesis is dedicated to them.

Satish Shetty

Preface

The remarkable advances in nitride research and development of optoelectronic devices based on 2-D films has encountered limitations due to a large density of extended defects that arise due to the relaxation of the interface strain due to their lattice mismatch with available substrates. While several approaches such as buffer layers, surfactants, super-lattice matching epitaxy and Epitaxial Lateral Overgrowth (ELOG) have been successfully employed, each suffers with serious limitations. Of late, formation of defect-free nanocolumns of III-nitrides has demonstrated its potential to push the boundaries of what is possible in III-nitride device. These nanostructures have also raised the curiosity in fundamental studies due to the absence of residual strain, exclusion of most extended defects, long photoluminescence life-times, low surface recombination rates and high mechanical quality factors. The effort in this work is towards understanding the spontaneous catalyst free, kinetically controlled formation of nanostructures of GaN, on c-plane (0001) sapphire and low index Silicon (001) and (111) surfaces. The work involves synthesis in carefully controlled growth-parametric space by Molecular Beam Epitaxy followed by complementary characterization using sophisticated structural, optical, electrical and morphological techniques. The work of the thesis is systematically divided into seven chapters

Chapter I: This Chapter gives a brief introduction on III-nitride materials, growth techniques, substrates and the role of misfit induced dislocation formation in these systems. Formation of GaN structures by kinetically controlling growth in mitigating the interface generated defects is the main motivation for this work. A comprehensive Literature review of reported work describes the status of current research in this field. The context of this work with other efforts of formation of single crystalline nanostructure growth on Al_2O_3(0001) and Silicon substrates in highlighting the role of nitrogen rich condition for promoting nanostructures formation and the need to minimize process steps is explained.

Chapter II: The chapter describes the experimental details of growth and characterization techniques employed in this study and their calibration to identify optimized growth condition. The practical details of the MBE growth and the optimization of GaN growth on

sapphire and Si surface in a MBE system are presented, along with some detailed discussion of the influence of growth parameters on the microstructure. The working principles of the different *in situ* and *ex situ* characterization techniques that are related to our work are discussed.

Chapter III: Here, we present a phase diagram of the formation and characterization of GaN nanostructures in a nitrogen rich growth condition, by varying growth parameters such as substrate temperature, Ga flux and nitrogen flow rate. In the relatively low temperature growth regime (480-630°C) we observe the formation of dense GaN wedge-shaped single-crystalline nanowall hexagonal network which we attribute as due to open screw dislocations. At higher temperatures (730-880°C), 2-D films with extended dislocation density of $10^{10}/cm^2$ are formed, which transform into faceted mounds beyond 830°C. The results of the formation of c-oriented epitaxial GaN nanocolumns on bare sapphire and the effect of growth kinetics on nanowall and nanocolumn formation and their structural and optoelectronic properties are discussed. A narrow parametric window is identified by varying substrate temperature (480 to 880°C), Nitrogen flow rate (2 to 8 sccm) and Ga flux ($2.86x10^{14}$ to $4.84x10^{14}cm^{-2}s^{-1}$), where 1-D nanocolumns of GaN with a high density ($1x10^{8}cm^{-2}$) are observed. Epitaxy, assembly and shape of the c-orientated single-crystalline m-faceted nanocolumns that nucleate at the screw dislocations between the nanowalls demonstrate that spontaneous self assembled high quality nanocolumn assemblies can be formed in a single growth process.

Chapter IV: This chapter studies the nitridation process optimization for the formation of an intermediate layer on c-sapphire and Si(111) substrates by time and flux dependence of rf-nitrogen plasma. The variation of surface and interfacial chemical composition at different stages of nitridation of Al_2O_3(0001) surface is monitored by XPS. On this optimally nitrided surface, we deposit a thin layer of AlN, to understand how the properties of the nitridied sapphire surface determine the origin, shape and size of the AlN overlayer. In case of the Si(111) substrate, we have studied the initial stages of the formation of 2D single crystalline silicon nitride film with controlled N^*_2 plasma exposure times. We have also probed into the morphology, epitaxy, electronic structure and stoichiometry of the SiN_x interfacial layer obtained by the plasma nitridation of Si (111) surface.

Chapter V: This chapter shows the evolution of the GaN thin films on differently formed AlN intermediate layer. We show that GaN grown on c-plane sapphire, on the AlN layer formed by the exposure of the substrate to N^*_2 plasma, leads to the formation of dislocation-induced nano-petal-like morphology of GaN nanostructures. When an AlN intermediate layer is grown on the nitridied surface, under nitrogen rich conditions, AlN grows with a bimodal distribution of nanocolumns consisting of dislocation and diffusion mediated nucleation. We observe that GaN grown on this AlN intermediate layer prefers to grow only on the larger, faceted , dislocation induced AlN nanocolumns of sizes in the range of 80-120nm. We observe that the nano-features are c-oriented and epitaxial with high crystallinity and demonstrate a thirty times increase in band edge emission as compared to GaN 2-D film grown on bare sapphire. On the other hand, we demonstrate the growth of high quality 2-D film and nanostructure of GaN on nitrided surface (intermediate SiN_x layer) of Si (111). We study the structural, optical and magnetic properties of these films, which show very interesting morphological dependence.

Chapter VI: The chapter describes the growth of GaN nanocolumns on Si(111) surface and unveils the underlying mechanism for the evolution of spontaneous evolution of orientated and self assembled low dimensional features. The various nano-structures formed are understood in term of the kinetics of growth and its effect on the sticking coefficient of Ga adatoms. We also discuss the growth of high quality GaN films comprising of wurtzite nanorods and nanotubes on bare Si (001)2X1 surface and characterize them by RHEED, XRD, CL and TEM. We provide an explanation of the structure and morphology of the nanostructured GaN epitaxial overlayer at the atomistic level and schematically model the system.

Chapter VII: The final chapter consolidates the inferences drawn from the results presented in the previous chapters. This enables us to draw a few important conclusions, that highlight some of our novel observation and provides a direction for both scientific and technological research in the field.

TABLE OF CONTENTS

Chapter 5: Role of Intermediate Layer on the Evolution of GaN Films:

Chapter 6: Growth of Epitaxial GaN Nanostructures and 2-D Films on Si (111) and Si (100) Surfaces:

Chapter 7: Summary, Conclusions and Future Outlook:

ACRONYMS

AFM	Atomic Force Microscope
BEL	Band Edge Luminescence
BEP	Beam Equivalent Pressure
BSE	Back Scattering Electrons
CL	Cathodo-luminescence
EDS	Energy Dispersive Spectroscopy
ELOG	Epitaxial Lateral Overlayer Growth
FESEM	Field Emission Scanning Electron Microscope
FFT	Fast Fourier Transform
FWHM	Full Width Half Maximum
FR	Frank Read
FM	Frank van der Merwe
GPa	Giga Pascal
HEMT	High Electron Mobility Transistor
HVPE	Hydride Vapour Phase Epitaxy
HRTEM	High Resolution Transmission Electron Microscope
IC	Integrated circuit
LED	Light Emitting Diode
LD	Laser Diode
LBL	Layer By Layer
MBE	Molecular Beam Epitaxy
MOCVD	Metal Organic Chemical Vapour Deposition
MOVPE	Metal Organic Vapour Phase Epitaxy
NW, NR, NC	Nanowire, Nanorods, Nanocolumns

PL	Photoluminescence
PBN	Pyrolytic Boron Nitride
PAMBE	Plasma Assisted Molecular Beam Epitaxy
PXRD	Powder X-ray Diffractometer
QW	Quantum Well
QC	Quartz Crystal
RHEED	Reflection High Energy Electron Diffraction
RF	Radio Frequency
RGA	Residual Gas Analyzer
SEM	Scanning Electron Microscope
SCCM	Square Cubic Centimeter
SE	Secondary Electrons
SAD	Selected Area Diffraction
TD	Threading dislocation
TEM	Transmission Electron Microscope
TE	Transmitted Electrons
UV-VIS	Ultra Violet-Visible
UHV	Ultra High Vacuum
UV LED	Ultra Violet Light Emitting Diode
VW	Volmer Weber
VLS	Vapour Liquid Solid
XPS	X-ray Photoelectron Spectroscopy
XRD	X-ray Diffraction
YL	Yellow Luminescence
2DEG	Two Dimensional Electron Gas
1D/2D/3D	One Dimension/ Two Dimensions/Three Dimensions
III-N	Group Third Nitride

Chapter 1

Introduction, Motivation, Research Status and Current Issues

1.1 INTRODUCTION:

Group III-nitrides are the most promising wide bandgap semiconducting materials for high efficiency optoelectronic device applications[1,2] that operate very well without aging effects, even with very high dislocation densities. Several other semiconductors such as CdS, CdSe, ZnSe and ZnS are extensively used for short wavelength optoelectronic devices. But, due to their short lifetime and low bond energy, one cannot use these in high temperature and harsh chemical environments which limit the use of devices based on these materials. As compared to other competitive materials, GaN has bond energy of 2.3eV/bond, which is large compared to 1.2eV/bond in the case of ZnSe. The III-nitride semiconductors are well suited for devices operating at high temperatures, high current density, high frequency and in harsh chemical environments unlike the traditional Si and GaAs based semiconducting devices[3,4]. However, the progress in the development of nitride based optoelectronic devices towards their complete potential is hindered due to lack of native substrates, difficulties in making contacts p-type doping[5,6]. ZnO, an II-VI wide bandgap semiconductor, is intensively studied in recent years along with III-V materials for blue and UV optoelectronic devices. But, p-type doping in ZnO is nearly impossible and not reliable which is limiting its use in devices[7,8], explaining why there are no commercial device is available based on ZnO, while GaN is widely prevalent. For indoor/outdoor white lighting applications, yellow phosphor coatings on GaN based blue LEDs are being used. III-nitride semiconductors now have occupied second place in the semiconductor industry after silicon because of its potential applications in high efficiency devices such as blue light emitters and laser diodes. The band gap of III-nitrides (InN, GaN and AlN) semiconductors can be tuned to cover UV to IR region of the electromagnetic spectrum by alloying with each other[9,10]. **Fig. 1.1** shows band gap engineering possible in GaN by alloying with indium in which the band gap is tuned from 0.7 eV, that emits in the IR, to 3.4 eV that emits in the near-UV; in such a way that the spectrum range from 0.7-3.4 eV can be covered, which includes the complete visible range. On the other hand, on alloying Al to GaN, one can span the band gap from 6.2 eV to near-UV of around 3.4eV depending upon percentage composition of alloying.

Earlier studies in the 1970's and 80's held that the efficiency of III-nitride devices is very low and is very difficult to achieve p-doping in these materials, and consequently

received very little attention. During 1988, Akasaki *et al.* achieved p-type doped GaN layers for the first time using Mg doping. Soon after, GaN was considered as a serious candidate for high mobility transistors as well as blue LEDs and laser LEDs[11]. In 1993, Nakamura developed the first blue-emitting diode on III-nitride based materials[12]. Current status indicates that it is now possible to obtain white light emitting diodes with efficiency of 250 Lumens/Watt, in the near future.

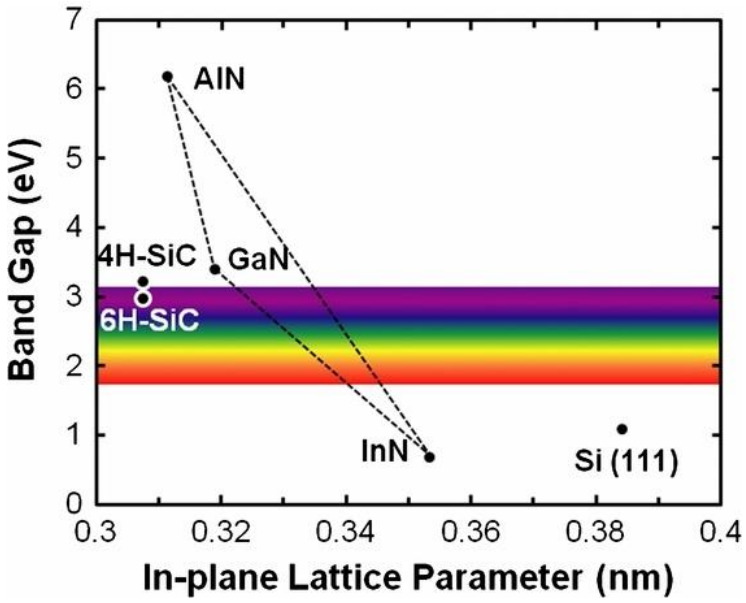

Fig.1.1: *The plot of RT band-gap energy v/s lattice constant of III-Nitride semiconductors*[13].

In comparison to standard incandescent lighting and fluorescent lamps, the efficiency of LEDs is much higher, lasts 100 times longer, have a wide color regime and use 90% less energy. Now commercial white LEDs that operate at about 40 Lumens/Watt involve GaN based blue LEDs, coated with yellow phosphorus. Clear white light generation is achieved by combining light from three complimentary colors such as red blue and green LEDs, but this configuration has not yet been commercially available due to issues like 'green droop'. The power saving capabilities of solid-state devices as compared to that for other conventional light sources[14], remains as the strongest motivation, along with other virtues like quality of light, longevity, fast switching and a low carbon foot print. Of late, new strategies for High Brightness LED_S and other devices tend to adopt formation of nanostructures, which can reduce several of the impending limitations.

1.2 PROPERTIES OF III-NITRIDES:

The fact that III-nitrides, namely GaN, InN and AlN display partially ionic bonding with a strong charge transfer between the highly electronegative nitrogen atoms and the less electronegative metal atoms (In, Ga, or Al). The bond strength of Ga-N is 2.23eV, which is comparable to the C-C bond strength of 1.9 eV in diamond and is also much larger than Ga-As bond strength of 1.0eV. Usually more thermodynamically stable in wurtzite crystal structure, these materials also exist in meta-stable zinc-blende (ZB) structure, as shown in **Fig. 1.2(a)**.

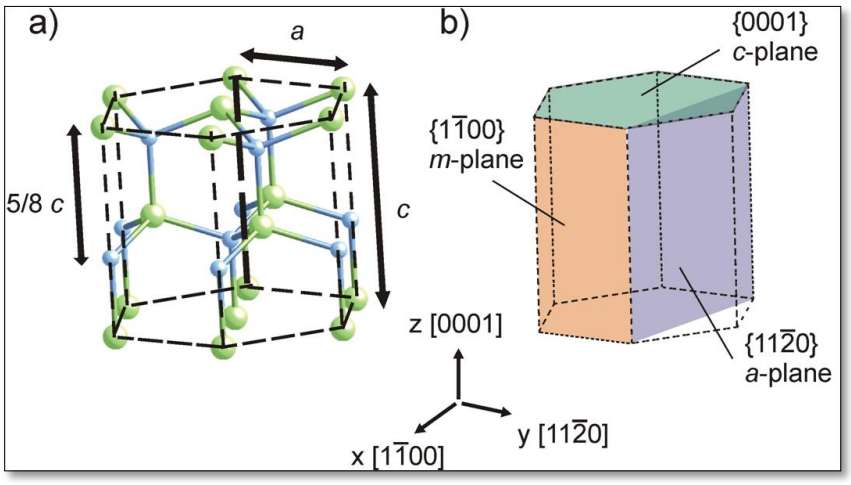

Fig.1.2: (a) *Unit cell for the hexagonal crystal structure of wurtzite gallium nitride* ***(b)*** *planes present in hexagonal crystal structure (image courtesy- Christof Mauder thesis-2011*[15]*).*

The wurtzite crystal structure consists of two interpenetrating hexagonal close packed (hcp) sub-lattices of both metal and the small sized N atoms, which are shifted with respect to each other in *c*-direction by 62% of its unit cell length as shown in the **Fig.1.2 (a)**. **Fig.1.2 (b)** represents the different planes present in the hexagonal crystal structure; the family of {0001} planes is denoted as basal plane or *c*-plane, while the family of {10-10} planes is denoted as prismatic plane or *m*-plane. Another kind of plane perpendicular to the *m*-plane is the {11-20} family, called the *a*-plane. Interestingly, both the *m*-plane and the *a*-plane have a special feature of containing equal number of Ga and N atoms making them non-polar. Films grown on these planes do not have in-built polarization, which has removed a long standing obstacle in the path to achieve highly efficient devices. In the c-direction, the stacking

sequence of closest packed diatomic planes is different for the wurtzite and zinc-blende structures. In the case of wurtzite structure, the configuration of stacking sequence in the <0001> direction is AaBbAaBb, while in the zinc blende structure, the stacking sequence in the <111> direction is ABCAB. Any deviation from this sequence results in a defect called as stacking fault. The formation of stacking faults during growth is most prevalent due to low formation energy of about 10meV in GaN and 19meV for InN. One unit cell of III-nitrides contains six atoms of the group III elements (Al, Ga, In) and six atoms of nitrogen. In the schematic (**Fig.1.2 (a)**) large size Ga atoms are represented by green beads and N atoms by small gray beads. Depending on the growth conditions the polarity of the resulting film is either Ga- or N-polar. Polarity is generally defined as the bonding sequence arising out of stacking configuration within the atomic layers. This is due to the non-centrosymmetric nature of group III-nitrides along the <0001> direction in the wurtzite crystal structure which gives the probability of the film having two opposite stacking sequences of atomic layering. For instance, GaN (0001) is Ga-polar and the vertical bond is from a Ga atom to N atom above it, whereas GaN (000-1) is N-polar, and the vertical bond is from N atom to a Ga atom above it as shown in **Fig.1.3**.

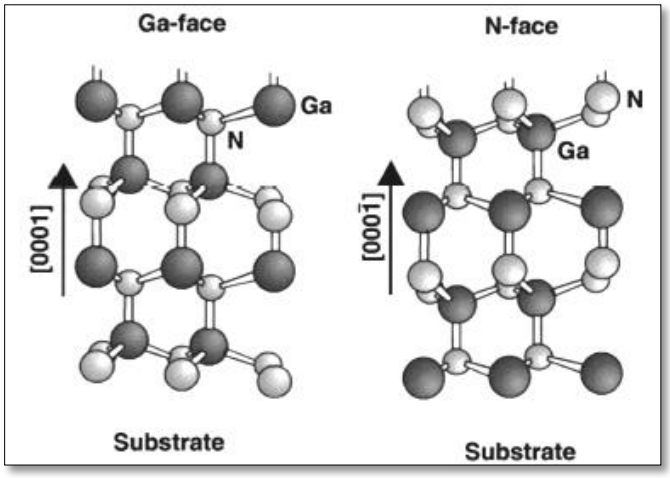

Fig. 1.3: *Schematic model illustrating the crystal structure of Wurtzite Ga-polar and N-polar GaN film*[16].

In MBE and MOCVD growths, the polarity of the films grown on sapphire is determined by the buffer layer used. AlN buffer layers are known to initiate Ga-polar and GaN buffer layers result in N-polar GaN. A more common method to determine GaN polarity is to use a chemical etching method, where relative etching rate is high for N-polar

surface, but in the case of Ga-polar surfaces the film remains unaffected even after long time of exposure to the etchant.

Since the atomic arrangements are different in wurtzite and zinc-blende structures of III-Nitride semiconductors, the basic physical properties of both structures are different. The basic characteristics of electronic properties of the hexagonal III-nitrides are given in **Table 1.1** (and the properties of the cubic III-nitrides are beyond the scope of this thesis).

Properties	GaN	AlN	InN
Band-gap energy	3.425	6.28	0.77
Electron mobility (cm^2/V-s)	1250	300	3200
Hole mobility (cm^2/V-s)	30	14	–
Thermal conductivity (κ) [W/cm-K]	2.3	2	0.8
Static dielectric constant (ε_o)	9.5	8.5	15
Electron effective mass (m_e)	$0.20m_o$	0.40 me	$0.11m_0$
Relative dielectric constant	8.9	8.5	15.3
Electron Affinity (eV)	4.1	1.9	–
Absorption coefficient near Eg (cm^{-1})	10^5	3×10^5	6×10^4
Refractive index near Eg	2.5	2.15	2.9

Table1.1: *Room temperature properties of III–V semiconductors.*

The characteristics of III-nitrides include good thermal, mechanical and chemical stability which are mostly related to the strong bonding between the metal and nitrogen (N) atom. The other properties such as wide and direct band gap, high charge carrier mobility and high operating voltages and temperatures are advantageous compared to other semiconductors such as GaAs and Si. GaN and its alloys with In and Al have emerged as important semiconductor materials with their band gap energies being about two to three times those of conventional semiconductors such as Si, GaAs and InP, this also results in high electric breakdown fields (E_c), which makes it suitable for high voltage devices. Furthermore, its favorable high thermal conductivity allows the material to withstand high operating temperatures and provides improved radiation hardness. For field-effect transistors

and high-frequency performance electronic applications, GaN which possess electron mobility in excess of 2000 $cm^2V^{-1}s^{-1}$ and peak velocity approaching $3x10^7cms^{-1}$ at room temperature, makes this material appropriate for diverse applications. **Table 1.1** summaries the important materials properties of III-nitrides semiconductors[17–20], which can all be harnessed for several conventional and novel applications.

1.3. SUBSTRATE ISSUE:

(A) Sapphire Substrate for III-Nitrides:

It is very evident now that crystal quality (defects: such as dislocations, stacking faults etc.) and epitaxy are very important parameters to achieve sufficient gain in electrical conductivity and optoelectronic responses as shown in **Fig. 1.4.** The variation of normalized efficiency with respect to dislocation density can be seen in the figure, which clearly shows that increase in dislocation density either directly or indirectly reduce the efficiency of devices[21].

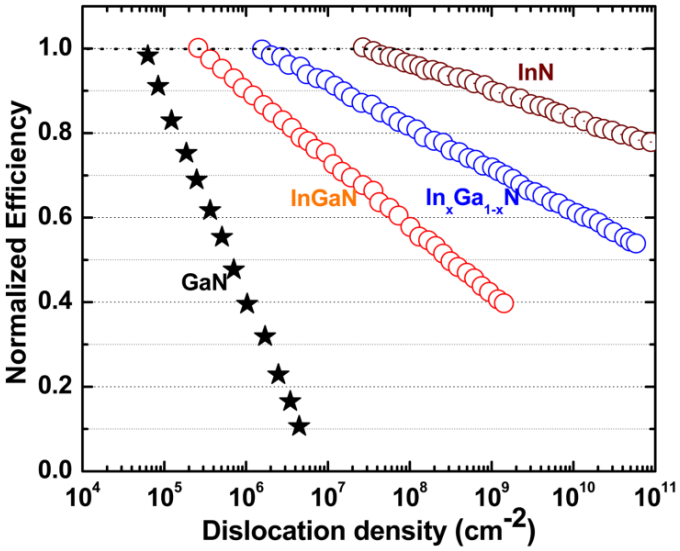

Fig.1.4: *The plot of normalized efficiency v/s dislocation density in III-Nitride semiconductors.*

Unfortunately, due to the lack of native substrates, the use of foreign substrates has led to high dislocation density caused by lattice mismatches[22,23]. The choice of substrates depends on the application of the nitride layers grown. For example, SiC is the best suitable

substrate for high power applications due to its good thermal conductivity along with better thermal expansion and lattice matching with GaN. Sapphire remains the most commonly used substrate due to its availability, structural compatibility with GaN, low cost, transparency over a wide spectral region, stability at high temperatures and matured manufacturing technology. Thus, most of the growth of commercial devices like LEDs is being carried out hetero-epitaxially on c-plane sapphire. Sapphire has also a hexagonal crystal structure and exists in the following crystallographic orientations: (0001)-c, (10-10)-m, (11-20)-a, (10-11)-s, (1-102)-r and (11-23)-n. However, there are still serious issues that need to be addressed in the use of sapphire as a substrate. The a-lattice parameter of sapphire is 0.47 nm, while for GaN it is 0.32 nm, yielding a lattice mismatch of 36%. Though while growth the GaN lattice undergoes an azimuthal rotation of 30^o with respect to that of sapphire to reduce the lattice mismatch to about 16%. However, the lattice mismatch between 6 lattice spacing of GaN and 7 lattice spacing of Al_2O_3 is 0.5% and in that context, sapphire can be used as a reasonably good substrate for GaN growth[24]. The lattice mismatch between different epitaxial relation and angles between the individual planes are listed in **Fig. 1.6.**

Lattice mismatch: $\dfrac{a_{III-N} - a_{Sapphire}}{a_{Sapphire}}$

	$[11\underline{2}0]_{III\text{-}N}$ || $[11\underline{2}0]_{sap}$	$[10\underline{1}0]_{III\text{-}N}$ || $[11\underline{2}0]_{sap}$
GaN	-33.0%	+16.0%
AlN	-34.6%	+13.3%

Planes	Angle between planes
(0001)^(1-102)	57°31’
(0001)^(11-23)	61°11’
(0001)^(10-11)	72°23’
(0001)^(11-21)	79°37’
(0001)^(11-20)	90°00’
(0001)^(10-10)	90°00’
(11-20)^(10-10)	30°00’

Fig.1.6: *Orientation and lattice mismatch between GaN, AlN and Al_2O_3 in-plane direction.*

However, even if sapphire were perfectly lattice matched to GaN during growth, the difference in thermal expansion coefficients between the two materials, 7.50x10^6 K^{-1} for sapphire and 5.45 x10^6 K^{-1} for GaN, would still induce strong biaxial compressive stresses in the GaN film after cooling down from growth temperatures. This stress is not enough to

induce crack in the film, which happens in the case of GaN films grown on silicon (Si), but is sufficient to create a large number of dislocations at the interface due to the relaxation of the strain built up within the GaN film due to mismatch after a certain thickness, through energetically favourable misfit dislocation generation. **Fig.1.5** shows a representative TEM micrograph of a very high density of threading dislocations observed in a typical GaN film grown on bare c-plane sapphire, which is detrimental to optimal device performance.

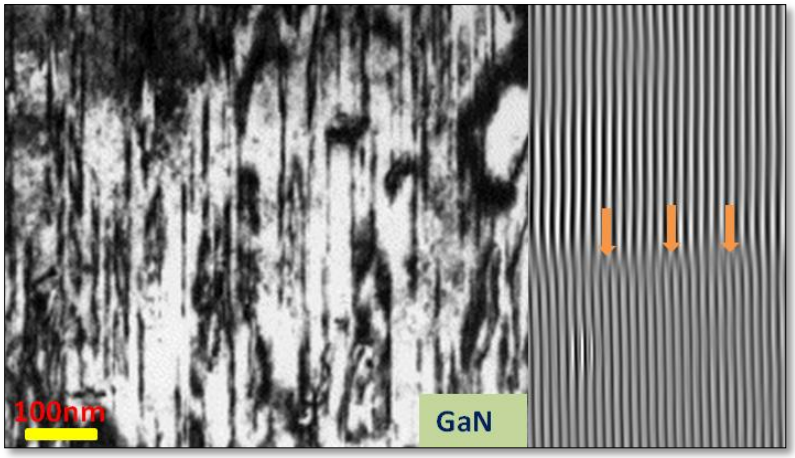

Fig.1.5: *TEM image of threading dislocations in a GaN film grown on sapphire surface*[25].

Sapphire's thermal conductivity at room temperature of 0.3 W/cm K is about 7 times lower than that of GaN, 2.1 W/cm K rendering it a bad dissipater of heat compared to silicon. Sapphire is electrically insulating with a resistivity higher than $10^{11}\Omega$ cm, therefore only planar device structures with contacts on the front side are possible. Due to these drawbacks and due to costs and availability, Si substrates have of late attracted enormous attention for the fabrication of III-nitride based electronic devices.

(B) Si Substrate for III-Nitrides:

The possibility of integrating the well established Si-based industry with III-nitride based devices will become more feasible with further improvement of technology. For the last 15 years, silicon as a substrate has attracted much attention for the growth of GaN because of its low price and its availability in large diameters, up to 12" wafers. Si also possesses other favourable qualities such as high crystal perfection (very low defect density), smooth surfaces and a good thermal stability for GaN growth at high temperatures. On the

other hand, from crystal structure point of view, Si has a diamond cubic crystal structure, and so to grow single phase hexagonal wurtzite GaN, Si (111) is the most appropriate surfaces, since its atomic structure is triangular and it shows a hexagonal closed packed (hcp) stacking along the [111] direction (**Fig.1.6(a)**).

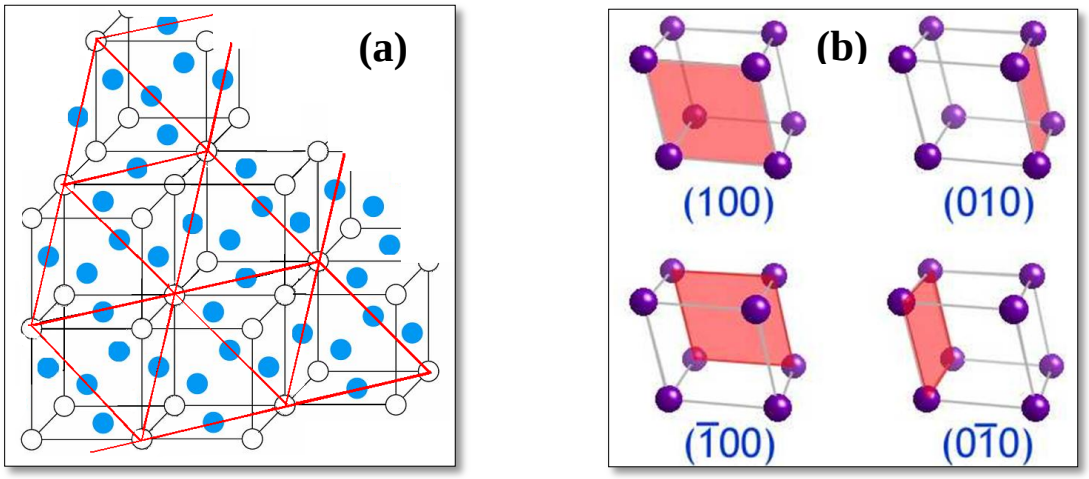

Fig.1.6: *Unit cell for the cubic crystal structure of* ***(a)*** *triangular plane Si(111)surface and* ***(b)*** *square planar lattice of Si(100)surface (image courtesy- DoITPoMS Teaching and Learning packages from Cambridge University).*

Si has a 17% lattice mismatch with respect to GaN which is almost comparable with that of sapphire. The difference in thermal expansion coefficient between GaN ($5.6x10^{-6}K$) and Si ($2.6x10^{-6}K$) results in a thermal expansion mismatch of about 56% as shown in **Table 1.2**, resulting in a large density of cracks on the film surface upon growth.

In the case of sapphire, GaN epilayer undergoes a compressive strain during cooling, while in contrast GaN grown on Si substrate suffers tensile stress which makes the overgrown film more prone to cracks. To reduce the thermal stress mismatch in GaN films different attempts have been made, such as using buffer layers of AlN or AlGaN graded super lattices which have resulted in the reduction of mismatch induced stress[26–29]. The reaction between GaN and Si during growth causes inter-diffusion of Si to GaN leading to un-intentional n-type doping[30–32] which can be prevented by using either the aforementioned AlN buffer layers or by nitriding the Si surface to form an intermediate SiN_x layer between Si and GaN. **Table 1.2** summaries the some important parameters of III-nitrides semiconductors[25,33–35].

Materials	Lattice constant		Thermal Expansion		Thermal conductivity (W/cm-K)
	Unit (A°)	Lattice mismatch to GaN/AlN (%)	10^{-6} K^{-1}	Lattice mismatch to GaN/AlN (%)	
Sapphire	a=4.759 c=12.991	-16/-13.3 --	7.3 8.5	23.4/43.2 --	0.49
Si(111)	a=3.89	17/19	3.59	-56/-16	1.3
GaN	a=3.189 c=5.185	0/2.4 0/3.9	5.59 3.17	0/2.4 0/3.9	4.1
AlN	a=3.112 c=4.982	-2.5/0 -4.1/0	4.15 5.27	-34.7/0 -39.9/0	5.9

Table1.2: *Lattice constants, thermal expansion coefficients, thermal conductivity of III-V semiconductors on different substrates.*

The growth of GaN on (001) Si substrate is challenging, because of square planar crystal lattice (shown in **Fig.1.6(b)**) which usually results in bi-phasic mixture of GaN[36]. Recently Schulze *et al*. reported the formation of high quality device structures such as, LEDs and field effect transistors on 4^o off-axis (001) Si miscut substrate[37]. By using miscut (001) Si plane and AlN/GaN super-lattice buffer layer, a mono-phase with single crystalline GaN films are grown on (001) Si. Thus, all of these reports show that silicon based GaN-on-Si device structures have drawn large attention not only in academic work but also towards the commercialization of III-nitrides based devices with cost effective and high efficiency. Based on the stringent requirements, highly efficient nitride devices need high quality GaN-growth on Si substrates. But the conventional way of GaN epitaxial growth on Si substrate will end up with a dislocation density of around 10^{10}-$10^{12}$$cm^{-2}$. In spite of these limitations, recent years several advances in lasing emission from rare earth (RE) elements doped GaN hetero-epitaxially grown on Si surface are achieved[38]. By using this approach, it has been demonstrated that the visible lasing action ranges from the wavelength of visible light to near-infrared (IR)[38,39]. Thus, improving the performance and integration of III-nitrides on Si microelectronics has been one of the strongly pursued research activities.

1.4 GROWTH ISSUES AND CURRENT STATUS:

In the past three decades, miniaturization of devices has seen according to the Moore's law that every two to three years, the density of logic devices is doubled with lowered cost per logic function, and increased chip performance[40–43]. When a device operates in the deep sub-micrometer regime, many physical phenomena such as, short-channel effect (SCE), velocity saturation, high leakage current, and dielectric breakdown, limit the benefits of conventional scaling and lifetime become worse as the device size become smaller and smaller[44]. Thus, the scaling down of devices with improved performance is possible when new hetero-structure devices are fabricated with the help improved growth techniques such MBE and MOCVD to satisfy the future requirement. As discussed earlier, the major issue of strain accommodation during the growth of device structures is being reviewed with new approaches. Among all the strain engineering process adopted nanocolumnar based growth has generated lot of attention of researchers due to the potential enhancement in device performance and possibility of providing low-cost high efficiency device to mankind. Thus, efficiency enhancement is not straight forward and it needs growth of high crystal quality III-nitride materials. Though, GaN has great potential as High Electron Mobility Transistors (HEMTs) for high power application, its performance is limited by the issues such as strain induced gate leakage, defect induced current conduction path, hot electron injection, and barrier breakdown[45,46]. Understanding the effect of stress related failure in HEMTs is one of the crucial things during device operation, in addition, inverse piezoelectric effect also leads to the reduction in device performance. To resolve strain induced failure, one can look for strain-free films which have been obtained by new strategy of growth, such as nanostructure formation instead of conventional 2-D films. Strain in the films can originate from the lattice-mismatch between film and substrate during the growth and temperature dependent phonon-induced lattice vibrations. As discussed, thermal expansion mismatch is the major problem to have a huge strain in the film and sometimes that leading to produce cracks in the film. These strain fields can reduce crystal symmetry, thus lifting band degeneracy and causing undesirable band-gap narrowing[47] and making it difficult to obtain required device performance. In particularly, hydrostatic strain breaks the crystal symmetry and hence, lifting band degeneracy with band splitting which affects the transport behavior of devices.

Extensive research efforts have been dedicated to reduce strain and dislocation formation in these years. In that direction having an intermediate nitride layer on sapphire and Si has been promising for the optimization of epitaxial growth of GaN on nitrided sapphire and Si substrates. This approach may lead to controlled strain evolution by managing the lattice and thermal expansion mismatch and other alternative approach is the nanocolumnar growth which enables high quality films[48–51]. Nanostructure based device fabrication can accommodate strain field as well as thermal expansion mismatch. In addition, the self assembled nanostructure based transistors, ultra bright LEDs, high efficient tandem solar cells, gas sensors etc, may be achieved due to[52,53] reduced defect density, large surface-to-volume ratio, large light extraction efficiency, compatibility with low cost large area silicon substrate and reduced strain distribution which weaken piezoelectric polarization filed. The use of nanostructures in the design of white LEDs is technologically important and advantageous due to many reasons, such as Ga (In) N nanostructures can be grown directly on bare substrate such as sapphire and Si without using any intermediate layer, buffer layer or catalyst. Extensive structural characterization done by several groups[45,60,61] have suggested that the nanostructures are free of extended defects such as dislocations, stacking faults, and twin boundaries and thus the surface recombination probability of nanostructures are two orders of magnitude smaller than the conventional films of III-nitrides.

1.5 NANOSTRUCTURE FORMATION:

It is evident now that the remarkable advances in nitride research and development of devices such as laser diode, High Brightness LEDs based on 2-D films; exhibit limited lifetimes due to large densities of extended defects. In that direction, fundamental issues of thin film growth, such as strain control, defects and novel alternative means to reduce threading dislocation densities by ELOG, Nano-ELOG, and Domain Matching Epitaxy etc are reported[56]. The motivation of the present work is to get rid of these dislocations by nanocolumnar growth which pushes the boundaries of what is possible in III-nitride devices in place of traditional thin films. The efforts in this work are towards understanding the role of kinetics of growth and substrate effects on formation of 2-D films and nanostructures of GaN grown mainly on c-plane sapphire on Silicon. From early 2000, significant research on GaN has been directed towards the fabrication of device in quasi-one-dimensional GaN

nanocolumns with low defect density. The growth of GaN 1-D structures are reported on different substrate including Si(111), Si(100) and sapphire by using differently modified surface and buffer layer of AlN and some time Ni catalyst as wetting layer is employed. The film which grown by these methods, yields randomly orientated nanorods with a high density of basal stacking faults as well as there is a sharp decrease in band edge emission was observed.

Upto now, many groups have shown GaN nanostructure formation at different growth condition and propose different mechanisms involved in the nanorod formation. In 1964, Wanger *et al*[57] reported the formation of Si whiskers by using Au as a catalyst. Almost same method is adapted to the growth of III-nitrides based materials particularly by using Au and Ni as catalyst. Recently, many researchers have observed homogeneous growth of NR with reduced tilting angles for longer nitridation duration on Si surface[55]. The high reactivity of Si surface enables formation of silicon nitride layer during the initial stages of NR growth when substrate is exposed to nitrogen plasma and leads to the formation of inhomogeneous silicon nitride at the interface. Although GaN rods formed by catalyst assisted growth via VLS mechanism, the size, tilt and tendency of formation of twisted nanostructures were observed. Cheze *et al*[58] have compared result s of GaN nanorods grown through the catalyst and without catalyst routes. They claim that the GaN nanorod formed by catalyst assisted method gives rise to a high density of basal stacking faults due to the presence of the catalyst at the nanorods tip, due to the lower surface mobility of adatoms at the tip of NRs. They observed that the metal catalysts not only enable the 1-D growth of GaN and also affect the structural, electrical and optical properties. The main debated issues of catalyst-assisted nanorods formation is the contamination and solid solution or alloy formation. The photoluminescence of nanorods grown in the VLS route reveal additional peak to the band transition, which could belong to the stacking fault or diffusive incorporation of metal catalyst into crystal lattice as a contamination. Thus, self -assembled nanorods grown without catalyst are more suitable for device applications. At the initial stage, growth of well aligned nanorods in a controlled fashion is challenging. It was found by many groups the ratio of III-V play major role in determining the growth of self assembled GaN nanostructure. The high value of V/III ratio is found to control the nucleation and density of the nanorods and that of lower value eventually favors to formation 2-D films. Bertness *et al*[59]demonstrated the growth GaN NRs

by using buffer layer of AlN and also showed that the thickness of the buffer layer plays an important role in deciding the density of nanorods. Landre *et al*[60] pointed out that the morphology of AlN buffer layer decides the subsequent GaN rods formation by easy plastic relaxation process. Besides that, AlN intermediate layer also decides the orientation of GaN rods and epitaxial relation, tilt and twist in the nanorods. The importance of the AlN buffer layer and their thickness are done on sapphire substrate. Interestingly, it is found that the thickness of the AlN intermediate layer affects the column configuration, density and their optical properties. It is important to note that the growth condition of the nanorods enormously affect the properties of the films. The atomistic process involved in the initial stage of the GaN film growth is shown schematically in **Fig.1.7**.

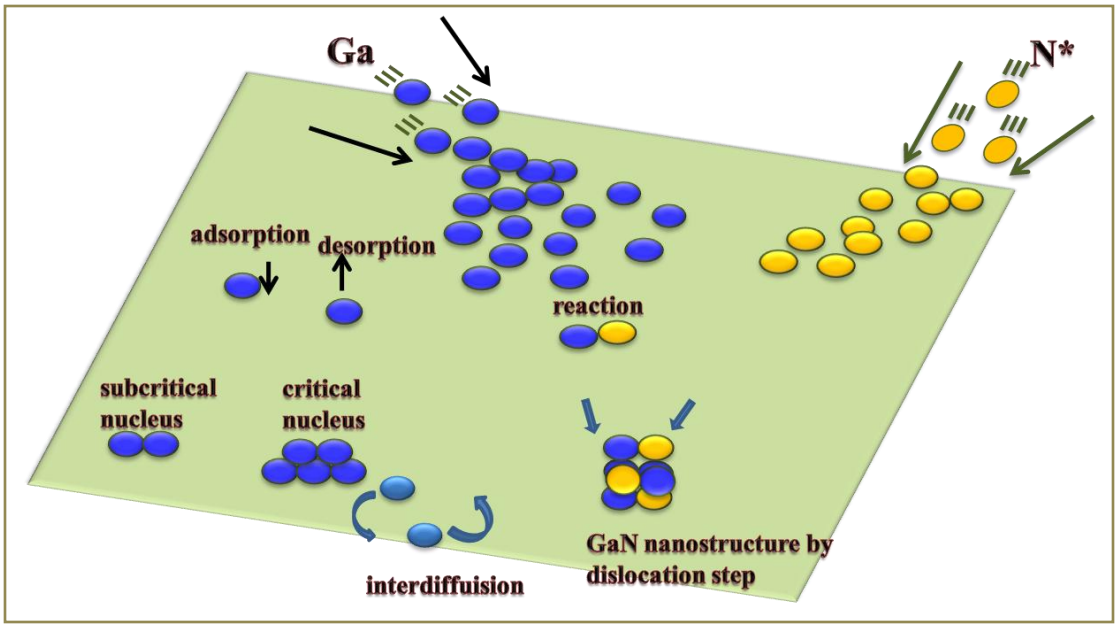

Fig.1.7: *Schematics of the surface processes occurring during film growth by MBE.*

Though most of the discussion has been on reports of growth of GaN nanostructure by using catalyst buffer layer, growth without catalysts and also on differently modified substrate is gathering momentum. As yet to tailor-make these nanorods, a clear picture of the nucleation mechanism involved in the formation of nanorods is not clearly understood yet. Bertness *et al*[61,62] show that the GaN nanorods do not nucleate on top of the AlN buffer layer, but rather strongly correlates with their {1-102} facets. Sekiguchi *et al*[63,64] suggested that the GaN nanorods are not directly grown on the grains of AlN, but rather form on the edge of it. Furthermore, Consonni *et al*[65] offer a growth mechanism based on total surface energy which

explains the growth of GaN nanorods from the transition of GaN truncated nanostructure. Ristic *et al*[66,67] have shown that GaN nanostructures are formed by nucleation and diffusion limited process yielding different sized islands and thus different size nanorods formation. The proposed mechanism of growth involves the diffusion of Ga along the side walls up to apex, promoting 1-D growth. They suggest that the nanorods started to grow as GaN islands once it reaches a critical stable nuclei size. Debanath *et al*[68]propose a diffusion –induced growth model in which they explain the size dependent nanorod formation by adatoms diffusion process as well as adsorption process at the tip of rods.

Only a few reports demonstrate the role of intentional and unintentional nitridation on nucleation process of GaN nanorods formation. The orientation, size, tilt and twist of the nanostructures mainly depend on the intermediate nitridation. In this thesis, we address the role of intermediate layer in determining the morphological evolution of nanorods by spontaneous nucleation in axial screw dislocation. Here, we initially form phase diagram of growth by carefully varying the growth parameter, which yield 2-D films, nanostructures, etc. From this growth map, we get a handle of forming various growth configuration of GaN by sheer kinetic growth. We also carefully modify Al_2O_3 and Si surfaces by nitriding them, and then grow nanostructures in a controlled way. To consolidate, the clear picture of GaN nanostructure formation and their orientation on modified substrate as well as bare substrate are investigated in this dissertation. The effort in this work is towards the understanding the spontaneous catalyst free, kinetically controlled formation of nanostructures of GaN, on c-plane (0001) sapphire and low index Silicon (001) and (111) surfaces. The work involves synthesis in carefully controlled growth-parametric space by Molecular Beam Epitaxy followed by complementary characterization using sophisticated structural, optical, electrical and morphological techniques.

1.6: REFERENCES:

1. J. Arbiol, C. Magen, P. Becker, G. Jacopin, A. Chernikov, S. Schäfer, F. Furtmayr, M. Tchernycheva, L. Rigutti, J. Teubert, S. Chatterjee, J. R. Morante, and M. Eickhoff, *Nanoscale*, 2012, **4**, 7517–24.

2. M. I. den Hertog, F. González-Posada, R. Songmuang, J. L. Rouviere, T. Fournier, B. Fernandez, and E. Monroy, *Nano Lett.*, 2012, **12**, 5691–6.

3. H. Morkoc, *Sel. Top. Quantum Electron. IEEE …*, 1998, **4**, 537–549.

4. T.-C. Lu, J.-R. Chen, S.-C. Lin, S.-W. Huang, S.-C. Wang, and Y. Yamamoto, *Nano Lett.*, 2011, **11**, 2791–5.

5. J. Huang, K. Xu, X. J. Gong, J. F. Wang, Y. M. Fan, J. Q. Liu, X. H. Zeng, G. Q. Ren, T. F. Zhou, and H. Yang, *Appl. Phys. Lett.*, 2011, **98**, 221906.

6. X. Chen and T. Uesugi, *Appl. Phys. Lett.*, 2006, **88**, 031916.

7. G. Perillat-Merceroz, P. H. Jouneau, G. Feuillet, R. Thierry, M. Rosina, and P. Ferret, *J. Phys. Conf. Ser.*, 2010, **209**, 012034.

8. L. J. Mandalapu, F. X. Xiu, Z. Yang, and J. L. Liu, *J. Appl. Phys.*, 2007, **102**, 023716.

9. Y. Huang, X. Duan, and C. M. Lieber, *Small*, 2005, **1**, 142–7.

10. A. I. Hochbaum and P. Yang, *Chem. Rev.*, 2010, **110**, 527–46.

11. S. Strite, *J. Vac. Sci. Technol. B Microelectron. Nanom. Struct.*, 1992, **10**, 1237.

12. S. Nakamura, M. Senoh, N. Iwasa, and S. Nagahama, *Appl. Phys. Lett.*, 1995, **67**, 1868.

13. S. W. Kaun, M. H. Wong, U. K. Mishra, and J. S. Speck, *Semicond. Sci. Technol.*, 2013, **28**, 074001.

14. S. Kukushkin and A. Osipov, *Rev. Adv. Mater. …*, 2008, **17**.

15. C. Mauder, 2011, 1–133- Thesis- "Physics, MOVPE growth, and investigation of *m*-plane GaN films and InGaN/GaN quantum wells on γ-LiAlO2 substrates".

16. O. Ambacher, *J. Phys. D. Appl. Phys.*, 1998, **2653**.

17. A. Jiménez, Z. Bougrioua, J. M. Tirado, A. F. Braña, E. Calleja, E. Muñoz, and I. Moerman, *Appl. Phys. Lett.*, 2003, **82**, 4827.

18. K. M. A. Saron, M. R. Hashim, N. Naderi, and N. K. Allam, *J. Appl. Phys.*, 2013, **114**, 134510.

19. J. Choi, R. Puthenkovilakam, and J. P. Chang, *Appl. Phys. Lett.*, 2005, **86**, 192101.

20. R. GLASS and I. GLASS, *J. Appl. Phys.*, 2000, **87**.

21. W. A. Brantley, O. G. Lorimor, P. D. Dapkus, S. E. Haszko, and R. H. Saul, *J. Appl. Phys.*, 1975, **46**, 2629.

22. B. Ding, *Chinese J. Phys.*, 2012, **50**, 508–518.

23. P. Dong, J. Yan, J. Wang, Y. Zhang, C. Geng, T. Wei, P. Cong, Y. Zhang, J. Zeng, Y. Tian, L. Sun, Q. Yan, J. Li, S. Fan, and Z. Qin, *Appl. Phys. Lett.*, 2013, **102**, 241113.

24. S. Shetty, J. Ghatak, and S. M. Shivaprasad, *Solid State Commun.*, 2014, **180**, 7–10.

25. L. Liu and J. H. Edgar, *Mater. Sci. Eng. R Reports*, 2002, **37**, 61–127.

26. P. Xu, Y. Jiang, Y. Chen, Z. Ma, X. Wang, Z. Deng, Y. Li, H. Jia, W. Wang, and H. Chen, *Nanoscale Res. Lett.*, 2012, **7**, 141.

27. J. R. L. Fernandez, O. C. Noriega, J. A. N. T. Soares, F. Cerdeira, E. A. Meneses, J. R. Leite, D. J. As, D. Schikora, and K. Lischka, *Solid State Commun.*, 2003, **125**, 205–208.

28. M. Wölz, V. M. Kaganer, O. Brandt, L. Geelhaar, and H. Riechert, *Appl. Phys. Lett.*, 2011, **98**, 261907.

29. C. Teichert, *Phys. Rep.*, 2002, **365**, 335–432.

30. E. Calleja, M. A. Sa, H. H, F. J. Sa, F. Calle, F. B. Naranjo, S. I. Molina, A. M. Sa, F. J. Pacheco, and R. H. Garc, *... Cryst. growth*, 1999, **202**, 296–317.

31. M. A. Reshchikov and H. Morkoç, *J. Appl. Phys.*, 2005, **97**, 061301.

32. A. S. Brown, M. Losurdo, T. H. Kim, M. M. Giangregorio, S. Choi, M. Morse, P. Wu, P. Capezzuto, and G. Bruno, *Cryst. Res. Technol.*, 2005, **40**, 997–1002.

33. B. Bairamov, O. Gürdal, A. Botchkarev, H. Morkoç, G. Irmer, and J. Monecke, *Phys. Rev. B*, 1999, **60**, 16741–16746.

34. O. Ambacher, *J. Phys. D. Appl. Phys.*, 1998, **31**, 2653–2710.

35. H. Xing, S. Keller, and Y. Wu, *J. Phys. ...*, 2001, **7139**.

36. S. Shetty, M. Kesaria, J. Ghatak, and S. M. Shivaprasad, *Cryst. Growth Des.*, 2013, **13**, 2407–2412.

37. A. Dadgar, P. Veit, F. Schulze, J. Bläsing, a. Krtschil, H. Witte, A. Diez, T. Hempel, J. Christen, R. Clos, and A. Krost, *Thin Solid Films*, 2007, **515**, 4356–4361.

38. A. J. Steckl, J. H. Park, and J. M. Zavada, *Mater. Today*, 2007, **10**, 20–27.

39. I. Aharonovich, A. Woolf, K. J. Russell, T. Zhu, N. Niu, M. J. Kappers, R. A. Oliver, and E. L. Hu, *Appl. Phys. Lett.*, 2013, **103**, 021112.

40. K. Tomioka, M. Yoshimura, and T. Fukui, *Nature*, 2012, **488**, 189–92.

41. J. C. Johnson, H.-J. Choi, K. P. Knutsen, R. D. Schaller, P. Yang, and R. J. Saykally, *Nat. Mater.*, 2002, **1**, 106–10.

42. J. Simon, Z. Zhang, K. Goodman, H. Xing, T. Kosel, P. Fay, and D. Jena, *Phys. Rev. Lett.*, 2009, **103**, 026801.

43. H.-J. Choi, H.-K. Seong, J. Chang, K.-I. Lee, Y.-J. Park, J.-J. Kim, S.-K. Lee, R. He, T. Kuykendall, and P. Yang, *Adv. Mater.*, 2005, **17**, 1351–1356.

44. S. Hwang, D. Morgan, A. Kesler, M. Lachab, B. Zhang, A. Heidari, H. Nazir, I. Ahmad, J. Dion, Q. Fareed, V. Adivarahan, M. Islam, and A. Khan, *Appl. Phys. Express*, 2011, **4**, 032102.

45. G. Meneghesso, G. Verzellesi, R. Pierobon, F. Rampazzo, A. Chini, U. K. Mishra, C. Canali, A. Member, E. Zanoni, and S. Member, 2004, **51**, 1554–1561.

46. X.-H. Ma, J.-J. Zhu, X.-Y. Liao, T. Yue, W.-W. Chen, and Y. Hao, *Appl. Phys. Lett.*, 2013, **103**, 033510.

47. V. Fiorentini, F. Bernardini, and F. Della Sala, *Phys. Rev. B*, 1999, **60**, 8849–8858.

48. D. Cherns, L. Meshi, I. Griffiths, S. Khongphetsak, S. V. Novikov, N. Farley, R. P. Campion, and C. T. Foxon, *Appl. Phys. Lett.*, 2008, **92**, 121902.

49. J. Ristić, C. Rivera, E. Calleja, S. Fernández-Garrido, M. Povoloskyi, and A. Di Carlo, *Phys. Rev. B*, 2005, **72**, 085330.

50. T. Iwanaga, T. Suzuki, S. Yagi, and T. Motooka, *Appl. Phys. Lett.*, 2005, **86**, 263102.

51. E. Calleja, J. Ristić, S. Fernández-Garrido, L. Cerutti, M. A. Sánchez-García, J. Grandal, A. Trampert, U. Jahn, G. Sánchez, A. Griol, and B. Sánchez, *Phys. Status Solidi*, 2007, **244**, 2816–2837.

52. P. Yang, R. Yan, and M. Fardy, *Nano Lett.*, 2010, **10**, 1529–36.

53. M. Hegde, S. S. Farvid, I. D. Hosein, and P. V Radovanovic, *ACS Nano*, 2011, **5**, 6365–73.

54. R. Colby, Z. Liang, I. H. Wildeson, D. A Ewoldt, T. D. Sands, R. E. García, and E. A Stach, *Nano Lett.*, 2010, **10**, 1568–73.

55. S. Li and A. Waag, *J. Appl. Phys.*, 2012, **111**, 071101.

56. M. Kesaria, S. Shetty, and S. M. Shivaprasad, *Cryst. Growth Des.*, 2011, **11**, 4900–4903.

57. R. S. Wagner and W. C. Ellis, *Appl. Phys. Lett.*, 1964, **4**, 89.

58. C. Chèze, L. Geelhaar, B. Jenichen, and H. Riechert, *Appl. Phys. Lett.*, 2010, **97**, 153105.

59. K. A. Bertness, N. A. Sanford, J. M. Barker, J. B. Schlager, A. Roshko, A. V. Davydov, and I. Levin, *J. Electron. Mater.*, 2006, **35**, 576–580.

60. O. Landré, V. Fellmann, P. Jaffrennou, C. Bougerol, H. Renevier, A. Cros, and B. Daudin, *Appl. Phys. Lett.*, 2010, **96**, 061912.

61. K. A. Bertness, A. Roshko, N. A. Sanford, J. M. Barker, and A. V. Davydov, *J. Cryst. Growth*, 2006, **287**, 522–527.

62. K. A. Bertness, A. Roshko, L. M. Mansfield, T. E. Harvey, and N. A. Sanford, *J. Cryst. Growth*, 2008, **310**, 3154–3158.

63. T. Sekiguchi, J. Hu, and Y. Bando, *J. Electron Microsc. (Tokyo).*, 2004, **53**, 203–8.

64. H. Sekiguchi, T. Nakazato, A. Kikuchi, and K. Kishino, *J. Cryst. Growth*, 2007, **300**, 259–262.

65. V. Consonni, M. Knelangen, U. Jahn, A. Trampert, L. Geelhaar, and H. Riechert, *Appl. Phys. Lett.*, 2009, **95**, 241910.

66. L. Cerutti, J. Ristić, S. Fernández-Garrido, E. Calleja, A. Trampert, K. H. Ploog, S. Lazic, and J. M. Calleja, *Appl. Phys. Lett.*, 2006, **88**, 213114.

67. J. Ristić, E. Calleja, M. Sánchez-García, J. Ulloa, J. Sánchez-Páramo, J. Calleja, U. Jahn, a. Trampert, and K. Ploog, *Phys. Rev. B*, 2003, **68**, 125305.

68. R. K. Debnath, R. Meijers, T. Richter, T. Stoica, R. Calarco, and H. Lüth, *Appl. Phys. Lett.*, 2007, **90**, 123117.

Chapter 2

Experiments and Characterization

2. Experiments and Characterization:

This chapter essentially describes the growth technique and characterization tools involved in the present study. Firstly, we give a brief description about the fundamental concepts, basic operation principles of the Molecular Beam Epitaxy System (MBE) growth technique. During, growth we have used various *in-situ* characterization tools that are used to monitor growth such as RHEED, Atomic Absorption, QCTM and CL. The *ex-situ* characterization techniques employed in this work such as X-ray Diffraction (XRD), Scanning Electron Microscopy (SEM), Transmission Electron Microscopy (TEM), X-ray Photoelectron Spectroscopy (XPS) and Raman Spectroscopy are also briefly described here.

2.1 Molecular Beam Epitaxy System (MBE):

Molecular Beam Epitaxy is a Ultra-High-Vacuum (UHV)-based growth technique with sub-monolayer growth control (<0.01nm) by the interaction of a single or multiple molecular or atomic beams at the surface of a heated substrate. Thus, the density of contaminant molecules such as oxygen, carbon is significantly less than other growth techniques and hence MBE growth provides impurity-free, high quality films with abrupt interfaces[1]**.** Hence MBE has been one of the most widely used techniques for producing epitaxial layers of compound semiconductors by using high purity materials (>99.99999%) for research and development, and has been also used commercially. The precise stacking layer by layer of semiconducting thin films enables achieving high efficient devices such as solar cells, LEDs and HEMT. Underlying the growth mechanism of MBE is relatively simple: ultra-pure solid-source that are to be grown are heated in a Knudsen cell to produce beams of atoms or clusters. The base pressure of our system is about $5x10^{-11}$ Torr. Due to this high order of vacuum, the mean free path of the ambient gas molecules is about 38km and hence it provides a clean substrate surface for a very long time to deposit the films. The extremely precise control on the vacuum environment and on the quality of the source materials that is possible by this technique allows the growth of high purity films, compared to non-UHV-based techniques. To achieve such a high vacuum, a cryo, getter-ion and turbo molecular pumps are employed in attaining a base pressure of $5x10^{-11}$ Torr in the growth chamber. The chamber has a doubled walled cryo-panel which prevents degassing from the

walls and also adsorbs the unwanted gas molecules that emanate by heating the substrate. The schematic MBE growth chamber is as shown in **Fig.2.1**.

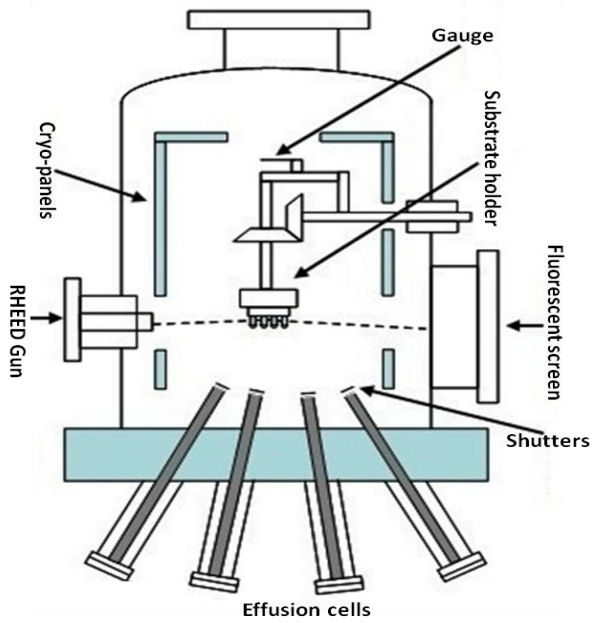

Fig.2.1: *Schematic diagram of Molecular Beam Epitaxy system*[2].

The high purity growth materials and doping metals loaded in effusion cell contained in pyrolytic boron nitride (PBN) crucible is heated to high temperatures until the material sublimates or evaporates from effusion cell. Shutters that are mounted in front of Knudsen cells mouth, that provide the direct control of the molecular beam (atoms or clusters) during the epitaxial growth in a precise monolayer scale. The nitrogen source to react with the metal atoms to yield the nitride is from nitrogen plasma that is created by using a radio frequency inductive coupled plasma source. In our work, we used Plasma Assisted Molecular Beam Epitaxy (PA-MBE) system (SVTA Assoc. Inc., USA). Our JNCASR MBE (shown **in Fig. 2.2**) system is configured for growth on 3" wafer with high uniformity of <1% all around 2.8" diameter of the wafer. The samples are loaded in load-lock chamber and followed by a initial preparation procedure are carried out in the prep chamber by annealing the substrate (degassing) at 500^{o}C for an hour. Our MBE system has 10 Knudsen cells (k-cells-Ga, In, Al, Mg, and Si), among all, one is nitrogen plasma source and another one is Ammonia gas injector. The growth manipulator has a circular heating filament and substrate temperature (T_S) were calibrated with respect to the pyrometer and thermocouple for epitaxial growth.

Nitrogen gas is introduced into the chamber at a typical rate of 4.5sccm, while the growth was carried out at $2.5x10^{-5}$ Torr of nitrogen with $375W_f$ forward and 7Wr reflected power of the RF plasma is maintained all along the growth. The purity of the nitrogen gas is monitored by a quadruple mass spectrometer, which is also used for leak detection.

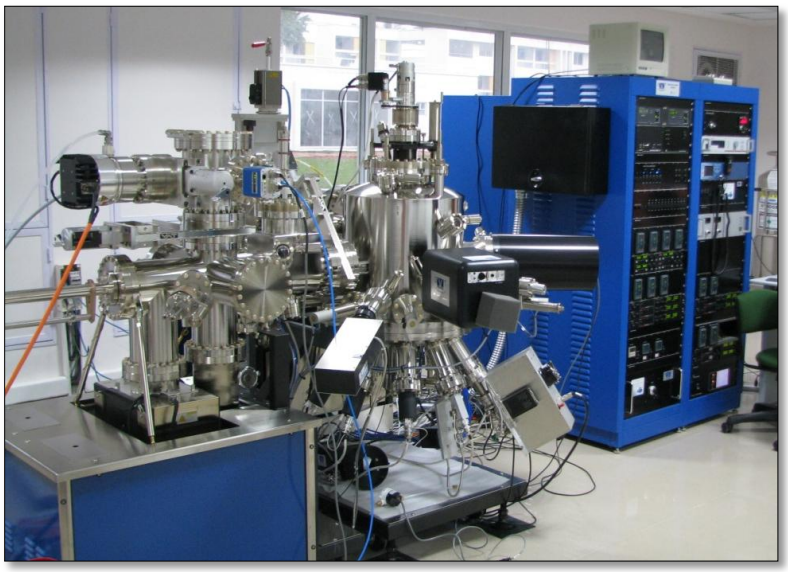

Fig.2.2: *SVTA MBE system used in the present study for the growth of GaN nano-structures.*

During growth, the deposition is monitored by *in-situ* reflection beam high energy electron diffraction (RHEED). Thickness and growth rate of individual depositing materials are monitored by an Atomic absorption spectrometer which determines the species flux rate with respect to k-cell temperature which is recombined by a QCTM which is used for thickness measurement.

2.2 Effusion Cells (Knudsen Cells):

Effusion cells are one of the most crucial components of molecular beam epitaxy (MBE) systems. Effusion Cells are used to generate ultrapure molecular and atomic beams from a large variety of elements and compounds. The charging materials placed in crucibles are made up of pyrolytic boron nitride (PBN). The crucibles are heated radiatively by electrically insulated heater filaments which are wounded in end-to-end fashion in our SVTA MBE system to prevent magnetic interference, and the thermocouple is positioned such way that it has intimate contact with the crucible as shown in **Fig.2.3**. For our growth, we have

calibrated all metal flux such as Ga, Al and In by using ion gauge and atomic absorption spectroscopy and QCTM.

The k-cell of Ga and In are designed as a hot lip (heater at the mouth of the k-cell to avoid deposition at those coldest parts of the cell) and the Al k-cell has a cold lip in order avoid thermal crack formation during ramping up and down the k-cell. The effusion cell temperature is controlled by PID temperature controller and a heater power supply. Prior to loading the charge (7N purity ingots), the crucibles were out gassed at 1200°C to make sure that the crucibles are free of contamination. After loading the charge effusion cells were ramped up to the operating temperature at the rate of 200^{o}C for 15mins. The growth element were deposited on the substrate, which is evaporated from Knudsen crucibles, the evaporation rates is governed by formula (Knudsen effusion equation) with a given temperature is

$$d\Gamma_e = \frac{dN_e}{A_e dt} = P_{eq}\sqrt{\frac{N_A}{2\pi M k_B T}}[m^{-2}s^{-1}]$$ Where N_e the number of molecules evaporating from the surface area A_e, N_A the Avogadro constant, T the temperature, P_{eq} the equilibrium evaporant pressure, k_B the Boltzmann constant and M is the molecular weight of the evaporated material.

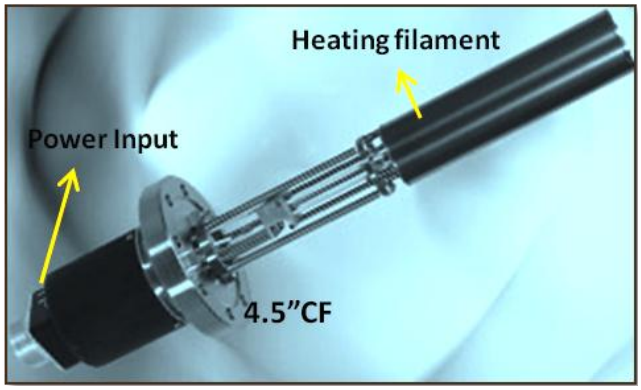

Fig.2.3: *The photograph of effusion cell of SVTA MBE system*[3].

2.3 MBE Flux- Calibration:

Before doing MBE growth, first we carried out optimization of K-shell temperature and substrate temperature using atomic absorption. Due to this calibration we found that

maximum optimum flux generated at 1000^{o}C for gallium, which will give proper control over the growth at nitrogen flow rate of 4.5 sccm. Whole calibration was done, by using AccuFlux monitor (atomic absorption) made by SVT associate USA. We found that around 800^{o}C vaporization gallium of starts in low magnitude, exactly at 1000^{o}C one can achieve appropriate gallium flux to grow GaN. The base pressure of the growth chamber was ~1x10^{-10} Torr and Ga K-cell temperature was maintained at 100^{o}C. Before performing the calibration, Ga K-cell was thoroughly degassed at 1100^{o}C to remove unwanted water vapor and other contamination. Prior to calibration, the initial adjustment of AccuFlux monitor was done.

The Ga K-cell temperature is ramped up to 600^{o}C at the interval of 20^{o}C/mins; during this temperature there no change in AccuFlux reading. The K-cell temperature is increased further to 650^{o}C still there no change is observed upto 800^{o}C. The deposition rate and absorption rates are calculated by computing based on above equations shown in previous section **2.4.** The same method is followed for Al calibration; the respective plots are shown in **Fig. 2.16.**

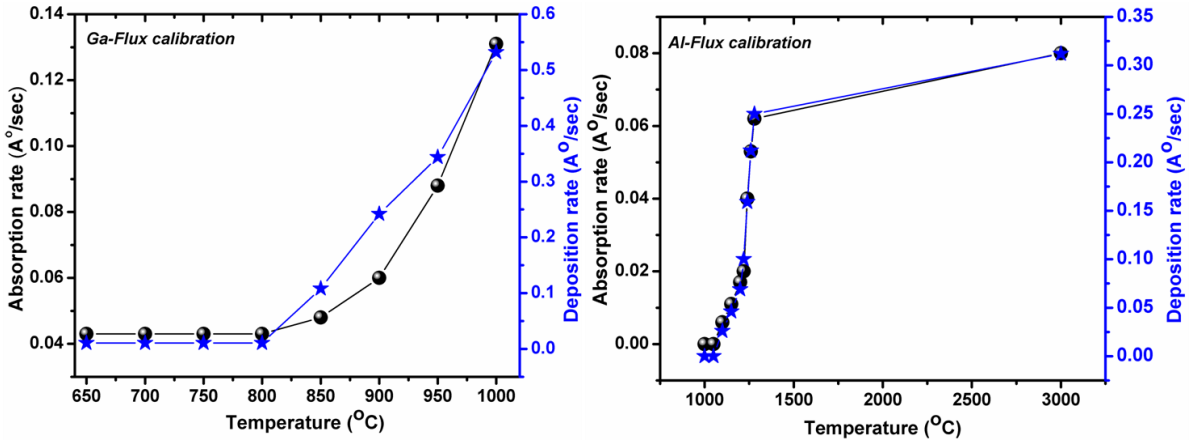

Fig. 2.16: *show plots of variation in absorption rate and deposition rate in alternative (y-axis) with respect to K-cell temperature.*

2.4 Radio Frequency Nitrogen Plasma Source:

In a molecular beam epitaxy system, the charge materials are usually in the form of solid ingots. To nitride them, N_2 gas molecules or Ammonia are injected into the chamber in a form where the reactivity is effective. In that context, there are different methods to produce active nitrogen species. Ammonia is an effective source of nitrogen, but the

substrate temperature required is sufficiently high to break the ammonia molecules and so limits parametric control of growth. Other way around is to have reactive nitrogen by exciting N_2 molecules by using radio frequency plasma source. There are different methods of plasma creation; one is electron cyclotron resonance plasma and the other is the radio frequency plasma source. In our study, we used SVTA nitrogen plasma source with a power supply operating at 13.5 MHz power supply and consists of an inductively couple plasma tube at the end of the source via a short coil. The forward power of $375W_f$ and reflection power of $7W_r$ is maintained during the growth. The image of the RF plasma ion source is shown in ***Fig.2.4(a)***. The plasma alignments are done by using deflection plates to have maximum intensity at the centre of growth manipulator.

We used ultra high pure nitrogen gas, and this gas is passed through a standard flow rate of 4.5sccm. A typical optical emission spectrum from the SVTA-4.5 plasma source is shown in ***Fig.2.4(b)***. The coil of plasma source has built in water (16^oC) circulation to reduce excess heating. Finally, the benefit of the plasma source is that the efficiency is independent of the substrate temperature, this allows for growth rates irrespective of substrate the temperature.

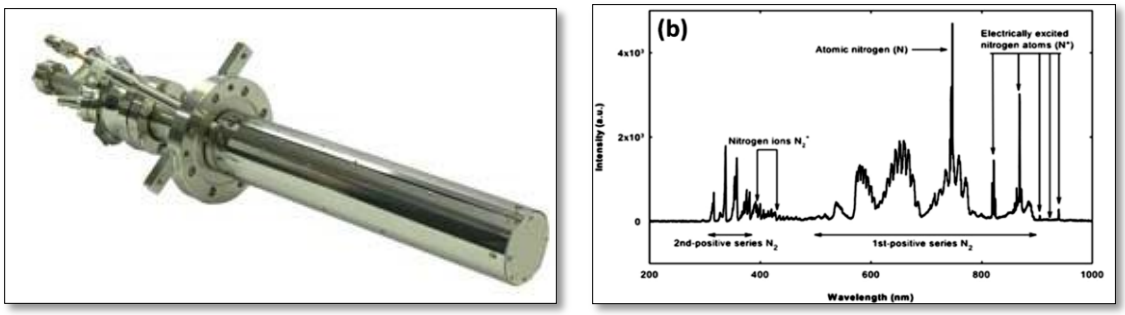

Fig.2.4: *The schematic geometry of plasma chamber set up in MBE system of SVTA make and a typical optical emission spectroscopy spectrum taken at a nitrogen pressure of* $1x10^{-5}$*torr*[3].

2.5 Atomic Absorption Spectroscopy:

In our study, we have extensively used atomic absorption spectroscopy of SVT Associates (as shown in ***Fig.2.5)***, to monitor film thickness and flux rate and deposition rate. The AccuFlux monitor is designed by SVTA for *in-situ* monitoring accurate information about material fluxes for different k-cell temperatures. Atomic Absorption Spectroscopy is a

non-destructive optical selective method to determine concentrations of atoms in vapor phase. A beam of light with their wavelength is suitable for absorbing corresponding atomic species of interest and which is aligned in the direction towards the growth manipulator in the deposition chamber. The exiting beam is detected back and depending upon amount of absorption, the absorption coefficient is used to compute the flux density. In our system, the instrumentation is located outside of the vacuum chamber, thus fully compatible with standard thin film deposition environment as shown in schematic diagram below[1].

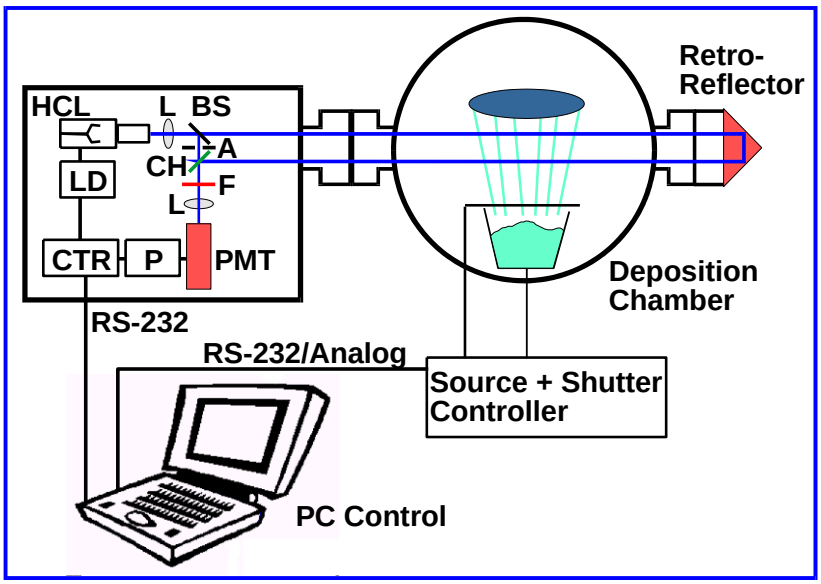

Fig.2.5: *Atomic Absorption Monitoring Technique: HCL= Material Specific Hollow Cathode Lamp, L=Lens, BS=Beam Splitter, A=Aperture, CH=Chopper, F=Filter, PMT=Detector, P=Lock-in-Amplifier, LD= Light Source Drive, CTR=Digital Signal Processor*[3].

The Accuflux Process Monitor essentially makes use of Hollow Cathode Lamp (HCL) technology for the creation of material selective as well as sensitive and ultra bright radiation. In our study, we use the charge materials like Gallium, Aluminum and Indium, and hence, different HCLs with highly selective UV filters are used for the respective material. To increase the absorption signal and also enhance the opto-mechanical stability the retro-reflector reflects the beam back to the entering viewport regardless of its incident angle. A single, enhanced photomultiplier (PMT) accurately detects the radiation even at low light levels. PID temperature control of the PMT module ensures reduced drift and exceptional noise performance. The optical design includes a modulator ("chopper") that alternately exposes the photo detector to a reference beam of the lamp and the sensing beam. The ratio

of these two signals is then digitally processed with a lock-in technique that provides high noise rejection of stray light. The digital signal processor provides the necessary timing and optimum signal filtering, as well as communication to a host PC.

Let $\mathbf{I_0^{chamber}}$ be the light intensity of the signal having no flux, and $\mathbf{I_0^{ref}}$ be the reference signal (coming from the chopper) and $\mathbf{I_0^{noise}}$ be the noise signal detected by PMT. Then, $\mathbf{I_0^{norm} = (I_0^{ref} - I_0^{noise})/ (I_0^{chamber} - I_0^{noise})}$ is the normalized intensity of the light going through the chamber when there is no evaporation.

Let $\mathbf{I_f^{chamber}}$ be the intensity of the signal, when evaporation of the material occurs and the light goes through the **f**lux.

$$\mathbf{I_f^{norm} = (I_0^{ref} - I_0^{noise}) / (I_f^{chamber} - I_0^{noise})}$$

Transmission of the light through the flux can be calculated as: $\mathbf{T = I_0^{norm} / I_f^{norm}}$

Absorption coefficient (**A) = 1 – T**

DR = SF* × *A, where SF is a scaling factor. Therefore, deposition rate can be computed based on above equations.

2.6 Reflection High Energy Electron Diffraction (RHEED):

Our MBE system contains *in-situ* RHEED to obtain information about growth modes. The technique involves grazing incidence (1-3^o) of high energy electron beam of about 9kV in which wavelength of the electron satisfies the diffraction condition. The grazing incidence on the sample surface restricts penetration depth of electron making it surface sensitive. Thus, the electron gets reflected from different crystal planes with depth of few nanometers of the film. The schematic and a typical image of the RHEED diffraction is shown in **Fig.2.6**. The beams reflected from different atomic planes interfere constructively or destructively and form the diffraction pattern on the fluorescent screen. The diffraction pattern observed on the screen corresponds to the intersection of the reciprocal lattice of the sample with the Ewalds sphere of radius $k = 2\pi/\lambda$ where k is the wave number and λ the wavelength[4]**.** As the name suggests, the spacing of the reciprocal lattice streaks is inversely proportional to the spacing of the atomic planes taking part in diffraction. From this diffraction pattern spacing of the lines is used to determine the inter-planar spacing for different crystallographic

orientations. By using RHEED intensity oscillations one can monitor film thicknesses. The typical RHEED patterns are the combination of reciprocal lattice streaks and Kikuchi lines. **Fig. 2.7** represents the RHEED evolution with respect to surface morphology[5]**.** Depending on the surface features the emerging RHEED pattern is made up of long, uniform streaks that mean lattice of rods perpendicular to the surface in real space and hence indicate the surface is growing smoothly, in a two-dimensional fashion as the electrons are exhibiting true reflection diffraction. If however, the reciprocal lattice features are spotty, the surface is more three-dimensional and rough on the nm scale, exhibiting transmission reflection diffraction as shown in **Fig 2.7**.

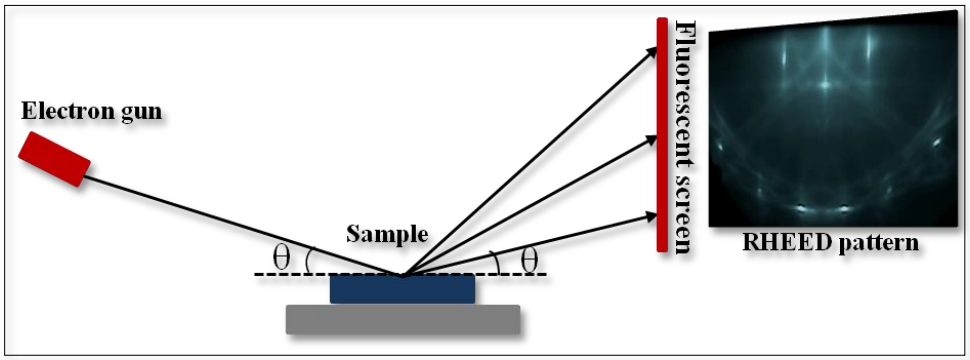

Fig.2.6: *the schematic of the experimental set-up and a representative RHEED Pattern.*

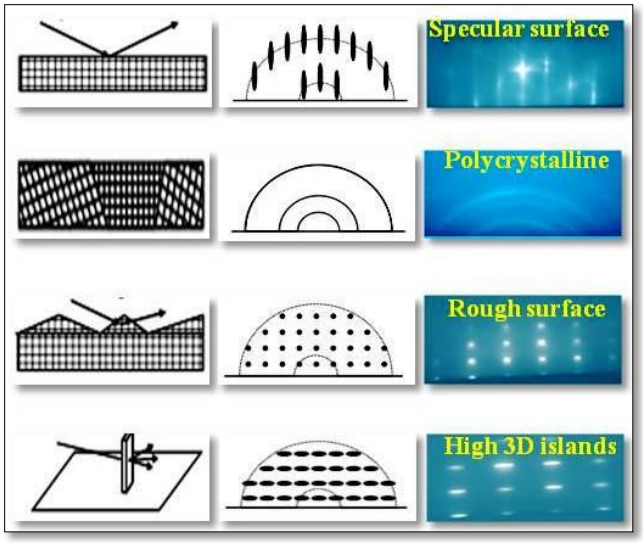

Fig.2.7: *The representative pattern of RHEED evolution with respect to surface morphology.*

That means some electrons are transmitted through surface features and cause interference pattern in spotty reciprocal lattice features. If the diffraction pattern appears ring-like it is an

indication that a sample is polycrystalline. Finally from the RHEED pattern, it is possible to calculate the crystal lattice constant. Indeed, the distance between the streaks provides the lattice parameter in the surface plane. In case of spotty pattern the distance in horizontal and vertical direction between the spots give a-and-c lattice parameter[6]**.** One can have clear information about surface reconstructions in along with the growth modes and crystallinity.

2.7 Photoluminescence (PL):

Photoluminescence spectroscopy is a non-contact, nondestructive method that provides information regarding the electron band gap and the impurity and defect levels in the electronic structure. Photoluminescence process is of corresponding energy[7]**.** Quantum mechanically, described as an excitation of an electron to a higher energy electronic state and then it relaxes and returns to a lower energy level accompanied by the emission of a photon. The time domain between absorption and emission process is extremely short, of the order of tens of nanoseconds often called its life time. If the incident light photon energy is higher than the band gap of the semiconductor then the valence electrons move into the conduction band, generating electron hole pairs. After certain time, the electron then relaxes to the bottom of the conduction band followed by the electron hole pair recombination, often through a radiative transition. The intensity and the spectral contents of the PL is the direct measure of various material properties. The observed recombination pathways provide important information about the sample quality, band gap and band structure, donor and acceptor levels, defect types, impurities, crystalline quality, and defect densities.

In case of most semiconductors there will be an optimum magnitude of concentrations of impurities and structural defects. These imperfections cause a periodicity of a lattice potential and form trap centres and localization energy state at the band gap, whose energy depends on the nature of the defect. At low temperatures, most of the excitons are trapped due to low thermal energy and they are bound at defects state. As thermal energy raises gradually the bound exciton get released to form a free exciton. In the case of doped material, these defects create new states at the forbidden gap as shown in **Fig. 2.7(***d-transition***)**. In the present study, we used Horiba PL system with mercury lamp and He– Cd laser of 325 nm excitation wavelength with a maximum input power of 30mW and by using optical grating generated the required excitation wavelength.

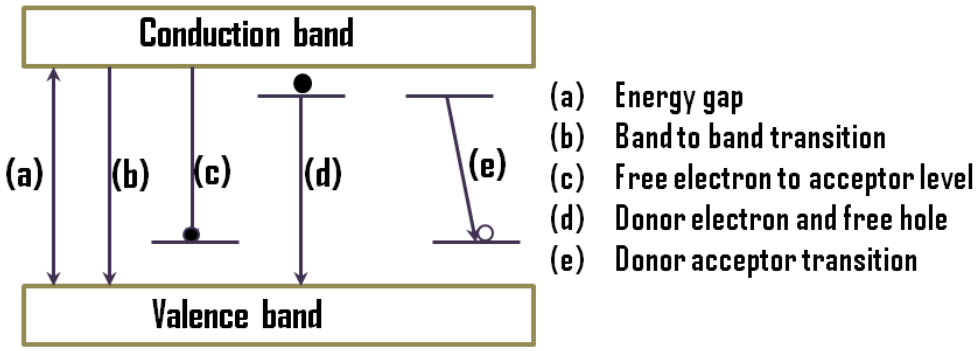

Fig.2.7: *The schematic representative electron transition at different energy state.*

2.8 Cathodo-Luminescence (CL):

Cathodo-luminescence (CL) is a light emitting phenomena similar to photoluminescence induced by the exciting electrons in the lower energy states to higher energy state in material by using high energy electrons. Highly focused beam of electrons is directed onto a sample in a noncontact mode and can be sometimes a destructive technique for high resistance materials due to electron stimulated deposition. This technique is used to assess electronic and optical properties of semiconductors with high spatial and spectral resolution. The light emission is mainly caused by inner electronic transition which may originate due to crystal imperfection or between the electronic states in the band gap associated with excitation by the incident electron beam. This transition may be the radiative recombination of carriers in semiconductors, such as the band to band transition and in some cases; transition from inter-state transition can also be radiative.

In our study, we used inbuilt CL which is attached to the MBE system as shown in **Fig. 2.8** and also *ex-situ* CL measurements have been performed by combining with a scanning electron microscope (FE-SEM). The advantage of coupling these two, gives a focused electron beam that is scanned over a specimen and simultaneously the CL spectrum by using an emitted light signal is recorded. Clearly CL spectra provide the information about local electronic states and the spatial distribution of luminescence centers from the CL image. Hence CL emissions are strongly dependent on material properties, electron beam energy and defect centers. Thus, this characterization tool is applied to probe the structural defects such as dislocations or quantum structures of grown materials. The morphology

dependent size effect can easily be investigated by CL mapping of nanostructure along the length will give distinctive difference in the luminescence. Therefore CL emission has been exploited as a probe to map the local density of states of nanostructured photonic materials.

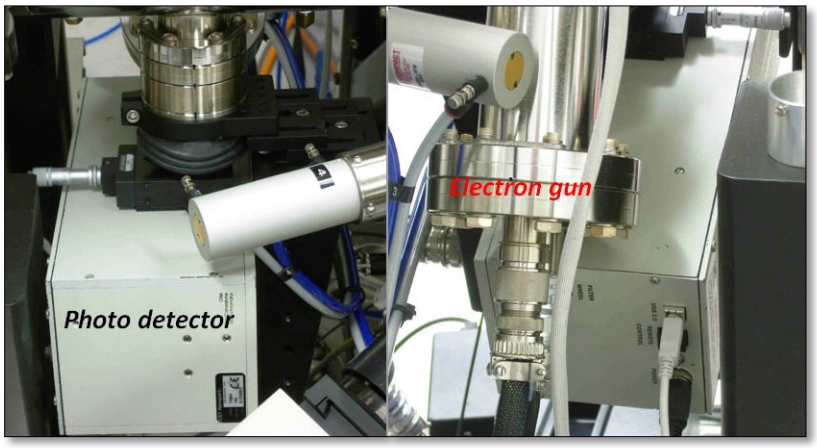

Fig. 2.8: *System Photos for CL at preparation chamber configuration in MBE system of SVTA make.*

2.9 Raman Spectroscopy:

The Raman Effect was first observed in 1928 by Sir. C.V. Raman and the effect named after him[8]**.** When light is illuminated on materials, the majority of the light is elastically scattered from materials, this is called Rayleigh scattering, where the scattered light has the same wavelength of the light source. But in case of Raman scattering there is an inelastic scattering process of the electromagnetic radiation. Raman spectroscopy with many advantages such as versatility, convenience, nondestructive nature and being a non-contact technique requiring no special sample preparation, is a very widely used as characterization tool also in the field of semiconductors. Raman scattering spectroscopy probes the energy shift of in-elastically scattered light corresponding to a specific resonant frequency of quantized lattice vibrations providing the information of material such as electronic and magnetic properties. Thus, the light interaction with the solid gives rise to a scattered radiation both in higher and lower frequencies of spectral distribution. The higher frequency line observed is called as anti-stokes and the lower frequency line is called as stokes line. Furthermore, in our study, we have used a visible laser for excitation, and obtain a lateral resolution of ~1μm which is determined by the beam waist of the probe laser at the sample

surface. In case of III-nitride semiconductors, Raman spectroscopy is extensively used to measure alloy composition, Ga and N vacancy and strain the materials.

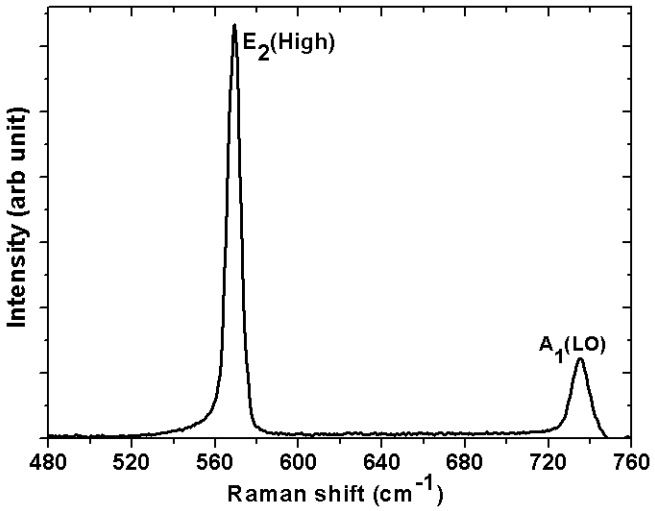

Fig.2.9: *Representative Raman spectra of GaN showing E_2(high) and A_1(LO) mode.*

The representative Raman spectra is shown in the **Fig. 2.9**, the marked E_2 high mode shift is characteristics of residual strain in the film. In our study indigenously assembled Raman scattering spectroscopy was employed to characterize the film stress of MBE grown films with respect to standard bulk samples.

2.10 Atomic Force Microscopy (AFM):

Atomic force microscopy is a robust technique used to study the surface topography and roughness of a variety of materials in nanometer to micrometer scale[9]**.** The Schematic representative image of AFM configuration is shown in **Fig.2.10**. In this technique, an atomically sharp tip ~ 2μm long and often less than 100Å diameter, which is mounted at the free end of a cantilever of 100-200 μm long is scanned across the surface of the sample. When a tip moves toward a sample, it may interact with the sample surface when the two are sufficiently close. The tip is then rastered by piezo-electric devices over the sample and the displacement caused by the atomic forces of the features on the surface can be obtained as surface topology map of the sample. The interaction can be due to van-der-Waals-force, capillary force, electrostatic force, or either the short-range repulsive force and magnetic force between sample and tip. A tip motion causes a detectable change in the laser's path and position sensitive photo detector (PSPD) measures the cantilever deflection as the sample is

scanned under the tip. The measured cantilever deflections allow a computer to generate a map of surface topography.

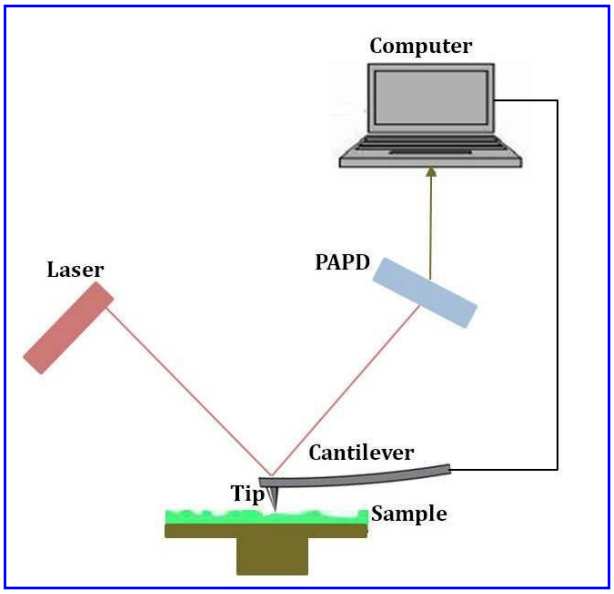

Fig.2.10: *Schematic representative image of AFM configuration.*

There are different modes in which the AFM can be used: namely; contact mode, non-contact mode, and tapping mode. In case Contact mode the tip is in contact with the surface and the image is obtained by repulsive forces between tip and the sample. In tapping mode, the image is obtained by the tip, which just taps the surface for small periods of time at regular intervals. In non-contact mode, the tip oscillates above the surface, and the image is obtained from the columbic forces between the tip and the sample. The tip is scanned over a surface with a feedback mechanism that enable the piezo-electric scanners to maintain the tip at a constant force (to obtain height information) or constant height above the sample surface (to obtain force information). As the tip scans, the surface of the sample, the focussed laser beam is deflected off the attached cantilever into a photodiode system which provides the feedback enabling the tip to maintain either a constant force or constant height above the sample. The surface morphology including rms surface roughness of the GaN layers in this thesis was analyzed using Veeco-AFM in both contact and non-contact modes.

2.11 Transmission Electron Microscope (TEM):

TEM is a very versatile tool and is an electrons analog of optical microscope, which means operates much like a light microscope, but uses electrons instead of visible light. Since

the wavelength of electrons is much smaller than visible light, one can achieve extremely high spatially resolution as compared to optical microscopes. A TEM like a conventional microscope consists of a condenser lenses, objective lenses, and projector lenses. The electron focusing (lens) is achieved by electrostatic and magnetic lenses which are also used to deflect electrons for scanning purposes. It is an extremely powerful tool employed in the characterization of materials, crystal structure and microstructure simultaneously by diffraction and imaging up to atomic resolution of lattice images of the nanoscale materials. Electrons are collimated from the source and the beam of electron passes through thin slices of the sample, resulting the diffraction pattern and absorption which is magnified onto a viewing screen (with a CCD camera). The detection is done with the aid of a fluorescent screen or the camera and the image which is generated is a 2D map of the material's density, which can be used to map topography in thin samples. Schematic of transmission electron microscope is shown in **Fig. 2.11**. The transmission of electron through the sample yield diffraction patterns' due to constructive and destructive interference. The high energy of electrons are limited in resolution by chromatic and monochromatic aberration. Aberration corrected TEM can have sub-nanometer resolution and can resolve the electron density of individual atoms. A TEM tool can be used to perform a wide range of experiments that involve conventional imaging (bright field (BF) and dark field (DF) TEM), phase contrast imaging (high resolution TEM), selected area electron diffraction (SAED), convergent-beam electron diffraction (CBED), Z-contrast imaging, energy-dispersive x-ray spectroscopy (EDS) and electron energy-loss spectroscopy (EELS). In our study, transmission electron microscopy (TEM) was performed to investigate the dislocation and interface details. To have good image, the sample preparation is very important and which is thin enough to transmit electrons. The TEM samples were prepared by mechanical grinding, polishing, and ion milling by using Gatan Precision Polishing System (PIPS). To have dislocation imaging, the samples were examined using two-beam conditions in which it satisfies the condition g.b=0, is as shown in **Fig. 2.11**. From this condition, we have observed the edge, screw and mixed dislocations, stacking faults. In our study, we have used Tecnai and high resolution by using the aberration corrected units of FEI Titan. Multiple BF and DF TEM images were taken to study the behavior of threading dislocation propagation and their bending phenomenon.

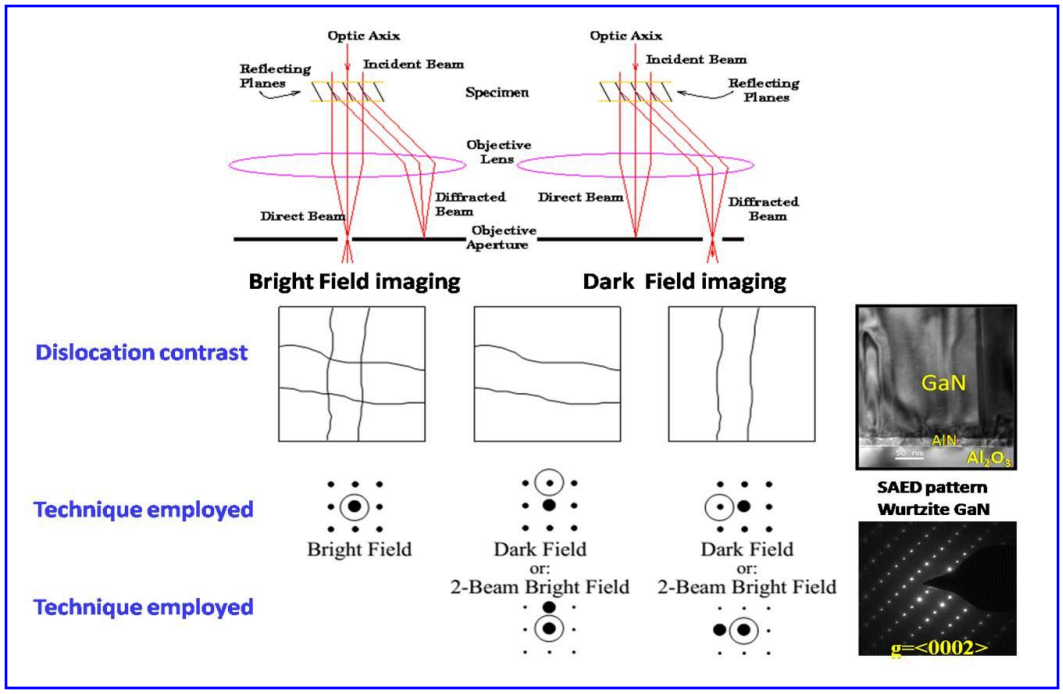

Fig.2.11: *The schematic of transmission electron microscope and technique involved for dislocation imaging*[10].

2.12 Scanning Electron Microscope (SEM):

The scanning electron microscopy is used to observe the topography and morphology of the GaN epilayers and nanostructure surface with high resolution. The typical SEM system as shown in **Fig. 2.12** consists of an electron gun which is the source of electrons, and the condenser lenses which regulate the intensity of electron beam and direct it onto the specimen**.** The basic principle behind SEM is scanning of a finely focused electron beam of 5-30 kV energy over the surface of the specimen. The scanning is carried out point by point in a time sequence with a high energy beam of electrons in a raster scan pattern. When electron interacts with specimen most important emission phenomena observed are (I) Secondary electrons, (II) Back-Scattered Electrons (BSEs) and (III) X-rays from the specimen, that are widely utilized for imaging and compositional analysis. The emission of secondary electrons from sample at each point on the specimen surface is strongly dependent on its shape[11]**.** Generally secondary electrons are collected at low angles from the surface of the sample and are utilized for better resolution of imaging rough surfaces of the specimen. The imaging is done in this process by scanning the electron beam across a sample and collecting the secondary electron signal from the beam-sample interaction. On the other

hand, BSEs are scattered electrons that emerge from greater depths in the sample and their number density is strongly dependent on the atomic number of the specimen, thus providing information about the distribution of different elements and atomic number contrast within the image.

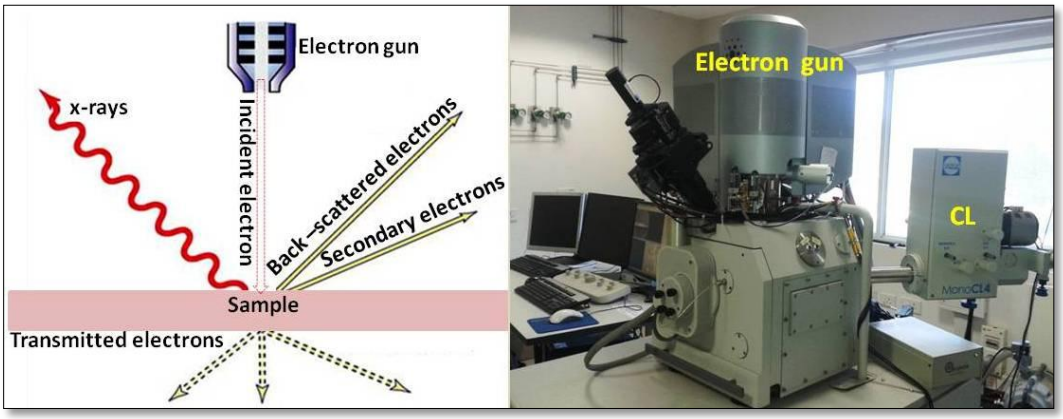

Fig.2.12: *The schematic of scanning electron microscope and technique involved in imaging.*

The characteristic X-rays are emitted when the electron beam removes an inner shell electron from the sample which is used to identify the atomic composition, and measure the abundance of elements in the sample by Energy Dispersive Spectroscopy (EDS). In our case imaging of our sample were done in standard secondary electron imaging (SEI) mode, used to produce two dimensional topographical imaging of specimen.

2.13 X-ray Diffraction (XRD):

X-ray diffraction is a powerful, non-contact method used to understand the crystalline phases in bulk materials, thin films and powder samples. In this process, X-rays of wavelength of 0.5~2.5 Å, which is close to the spacing of atoms in crystals, penetrate the sample and produced diffraction pattern due to scattering from the electron clouds of atoms. The diffraction patterns have different intensity that corresponds to the x-rays scattered coherently by the inter-atomic planes and intensity depends on atomic density in the planes. The X-rays scattering of neighboring parallel planes of atoms either interfere destructively or constructively at a certain angle of incidence. If the waves interfere constructively it leads to large intensity signal at that angle. The constructive interferences occur when the planes satisfy the Bragg condition written as: $2d\sin\theta=n\lambda$, Where *n* is an integer, λ is the wavelength of the X-ray, *d* is the lattice spacing, and θ is the Bragg angle[12].

The most important and simple scan is *2θ*- ω scan for both symmetric and asymmetric reflection which gives c-and a-lattice parameter. Rocking curve (ω-scan) is used to analyze dislocation density and twist tilt mosaicity in the epitaxial layers. In this geometry, the detector is kept at a fixed angle with respect to the primary beam (*2θ*) while the sample is rocked around the plane of interest as shown in **Fig. 2.13**[13].

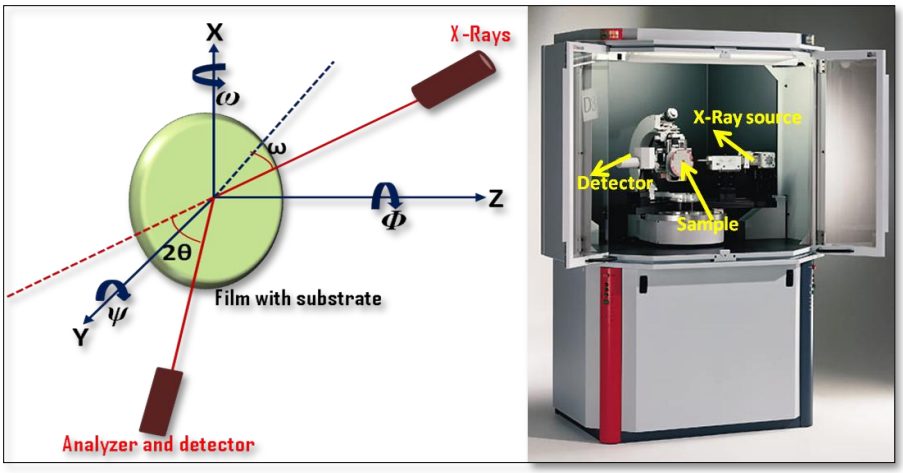

Fig.2.13: *The schematic of axis rotations in HRXRD and Bruker-D8 DISCOVER high-resolution X-ray diffractometer*[13, 14]**.**

The phi scan φ- axis (sample rotation), (φ) scan, and sample is rotated 360º keeping both sample and detector at a fixed angle and ψ-axis (sample tilt) as shown in **Fig. 2.13**. Here, we can have information about epitaxial relation between film and substrate. In case of III-nitride semiconductors, XRD is mainly used to evaluate the quality of the film including strain and threading dislocation density determination along with crystallinity information. The mole fraction of alloys, the thickness and fine structure of materials are investigated with super-lattice structures. The line width of a rocking curve that is the full width at half maximum (FWHM) determines the crystalline quality and the determination of layer parameters such as alloy composition, uniformity of epitaxial layers, thickness, built-in strain and strain relaxation, and crystalline perfection related to the dislocation density possible. The FWHM broadening is due to the presence of defects such as dislocations or stacking faults which are thus the good indicator of the crystalline quality of the materials. **Fig. 2.13** show the photograph and schematic diagram of the Bruker-D8 DISCOVER X-ray diffractometer with high accuracy goniometer with 0.0001° step resolution for the sample which we have used in our study.

2.14 REFERENCES:

1. A. Cho, Molecular Beam Epitaxy, American Institute of Physics (1994).

2. Growth and structural characterization of III-V nanowires grown by molecular beam epitaxy: PhD Thesis by Dheeraj Dasa Lakshmi Narayana: ISBN 978-82-471-2358-4 (electronic ver.)

3. SVT Associates: http://www.svta.com/

4. A. Y. Cho, Journal of Applied Physics 42, 2074 (1971).

5. Ichimiya and P. I. Cohen, Reflection High Energy Electron Diffraction, Cambridge University Press (2004).

6. H.Y. Chen, H.W. Lin, C.-H. Shen, and S. Gwo, Applied Physics Letters 89, 2431059(2006).

7. S. Perkowitz, Optical Characterization of Semiconductors: Infrared, Raman, and Photoluminescence Spectroscopy (Techniques of Physics), Academic Press (1993).

8. C. V. Raman. Nature, 121, 619 (1928).

9. Franz J. Giessibl, Rev. Mod. Phys. 75, 949 (2003).

10. Transmission Electron Microscopy and Diffractometry of Materials by Brent Fultz and James Howe: ISBN-13: 978-3540738855

11. G. I. Goldstein, D. E. Newbury, P. Echlin, D. C. Joy, C. Fiori, and E Lifshin, Scanning Electron Microscopy and X-ray Microanalysis. New York: Plenum Press. (1981).

12. S. L. Chang, X-ray Multiple-wave Diffraction: Theory and application, Springer-Verlag Berlin Heidelbergy (2004).

13. High Resolution X-ray Diffraction, Www2009.ph.tum.de, HR-XRD User guide (2009),

14. HR-XRD User guide Bruker instrument D8 DISCOVER HR-XRD.

Chapter 3

Growth of Nanowalls, Nanorods and 2-D Films on c-Plane Sapphire Substrate

3. Growth of Nanowalls, Nanorods and 2-D Films on bare c-Plane Sapphire Substrate:

3.1 Introduction:

As described in chapter I, the reduction of dislocation density in GaN films formed on non-native substrates improves the performance of their electronic and optoelectronic devices of which one of the approaches is to form nanostructure. The exploration of GaN nanorod and nanowire growth by different methods started in the late 1990s. The Catalyst assisted growth yield GaN nanocolumns and that are random in orientation, as well as uneven size distribution due to random size distribution of catalyst particle[1]. Another route is selective area growth of GaN nanorods, though it is difficult, especially during MOCVD growth due to its high growth rate. Spontaneous formation of epitaxially ordered nanostructures such as nanorods and nanowalls are desirable, because catalyst assisted nanorods show high basal stacking faults and extra emission peaks near the band edge emission[1–4]. Pioneering research on GaN nanorod growth focused on the self-assembled catalyst free growth of GaN nanorods by molecular beam epitaxy (MBE). Initially, Sanchez-Garcia *et al*[5] found that high V/III ratio i.e. nitrogen rich conditions favour the growth of GaN columnar structures. In contrast, GaN films grown under low V/III ratio lead to layer-by-layer growth and weak PL emission. Films grown under high V/III ratio promote 3-D growth and high PL emission without showing any defect peaks. The major challenge is to understand and tailor-make nanostructure assembly to generate ordered epitaxial structures with desired properties. For High Brightness LED production the controlled growth of GaN nanorods with proper size distribution is essential[6–8]. In MBE growth, a significantly higher growth temperature is required in order to achieve vertical growth so as to avoid random nucleation on lithographic patterns[1]. However, the growth temperature window here is extremely narrow and higher temperatures increase the desorption rate and maintaining Ga rich condition becomes very difficult. Thus, even though several reports on the spontaneous formation of nanostructures and their growth conditions exist, a complete understanding on the growth mechanism is still under debate[1,9–11].

In this chapter we report on our studies of the growth of spontaneous, catalyst-free GaN nanostructures on bare c-sapphire in nitrogen rich conditions. These GaN

nanostructures are all vertically aligned with respect to the substrate normal, with the *c* axis pointing along the growth direction, and show m-faceted hexagonal crystal shape. The mechanism of spontaneous catalyst free formation of GaN nanostructures is not yet understood[10,12–14]. It is crucial to understand the growth mechanism since that gives a control over the growth and orientation of nanorods, reduce defect concentration and to tune the aspect ratio of the epitaxially grown nanostructure. We present experimental results that demonstrate the spontaneous formation of catalyst free c-oriented GaN nanocolumns and a hexagonal nanowall network on bare c-plane sapphire. The precise control of nanostructure is achieved by controlling growth parameters at these nitrogen rich conditions without employing any buffer layers or catalyst. The structural and optical properties of the nanostructures formed are also discussed.

3.2 Experimental Section:

In the first set of experiments, GaN growth was carried out by varying substrate temperatures from 450 to 850^{o}C at a fixed Ga effusion cell temperature of 1000^{o}C and with the nitrogen flow being maintained at 4.5sccm. In the second set of experiments, the nitrogen flow rate was varied from 2 to 8 sccm by using a high precision mass flow controller; other parameters such Ga effusion cell temperature (1000^{o}C) and substrate temperature (680^{o}C) remained fixed. In the third case, Ga flux was varied from 2.86x10^{14}cm^{-2}s^{-1} to 4.84x10^{14}cm^{-2}s^{-1} by changing the temperature of the effusion cell; other parameters were fixed at 680^{o}C substrate temperature and 4.5sccm nitrogen flow rate (Standard Cubic Centimeter per Minute) while radio frequency (RF) plasma forward power of 375W. The morphology and structure analysis was done by high resolution FESEM and high resolution X-ray Diffraction. Cathodo-luminescence (CL) measurement was done *in situ* at room temperature, with electron energy being varied from 0 to 5keV. Raman spectra were acquired at room temperature for all GaN films. X-ray photoelectron spectroscopy was used for quantitative estimation of the surface composition of GaN films in an Omicron system. Generally both AlK_{α}(1486.6 eV) and MgK_{α}(1253.6eV) X-ray radiations were used for the quantitative measurements of GaN surface, since the Ga LNN Auger series overlaps with C 1s, O 1s XPS lines for MgK_{α} source and N 1s , Ga 3s XPS lines for AlK_{α} source. In this study AlK_{α} source is employed for acquiring N1s core level spectra with constant pass energy of 20eV and step

size of 0.1eV. The charging effect induces 1-6eV shift toward higher binding energies, therefore all core level spectra are referenced to the adventitious carbon peak at 284.6eV.

3.3 Effect of substrate temperature on morphology of GaN film grown at temperature ranging from 480^{o}C-880^{o}C:

To understand the precise control of GaN nanostructure morphology, growth was carried out at different substrate temperatures varying from 480^{o}C-880^{o}C at step sizes of 50^{o}C. This experiment was divided into three subsections based on different morphological manifestations of GaN films. The first section deals with films grown between temperatures of 480^{o}C -630^{o}C which result in the formation of 3-D GaN nanowall network morphology with variation in the nanostructure dimensions. The second section deals with films grown at 680^{o}C which show an evolution of nanorods in addition to the nanowall morphology. The third and final section deals with films grown between 730^{o}C -880^{o}C showing 2-D morphology.

3.3.1 Effect of substrate temperature on morphology of GaN film grown at temperature ranging from 480^{o}C-630^{o}C:

In the first set, the substrate temperature was varied from 480^{o}C to 630^{o}C in steps of 50^{o}C with the Ga/N BEP ratio being fixed at 100 and N_2 flow rate at 4.5sccm. The corresponding plan view FESEM images of GaN grown on Al_2O_3 (0001) surface are shown in **Fig.3.1**. Among the several growth temperature studied, the figure below consists of representative FESEM images obtained from samples grown at 480, 530, 580 and 630^{o}C. The RHEED pattern acquired along the [11-20] azimuthal direction of the GaN films are shown on top of their respective FESEM images in **Fig. 3.1**. The spotty RHEED pattern observed in all cases indicates transmission of electrons through the 3D morphology. The RHEED pattern also show an epitaxy of [10-10]Al_2O_3// [11-20]GaN planes. **Fig. 3.1 (a)** shows characteristic spotty RHEED pattern of GaN film grown at 480^{o}C acquired along the [11-20] azimuthal direction. The ratio c/a≈1.63 as calculated from the RHEED pattern indicates a wurtzite crystal phase of GaN. **Fig. 3.1(a')** is the FESEM image of GaN film grown at 480^{o}C substrate temperature, which shows a diffused tri-branched network-like morphology with an average branch length of 100nm and a void density of 5x10^{10}/cm^{2}.

These networks are oriented along c-direction and the average branch length is about ≈100nm. The Fast Fourier Transform (FFT) shows a 3-fold symmetry in the corresponding FESEM image as shown in **Fig. 3.1(a'')**. The RHEED pattern of GaN film grown at 530^{o}C acquired along the [11-20] azimuthal direction is shown in **Fig. 3.1(b)**. The c/a ratio calculated from the RHEED is ≈1.63 which reveals the existence of a wurtzite crystal phase in the GaN film[15]. The slight anisotropy in films indicates the presence of misalignment of nanowalls along <11-20> and <10-10> directions. **Fig. 3.1(b')** corresponds to FESEM image of GaN films grown at 530^{o}C which show network morphology with average branch length ≈130nmn and void density of about ~3.5X10^{10}/cm^{2}. The FFT shows 3-fold symmetry as shown in **Fig. 3.1(b'')**.

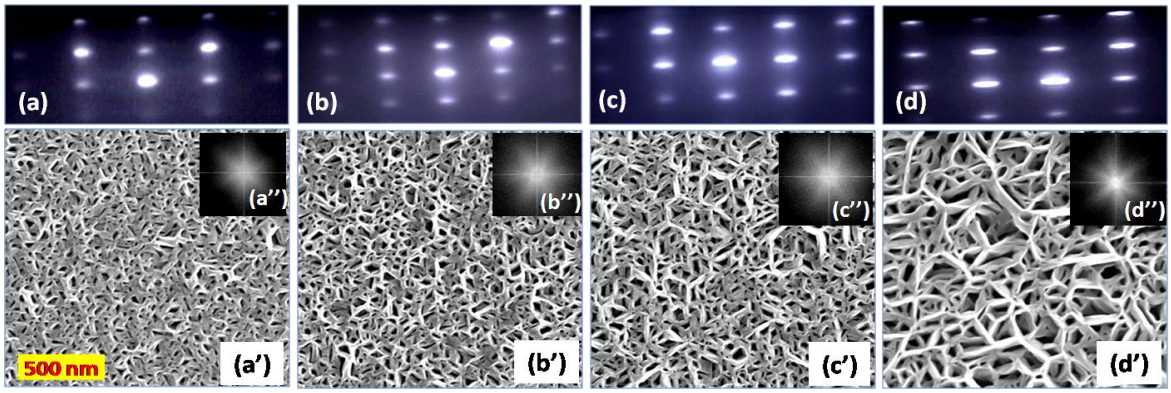

Fig.3.1: (a'-d')*Plan view FESEM images with their corresponding RHEED pattern* ***(a-d)*** *taken along the [11-20] zone axis and Fast Fourier Transform (FFT)* ***(a''- d'')*** *of the respective images of GaN films grown on c-plane Al_2O_3 at 480^{o}C, 530^{o}C, 580^{o}C, and 630^{o}C respectively.*

The RHEED pattern of GaN film grown at 580^{o}C acquired along the [11-20] azimuthal direction is shown in **Fig. 3.1(c)**. The RHEED pattern becomes spotty due to transmission of electrons through the 3-D surface. The c/a ratio calculated from the RHEED pattern is ≈1.63 is the characteristics of wurtzite GaN. The RHEED spot is observed to be anisotropic with an aspect ratio of ≈2.9 along the horizontal and vertical directions, suggesting a higher degree of misalignment. The GaN film grown at 580^{o}C seems to be almost similar in morphology to the previous film. The void size is relatively larger than in the earlier case and average void density is ~2.5x10^{10}/cm^{2}. The nanowalls are also steeper compared to other films which could be a function of a higher diffusion due to increased substrate temperature. FFT shows a clear 3-fold symmetry, same as in the earlier case (**Fig.**

3.1(c'')). **Fig. 3.1(d**) is the typical RHEED pattern of GaN films grown at 630^{o}C substrate temperature. Increased spread in RHEED spots indicates anisotropic growth along <11-20> and <10-10> directions, though they are well ordered along the <0002> direction. The c/a ratio as calculated from distances between the RHEED spots in vertical and horizontal direction is ≈1.63 that clearly indicates the wurtzite nature of nanowalls. **Fig. 3.1(d')** is the representative FESEM image of the film grown at 630^{o}C showing similar network structure with larger voids and steeper walls. The average wall length is ≈325nm, forming a hexagonal structure surrounding the voids. Fast Fourier Transform (FFT) of FESEM image possessing a 3-fold symmetry is shown in **Fig. 3.1(d'')**.

The density of voids as calculated from the plan view FESEM images and the Full Width at Half-Maximum (FWHM) of rocking curve taken along the (0002) reflection for GaN films grown at substrate temperature ranging from 480 to 630^{o}C are plotted in **Fig.3.2**.

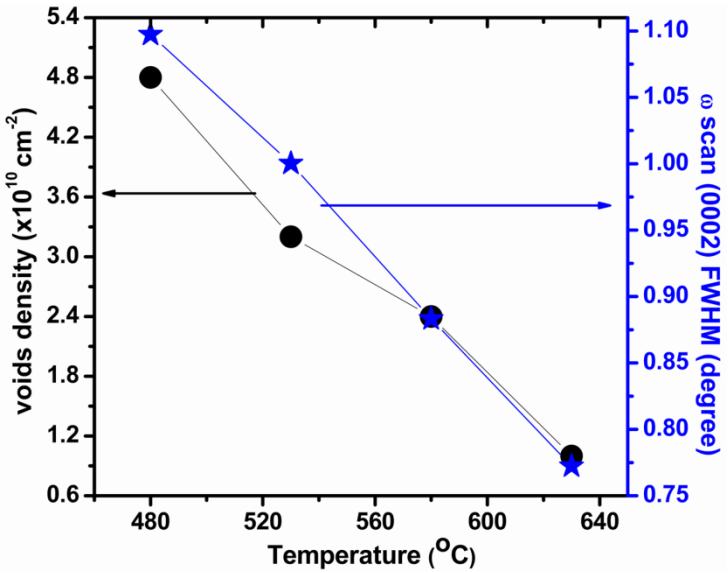

Fig.3.2: *Plot of variation in density of voids and FWHM of (0002) plane versus substrate temperature.*

The density of voids decreases monotonically with respect to substrate temperature and corresponding FWHM of (0002) reflection decreases with increase in growth temperature from 480 to 630^{o}C. A decrease in FWHM clearly indicates improvement in film quality as well as strain relaxation which, in our case, occurs due to the opening up of the nanowall matrix giving a higher surface area. It is important to note that the screw dislocation density is directly related to FWHM of (0002) reflection as shown in equation below[16]. The dislocation densities of the GaN films were estimated from the following equations.

$D_{Screw} = \frac{\beta^2_{(0002)}}{9b^2_{Screw}}$ where D_{screw} is the screw dislocation density, β is the spread in FWHM of (0002) reflection in the HR-XRD rocking curve, and b is the Burgers vector (b_{screw}=0.5185 nm). Thus the overlapping trends of density of voids and rocking curve FWHM of (0002) reflection, suggests that the voids present in between the nanowall networks are open screw dislocations due to high strain field generated due to lattice mismatch.

To see a clearer picture of the tri-branched nanowall network structured GaN film, we have obtained high resolution FESEM images of the 630^{o}C grown film, a representative image is shown in **Fig. 3.3**. This FESEM, acquired at 30^o tilt, clearly shows each bigger hexagonal void encompasses smaller voids, and also the larger ones start forming after the smaller ones stop growing in height which is also evident in **Fig. 3.3.**

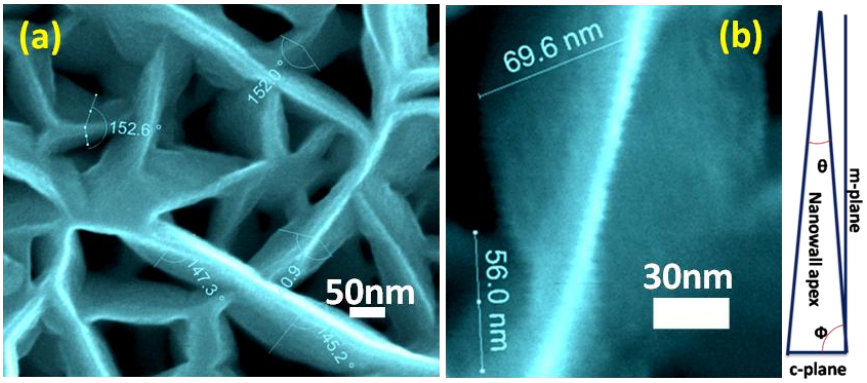

Fig.3.3: ***(a)*** *Shows high resolution FE-SEM image of film grown at 630^{o}C* ***(b)*** *image taken single nanowall and corresponding schematic.*

The approximate angle between the inclined faces and base of nanowalls vary with growth temperatures which can be attributed to thickness variation with growth temperature. It is very clear that the film thickness increases from 0.8-1μm with the substrate temperature increase from 480^{o}C to 630^{o}C. It is well known that the growth rate is high for dislocation mediated growth than for diffusion mediated one[17]. Thus, increasing thickness indicates that the dislocation mediated morphological evolution is the dominating growth mechanism. The angle 72^o corresponds to crystallographic s-plane (10 -11), and angle 57 ^{o} to r-plane (-1102) plane. In 480^{o}C case, dominance of s-plane is observed which decreases with increase in growth temperature with a weak shoulder of r-plane observed at low temperature which begins to dominate at higher temperatures. Thus, in the 630^{o}C case, combination of m-plane (10 -10), s-plane and r-plane is observed. In case of 480^{o}C, the film appears to have triple-

layer cavity structure whose length varies from 0.07-0.14μm, and in 630^{o}C case, the film has a bi-layer cavity structure whose length varies from 0.13-0.25μm. The depth information is limited by the depth contrast from FESEM images, so for deeper region, and it is only speculative.

3.3.2 Morphological evolution 2-D films of GaN grown at 730-880^{o}C:

Fig. 3.4 represents the plan view FESEM image of GaN films grown at 730-880^{o}C substrate temperature and corresponding RHEED pattern shown along with the FESEM images. As is reported in literature, high temperature growth usually favours 2-D growth due to high diffusion of Ga adatoms.

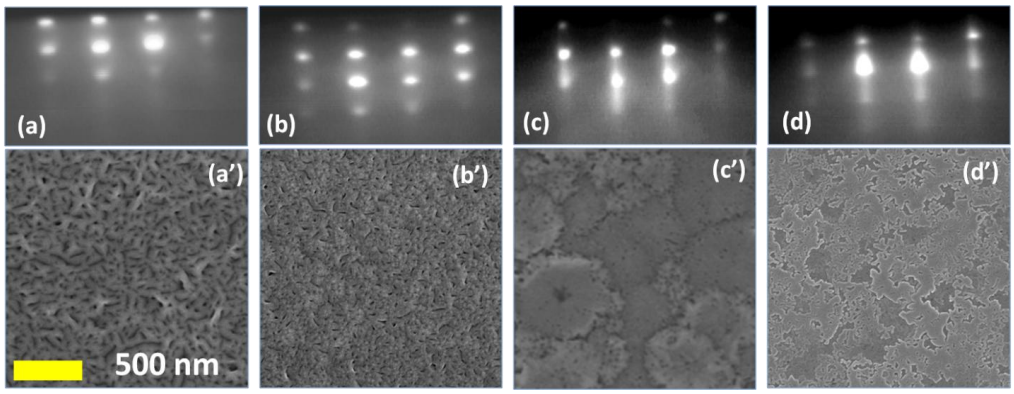

Fig.3.4: (a'-d') *Plan view FESEM images with their corresponding RHEED pattern* ***(a-d)*** *acquired along the <11-20> zone axis of the GaN films grown on c-plane Al_2O_3 at 730^{o}C, 780^{o}C, 830^{o}C, and 880^{o}C respectively.*

Fig. 3.4(a-b) is the typical RHEED pattern of GaN films grown at 730^{o}C and 780^{o}C substrate temperatures. The spotty RHEED indicates the transmission pattern through rough surface morphology as shown in **Fig. 3.4(a-b)**. Sharp circular RHEED spots indicate that no anisotropy exists which is attributed to domains aligned along c-direction. The image shown in **Fig. 3.4(a'-b')** is the FESEM morphology of GaN films, which is grown at 730^{o}C and 780^{o}C substrate temperature. The voids which we observed in nanowalls are completely replaced by holes corresponding to axial threading dislocations, though their density is similar to the density of voids pertaining to screw dislocations in case of nanowalls. **Fig. 3.4(c-d)** shows the RHEED pattern of the GaN film grown at 830^{o}C and 880^{o}C substrate temperatures. Streaky nature and a slight overlap with spotty pattern are attributed to a faceted smooth surface. The gradual evolution of streaks in RHEED pattern along the [0001]

direction indicates that the film is tending towards a smooth 2-D surface. The FESEM images of GaN film grown at 830^{o}C and 880^{o}C substrate temperature are shown in **Fig. 3.4(c'-d')**. Droplets of GaN due to its high desorption rate at high temperatures are seen and a high diffusion of Ga adatoms leads to random nucleation, which is clearly visible on the film surface.

3.3.3 Morphology of GaN film grown at 680^{o}C:

Fig. 3.5 shows a typical FESEM image of GaN layer consisting of a high density of *c*-axis oriented nanorods grown at 680^{o}C. The RHEED pattern acquired along [11-20] azimuthal direction is shown in the **Fig. 3.5(a)** inset. The spotty RHEED pattern with a slight anisotropic spread along the [10-10] direction indicates the anisotropic growth of GaN film. From the **Fig. 3.5(a)** it is clear that the nanocolumns have a typical length of 1μm and their diameter is ≈140nm. These hexagonal shaped GaN nanocolumns originate from the void regions of the nanowall network. Initially, with increasing coverage the nanowalls grow upto a certain thickness, after which we see the growth of nanocolumns while the nanowalls do not extend further. The side facets of these hexagonal nanorods correspond to m-plane which is perpendicular to the c-plane of the wurtzite GaN nanocolumns.

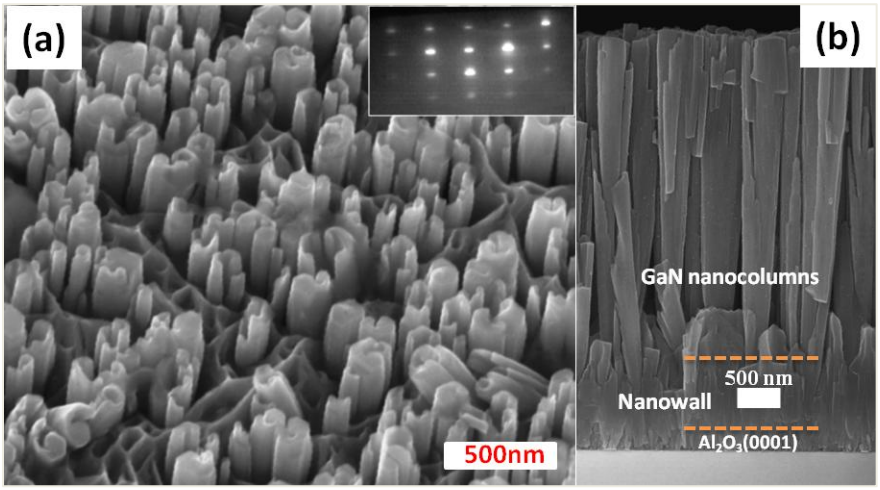

Fig.3.5: ***(a)*** *FESEM images acquired at 30^{o} tilt of the GaN films grown on c-plane Al_2O_3 at 680^{o}C and inset shows a RHEED pattern taken along the [11-20] zone axis, and* ***(b)*** *is the cross-sectional view FESEM image of 4.0μm GaN nanocolumns.*

Fig. 3.5(b) shows the cross section FESEM image of 4.0μm length nanocolumns which are seen to protruding outward from a matrix layer of height ≈300nm. These

nanostructures are well aligned and their density is ~$1x10^8/cm^2$ and diameter is ≈400nm. These nanocolumns nucleate at the film-substrate interface due to the spiral step provided by the axial screw dislocations arising as a result of lattice mismatch between GaN and Al_2O_3 and then they grow continuously within the void region of the underlying nanowall network which will be discussed in more detail in the following section.

3.4 Structural and Optical studies of GaN films grown on c-plane sapphire at 480°C -880°C substrate temperature:

Structural characteristics of the GaN films were evaluated by HR-XRD. **Fig. 3.6(a)** shows a representative 2θ-ω scan of GaN film with intense peaks at 2θ= 34.54° and 72.8°, which correspond to symmetric reflections of (0002) and (0004) planes of GaN, and the peaks at 2θ= 42.68°, 91.40° correspond to symmetric reflections of (0006) and (00012) planes of c-plane sapphire substrate. In-plane φ scans were acquired by rotating the samples around their surface normal direction in order to investigate the in-plane alignment of the GaN film.

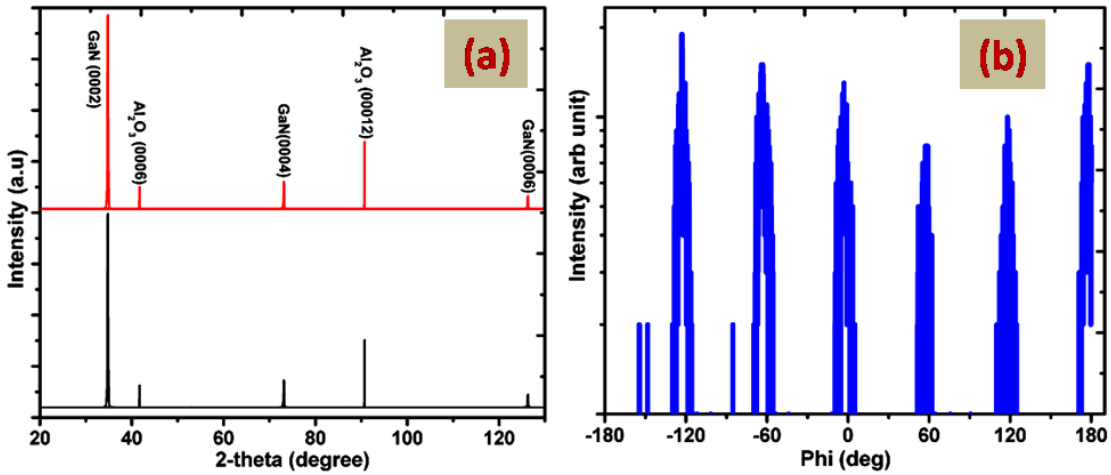

Fig.3.6: ***(a)*** *Shows representative 2θ-ω XRD pattern and* ***(b)*** *plot of representative azimuthal angle dependence (φ scan) of the intensity of GaN (10-11) plane.*

Fig. 3.6(*b*) is the representative φ scan of the (10-11) plane of all GaN films showing six diffraction peaks at 60° interval, confirming the hexagonal wurtzite structure with a 6-fold symmetry[18]. Off-axis diffraction peaks were used to determine the in-plane orientation of the GaN film with respect to the substrate. Two sample rotations, φ and χ were adjusted in order to get off-axis reflections onto the scattering plane of the diffractometer. Here, φ is the angle

of rotation about the surface normal and χ is the angle of the sample tilted about the axis formed by the intersection of the Bragg and scattering planes. The structural quality of the samples was evaluated from the FWHM of rocking curve of the (0002) reflection and was found to be strongly dependent on the growth temperature. The thickness of the films was obtained from the cross-section FESEM image. **Fig. 3.7** represents the variation in (FWHM) of the (0002) reflection as a function of substrate temperature and corresponding alternative axis corresponds to thickness variation with substrate temperature.

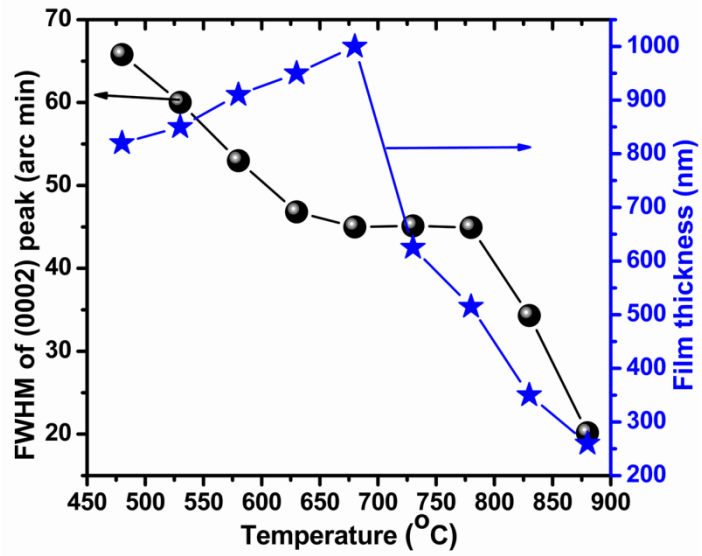

Fig.3.7: *The plot of FWHM of the rocking of (0002) plane of GaN and film thickness verses substrate temperature.*

The FWHM of the (0002) peak is observed to decrease from 70 arc min. at 480°C to 15 arc min. at 880°C, with a flat region from 630°C to 780°C growth temperatures. The decrease in FWHM is attributed to more compact films at high temperature and reduced tilt and twist mosaicity of the film with increasing growth temperature. The rocking curve of the symmetric (0002) GaN reflections is a direct measure of threading dislocation density. In the substrate temperature range of 480 to 680°C, the thickness of the film increases from 0.8-1μm, though the flux rate remains same and is attributed to voids in the nanostructure formation. The FWHM of GaN films decreases linearly from ≈65-45arc min. In the substrate temperature range 680 to 780°C, we have observed a fall in film thickness from 1-0.5μm, but the FWHM remains constant, this suggests that the GaN film has attained maximum compaction with a constant FWHM. However, at higher substrate temperatures, i.e. at temperatures >780°C, reduction in sticking coefficient of the impinging Ga or N species and

dissociation of GaN prior to incorporation into the GaN film and increase in desorption rates can lead to the formation of thinner films of thickness < 500nm.

To study optical property we have done CL measurements at room temperature for each sample and the consolidated data is presented in **Fig.3.8.** The representative CL spectrum is shown in **Fig 3.8(a)**; the spectra consists of two distinct emission peaks around 365.2nm (3.40 eV) that correspond to the band-edge luminescence (BEL), and another peak at 420-500nm corresponding to defect emission. The peak positions (along y-axis) and FWHM (along alternate y-axis) for BEL of CL spectrum of the GaN films grown at substrate temperatures from 480^{o}C to 880^{o}C are shown in **Fig. 3.8(b).** The band-edge emission energy is 3.43 eV for the GaN film which is grown at 480^{o}C, and the band edge emission of the film grown at 630^{o}C increases to 3.53eV. At an increase in substrate temperature beyond 630^{o}C, the band edge emission reaches the bulk value of GaN (3.40 eV). The alternative y-axis of the figure represents the FWHM of band edge emission of CL spectra and is almost similar to the plot of film thickness versus temperature shown in **Fig.3.7**.

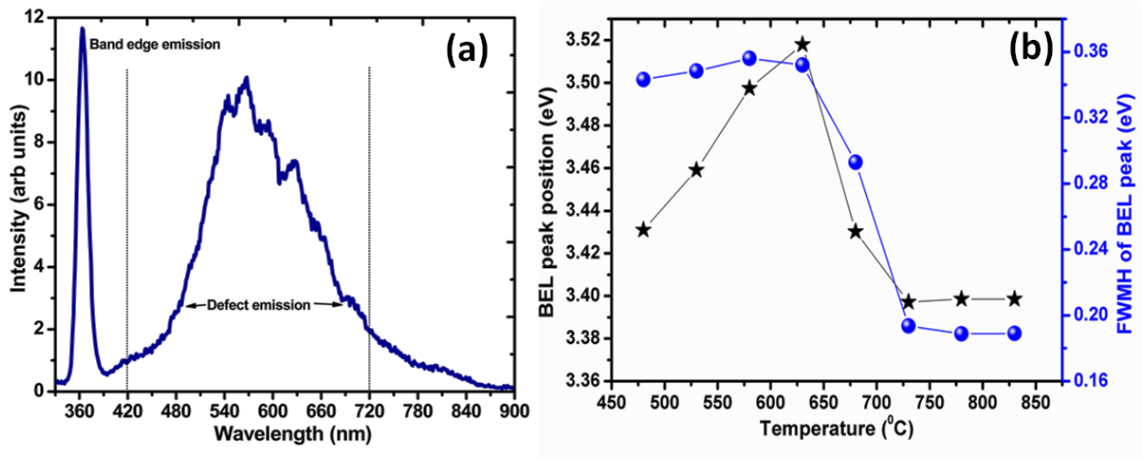

Fig.3.8: ***(a)*** *Shows typical room temperature CL spectra of GaN and* ***(b)*** *plot of CL spectrum FWHM and BEL peak position versus substrate temperatures.*

We attribute this variation in position of BEL peak positions and FWHM to the reduction in strain by nanostructure formation and consequent defect and dislocation reduction in the GaN films. It is important to note that the intensity variation of XRD rocking curve of (0002) reflection and CL band edge luminescence (BEL) shows similar trend with respect to growth temperature. It is well known that the emission intensity is an important parameter to evaluate the quality of the grown material. XRD rocking curve show a similar trend and a strong correlation between the CL intensity of BEL and the densities of screw-

type dislocations is described by rocking curve FWHM along (0002) reflection, as shown in **Fig 3.7**. The intensities of the BEL of CL spectrum decreases with decrease in FWHM of rocking curve along (0002) reflection for films grown beyond 680^{o}C, suggesting that the screw dislocation density decreases with increase in temperature greater than 680^{o}C. At temperatures below 680^{o}C, the intensity of the BEL of CL spectrum increases with decrease in FWHM of rocking curve along (0002) refection when the temperature is increased from 480 to 680^{o}C indicating a decrease in screw dislocation density. It is known that the energy band gap of a semiconductor is affected by the residual stress in film. A tensile stress will result in a decrease of energy band gap while a compressive stress causes an increase of the band gap, according to Zhao *et al.*[19].

Raman spectroscopy allows us to estimate the stress in the GaN films which are grown at different substrate temperatures ranging from 480-880^{o}C. It is well known from literature that the E_2-high mode is very sensitive to residual strain. Thus E_2 (high) mode in the Raman spectra can be used to determine stress in GaN films with respect to a bulk reference sample. Since strain in GaN films affects the wavelength of the E_2 mode and its replicates, the location of E_2 peaks is used to determine the amount of strain in a film. The red shift of the E_2 (high) phonon band with respect to the standard value of 567.7cm^{-1} implies a biaxial tensile stress in the GaN layer and a blue shift indicates compressive stress in the film[20]. The E_2 (high) mode of strain free GaN is known to be at 567.6cm^{-1} at room temperature[21]. **Fig. 3.9** shows a variation in stress with respect to growth temperature.

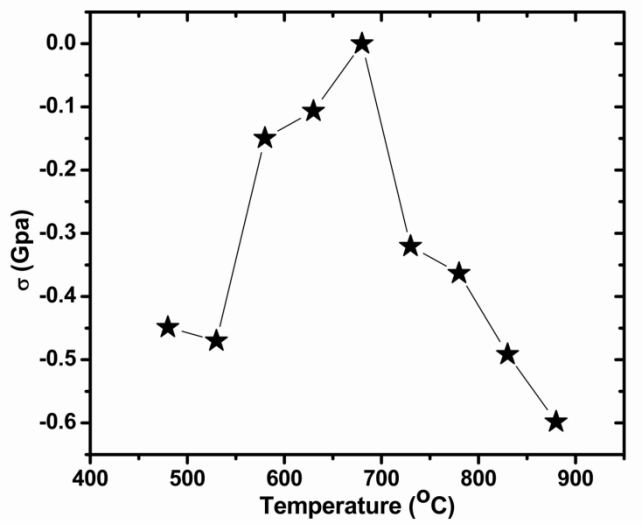

Fig.3.9: *Plot of biaxial stress of the GaN films grown at temperatures from 480^{o}C to 880^{o}C substrate temperature.*

The minimum residual strain is observed in the case of film grown at 680^{o}C, slightly higher than the bulk value. This suggests that as growth temperature is increased from 480-680^{o}C the in-plane compressive stress in the film decreases and at 680^{o}C minimum in-plane tensile stress is observed. **Fig. 3.9** is a plot of variation in stress in GaN films grown with respect to growth temperature range 480^{o}C-880^{o}C. The relation between the frequency shift $\Delta\omega$ (cm^{-1}) of E_2 (high) mode and biaxial stress (GPa) can be expressed[22,23] as $\Delta\omega=4.3\sigma_{xx}$cm^{-1}GaPa^{-1}. For GaN films grown in the temperature range 480-680^{o}C, biaxial stress decreases with temperature and reaches the bulk value of strain free GaN at 680^{o}C. The $\Delta\omega$ is positive, and signifies tensile stress in the films. In case of GaN films grown between 730^{o}C- 880^{o}C, a biaxial compressive stress of the film is observed which reaches a maximum at 880^{o}C.

X-ray photoelectron spectroscope (XPS) studies were carried out to determine the surface chemical composition of the films using core level spectra of N1s. Thus, it enables us to extract information about surface elemental composition and stoichiometry of GaN films within the detection limit of about 5nm. The XPS measurements were made on GaN films grown in substrate temperature range of 480-880^{o}C. **Fig.3.10** shows the representative core level spectra of N1s of GaN films grown at 880^{o}C substrate temperature.

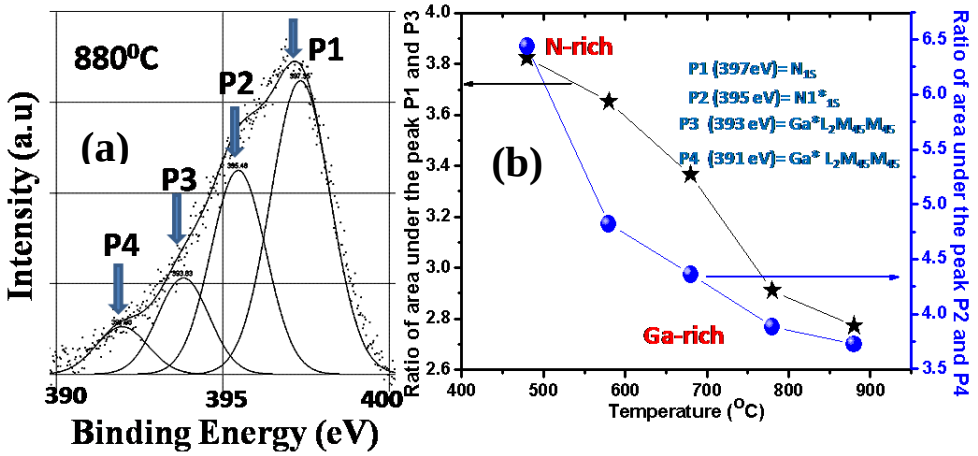

Fig.3.10: (a) *N(1$_S$) Core level spectrum of GaN films grown at substrate temperature 880^{o}C and plot* ***(b)*** *y-axis show ratio of area under the peak P1 and P3 and on the alternate y-axis ratio of area under the peak P2 and P4 versus substrate temperature ranging from 480^{o}C to 880^{o}C.*

They are deconvoluted into four Gaussian peaks labeled as P1, P2, P3, and P4. Peaks P1 and P2 correspond to the N (1_s) core levels observed at binding energies 397.0 eV (FWHM=2.0 eV) and 395.0 eV (FWHM=1.9 eV), respectively. Peaks P3 and P4 correspond to the Ga $L_2M_{45}M_{45}$ Auger lines at binding energies 393.0eV (FWHM=1.8eV) and 391.0eV

(FWHM=1.8eV), respectively. In **Fig. 3.10(b)**, ratio of area under the peaks P1 and P3 are plotted on y-axis and ratio of area under the peaks P2 and P4 versus growth temperature is plotted on alternate y-axis. In the case of GaN film grown at 480^{o}C, the ratio of areas is highest, but decreases monotonically with an increase in substrate temperature. We attributed this to the formation of a nitrogen rich surface at a lower substrate temperature, due to the presence of nitrogen rich environment. The surface of films grown at higher temperatures, i.e.880^{o}C, becomes more and more Ga rich probably due to Ga droplets formation at higher temperatures. High desorption rates of Ga at higher temperatures leads to more Ga droplets at the surface. Thus, GaN film grown at 480^{o}C is more nitrogen rich with respect to the film grown at 880^{o}C, whereas film grown at 880^{o}C is gallium rich.

We have discussed morphological evolution of GaN films grown at different substrate temperatures, the structural quality and optical properties of GaN films grown in the temperature range of 480-880^{o}C is discussed. We have found that the structural and optical properties changes on both sides of 680^{o}C growth temperature. Raman measurements show that the film grown at 680^{o}C shows a relatively strain free and almost bulk-like GaN film. XPS measurements show that on alternate sides of this temperature, the film surface is either N-rich or Ga-rich. This variation in Ga-, N-rich surface of films grown in nitrogen rich conditions suggest that films are transforming from 3D growth mode as expected in N-rich condition to 2D growth mode in Ga-rich condition.

3.5 Nitrogen flux dependent GaN nanostructure formation:

We have studied nitrogen flux dependent morphological evolution of GaN films, while the substrate temperature is kept at 680^{o}C and Ga flux at 3.86 x10^{14} atoms cm^{-2} s^{-1}, varying only the nitrogen flow rate. The representative FESEM images of the GaN films grown at nitrogen flow rates of 2, 4.5, 6 and 8sccm are shown in **Fig. 3.11(a-d).** The films which are grown at nitrogen flow rates of 2, 6 and 8 sccm show nanowall network-like morphology as shown in **Fig. 3.11(a, c, d).** These films show 3-fold symmetry as confirmed by FFT on these images, as shown below the FESEM micrographs. The apex of these nanowalls is tapers to <10nm and the bottom is ≈150nm. These tri-branched nanowall networks are oriented along the (0001) crystallographic direction. The voids in the matrix have a density ~10^{9}cm^{-2}, the origin of which could be due to open screw dislocations arising

due to a high strain field round the core. As nitrogen flux is increased from 6 to 8sccm, the nanowall length and width increases. A line scan across the plan-view FESEM images of the nanowalls clearly shows the triangular features with an average angle of φ ≈72, 45 and 22^{o} with respect to the (0001) plane normal for different N_2 flow rates and the corresponding plots are included in the respective micrographs.

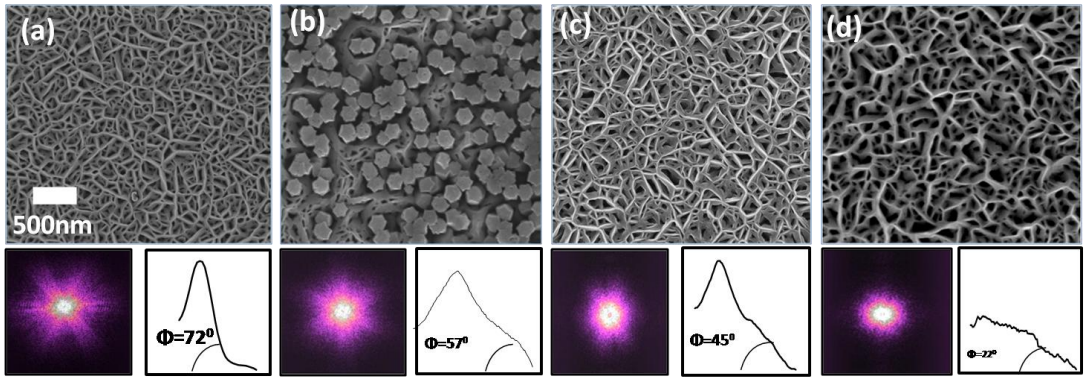

Fig.3.11: *Plan view FESEM images of GaN nanowall network grown at 2, 6 and 8 sccm and nanocolumns grown at 4.5 sccm nitrogen flow rate on bare c-plane sapphire. Φ the angle between the inclined faces of nanowalls with respect to (0001) plane and corresponding (FFT) is shown in each image.*

Fig. 3.11(b) shows a plan view FESEM image of the GaN film formed at a nitrogen flux of 4.5 sccm. Apart from the nanowall network morphology, hexagonal nanocolumns of diameters ≈150nm originating in void regions of GaN nanowall matrix were observed. The density of nanocolumns is approximately ~10^{9}cm^{-2} and their length is ≈1μm for 2 hour growth times as measured from cross-sectional FESEM images. For the nanowalls shown in **Fig. 3.11(b),** the sides of are formed by facets corresponding to r-plane ({-1102}), which describes an angle of 57^{o} with respect to surface normal to (0001) plane. It is well known from literature that the r-plane has a lower sticking coefficient for Ga adatoms than other planes[10,24,25]. The side walls of the hexagonal nanocolumns are m- faceted planes {10-10} which also have a very low surface energy and low sticking coefficients. Interestingly, we found that, by increasing the nitrogen flux rate the width of nanowalls increases and tapering of apex decreases as seen in **Fig. 3.11(a, c, d).** We reason that at higher nitrogen flux, the Ga adatoms diffuse only for shorter lengths due to collision with excess nitrogen molecules which hinder the Ga adatoms mobility, by reducing the average diffusion length of Ga adatoms. Thus, increasing the nitrogen flux rate reduces diffusion of Ga adatoms, leading to lateral growth of the nanowalls, making them wider at the same rate as vertical growth, and

thus the reduction in the nanowall angle (φ). Finally, The Fast Fourier Transform (FFT) shows a 3-fold symmetry[7] in the corresponding FESEM image as shown in **Fig. 3.11(a-c)** except sample (d)**.**

3.6 Structural and Optical studies of nitrogen flux dependent GaN nanostructure:

The structural quality of the films was investigated by 2θ-ω scan in HR-XRD as shown in **Fig. 3.12(a)**. Films grown at 2, 4.5, 6 and 8 sccm show prominent peaks at 2θ=34.5, 72.8 and 126.3, which are assigned to the reflections from (0002), (0004) and (0006) planes of wurtzite GaN. Peaks at 2θ= 41.6, 90.8 correspond to the reflections from (0006), (000 12) planes of the sapphire substrate. It is clearly visible that the absence of other phases proves the high quality single crystalline nature of the c-oriented wurtzite GaN and nanowalls and nanocolumns. **Fig. 3.12(b-c)** shows the RHEED pattern acquired along the {11-20} direction for the GaN nanowall and nanorods respectively.

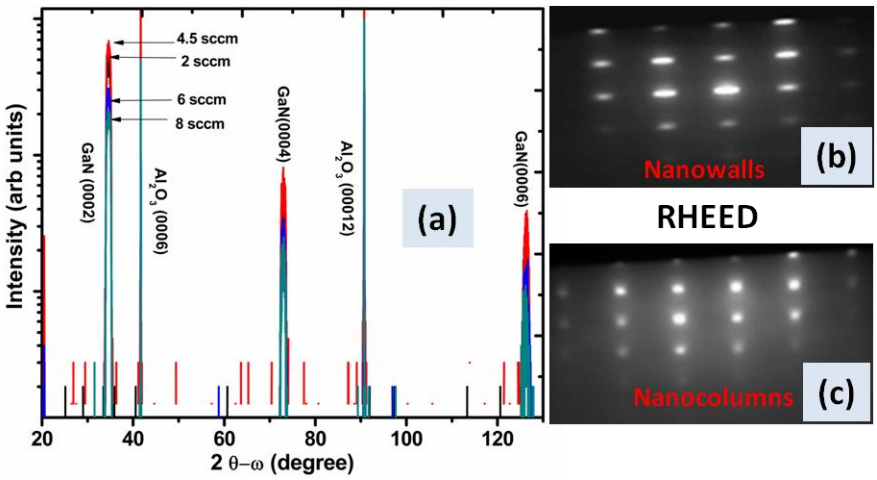

Fig.3.12: (a) *Typical 2θ-ω HR-XRD pattern of wurtzite GaN nanowall and nanorods.* ***(b-c)*** *is the representative RHEED pattern of nanowall and nanorods.*

The distance between lateral and vertical direction is 1.89 which is equal to 2a*/√3c* ratio and the corresponding c/a ratio is 1.63[26], confirming the wurtzite structures of GaN nanowalls and nanocolumns. The RHEED pattern corresponding to the GaN films grown at 6sccm shows a spread which has earlier been attributed to the anisotropic growth of the GaN nanowalls. However, the RHEED pattern of the nanocolumn sample shows sharp circular spots, indicating no anisotropy.

To study the optical properties of nitrogen flux dependent study of GaN films are investigated by using Cathodo-luminescence spectra are recorded at room temperature. In our study we have used 5kV incident electron beam energy the corresponding spectra are shown in **Fig.3.13 (a)**. The CL spectra show two distinct emissions at 3.40eV corresponds to band to band emission and other peaks is observed at 1.40-2.80eV corresponds to defect emission[27]. The spectra clearly show that as nitrogen flux increase from 2.0 to 8.0sccm, the band edge emission quenches and defects emission become prominent. However, in case of the 4.5sccm nanowall and nanocolumnar growth show strong band-edge emission and the defect related emission is almost nullified, as evident in **Fig.3.13 (b)**. Interestingly, the FWHM of the CL band edge emission is very less for the 4.5sccm nitrogen flow nanowall and nanocolumnar growth (0.2eV) as compared to the other morphologies suggesting some defect states, before the nanocolumnar growth that shows excellent crystallinity and optical quality.

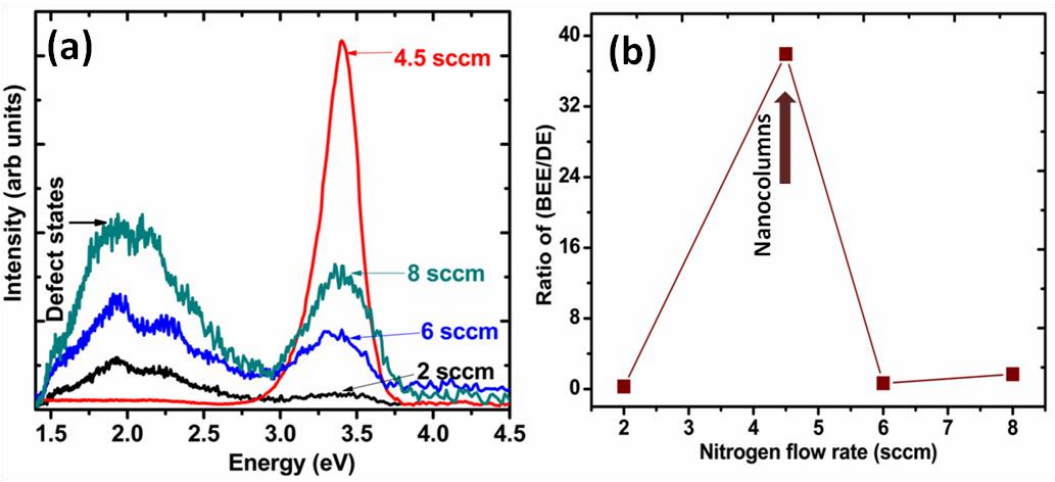

Fig.3.13 (a) *Room temperature cathodo-luminescence spectra of the GaN nanowall network grown at 2, 6 and 8 sccm and nanocolumns grown at 4.5 sccm nitrogen flow rate.* ***(b)*** *Ratio of band edge emission to defect emission*

Raman scattering provides the information on the stress field in epitaxially grown GaN films. **Fig.3.14** shows a representative room temperature Raman spectrum of GaN films grown at 2, 4.5, 6 and 8 sccm of nitrogen flow rate. In particularly the E_2 (high) mode in the Raman spectra can be used to estimate the stress because it has been proven to be particularly sensitive to biaxial stress in the film. The red shift of the E_2 (high) phonon mode with respect to the standard value of 567.7 cm^{-1} implies a biaxial tensile stress in the GaN film as well as blue shift with respect to bulk implies the compressive strain. In our case, the GaN film

grown at 4.5sccm show strong higher intense E_2 (high) mode. The FWHM of the E_2 (high) phonon mode is ~8 cm^{-1}, is comparable to that of high quality epitaxial grown bulk GaN films. Raman Spectrum acquired for 2, 6 and 8 sccm films show strong E_2 (high) mode with line widths of ≈12cm^{-1}, 14$cm^{-1}$and 15cm^{-1}, respectively. The Raman spectra of GaN nanocolumns grown at 4.5 sccm have E_2 line at 568cm^{-1} which has a shift of $\Delta\omega \approx 0.3 cm^{-1}$ with respect to stress free bulk GaN film. Raman shift $\Delta\omega < 3$ cm^{-1} corresponds to biaxial tensile stress, thus GaN nanocolumns has biaxial tensile stress of 0.06GPa. For films grown at 2, 6 and 8 sccm has Raman shift $\Delta\omega \approx 6.6, 6.8, 8.6 cm^{-1}$ which correspond to -1.4, -1.6, -2GPa compressive stress, respectively. Blue shift of the E_2 (high) line may be due to increase in free electron concentration or due to enhanced compressive stress. Using these values, and recently proposed relation[22] $\Delta\omega = 4.3\sigma_{xx}$ cm^{-1} GPa^{-1}, the value of tensile stress in all samples were estimated.

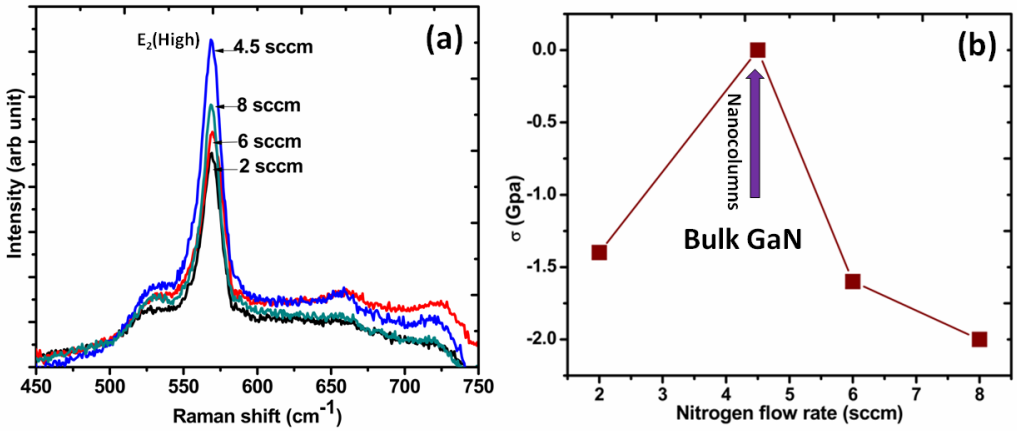

Fig.3.14: (a) *Room temperature Raman spectra acquired of GaN films grown at 2, 4.5, 6, and 8 sccm nitrogen flow rate at a substrate temperature of 680°C and fixed Ga flux.* ***(b)*** *calculated stress variation with respect to nitrogen flow rate.*

3.7 Ga flux induced morphological evolution of GaN nanostructure:

After seeing substrate temperature and nitrogen flux dependent growth, now we report our study of the role of Ga flux on the kinetics of GaN nanostructure growth. We have performed GaN growth at 680°C substrate temperature and N_2 flow rate of 4.5sccmm and only varied the Ga flux from 2.86x$10^{14}$$cm^{-2}$ s^{-1} to 4.84 x$10^{14}$$cm^{-2}s^{-1}$. The N/Ga Beam Equivalent Pressure (BEP) ratio of this growth is varied by changing the Ga effusion cell temperature from 940 to 1060°C. The **Fig. 3.15**(a'), (b') and (c') show FESEM images of

GaN films obtained and the corresponding RHEED pattern acquired along [11-20] direction as shown in **Fig. 3.15**(a), (b) and (c). **Fig.3.15 (a')** shows granular morphology of film which is grown at N/Ga BEP ratio of 200. The corresponding RHEED pattern is spotty transmission pattern with faint vertical streaks. The spotty patterns are due to the rough morphology of the surface.

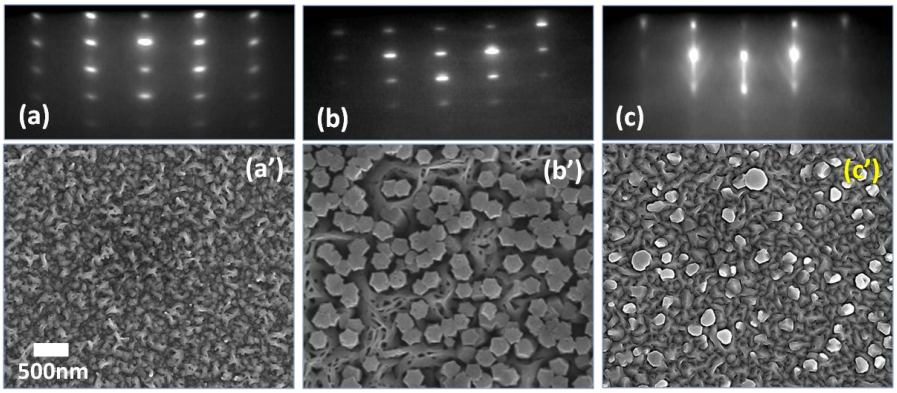

Fig.3.15: *FESEM images and corresponding RHEED patterns acquired along [11-20] azimuth of GaN films grown at N/Ga (BEP ratio) of 200, 100, and 25 at substrate temperature of 680^{o}C.*

Fig. 3.15(b) shows that the GaN nanocolumns are surrounded by nanowall network structure obtained at N/Ga BEP ratio 100. Spotty RHEED pattern indicate a 3-D morphology. **Fig.3.15** (c) shows that by increasing Ga flux, where we maintain the N/Ga BEP ratio is 25, the RHEED streaky + spotty pattern suggests that the island of large sized terraces are formed on surface.

3.8 Structural and Optical studies of Ga flux dependent GaN nanostructures:

Fig. 3.16(a) shows the representative HRXRD patterns of GaN film. Inset of **Fig. 3.16(a)** shows the rocking curve obtained for the films which are grown at different Ga flux. **Fig. 3.16(b)** show the growth rate and alternative y-axis deals with full width at half-maximum (FWHM) of rocking curve along (0002) reflection is plotted versus variation in N/Ga BEP ratio along the x axis. The observed FWHM of the (0002) peak decreases from 1.4 to 0.4 with respect to N/Ga BEP ratio of 200 and 25 respectively. The reduction in FWHM indicates high crystalline quality which arises due to reduction in the mosiacity. With an increase in N/Ga BEP ratio, the growth rate reduces, because of low flux of Ga adatoms.

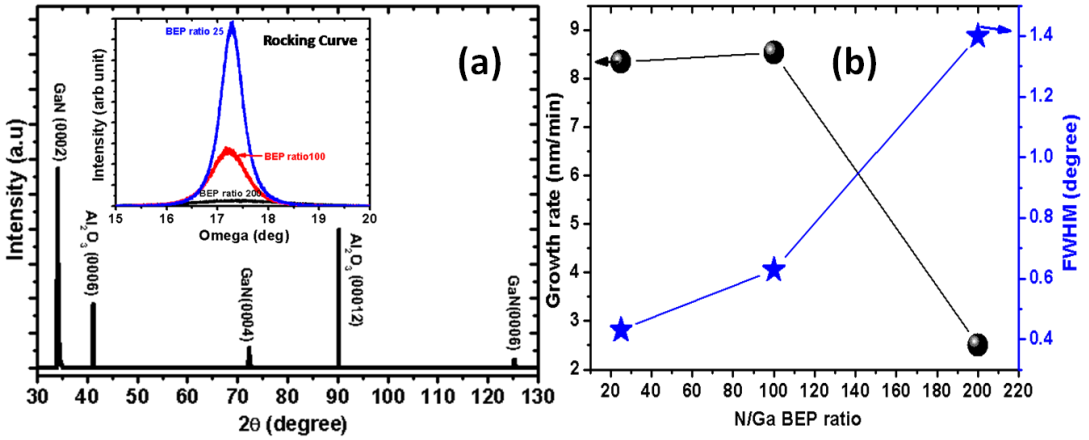

Fig.3.16: (a) *HR-XRD rocking curves of GaN films grown at BEP ratio of 25, 100 and 200 at substrate temperature of 680^{o}C and N_2 flux 4.5sccm,* ***(b)*** *plot of growth rate and FWHM of rocking curve along (0002) reflection versus N/Ga BEP ratio.*

PL spectroscopy was performed to investigate the optical quality of the film. **Fig. 3.17** is the PL spectra of GaN film grown at different N/Ga (BEP) ratio of 25, 100 and 200 respectively. The PL spectra of sample show two transition peaks at 363.1nm (3.42eV) and another at 455 to 850nm respectively.

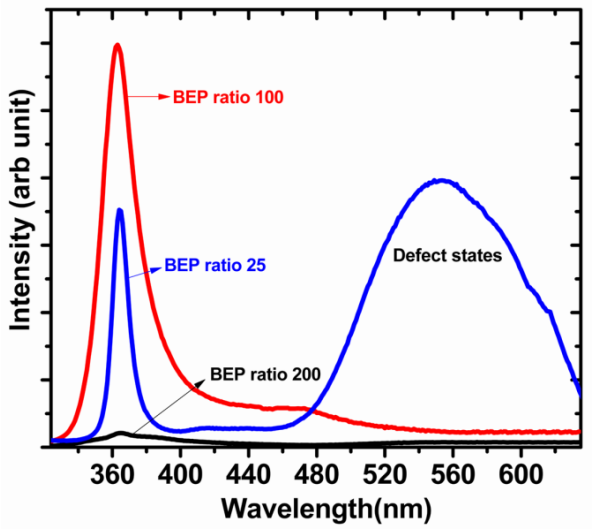

Fig.3.17: *Room temperature photoluminescence spectra of GaN films grown at N//Ga BEP ratio of 25, 100 and 200 at fixed nitrogen flow rate 4.5 sccm and substrate temperature of 680^{o}C.*

The peak originated at 363.2nm corresponds to the band-edge emission and another broad peak in the 450 to 850nm range is attributed to the defect transitions. The film grown at BEP ratio of 100 shows a strong band-edge emission at 363.1nm and low defect emission at 450 to 850 nm range. The ratio of band edge luminescence (BEL) to yellow luminescence

(YL) is 23. In case of a film which is grown at BEP ratio~25, show strong yellow luminescence and the intensity ratio between the band-edge peaks to yellow luminescence is 0.9. The GaN film grown at BEP ratio 200 shows the ratio between band-edge to yellow luminescence is 2.4. The FWHM of band-edge emission is 4 nm (32meV), which suggesting that the GaN film grown at BEP ratio 25 is compact 2-D film and it has high density of defects as a result of which one can see strong defect emission. The GaN nanostructure shows strong PL emission and ratio of band edge to the defect emission intensity is 23 which is twenty four times higher than that of 2-D GaN film grown at BEP ratio of 25, and 10 times more than the film which is grown at BEP ratio 200. Thus, GaN nanocolumnar morphology show low defect density and strain relaxed and shows high optical quality. The band edge emission of GaN nanocolumns are shifted to higher energy side (blue shift) with respect to film grown at BEP ratio 25, that clearly suggesting low compressive stress in film. In case of GaN film grown at BEP ratio 200 and 25, the band edge emission shifted toward lower energy, that suggesting tensile stress in the films.

The crystalline quality and lattice structure and stress in the GaN film was further investigated by Raman spectroscopy. A typical room temperature Raman spectrum of GaN films grown at N/Ga BEP ratio 25, 100, 200 at substrate temperature 680^{o}C is shown in **Fig. 3.18(a).**

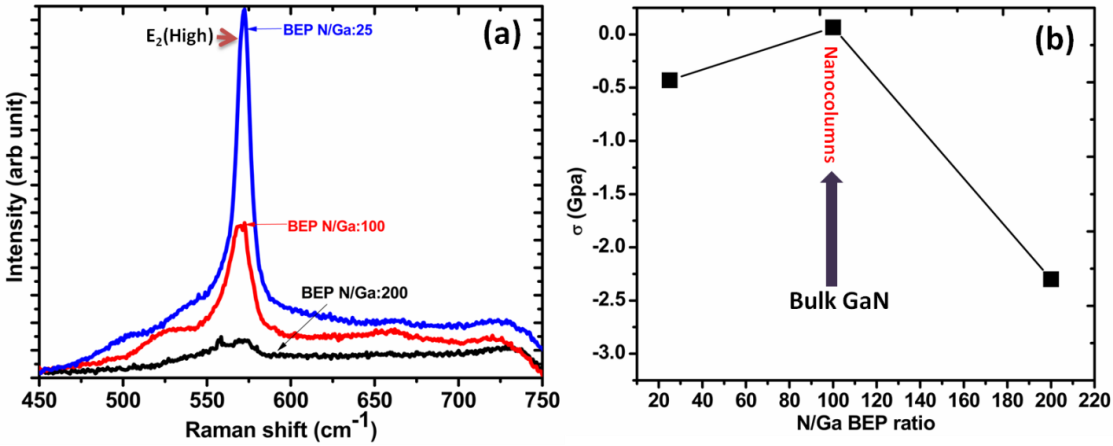

Fig.3.18: (a) *Room temperature Raman spectra of GaN films grown at N/Ga BEP ratio 25, 100 and 200 at fixed substrate temperature of 680^{o}C and nitrogen flow rate 4.5 sccm* ***(b)*** *Calculated stress v/s nitrogen flow rate of respective film.*

The Raman spectra are dominated by strong E_2 (high) mode. The Raman spectra of GaN nanocolumns grown at N/Ga BEP ratio 100, shows intense E_2 (High) mode and shows

narrow line width of about 8cm^{-1}, which suggests the high quality epitaxial grown GaN nanocolumns. The Raman spectra of film grown at N/Ga BEP ratio 25 show strong symmetric line E_2 (High) of line width of 6 cm^{-1}. Raman spectrum of N/Ga BEP ratio 200 has broader E_2 (high) mode and suggesting inferior quality of the film. Raman spectra obtained from film grown at N/Ga BEP ratio 100 has E_2 line at 568 cm^{-1} which has a shift of $\Delta\omega$ 0.3 cm^{-1} with respect to 567.7 cm^{-1} stress free bulk GaN sample and the biaxial tensile stress is estimated to be 0.06GPa. For films grown at N/Ga BEP ratio 25, the Raman shift $\Delta\omega$ is ≈1.8 cm^{-1} which corresponds to -0.43GPa. And in case of N/Ga BEP ratio 200 Raman shift $\Delta\omega$=-10 cm^{-1} which corresponds to biaxial compressive[28–32] stress of 2.3GPa as shown in **Fig 3.18(b)**.

3.9 Summary:

This chapter consisted of extensive studies of GaN on bare Al_2O_3 (0001) surface, by varying the growth parameter systematically and studying the morphological, structural, optical and mechanical properties of the resulting films. The consolidated morphological evolution of GaN on bare sapphire surface were elucidated by varying a) substrate temperature, b) Ga flux and c) N_2 flux and is depicted in **Fig.3.19**.

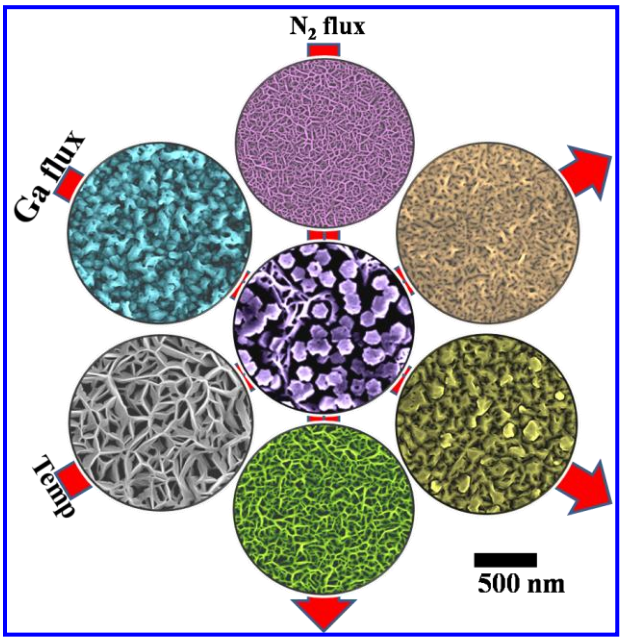

Fig. 3.19: *Plan view FESEM images of GaN films grown at three pathways by varying substrate temperature, nitrogen flux rate and gallium flux respectively.*

In the first set of experiments, we have presented the formation and characterization of GaN nanostructures grown at low temperatures (480-630°C) in nitrogen rich conditions. Hexagonal nanowall network of GaN were observed to form in these conditions. The walls are seen to be about 150nm at the bottom, tapering to 10 nm at their apex. Further increase in substrate temperature to 680^{o}C leads to the formation of a combination of nanowall and nanorods. We have discussed the mechanism of nanorod formation which is observed in a very narrow growth parametric of 680^{o}C substrate temperature, 4.5sccm N_2 flow rate and $3.86x10^{14}$ $cm^{-2}s^{-1}$ Ga flux window. Further increase in substrate temperature (730-880°C) leads to the formation of flat 2D films, which results in a degradation of optical and crystal quality. After the identification of a growth temperature regime for GaN nanocolumn formation the effect of variation in other growth parameters (N2 and Ga flux) was studied. A consolidated picture of a narrow parametric window by kinetic control to form nanostructures is identified by varying Ga flux ($2.86\text{-}4.84x10^{14}cm^{-2}s^{-1}$), nitrogen flow rate (2-8sccm) and substrate temperature (480-880°C). Thus, this study clearly defines the role of the kinetics of film formation on the morphology and consequently on film properties of the GaN films. The investigation of structural and optical properties of these nanocolumns reveals almost defect free GaN and shows very sharp band edge emission.

3.10 REFRENCES:

1. S. Li and A. Waag, *J. Appl. Phys.*, 2012, **111**, 071101.

2. M. A. Reshchikov, D. Huang, F. Yun, P. Visconti, L. He, H. Morkoç, J. Jasinski, Z. Liliental-Weber, R. J. Molnar, S. S. Park, and K. Y. Lee, *J. Appl. Phys.*, 2003, **94**, 5623.

3. D. Cherns, L. Meshi, I. Griffiths, S. Khongphetsak, S. V. Novikov, N. R. S. Farley, R. P. Campion, and C. T. Foxon, *Appl. Phys. Lett.*, 2008, **93**, 111911.

4. C. Chèze, L. Geelhaar, O. Brandt, W. M. Weber, H. Riechert, S. Münch, R. Rothemund, S. Reitzenstein, A. Forchel, T. Kehagias, P. Komninou, G. P. Dimitrakopulos, and T. Karakostas, *Nano Res.*, 2010, **3**, 528–536.

5. M. A. Sanchez-Garcia, E. Calleja, E. Monroy, F. J. Sanchez, F. Calle, E. Muñoz, and R. Beresford, *J. Cryst. Growth*, 1998, **183**, 23–30.

6. O. Ambacher, *J. Phys. D. Appl. Phys.*, 1998, **31**, 2653–2710.

7. P. Kumar, M. Tuteja, M. Kesaria, U. V. Waghmare, and S. M. Shivaprasad, *Appl. Phys. Lett.*, 2012, **101**, 131605.

8. H. Sekiguchi, K. Kato, J. Tanaka, A. Kikuchi, and K. Kishino, *Phys. Status Solidi*, 2008, **205**, 1067–1069.

9. S. Fernández-Garrido, X. Kong, T. Gotschke, R. Calarco, L. Geelhaar, A. Trampert, and O. Brandt, *Nano Lett.*, 2012, **12**, 6119–25.

10. K. A. Bertness, A. Roshko, L. M. Mansfield, T. E. Harvey, and N. A. Sanford, *J. Cryst. Growth*, 2007, **300**, 94–99.

11. F. Meng, S. A Morin, A. Forticaux, and S. Jin, *Acc. Chem. Res.*, 2013, **46**, 1616–26.

12. M. Kesaria and S. M. Shivaprasad, *Appl. Phys. Lett.*, 2011, **99**, 143105.

13. M. Kesaria, S. Shetty, P. I. Cohen, and S. M. Shivaprasad, *Mater. Res. Bull.*, 2011, **46**, 1811–1813.

14. B. Alloing, S. Vézian, O. Tottereau, P. Vennéguès, E. Beraudo, and J. Zuniga-Pérez, *Appl. Phys. Lett.*, 2011, **98**, 011914.

15. H.-Y. Chen, H.-W. Lin, C.-H. Shen, and S. Gwo, *Appl. Phys. Lett.*, 2006, **89**, 243105.

16. B. Roul, M. Kumar, M. K. Rajpalke, T. N. Bhat, N. Sinha, A. T. Kalghatgi, and S. B. Krupanidhi, *J. Appl. Phys.*, 2011, **110**, 064502.

17. T. Akasaka, Y. Kobayashi, and M. Kasu, *Appl. Phys. Lett.*, 2010, **97**, 141902.

18. W.-Y. Shiao, C.-Y. Chi, S.-C. Chin, C.-F. Huang, T.-Y. Tang, Y.-C. Lu, Y.-L. Lin, L. Hong, F.-Y. Jen, C. C. Yang, B.-P. Zhang, and Y. Segawa, *J. Appl. Phys.*, 2006, **99**, 054301.

19. D. G. Zhao, D. S. Jiang, J. J. Zhu, Z. S. Liu, S. M. Zhang, J. W. Liang, and H. Yang, *J. Appl. Phys.*, 2007, **102**, 113521.

20. M. K. Rajpalke, B. Roul, M. Kumar, T. N. Bhat, N. Sinha, and S. B. Krupanidhi, *Scr. Mater.*, 2011, **65**, 33–36.

21. M. Kumar, B. Roul, T. N. Bhat, M. K. Rajpalke, P. Misra, L. M. Kukreja, N. Sinha, a. T. Kalghatgi, and S. B. Krupanidhi, *Mater. Res. Bull.*, 2010, **45**, 1581–1585.

22. M. Kumar, M. K. Rajpalke, B. Roul, T. N. Bhat, N. Sinha, A. T. Kalghatgi, and S. B. Krupanidhi, *Appl. Surf. Sci.*, 2011, **257**, 2107–2110.

23. A. G. Milekhin, R. J. Meijers, T. Richter, R. Calarco, S. Montanari, H. Lüth, B. A Paez Sierra, and D. R. T. Zahn, *J. Phys. Condens. Matter*, 2006, **18**, 5825–34.

24. M. Kesaria and S. M. Shivaprasad, *Appl. Phys. Lett.*, 2011, **99**, 143105.

25. C. Constantin, H. Al-Brithen, and M. Haider, *Phys. Rev. B*, 2004, **1**.

26. S. W. Lee, J.-S. Ha, H.-J. Lee, H.-J. Lee, H. Goto, T. Hanada, T. Goto, K. Fujii, M. W. Cho, and T. Yao, *Appl. Phys. Lett.*, 2009, **94**, 082105.

27. V. Consonni, M. Knelangen, U. Jahn, A. Trampert, L. Geelhaar, and H. Riechert, *Appl. Phys. Lett.*, 2009, **95**, 241910.

28. H. Harima, *J. Phys. Condens. Matter*, 2002, **967**.

29. D. Wang, S. Jia, K. J. Chen, K. M. Lau, Y. Dikme, P. van Gemmern, Y. C. Lin, H. Kalisch, R. H. Jansen, and M. Heuken, *J. Appl. Phys.*, 2005, **97**, 056103.

30. S. Yang, R. Miyagawa, H. Miyake, K. Hiramatsu, and H. Harima, *Appl. Phys. Express*, 2011, **4**, 031001.

31. E. V. Konenkova, Y. V. Zhilyaev, V. A. Fedirko, and D. R. T. Zahn, *Appl. Phys. Lett.*, 2003, **83**, 629.

32. D.-S. Jiang, M. Ramsteiner, K. Ploog, H. Tews, A. Graber, and H. Riechert, *Radiat. Eff. Defects Solids*, 1998, **146**, 99–111.

Chapter 4

Nitridation of c-Sapphire and Si (111) Surfaces

4: Nitrogen Plasma Assisted Surface Nitridation and Characterization of c-Sapphire and Si (111) Surfaces:

4.1 Introduction:

Since the realization of economically viable high efficacy III-V nitrides based optoelectronic devices operating in the blue and UV regions depends on the use of suitable substrates[1–3]. Improving the performance and functionality of the sapphire and Si substrates by surface modification is of great interest. In case of sapphire, it has been well established now that forming a thin AlN layer prior to depositing the GaN active layer significantly increases the structural and optoelectronic quality of the film due to a reduction in the lattice mismatch of 12% with sapphire and 3% with GaN along the [11-10]//[11-20] orientation[4,5]. On other hand, in case of Si, in the several attempts have been made to grow GaN on Si (111) surfaces by PA-MBE, the epitaxy of the intentional and unintentional formation of a SiN_x adlayer formed on the substrate due to the high reactivity of the silicon surface to the active nitrogen, prior to GaN growth, is still not clear[6,7]. Interestingly, a thin AlN layer also acts as a barrier for oxygen migration from the sapphire substrate and reduces unintentional Si doping from Si substrate. One can also control the polarity of the over grown film using the appropriate intermediate AlN layer [8–11]. To form the AlN layer, one way is to nitride the c-plane sapphire surface, which leads to the formation of a graded interface of AlN. This has been shown to promote the growth of high quality 2-D films due to a continuous reduced lattice mismatch. However, the understanding of the underlying mechanism at the atomistic level is not yet conclusive [12,13]. In the case of Si, a few attempts are reported in the literature where the initial stages of growth of single crystalline hexagonal SiN_x at the step edges of the silicon substrate by plasma nitridation of Si (111) surface were observed. Some groups[14,15] have also reported the formation of SiN_x nano-islands by plasma nitridation around 700^{o}C. These nano-islands can act as seed for fabrication of semiconductor nanostructures and promise to provide good quality GaN films without cracks[16,17] and low dislocation density. Our group has previously shown spontaneous formation of GaN nanostructures on modified Si surfaces by sheer kinetic control of growth parameters[18]. Complementing our earlier studies, we have done a systemic optimization of modification of sapphire and Si surfaces.

In this study, we have optimized the time and flux dependent nitridation of c-sapphire substrate by rf-assisted N_2* plasma, as a pre step before further deposition of AlN. The variation of surface and interfacial chemical composition is monitored by XPS. On this optimally nitrided surface, a thin layer of AlN is separately deposited in order to demonstrate how the properties of the nitrided sapphire surface determine the origin, shape and size of the AlN overlayer. In the case of Si, we have studied the initial stages of the formation of 2D single crystalline silicon nitride (SiN_x) film with controlled N_2* plasma exposure times on Si (111) surface in the temperature range of 700^{o}C to 850^{o}C. We have also probed into the morphology, epitaxy, band structure and stoichiometry of the SiN_x interfacial layer obtained by the nitridation of Si (111) surface. Crystal quality and morphology of the films were investigated with help of complementary techniques such as XRD, XPS, RHEED, FESEM and TEM.

4.2 Experimental Section:

A) Sapphire nitridation and growth of AlN on nitrided surface of sapphire

The study consists of two parts A) time, flux, and temperature dependent nitridation study of c-plane sapphire and B) growth of AlN film at 700^{o}C on the pre-nitrided surface. Nitridation of sapphire was carried out at 2.5x10^{-5} Torr beam equivalent pressure of nitrogen with 375W forward power of the RF plasma for different time durations (2, 4, 5, 6 and 8hrs). Surface structure is monitored *in situ* by RHEED and core-level x-ray photoelectron spectroscopy using an AlK_α(1486.6eV) source was carried out to understand the stoichiometry and chemical bonding at every stage of the nitridation process. Fingerprint analysis of XPS core levels, by Shirley background subtraction, deconvolution into Voigt (20% Lorentzian) components and using suitable atomic sensitivity factors, was performed on the raw data. Surface morphological and structural properties have been investigated by FESEM, powder X-ray diffraction and TEM.

B) Nitrogen plasma assisted nitridation of Si (111) surface

Prior to nitridation, the p-doped Si (111) substrate was chemically cleaned and annealed at 500^{o}C for 30 min. and repeatedly flashed at 950^{o}C to obtain atomically clean surface. The stable 7X7 reconstruction of Si(111) surface and the related kikuchi line were observed by RHEED by using electrons with an energy of 9keV incident at 2.6° glancing

angle along the [11-2] azimuth. The nitridation of the Si surface was done by the radio frequency nitrogen plasma source operating at a forward power of 375W and reflected power 7W, with a nitrogen flow rate of 4.5 sccm, at a substrate temperature of 750^{o}C, with N_2* plasma exposure times ranging from 2 to 60 min., at 2.5X10^{-5} Torr pressure. The surface chemical composition is probed by X-ray Photoelectron Spectroscopy (XPS) and the surface morphology by Atomic Force Microscopy (AFM). The XPS survey scans were obtained at pass energy of 100eV, while the core-levels were acquired at pass energy of 25eV. Linear background subtraction and deconvolution into 20% Voigt components were performed to identify the valence states.

4.3 Nitrogen plasma assisted nitridation of c-plane sapphire surface:

Nitrogen ions or nitrogen plasma have been used in the literature to nitride the Al_2O_3 surface, to form graded AlN top layers[19]. Namkoong et al[20] in their nitridation studies by N^*_2 plasma exposure to c-plane sapphire at 700°C found that the AlN formed, covered 70% of the surface and at 200°C the coverage was 90%. In view of this, we choose the nitridation temperature as 200^{o}C and N_2 Beam Equivalent Pressure (BEP) of 2.5×10^{-5} Torr and varied the exposure time from 2 to 8 hrs. **Fig. 4.1** consists of RHEED pattern obtained at different stages of the surface nitridation. **Fig. 4.1(a, b)** is the RHEED pattern obtained along the <10-10> and <11-20> azimuth of clean c- plane sapphire substrate before nitridation, displaying the characteristic streaky pattern with Kikuchi lines. **Fig. 4.1(c-f)** corresponds to the RHEED pattern acquired for 1, 2, 4, and 6 hrs nitridation of sapphire along <11-20> direction. At 1 hour (c) we can clearly see the co-existence of prominent sapphire streaks and emergence of dim AlN streaks (shown by arrows). Further nitridation for 2hrs **(Fig. 4.1d)**, the AlN streaks increase in clarity and the sapphire streaks get weaker in intensity and almost vanish in (f). **Fig. 4.1(g)** show the line scan of the intensity of Al_2O_3 and AlN streaks of sample A, B and C, corresponding to 1, 2, and 4hrs of sapphire nitridation, respectively. Inset of **Fig. 4.1(g)** shows the intensity ratio of the streaks corresponding to AlN and Al_2O_3, obtained by subtracting background intensity, depicting that the intensity of Al_2O_3 streak reduces and the AlN streak intensity get stronger with plasma exposure upto 4hrs, due to a linear increase in the formation of homogeneous AlN. After 4 hours of nitridation AlN streak intensity also gradually dims, due to an increase in the background intensity in RHEED. For clean Al_2O_3

(0001), the streaks in the RHEED image are in the <10-10> direction, but after nitridation for 1 hour the RHEED pattern shows the streaky pattern in the <11-20> direction, due to the 30^{o} in- plane rotation of AlN unit cell, with respect to that of sapphire, to attain the least misfit by the epitaxial relation [10-10]//[11-20]. **Fig. 4.1(f)** corresponds to the RHEED pattern obtained after 6hrs of exposure to the N_2* plasma, which shows a very weak streaky pattern with a bright background, suggesting the formation of both crystalline and non-crystalline (or mis-oriented) phases.

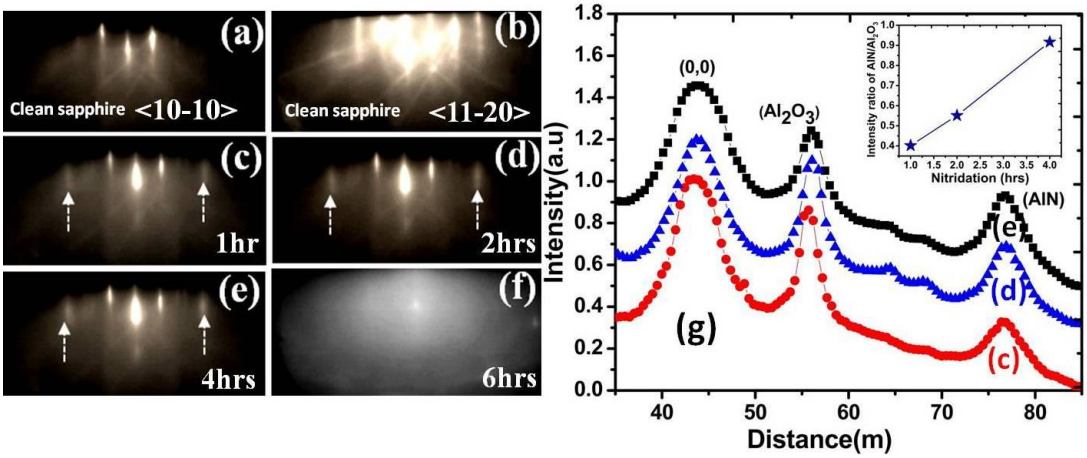

Fig.4.1: *Shows the RHEED patterns of (a, b) clean sapphire along <10-10> and <11-20> direction and (c-f) after 1, 2, 4 and 6 hrs nitridation, along <11-20> direction. (g) Line scan of RHEED pattern (c), (d), and (e) corresponds to 1, 2 and 4hrs of plasma nitridation. Inset of* ***Fig. 4.1(g)*** *shows the variation of ratio of intensity between AlN to sapphire related steaks as a function of nitridation time.*

To optimize the nitridation of c-plane sapphire surface, we look at the chemical constituents and stoichiometry at each stage, by a systematic core level XPS study. **Fig. 4.2(A)** shows the effect of the time dependent plasma exposure of the Al_2O_3 (0001) surface on the chemical composition of the films by monitoring the variations of the ratio of areas of the Al and N core level transitions on y-axis and O to Al ratio on the alternate y-axis. The **Fig. 4.2(B)** shows the representative deconvoluted N1s and Al2p core levels. It is clear that with increasing exposure to the excited N_2* species from the plasma, the N/Al ratio monotonically increases while the O/Al ratio decreases, suggesting that the oxygen present on the surface of Al_2O_3 is replaced by nitrogen, resulting in the AlN formation[19,21,22]. The curve shows that the intensity of the nitrogen core level peak saturates after 6 hours of exposure time when an AlN layer is formed. Since nitrogen has a lower diffusion coefficient ($1.33X10^{-16}cm^2/sec$) in AlN than in Al_2O_3, ($8X10^{-16}cm^2/sec$)[23], increasing AlN formation

forms a barrier for nitrogen diffusion, and consequently impedes further nitridation. **Fig. 4.2(B)** shows the deconvoluted core levels obtained after 6hrs of nitridation, where N (1s) shows Al-N bond related peak at 397.3eV and the another peak of N-O related bond of un-reacted substrate at higher energy side of 399.1eV. This can be attributed to the nitrogen interaction in the oxygen rich environment of the sapphire substrate, since oxygen is more electronegative than Al, some of the nearest neighboring Al atoms are still bonded with O. A recent report has suggested that the deconvoluted peak corresponding to 399.1 eV may be originating from a complex intermediate state involving Al, N and O[24]. The Al (2p) core-level is also seen to possess components of Al_2O_3 (73.1 eV) substrate and AlN (74.1eV) overlayer.

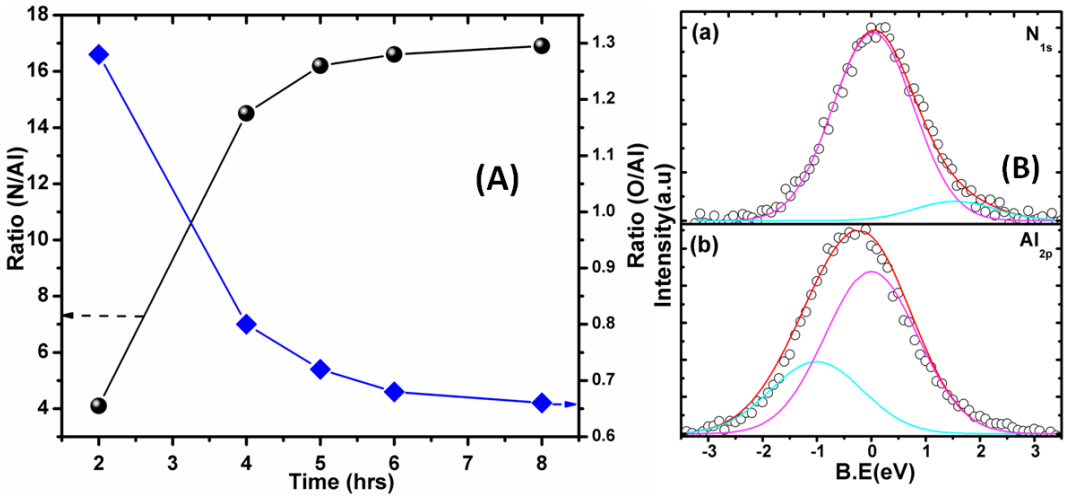

Fig.4.2 (A) *Shows the variation of ratio of chemical composition for N/Al and O/Al with exposure time of nitrogen plasma.* ***(B)*** *Shows the deconvoluted core level photoelectron spectra of (a) N 1s (b) Al2p for 6 hrs nitridation of the sapphire substrate.*

To find the dependence of the abundance of nitrogen availability, different nitrogen flow rates of 2, 4.5 and 7sccm are used, maintaining substrate temperature of 200^{o}C for 2 hours. There is no significant change in intensity of N1s level observed, indicating that the AlN formation by exposure to nitrogen plasma of sapphire is independent of the nitrogen flow rate as shown in **Fig. 4.3(b)**. We have also performed temperature dependent nitridation studies by keeping the nitrogen flow rate constant at 4.5sccm and by varying the substrate temperature from RT to 800^{o}C. The RHEED and XPS signals after nitridation at different temperatures do not show any significant change from the room temperature nitridation results, suggesting the insufficiency of the enthalpic driving force for replacing oxygen by

nitrogen to form AlN, in this temperature range, as evident in **Fig. 4.3(b)**. To find probable reasons for the above issue, we have looked into the relation between Arrhenius type of relation between the diffusion coefficient and activation energy is given by $D = D_o \exp\left(\frac{-Q}{kT}\right)$---- (1) Where D_o is a pre-exponential constant and Q is the activation energy for diffusion. At low temperature N* is species unable to surmount the activation energy barrier (1) and hence at room temperature we were unable to nitride the sapphire surface as evident by XPS and RHEED results. In order to quantify the thickness dependent change in the diffusion coefficient of the host material, XPS studies were used. Thickness of the AlN layer formed due to nitrogen plasma nitridation of sapphire was calculated using XPS general scans via the expression $d_{AlN} = \lambda_{Al(2p)} Sin\theta.In((I_N / I_{Al}\beta)+1)$ ----- (2), where d_{AlN} is thickness of AlN layer, $\lambda_{Al(2p)}$ is attenuation length of Al 2p peak = 2.433 nm, θ is angle between photoelectrons and detector, β is the ratio of XPS intensity N/Al in bulk AlN, I_N and I_{Al} is the intensity of Al 2p and N 1s peak in the general scan as shown in **Fig. 4.3(a)**.

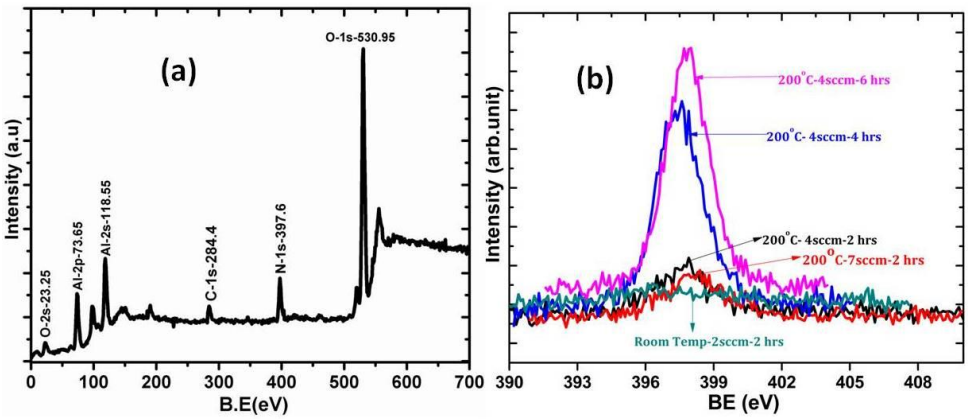

Fig.4.3: (a) *The representative general scan of nitrided surface of sapphire* ***(b)*** *the core level photoelectron spectra of N 1s of nitrided surface of sapphire.*

Fig. 4.4(a) represents the graph of change in diffusion coefficient associated with loss of oxygen from Al_2O_3 surface with respect to nitrogen plasma exposure time. The dependence of diffusion coefficient and relative oxygen loss with temperature is clearly demonstrated in **Fig. 4.4(a)**. The value of diffusion coefficient (D) was determined to be 1.80×10^{-17}, 1.28×10^{-17}, 1.21×10^{-17}, 1.06×10^{-17} and 8.02×10^{-18} $cm^2.S^{-1}$ for 2,4,5,6 and 8hrs sample respectively. The observed high value of nitrogen incorporation in 2, 4 and 6 hrs

nitrided samples was attributed to the thickness (or surface) dependent diffusion as shown in **Fig. 4.2(a)& Fig. 4.4(b)**, since the enthalpy of motion at the surface is less than that in the crystal lattice ($Q_{surface} < Q_{lattice}$). The diffusion length (x) of species in non steady state condition can be written as $x = 2\sqrt{Dt}$ -- (3) where x is diffusing depth, D the diffusion coefficient and t is the time. Equation 2 shows the nonlinear behaviour of penetration depth (x) from which it was inferred that relative oxygen loss and nitrogen incorporation in Al_2O_3 is a diffusion limited process. Thus, the conversion of initial layers of Al_2O_3 into AlN, which was observed to be a very fast process, was explained by the existence of surface dangling bonds which favour easy and rapid reaction compared to bulk due to a lack of coordination and high surface energy. Once the thickness of reacted layer increases, stoichiometry gradually changes from AlN_xO_{1-x} to AlN. The diffusion coefficients of N_2* are $1.33x10^{-16}$ and $8x10^{-16}cm^2/s$ of Al_2O_3 and AlN[25]which hinders the driving force required to move active nitrogen species within the respective media. Once the surface atoms react completely, for further reaction the active nitrogen species has to penetrate deeper and thus the activation energy for diffusion in crystal lattice becomes more than the surface diffusion.

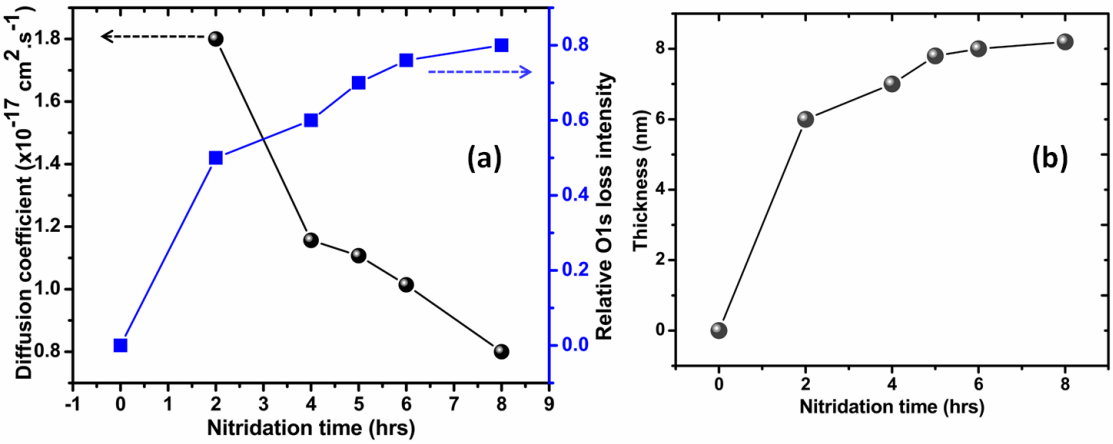

Fig.4.4: (a) *Shows the variation of diffusion coefficient and relative oxygen loss* ***(b)*** *thickness variation at different nitridation time.*

The observed low value of D in the cases of 6hrs and 8 hrs nitrided surfaces strongly suggests that the formation of dislocation at some critical thickness is the source for reduction in diffusion coefficient. Such intrinsic change is also corroborated with oxygen loss during nitridation. It is important to note that the relative oxygen loss does not reflect in film thickness, which indicates that nitrogen replacement is a non uniform process and all nitrogen will not react to form AlN. Clearly, initially diffused nitrogen forms AlN_xO_{1-x} and

on further exposure of nitrogen plasma, the aluminum oxy-nitride[25–28] species gets the required coordination to form AlN. We also suggest that the observed saturation of N/Al ratio in case of 6 and 8 hrs nitrided surface may result in the formation of dislocations at some critical thickness due to misfit induced strain relaxation[23].

4.4 Surface nitridation induced AlN nano-columnar growth on c-sapphire:

We have studied parametric dependence of the nitridation of Al_2O_3 surface in the earlier section. We now deposit a thin AlN layer on the optimized nitrided sapphire surface and study its characteristics. **Fig. 4.5(a)** is the RHEED pattern acquired for clean sapphire along <10-10> direction. **Fig. 4.5(b)** is the RHEED pattern acquired along the <11-20> azimuth of AlN buffer layer on the pre-nitrided sapphire substrate. It clearly shows the 30^o in-plane rotation to obtain minimum lattice mismatch with respect to substrate.

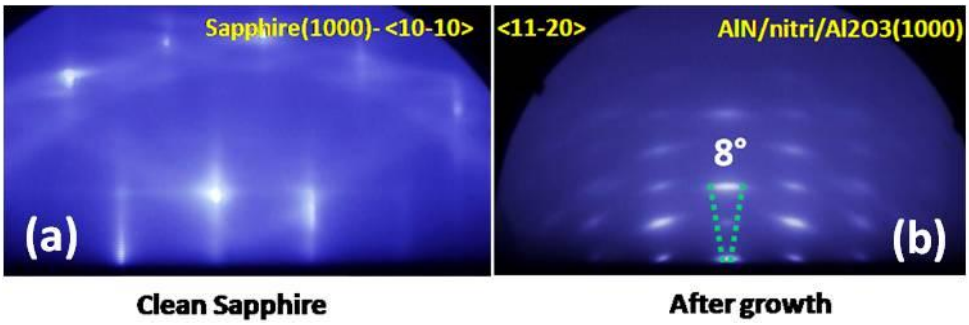

Fig.4.5: (a) *RHEED pattern of clean sapphire acquired along <10-10> direction* ***(b)*** *after 30mins growth of AlN acquired along <11-20> direction.*

The spots observed in this RHEED pattern are due to the transmission of electrons through the AlN 3-D features[29,30]. The spots are anisotropic, which can arise either from the polycrystallinity of the film or due to the in-plane tilt of the surface features observed. The ratio of the distance between the spots in horizontal and vertical directions is 1.85 and corresponding c/a ratio is 1.60. The calculated *d* value from RHEED pattern is 2.07 Å along the <11-20> direction, which is the bulk wurtzite AlN crystal lattice value. This suggests that the AlN grown is not strained in this nanocolumnar formation. To distinguish whether the anisotropy of the RHEED spots is from polycrystallinity or due to misorientation of the nano-features, we have performed XRD studies. **Fig. 4.6** shows the XRD pattern of AlN films comprising of the nano-features shown in **Fig.3.** Peaks at θ=35.8^o and 76.3^o are observed to

be the most intense peaks and corresponds to the (0002) and (0004) planes of the AlN films. The strong reflections and the minimal background show that AlN films consist of epitaxially grown single-crystalline wurtzite AlN nanostructures that are oriented along the (0001) growth direction. The **Fig. 4.6** inset is the JCPDS data of cubic AlN, no peak is matching with the XRD data of our sample providing no evidence for the presence of the cubic phase of AlN during the formation of the nitrided surface.

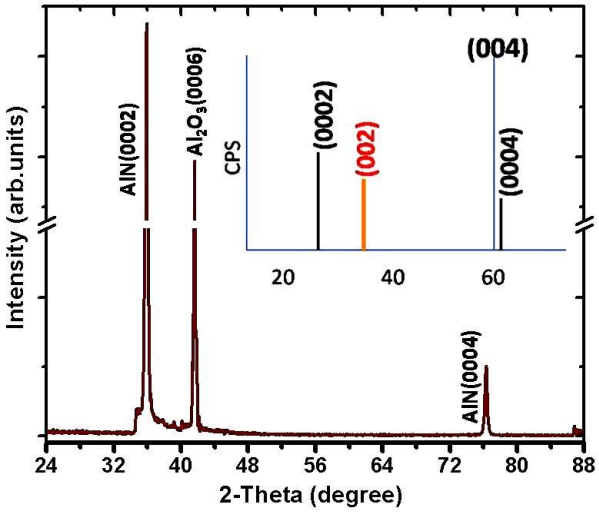

Fig.4.6: *XRD pattern obtained after the growth of AlN on nitrided surface of sapphire. Inset of* ***Fig. 4.6*** *represents the JCPDS pattern of cubic AlN.*

Fig. 4.7(a) is the top-view of the FE-SEM image which clearly shows a high density of nano-sized AlN. To confirm the structure in each 1-D feature, selected area electron diffraction (SAED) along the zone axis <$2\bar{1}\bar{1}0$>, obtained by TEM on one of these 1-D features, is shown in **Fig. 4.7(b).** This confirms that the observed 1-D nanostructures are single crystalline and wurtzite in structure with [0001] as the growth direction. Size distribution of the AlN pyramidal nanocolumns in **Fig. 4.7(c)** were found to be bimodal with $\approx 2 \times 10^9/cm^2$ of them having diameters ranging from 20-60 nm and $\approx 6 \times 10^9/cm^2$ of them having larger diameters in the range of 80-120nm. The image **Fig. 4.7 (d)** clearly shows that bigger AlN nano-features possess a faceted pyramidal apex and the smaller size AlN islands have oval apex, while some have a partially formed pyramidal apex. The number density of larger diameter (in the range 80-120nm) AlN nano-features with hexagonal pyramidal apex is approximately equal to the density of screw dislocations ($\sim 10^9/cm^2$), suggesting that this could be an interfacial dislocation mediated growth. The columnar growth of the larger

diameter nanocolumns of AlN appears to follow the Frank spiral growth mechanism under low supersaturation condition[31–34], where the axial screw dislocations originating at the interface, terminate at the surface in the form of a spiral staircase, enabling the spiral growth.

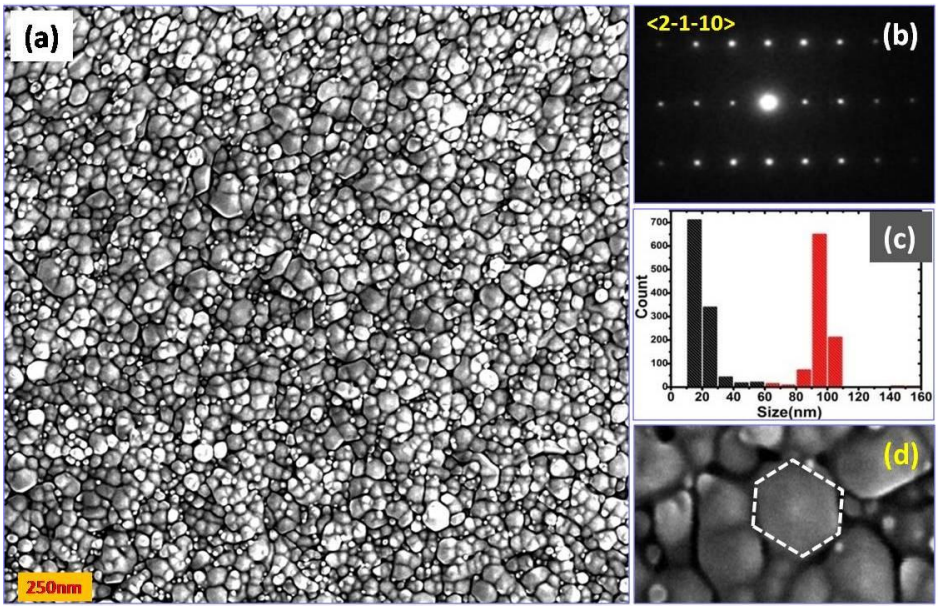

Fig 4.7: ***(a)*** *FE-SEM plan view image of AlN islands* ***(b)*** *the selective area electron diffraction of individual nanorods* ***(c)*** *The size distributions of pyramidal nanocolumns of AlN, showing a bimodal behavior.* ***(d)*** *Magnified region showing the morphology of pyramidal and oval apex of the nanocolumns.*

On the other hand, the small nano-features (ranging from 20-60nm) with oval apex could be formed by diffusion and nucleation mediated growth in the region between dislocations, with a relatively low growth rate as compared to the step assisted spiral growth[35] as will be shown later by TEM studies. It is important to note that the observed high density and closely packed nano-features suggest that the surface energy is higher on the amorphous crystal or polycrystalline phase of nitrided sapphire surface, enabling the high nucleation density as compared to that on the clean surface of sapphire, due to higher density of dangling bonds minimise the surface energy of clean sapphire[36].

To illustrate the growth mechanism of AlN nanocolumn formation on modified surface of sapphire, we have carried out TEM characterization in a two beam diffraction condition satisfying g.b≠0 where g-vector is perpendicular to burgers vector[37]. The select area electron diffraction (SAED) **(Fig. 4.8(a)inset)** confirms that the nanocolumns are single crystalline in nature with wurtzite crystal structure and the spread observed in the diffraction spots is attributed to misorientation in the nanocolumns with respect to c-direction. The low-

magnification cross-sectional bright-field and dark-field TEM image of AlN/Al_2O_3 interface is shown in **Fig. 4.8 (a-b)**, showing the overall morphology of the columns. Using two beam TEM diffraction contrast imaging, one can identify the axial threading dislocation in the bigger AlN nanocolumns along the nanocolumn growth c-direction as shown by arrows. It is clear that the axial threading dislocation propagates in the bigger AlN nanocolumns with g=0002, satisfying g.b≠0 where g-vector perpendicular to burgers vector i.e. c/2[38393733]. This clearly reveals that the growth mechanism underlying the formation of the bigger AlN nano-features is mediated by axial screw dislocations. It must be mentioned here that it is very difficult to have highly magnified and better contrast images because these nanocolumns are closely packed and are oriented in the same zone axis, matching to all AlN nanocolumns. The **Fig. 4.8 (c)** shows the smaller AlN nanocolumns without any dislocations and thus we attribute the growth of smaller nanorods to be diffusion mediated, between the dislocations mediated larger features.

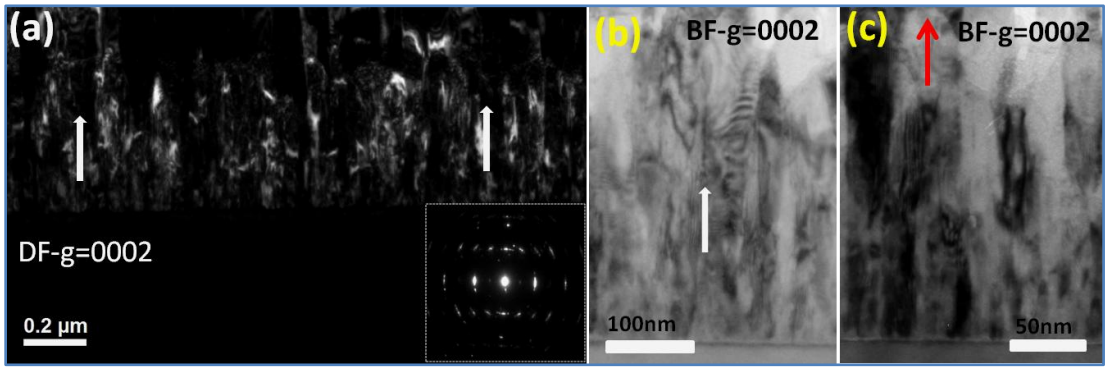

Fig.4.8: ***(a)*** *Cross-section TEM dark field image with g=0002 for different rods showing screw dislocations (marked as white arrow).* ***(b)*** *Cross-section TEM bright field image of larger AlN nanocolumns showing axial screw dislocation (marked as white arrow) with g=0002* ***(c)*** *Cross-section TEM bright field image of smaller AlN nanocolumns with g=0002.*

By relating **Fig. 4.7** and **Fig. 4.8**, we can infer that the nano features having the pyramidal apex have the orientation relationship [11-20] $_{AlN}$// [1-100] $_{sapphire}$ with sapphire, while the oval shaped islands possess the epitaxial relation [0002] $_{AlN}$// [0002] $_{sapphire,}$ suggesting a misfit dislocation density in the AlN/sapphire interface. The difference in the epitaxial relation of the two types of nano-features is consequence of the difference in the mechanism involved in AlN formation at the interface due to sapphire nitridation.

Cho *et al*[23] and some other groups[19,20,40,41] have observed the formation of a rough and polycrystalline AlN film after a few minutes of nitridation. We attribute the difference in

epitaxy of individual nano-features to the inhomogeneous AlN layer formed at the interface due to sapphire nitridation. **Fig. 4.9(a)** shows a FESEM micrograph of an amorphous AlN film with a region showing direct contact between the film and substrate. We reason that epitaxy between the sapphire substrate and the overgrown AlN film exists only in the direct contact region as shown in dotted rectangle. The presence of inhomogeneous protruded AlN islands on the nitrided surface of sapphire may restrict further diffusion of Al adatoms. This leads to a hindrance in the azimuthal rotation of the crystal lattice which is known to occur in order to reduce the lattice mismatch. Such behaviour eventually leads to a purely diffusion mediated growth with an onset of nanocolumnar growth which also show two separate epitaxial relations[40]. **Fig. 4.9(b-c)** shows the SAED patterns of pyramid-apexed AlN nanorods and sapphire substrate, and they were found to be in good agreement with the well known epitaxial relationship corresponding to 30^{o} in-plane rotation of AlN with respect to sapphire.

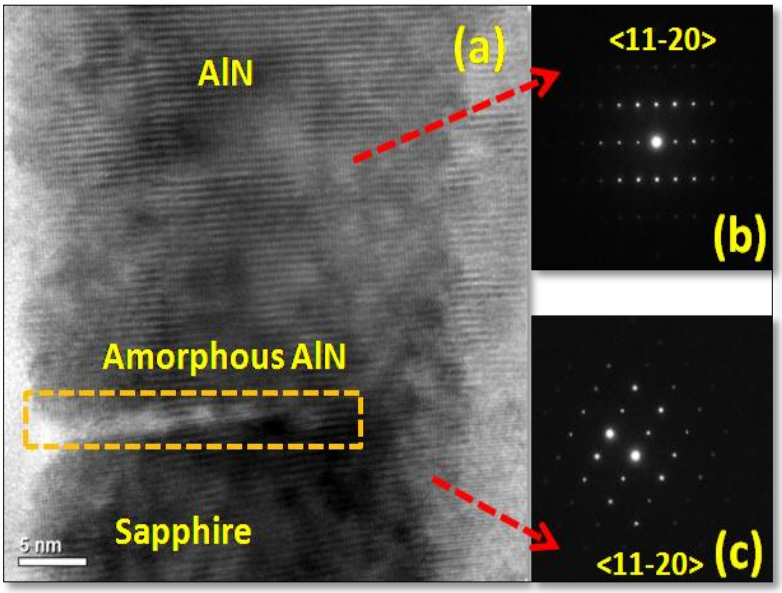

Fig.4.9: (a) *High resolution XTEM images acquired at the interface of a typical AlN nanorods/sapphire substrate showing amorphous region (marked as orange rectangle).* ***(b-c)*** *is the SAED pattern of individual AlN and sapphire substrate respectively.*

Until now we have discussed the optimized sapphire nitridation on which AlN islands are grown. XPS core level studies show a diffusion limited process of the conversion of Al_2O_3 into AlN, with a rate that saturates due to the AlN formed acting as a barrier for N* diffusion in AlN. Upon growth of a thin layer of AlN on the nitrided sapphire substrate,

bimodal c-oriented AlN nanocolumns are observed to be formed. The larger nanocolumns with pyramidal apex with axial screw dislocations are attributed to spiral growth that originate due to misfit at the interface. The smaller nanocolumns of AlN with oval apex are seen to be a consequence of the diffusion mediated nucleation growth, under N-rich conditions. However, both types of nanocolumns are seen to be single-crystalline, c–orientated and strain-relaxed with small difference in their in-plane rotation. We believe this nanocolumnar AlN film can be used as a seed for growing high quality 1-D GaN nanostructures.

4.5 Nitrogen plasma assisted nitridation of Si (111) surface:

We have now performed the nitrogen plasma nitridation experiments on Si (111) surface and corresponding growth sequence is shown below in **Fig. 4.10**.

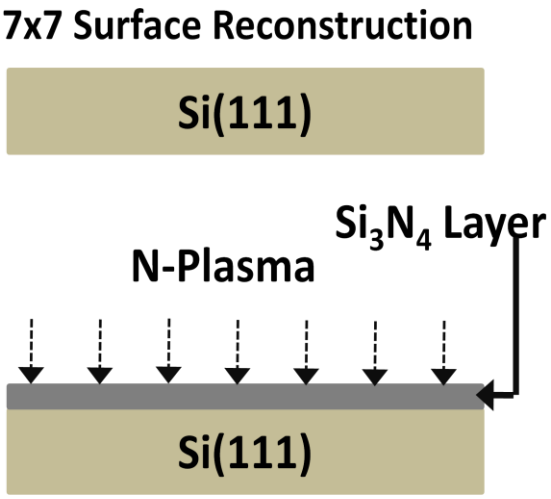

Fig.4.10: *Typical cleaning and growth sequence of Si(111) surface and nitrogen plasma assisted nitridation of Si(111)surface.*

Fig. 4.11 shows RHEED pattern acquired along the [11-2] azimuth of SiN_x formation on Si (111)-7x7 surfaces exposed to nitrogen rf-plasma for different exposure times. RHEED pattern (a) clearly shows the Si (111)-7x7 reconstruction with the occurrence of the (1/7) fractional spots and an envelope of crisscross Kikuchi lines, indicating that the surface is atomically clean. In the plasma condition utilized in this work, a two second N_2^* exposure of the Si (111)-7x7 surface results in the formation of single crystalline hexagonal β-Si_3N_4 (0001)-8x8/Si (111) surface **(Fig. 4.11(b))** with a faint (8/3x8/3) surface ordering,

corresponding to incommensurate surface arrangement of nitrogen adatoms, while the other spots completely disappear. On increasing exposure time from 2 to 8 seconds, RHEED pattern (c) is observed which consists of stronger, sharper and longer streaks which correspond to both (8x8) and (8/3x8/3) reconstructions[15,42,43]. This clearly suggests that, to have crystalline SiN_x one has tune the substrate temperature, exposure time and plasma condition, to obtain single crystalline β-Si_3N_4 (0001) on silicon substrate.

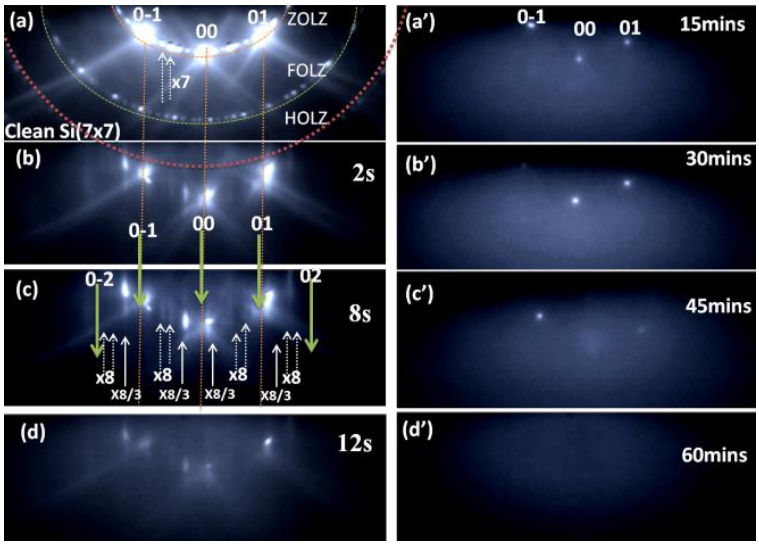

Fig.4.11: *Typical RHEED patterns of* ***(a)*** *clean Si (111)-7X7 surface and* ***(b-d)*** *are the 2, 8 and 12 sec, and* ***(a'-d')*** *are the 15 30 45 and 60mins of nitridation respectively, the patterns were acquired along [11-2] azimuth.*

At 12 seconds of exposure time, RHEED pattern **Fig. 4.11(d)** shows the prominent (8/3x8/3) reconstruction and dim spots of (8x8) ordering and low intensity bulk (-10), (00) and (10) spots. To study effect of higher nitrogen plasma, the silicon substrate was exposed to the plasma for 15, 30, 45 and 60 minutes. At 15, 30 and 45 minutes, only sharp spots corresponding to either (8x8) of SiN_x or (1x1) of Si are seen, with no other RHEED spots/streaks visible. RHEED corresponding to 15mins nitridation is shown in **Fig. 4.11(a').** With increase in exposure time to 60 minutes, the RHEED pattern **Fig. 4.11 (d')** becomes diffuse with no spots corresponding to (8x8) SiN_x or (1x1) Si visible suggesting the presence of an amorphous Si_xN_y layer. In an in-between stage we found the transition from crystalline Si_xN_y to amorphous phase at 45mins of nitridation and it is clearly visible in **Fig. 4.11(c')**. The (8/3x8/3) ordering of silicon nitride corresponds to nitrogen adatoms with 8X8 superstructure, which is characteristic of the β-Si_3N_4 (0001) phase[42,44].

To study the stoichiometry of the silicon nitride formed upon the nitridation of Si (111)-7x7 surfaces, XPS measurements are performed. The core-level spectra (CLS) of silicon and nitrogen are used to determine elemental composition and chemical bonding state of the nitrided Si (111) surface. The evolution of normalized CLS of Si2p peaks at 15mins and 60mins of nitridation is shown as a representative plot in the **Fig. 4.12(a)**, which consists of three deconvoluted peaks at 100.3eV, 101.3eV and 102.2 eV which are assigned to $Si^{1+,}$ Si^{3+} and Si^{4+} valence states after subtracting Si^{0} (bulk silicon) and SiO_2 contribution[45].

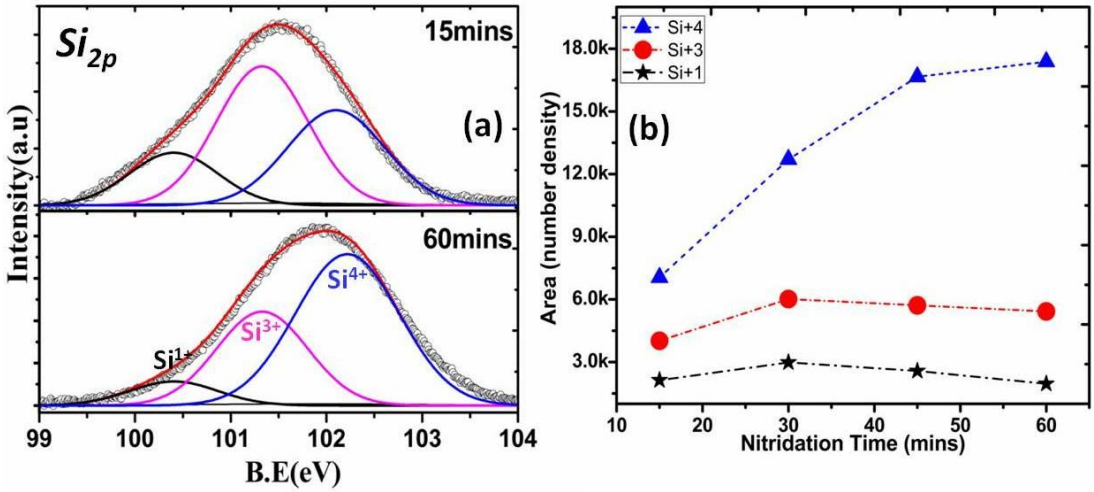

Fig.4.12: (a) *Representative deconvoluted core level photoelectron spectra of Si2p for 15 and 60mins nitridation of the Si (111) substrate.* ***(b)*** *shows plots of area under curve of* $Si^{1+,}$ Si^{3+} *and* Si^{4+} *state of deconvoluted core level spectra of Si2p for 15, 30, 45 and 60 minutes of nitridation, respectively.*

Fig.4.12(b) shows a plot of ratio of area under the peak corresponding to $Si^{1+,}$ Si^{3+} and Si^{4+} with respect to nitridation time and corresponding different states of nitrogen N1, N2, and N3 in the **Fig. 4.13(b)** with respect to exposure time. Though Si^{4+} state of silicon is expected in Si_3N_4, to obtain 2:1 coincidental match between β-Si_3N_4 (0001)-8x8 and Si (111)-7x7 at the interface, Si^{3+} , $Si^{2+}$and Si^{1+} oxidation states of silicon are also necessary[15,46–48]. Among all, we have not observed any Si^{2+} valence state at 100.8eV binding energy, which is ascribed to the atomically smooth abrupt and defect free interface, due to saturation of the interfacial bonds with the help of other valence state of Si as reported by Kim.et.al[46]. Lee.et.al[42] reported that the existence of Si^{1+} valence originates from the 8x8 reconstructed surface of SiN_x. The SiN_x surface shows two distinct reconstructions, with the upper region is 8/3x8/3

reconstructed and the lower is 8x8 reconstructed. Collectively, we suggest that Si^{1+} state is from both the reconstructed surface and the interface to have coincidental lattice matching. And the origin of Si^{3+} valence state corresponds to incomplete nitridation and structural defects at the interface of silicon nitride[49]. The non-uniform coverage of SiN_x with low exposure time can also result in the Si^{3+} state. The observed high value of B.E for Si^{4+} valence state can be attributed to either the core-hole screening effect or band bending at interface[46,50].

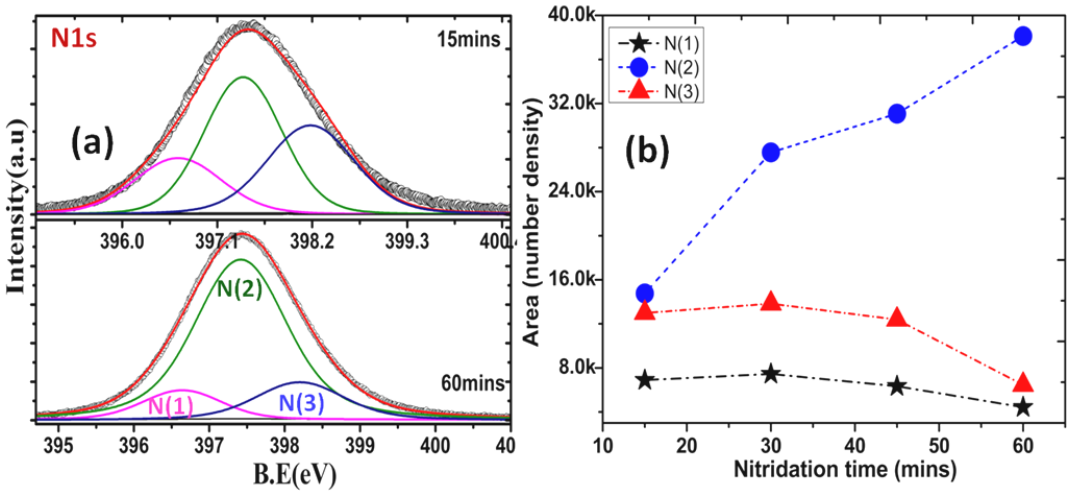

Fig.4.13: (a) *Representative deconvoluted core level photo-electron spectra of N1s for 15 and 60mins nitridation of the Si (111) substrate.* ***(b)*** *shows plots of area under curve of nitrogen N1, N2, and N3 state of deconvoluted core level spectra of N1s for 15, 30, 45 and 60 minutes of nitridation, respectively.*

The Si^{4+} oxidation state increases monotonically with N_2^* exposure time and Si^{3+} and Si^{1+} decreases beyond 30min with an increase in N_2^* exposure time. The increase in Si^{4+} component with decrease in S^{3+} and S^{1+} suggests the conversion of S^{3+} to S^{4+} state, leading to the formation of the more stable stoichiometric β-Si_3N_4 (0001). Intensity of Si2p CLS increases with N_2^* exposure time, upto 30mins suggesting incomplete coverage of SiN_x beyond which it saturates (complete coverage). Collectively it can be inferred that the saturation in intensity signifies that SiN_x layer formed beyond 30mins exposure time acts as a barrier for further nitridation. **Fig. 4.13(a)** shows the CLS of N1s which is de-convoluted into three peaks N1, N2 and N3 corresponding to binding energies 369.7eV, 397.4eV and 398.3eV, respectively[51,52]. The variation in nitrogen components N1, N2, and N3 with an increase in N_2^* exposure time is shown in the right panel of **Fig. 4.13(b)**, where N2 increases

and N1, N3 decreases with increase in N_2^* exposure time, showing that stoichiometric and stable β-Si_3N_4 is formed.

Fig. 4.14 shows an AFM image acquired on 5x5μm^2 of Si (111) surface which is exposed to nitrogen plasma for different times and also shown below each image is a line profile plot acquired over a solitary island. The rms roughness is observed to gradually increase from 35nm to 70nm with increase in exposure time from 15mins to 45mins, while at 60 minutes the rms roughness lowers down to 8.8nm. AFM image (5.4a) of Si (111) surface exposed to nitrogen plasma for 15 minutes has SiN_x islands with an average size 250nm, height 25nm and density of 1.7x10^{9}cm^{-2}. The line profile acquired over an individual bright spot/island denotes a dual step like profile with step height difference of 5nm as shown in **Fig. 4.14 (a')**.

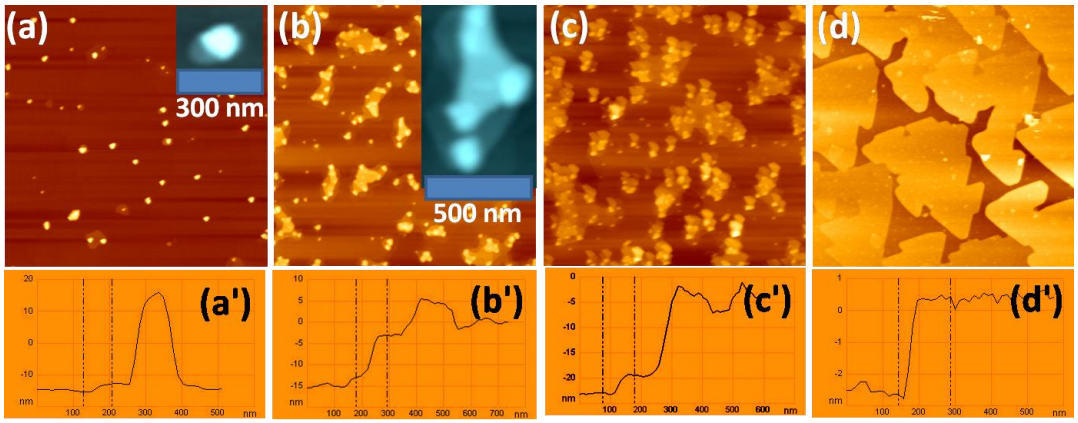

Fig.4.14: *The AFM images (a, b, c and d) acquired over an area 5 × 5 μm^2 on Si (111) surface nitrided at 15, 30, 45 and 60mins respectively, also representative line profile plots acquired over a solitary island is shown below each image.*

A magnified image is shown as inset of **Fig. 4.14(a)**, to probe the details on the surface of an individual island. The observed island is in shape of equilateral triangle with sides of 150nm on a flat 2D wetting layer. These triangular nano-crystals appear to be exclusively formed at the step edges of Si (111) surface with slight misalignment in their crystallographic directions and further nitridation (i.e. 30mins) leads to the growth of SiNx on terrace area of Si surface. Since at the step edges fewer bonds have to break than nitridation embedded in the terrace region, thus the initial nitridation occurs at step edges as shown in **Fig. 4.14(a)**. On doubling the exposure time to 30 minutes AFM image **Fig. 4.14 (b)** shows a relatively large sized SiN_x islands over Si (111) surface than those formed at

lower exposure time. The island density is $2.7x10^{9}$ cm^{-2} and average width is 800nm and height 35 nm.

It appears form the image **Fig. 4.14(b)** that the density of bright spots increases with increase in exposure time (with 2-D layer wetting below them). The line profile acquired over an individual 800nm sized island with multiple bright spots shows multiple steps each of 5nm height, and also suggests that a single large island consists of multiple small islands each of thickness of 5nm **Fig. 4.14(b)**. A magnified image of one such large island is shown as inset of **Fig. 4.14(b)**, which is a layered structure with two or more triangular layers of dimension around 150nm embedded. It also appears to be multilayer arrangement of triangles grown atop each other. The topmost layer has three smaller triangles facing in the same direction and the larger triangle beneath are oriented opposite to them. The misalignment in the in-plane growth direction can be attributed to preferential growth directions [11-2], [1-21] and [-211] in which SiN_x can grow. Depending on the growth velocity in a particular direction, shape of equilateral triangles can change to scalene triangles. Previous STM studies of SiN_x films suggest that because of three fold symmetry, the triangular islands are faceted along <11-2> principal axes[15], Only two types of triangles rotated by 30° with respect to each other are possible. The SiN_x triangular nano-crystals seems to adhere preferentially on upper, lower and across steps edges with slight misalignment in their crystallographic directions, which appears to be due to a dislocation mediated spiral growth. At certain film thickness Si^{4+} valence state is the prominent state to have stoichiometric SiN_x. It was mentioned earlier that to have coincident lattice matching between SiN_x/Si, both Si^{+} and $S1^{3+}$ valence states are required at the interface. The conversion of Si^{+} and $S1^{3+}$ to Si^{4+} with respect to exposure time changes the bonding configuration at the interface. The changed bonding arrangement generates stress at the interface, that will relaxed by the generation of dislocations. Upon further nitridation, dislocations drive permanent new step edges for further crystal growth and the resulting SiN_x film grows laterally on the screw dislocation cores. Eventually, all the islands coalesce with each other leading to bunching and merging. The growth proceeds by steps spiraling around screw dislocations which act as nucleation pinning centres around the triangular edge of the islands. The continuous growth loop bowing around the spiral steps due to higher coverage leads to 2-D morphology as seen in **Fig. 4.14(d)**. When N_2^{*} exposure time is increased to 45 minutes, the surface as seen in the

AFM image (**Fig.4.14(c)**) consists of islands with sizes ranging from 0.8 to 1.5µm and density of $2.9x10^{9}cm^{-2}$. Compared to the film grown after low plasma exposure times, the current film has reduced protruding features. The islands were observed to be multilayered and triangular in shape with irregular side faces comprising of coalesced smaller triangles. The line profile across the individual island shows a 5nm multi- steps as shown in **Fig. 4.14(c')**, with the bottom layer 15nm deeper than the top most layers. The silicon surface exposed to N_2^* 60 min **(Fig. 4.14(d))** consist of smooth 1 to 3µm sized islands with flatter terraces and steps, while the island density decreases to $4.4x10^{8}$ cm^{-2}. Clearly, **Fig.4.15** shows the variation in surface roughness and island density with respect nitridation time. It is clear that the roughness of the Si(111) surface increases upto 45mins of nitridation after which the surface become smooth as the island density also reduces.

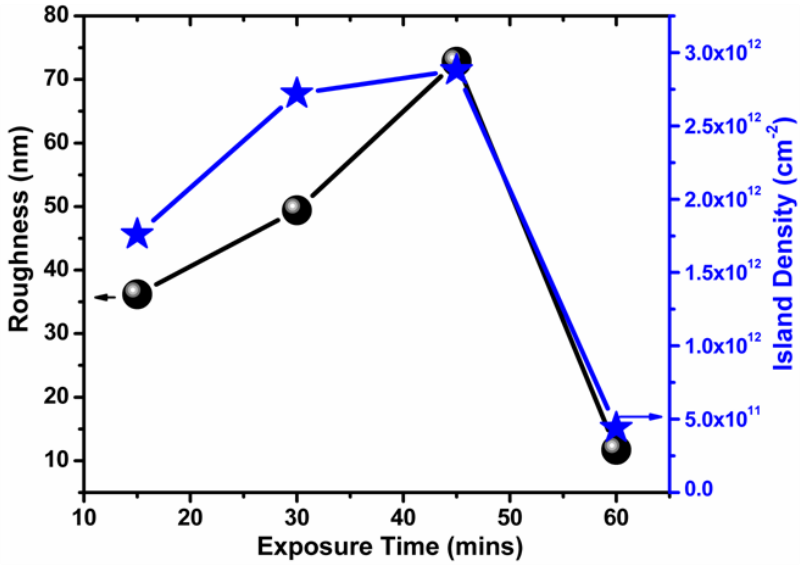

Fig.4.15: *Show the variation of surface roughness and island density in alternative y-axis's at different nitridation time.*

After discussing structure, stoichiometry and morphology, we now look into the valence and conduction band offset (VBO and CBO) between Si and SiN_x. The **Fig. 4.16(a)** shows the valence band spectra of SiN_x on Si (111) surface that is obtained for 30mins of nitrogen plasma exposure. It is clearly visible that there two slope changes at the point (A) and (B), the slope change at point (A) correspond to valence band maximum of Si (111) and the (B) corresponds to valence band maximum of SiN_x. **Fig. 4.16(b)** Shows the variation in VBO and CBO with respect to nitridation time. By using valance band spectra, we can

measure valence band offset between Si and SiN_x. On considering the band gap of Si =1.1 eV and β-Si_3N_4 =5.3 we have estimated the CBO. **Fig. 4.16(b)** plot of VBO of y-axis and CBO on alternate y-axis with respect to plasma exposure time from 15 to 60mins along with valence band spectra of sample exposed for 30mins as shown in **Fig. 4.16(a)**. The VBO increases from 1.78 eV to 1.91 eV and CBO decreases from 2.42 eV to 2.29 eV with increase in exposure time from 15 mins to 60 mins. The VBO=1.81eV and CBO=2.39eV for film exposed for 30mins, agrees with the value estimated both theoretically and experimentally[42].

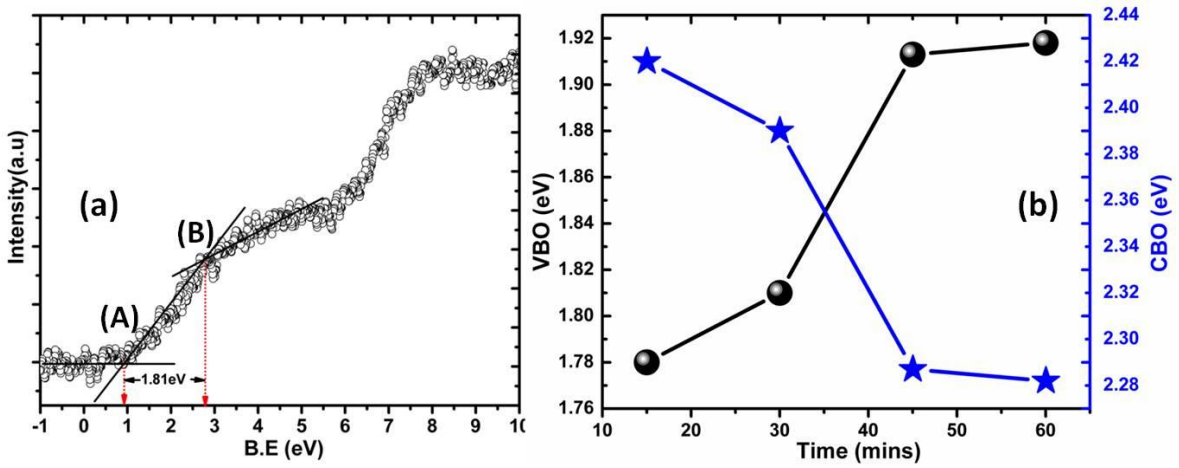

Fig.4.16: *The representative plot of Valence band spectra of nitrided surface of Si (111) surface for 30mins nitridation. (b) The plot of CBO and VBO with respect to nitrogen plasma exposure time.*

The variation in VBO with nitrogen plasma exposure time is due to variation in film thickness which leads to change in stoichiometry of SiN_x. Since the sub-stoichiometric interface has undesired oxidation state of Si^{4+} Si^{3+} and Si^{1+}. The valence state of Si varies because change in bonding sequence as well as coordination number variation leading to change in dipole moment as well as band bending at the interface. Thus, change in oxidation state at the interface leads to change in bonding sequence which counters the chemical shift of Si resulting in band offset of the interface. We suggest that the lattice mismatch induced stress modifies the dipole moment through depolarization at the interface, as thickness of SiN_x layer increases with respect to nitridation time, and the consequence effect will lead to change valence band alignment at SiN_x and Si (111) interface. Thus, the change in VBO with respect to plasma exposure is followed by interfacial bond formation and band bending

which result in the VBO variation with nitridation time. **Fig.4.17** is the representative band diagram of sample which is nitrided for 30mins.

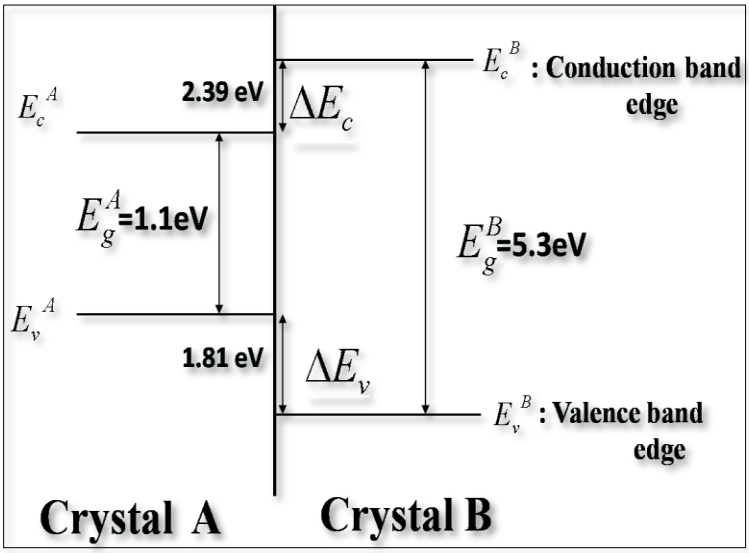

Fig.4.17: *The representative band diagram of nitrided surface of Si (111) surface for 30mins nitridation.*

4.6 Summary:

In summary, we have performed controlled sapphire nitridation experiments to identify the optimal nitridation process. XPS core level studies show a diffusion limited process of the conversion of Al_2O_3 into AlN, with a rate that saturates due to the AlN formed acting as a barrier for N* diffusion in AlN. Upon growth of a thin layer of AlN on the nitrided sapphire substrate, bimodal c-oriented AlN nanocolumns are observed to be formed. The larger nanocolumns with pyramidal apex with axial screw dislocations are attributed to spiral growth that originate due to misfit at the interface. The smaller nanocolumns of AlN with oval apex are seen to be consequence of diffusion mediated growth, under N-rich conditions. However, both types of nanocolumns are seen to be single-crystalline, c – orientated and strain-relaxed with difference in their in-plane rotation. We believe this nanocolumnar AlN film can be used as a seed for growing high quality 1-D GaN nanostructures.

We have also discussed the surface nitridation of the Si(111) plane by nitrogen plasma exposure. The study of Si (111) nitridation suggests that with exposure time, island

density gradually increases and the Si^{4+} oxidation state increases monotonically with N_2^* exposure time and Si^{3+} and Si^{1+} decreases. The increase in Si^{4+} component with decrease in S^{3+} and S^{1+} suggests the conversion of S^{3+} to S^{4+} state, leading to the formation of the more stable stoichiometric β-Si_3N_4 (0001). Our AFM image reveals that the beyond 30mins of nitridation, newly formed islands coalesce to form a flat SiN_x. And also we have observed that the 2-D layer beneath and on top of that SiN_x triangular nano-crystals formed and theses islands are pinned at the triangular corner by dislocation which appears to be due to a dislocation mediated spiral growth due to changing g bonding configuration. Upon further nitridation, dislocations drive permanent new step edges for further crystal growth resulting in the SiN_x film growing laterally on the screw dislocation cores, and further the continuous growth loop bowing around the spiral steps due to higher coverage leads to 2-D morphology. The electrical properties of the interface yield a VBO (Valence Band Offset) around 1.8eV and CBO (Conduction Band Offset) around 2.4 eV are estimated for SiN_x/Si interface, which is in agreement with literature values. The variation in VBO with nitrogen plasma exposure time is due to sub-stoichiometric interface and due to presence of oxidation state of Si^{4+} Si^{3+} and Si^{1+} followed by interfacial bond formation and band bending.

4.7 REFRENCES:

1. A. H. Mueller, M. A Petruska, M. Achermann, D. J. Werder, E. A Akhadov, D. D. Koleske, M. A Hoffbauer, and V. I. Klimov, *Nano Lett.*, 2005, **5**, 1039–44.

2. S. Fernández-Garrido, X. Kong, T. Gotschke, R. Calarco, L. Geelhaar, A. Trampert, and O. Brandt, *Nano Lett.*, 2012, **12**, 6119–25.

3. K. Zeng, J. Lin, and H. Jiang, *Appl. Phys. …*, 1997, **71**, 1368–1370.

4. C. Heinlein, J. Grepstad, T. Berge, and H. Riechert, *Appl. Phys. Lett.*, 1997, **71**, 341.

5. B. Agnarsson, M. Göthelid, S. Olafsson, H. P. Gislason, and U. O. Karlsson, *J. Appl. Phys.*, 2007, **101**, 013519.

6. M. Kesaria, S. Shetty, and S. M. Shivaprasad, *Cryst. Growth Des.*, 2011, **11**, 4900–4903.

7. S. Shetty, M. Kesaria, J. Ghatak, and S. M. Shivaprasad, *Cryst. Growth Des.*, 2013, **13**, 2407–2412.

8. S. Mikroulis, A. Georgakilas, A. Kostopoulos, V. Cimalla, E. Dimakis, and P. Komninou, *Appl. Phys. Lett.*, 2002, **80**, 2886.

9. D. Huang, M. A. Reshchikov, P. Visconti, F. Yun, A. A. Baski, T. King, H. Morkoç, J. Jasinski, Z. Liliental-Weber, and C. W. Litton, *J. Vac. Sci. Technol. B Microelectron. Nanom. Struct.*, 2002, **20**, 2256.

10. a Yoshikawa and K. Xu, *Thin Solid Films*, 2002, **412**, 38–43.

11. B. Alloing, S. Vézian, O. Tottereau, P. Vennéguès, E. Beraudo, and J. Zuniga-Pérez, *Appl. Phys. Lett.*, 2011, **98**, 011914.

12. M. Losurdo, P. Capezzuto, and G. Bruno, *J. Appl. Phys.*, 2000, **88**, 2138.

13. T. Hashimoto, Y. Terakoshi, M. Yuri, M. Ishida, O. Imafuji, T. Sugino, and K. Itoh, *J. Appl. Phys.*, 1999, **86**, 3670.

14. Z. Xu, L. Zhang, H. He, J. Wang, and M. Xie, *J. Appl. Phys.*, 2011, **110**, 093514.

15. C.-L. Wu, J.-L. Hsieh, H.-D. Hsueh, and S. Gwo, *Phys. Rev. B*, 2002, **65**, 045309.

16. C. Youtsey, L. T. Romano, and I. Adesida, *Appl. Phys. Lett.*, 1998, **73**, 797.

17. T. Yamashita, S. Hasegawa, S. Nishida, M. Ishimaru, Y. Hirotsu, and H. Asahi, *Appl. Phys. Lett.*, 2005, **86**, 082109.

18. P. Kumar, M. Tuteja, M. Kesaria, U. V. Waghmare, and S. M. Shivaprasad, *Appl. Phys. Lett.*, 2012, **101**, 131605.

19. F. Dwikusuma and T. F. Kuech, *J. Appl. Phys.*, 2003, **94**, 5656.

20. G. Namkoong, W. A. Doolittle, A. S. Brown, M. Losurdo, P. Capezzuto, and G. Bruno, *J. Appl. Phys.*, 2002, **91**, 2499.

21. M. Losurdo, P. Capezzuto, G. Bruno, G. Namkoong, W. A. Doolittle, and A. S. Brown, *J. Appl. Phys.*, 2002, **91**, 2508.

22. M. Yeadon, M. T. Marshall, F. Hamdani, S. Pekin, H. Morkoç, and J. M. Gibson, *J. Appl. Phys.*, 1998, **83**, 2847.

23. Y. Cho, Y. Kim, E. R. Weber, S. Ruvimov, and Z. Liliental-Weber, *J. Appl. Phys.*, 1999, **85**, 7909.

24. F. Dwikusuma and T. F. Kuech, *J. Appl. Phys.*, 2003, **94**, 5656.

25. Y. Cho, Y. Kim, E. R. Weber, S. Ruvimov, and Z. Liliental-Weber, *J. Appl. Phys.*, 1999, **85**, 7909.

26. F. Dwikusuma and T. F. Kuech, *J. Appl. Phys.*, 2003, **94**, 5656.

27. K. Uchida, A. Watanabe, F. Yano, M. Kouguchi, T. Tanaka, and S. Minagawa, 1996, **79**, 3487–3491.

28. F. Widmann, G. Feuillet, B. Daudin, J. L. Rouvie, and I. Introduction, 2000, **85**, 1550–1555.

29. M. Kesaria, S. Shetty, and S. M. Shivaprasad, *J. Cryst. Growth*, 2011, **326**, 191–194.

30. M. Kesaria, S. Shetty, P. I. Cohen, and S. M. Shivaprasad, *Mater. Res. Bull.*, 2011, **46**, 1811–1813.

31. S. Jin, M. J. Bierman, and S. A. Morin, *J. Phys. Chem. Lett.*, 2010, **1**, 1472–1480.

32. S. A Morin and S. Jin, *Nano Lett.*, 2010, **10**, 3459–63.

33. D. Cherns, L. Meshi, I. Griffiths, S. Khongphetsak, S. V Novikov, N. R. S. Farley, R. P. Campion, and C. T. Foxon, *Appl. Phys. Lett.*, 2008, **93**, 111911.

34. B. W. Jacobs, M. A Crimp, K. McElroy, and V. M. Ayres, *Nano Lett.*, 2008, **8**, 4353–8.

35. T. Akasaka, Y. Kobayashi, and M. Kasu, *Appl. Phys. Lett.*, 2010, **97**, 141902.

36. Y. Wang, X. L. Du, Z. X. Mei, Z. Q. Zeng, M. J. Ying, H. T. Yuan, J. F. Jia, Q. K. Xue, and Z. Zhang, *Appl. Phys. Lett.*, 2005, **87**, 051901.

37. D. Cherns, L. Meshi, I. Griffiths, S. Khongphetsak, S. V Novikov, N. Farley, R. P. Campion, and C. T. Foxon, *Appl. Phys. Lett.*, 2008, **92**, 121902.

38. D. Cherns, L. Meshi, I. Griffiths, S. Khongphetsak, S. V. Novikov, N. R. S. Farley, R. P. Campion, and C. T. Foxon, *Appl. Phys. Lett.*, 2008, **93**, 111911.

39. D. Cherns and Y. Sun, *Appl. Phys. Lett.*, 2008, **92**, 051909.

40. S. Shetty, J. Ghatak, and S. M. Shivaprasad, *Solid State Commun.*, 2014, **180**, 7–10.

41. T. Hashimoto, Y. Terakoshi, M. Ishida, M. Yuri, O. Imafuji, T. Sugino, A. Yoshikawa, and K. Itoh, *J. Cryst. Growth*, 1998, **189-190**, 254–258.

42. H.-M. Lee, C.-T. Kuo, H.-W. Shiu, C.-H. Chen, and S. Gwo, *Appl. Phys. Lett.*, 2009, **95**, 222104.

43. J. Sook Ha, *J. Vac. Sci. Technol. B Microelectron. Nanom. Struct.*, 1997, **15**, 1893.

44. H. Ahn, C.-L. Wu, S. Gwo, C. Wei, and Y. Chou, *Phys. Rev. Lett.*, 2001, **86**, 2818–2821.

45. M. Kumar, B. Roul, T. N. Bhat, M. K. Rajpalke, P. Misra, L. M. Kukreja, N. Sinha, A. T. Kalghatgi, and S. B. Krupanidhi, *Mater. Res. Bull.*, 2010, **45**, 1581–1585.

46. Y. Kim, H. Lee, H. Yeom, D.-Y. Ryoo, S.-B. Huh, and J.-G. Lee, *Phys. Rev. B*, 2004, **70**, 165320.

47. M. Yoshimura, *J. Vac. Sci. Technol. B Microelectron. Nanom. Struct.*, 1996, **14**, 1048.

48. X. Xu, S.-Y. Kang, and T. Yamabe, *Phys. Rev. Lett.*, 2002, **88**, 076106.

49. H.-M. Lee, C.-T. Kuo, H.-W. Shiu, C.-H. Chen, and S. Gwo, *Appl. Phys. Lett.*, 2009, **95**, 222104.

50. J. Kim and H. Yeom, *Phys. Rev. B*, 2003, **67**, 035304.

51. T. N. Bhat, M. K. Rajpalke, B. Roul, M. Kumar, and S. B. Krupanidhi, *J. Appl. Phys.*, 2011, **110**, 093718.

52. H. Lee, C. Kuo, H. Shiu, C. Chen, and S. Gwo, *Appl. Phys. Lett.*, 2009, **95**, 222104.

Chapter 5

Role of Intermediate Layer on Evolution of GaN Films

5. Role of Intermediate Layer on the Evolution of GaN Films on c-Sapphire and Si (111) Surfaces:

5.1 Introduction:

As discussed earlier, due to lack of lattice and thermal expansion matched substrates, 2-D GaN films grown on available substrates exhibit high dislocation and stacking fault densities deteriorate the efficiency of devices, especially at high injection currents. To overcome these issues, several schemes have been adopted namely, buffer layer, nanostructures, surface modification and intermediate layer formation. Since nanostructure arrays of GaN can help in miniaturization and fabrication of high efficiency optoelectronic and high-power electronic devices[1], utilizing their defect free and strain relaxed benefits also offer confinement related novel property tunability[2]. Several groups have employed AlN as an intermediate layer to obtain flat films and we have shown that kinetically controlled growth[3] on bare sapphire utilize interfacial dislocations to promote nanowall and nanorod formation. AlN having lattice parameter of a=b=0.3112nm and c= 0.4982nm and is iso-structural to GaN, provide a very good interfacial layer. A lattice mismatch of 12% with sapphire and 3% with GaN enables a less strained growth. However, the role of an intermediate AlN layer is effectively controlling columnar growth is poorly understood at present[4–7]. Though buffer and intermediate layer have been used in literature synonymously, we treat this surface modification by a thin AlN layer as an intermediate layer.

In this chapter, we describe the way we have made use of a nanostructured AlN intermediate layer that promotes the growth of high quality low dimension GaN nano-features. We have addressed the effect of pre-formed (a) ultra-thin AlN layer formed by plasma nitridation and (b) a thin AlN intermediate layer, on the spontaneous formation of aligned GaN nanostructures on both Si and c-Al_2O_3 surface. The density, diameter and aspect ratio of the nanocolumns is shown to be strongly influenced by the nature and morphology of the AlN intermediate layer. Morin et al[8] have explained the mechanism of the nanorods (NRs) and nanotube (NT) formation to be due to total energy minimization, based on the concept by Frank[9]. On the other hand, 2-D and 3-D nanostructures of GaN grown on Si (111) substrates are viewed as one of the most potential candidates for device applications. It has

been reported earlier [10,11] that 3-D growth is the dominant mode on Si substrate due to its large lattice and thermal expansion mismatch with GaN while a few research groups have reported the successful 2-D growth of GaN on Si substrate by using AlN intermediate layers. To date, GaN growth has been carried out using the AlN buffer layer approach, which is known to yield the best quality film[12–15]. The defect-induced yellow luminescence (YL) was commonly observed even in these cases, adversely affecting the optical properties of GaN and downgrading the film for optoelectronic device purposes. The mutual solubility of Al and Si is also not negligible at the intermediate layer growth temperature (~820°C versus eutectic temperature 577°C). Therefore, inter-diffusion of Al and Si at the interface can be severe, resulting in high unintentional doping levels in the epilayers and Si substrates[16]. To overcome this serious drawback, an alternative to AlN growth it has been demonstrated that a silicon nitride buffer layer can be effectively used for the GaN growth[12,17–21]. In this chapter, we demonstrate the growth of high quality 2-D and nanostructure GaN films on nitrided surface (intermediate SiN_x layer) of Si (111). We have then also explored the crystal quality and other properties of the GaN films thus formed.

In our study, by complementary information from Reflection High Energy Electron Diffraction (RHEED), Field Emission Scanning Electron Microscope (FESEM), Transmission Electron Microscopy (TEM), X- ray Diffractometer (XRD), X-ray Photoelectron Spectroscopy (XPS) and Cathodo-Luminescence (CL), we provide evidence for the dislocation mediated growth of these spontaneously formed nanostructures yielding high structural and optical quality GaN films.

5.2 Experimental Section:

(A) The Substrates were thermally degassed in the preparation chamber for 30 min at 500°C followed by 10 min annealing at 800 °C in the growth chamber and then ramped down to the desired growth temperature. GaN films are grown on three differently modified substrates to study the effect of the interface. Sample (A) is a 0.7μm thick GaN film grown on bare c-plane sapphire held at 730°C, Sample (B) is a 1μm GaN film grown at 730°C on 6-hrs pre-nitrided c-plane sapphire substrate, and sample (C) is a 1μm GaN film grown at 730°C on 6-hrs pre-nitrided c-plane sapphire on which 0.25μm AlN layer is grown at 700°C. Surface structure is monitored *in situ* by RHEED during every stage of film growth.

Morphological, structural and optical properties have been investigated by several complementary techniques as described earlier.

(B) (I) Nitridation of Si (111) surface is done at substrate temperature 750^{o}C and exposure time 15, 30, 45 and 60mins with 4.5sccm nitrogen flow respectively. After nitridation on the same sample we have grown 2hrs GaN at 4.5sccm with 750^{o}C substrate temperature respectively. (II) Nitridation of Si (111) surface is done at substrate temperature 750^{o}C a) 10mins of Ga deposition and 10mins of nitridation on Si(111)7x7 surface, b) after 10sec c) 20sec Si(111), d) 30sec nitrided surface of Si(111) with 4.5sccm nitrogen flow respectively. After surface nitridation we have grown GaN at 650^{o}C substrate temperature with 4.5sccm nitrogen flow on same sample.

5.3 Role of intermediate layer in the morphological evolution of GaN films on sapphire:

On the unmodified (Sample A) and the two modified surfaces (Sample B and C), 2hrs of GaN (0.7µm) was grown by MBE with conditions defined earlier. ***Fig.5.1*** **(a)-(b)** are the plan view FE-SEM images and the corresponding RHEED pattern for samples A and B respectively.

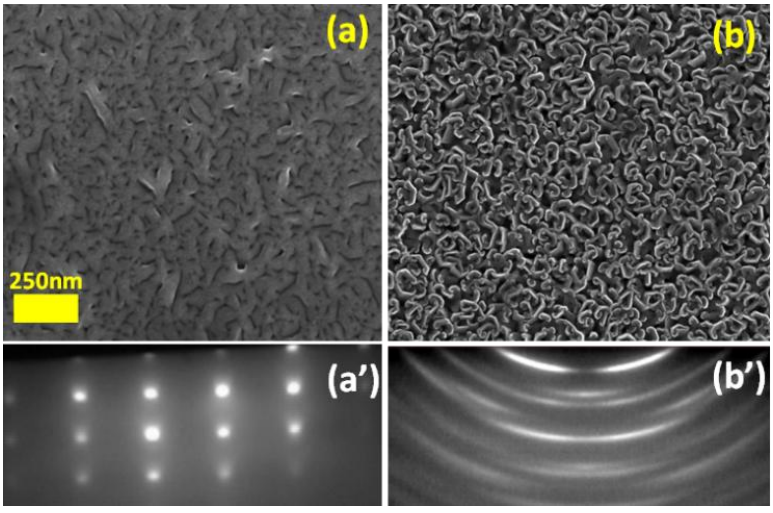

Fig.5.1: *Plan view FE-SEM image of* ***(a)*** *0.6µm thick GaN film grown on bare c-plane sapphire at 730^{o}C substrate temperature (sample A);* ***(b)*** *1µm GaN film on pre-nitrided c-plane sapphire substrate (sample B) and (a'-b') show the RHEED pattern acquired along <11-20> direction for Samples A and B. Scale bar corresponds to* ***250nm*** *in all FESEM images.*

Fig. 5.1*(a)** shows the plan view of a 0.7μm GaN film grown on (Sample A) clean c-plane sapphire substrate. The image shows the formation of a flat 2D GaN film, with rms roughness of ≈20nm (measured by AFM) with threading dislocation defect density estimated to be ~10^{10}cm^{-2}. The post-GaN deposition RHEED pattern (Fig 5.1(*a')**) taken along the <11-20> direction, consists of spots, characteristic of a transmission pattern through the rough surface formed by the 1-D features. The ratio of the distance between the hexagonally arranged spots in the horizontal and vertical directions is ≈1.87, equivalent to c/a≈1.62, confirming the GaN film has single crystalline wurtzite structure. ***Fig 5.1*(b)** shows the morphology of the 1μm GaN film grown on 6-hrs pre-nitrided surface of sapphire substrate (Sample B). The top-view FESEM image of this GaN film consist of densely-packed c-shaped (petal-like) nanostructures of sizes ranging from 40 to 120nm, with approximate density of ~5x10^{9}cm^{-2}. This morphology also suggests that the GaN features formed are dependent on the threading dislocations. Two proximal screw dislocations with similar Burger vectors appeared to be pinned with opposite screw-sense aligning the atomic steps like in a Frank-Read mode. The deposition on those bowed steps enables the nucleation and continuous spiral propagation around the two screw dislocations and the step joining them yielding the petal-like morphology in the plan view. The proximity between the dislocations appears to determine the different diameters of the nanopetals observed. ***Fig 5.1*(b')** is the RHEED pattern of this film that shows intensity modulated circular arcs, reflecting some form of disorder in the GaN film. The ratio of distance along the horizontal and vertical directions between the centres of the arcs of the pattern is ≈1.86, which again correspond to c/a ≈1.62 ratio of wurtzite GaN. Our XRD and SAED results (which will be discussed later) show high single-crystallinity of the individual nano-features. Thus, the elongated RHEED spots can be attributed to an orientational disorder of the c-shaped nanostructures. Since the cross-section SEM (**Fig.5.2d**) show reasonable vertical alignment of the nanorods formed (which has the C-shaped cross section shape at the top) the orientation disorder is observed in the plan view (**Fig.5.2a**), which results in the circular arcs in the RHEED pattern. ***Fig. 5.2*(a)** displays the morphology of Sample (C) where GaN film was grown on the AlN intermediate layer. The image exhibits relatively less dense c-shaped 1-D structures in comparison to *Sample B* and the size of these features vary from 50-160nm. The histogram in **Fig 5.2(c)** clearly shows that the diameter of the nano-features are distributed in size range of 50-

160nm, with most of the nanorods has diameter in the range of 80-90nm. The cross-sectional FE-SEM image (**Fig. 5.2(d)**) clearly shows that the nano-features are columnar. Amidst solid hexagonal nanorods (NRs), there are also nanotubes (NTs) and partially formed hexagonal c-shaped tubes (NCTs) present in *Sample C* that are different from the nanopetals seen for sample B. However, careful analysis of the top view of the FE-SEM image (***Fig. 5.2*(a)**) shows that GaN nano-features have a hexagonal cross-section with the solid rods with density $\approx 4*10^8/cm^2$ are m-faceted while the hollow and c-shaped tubes with density $\approx 8*10^8/cm^2$ are a-bound. This evidence of m- and a-faceted nano-features by FESEM may be corroborated with the set of intense RHEED spots that are less elongated as circular arcs (***Fig. 5.2*(b)**).

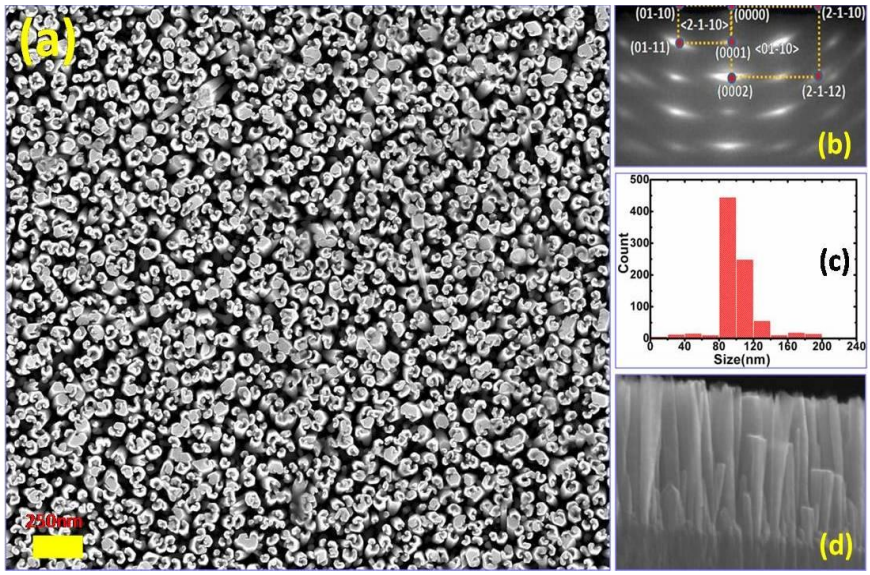

Fig.5.2: *Plan view FE-SEM image of* ***(a)*** *1μm GaN film/0.25μm AlN/pre-nitrided c-plane sapphire substrate (sample C) and their RHEED pattern* ***(b)*** *acquired along <11-20> direction.* ***(c)*** *Plot of size distribution 1D nanostructures* ***(d)*** *Cross-section image of nanostructures. Scale bar corresponds to* ***250nm*** *in all FESEM images.*

In case of *Sample B,* the RHEED pattern from the film has an additional set of arcs, whereas the same for *Sample C* consists of spots that are in addition to those for a single phase wurtzite. The spacing between these arcs and elongated spots is equivalent to typical spotty RHEED observed in the [10-10] azimuth, and thus the overlap of the two pattern indicates that these 1-D GaN features are of two types with distinct epitaxial relation with sapphire, namely AlN (10-10)// Al_2O_3 (10-10) and AlN (10-10)// Al_2O_3 (11-20), achieved by 30^0 in-plane rotation, which is also visible in the FESEM image ***Fig. 5.2*(a).** Calculated inter-planar

distance of (10-10) and (11-20) planes along <11-20> direction is 0.274 and 0.1581nm and the respective unit cells along <10-10> and <11-20> directions are marked by dotted lines in ***Fig. 5.2*(b).**

We probe further the structural properties by XRD. ***Fig. 5.3***(a) shows the Θ-2Θ vs log of intensity scan of XRD pattern of the GaN films A, B and C. The peaks that appears at 2Θ =34.59°, 72.96° for film A and 2Θ =34.55°, 72.84° for films B and C, are indexed as (0002), (0004) Bragg reflections of GaN. The intense peaks at 2Θ =41.68° observed in all the three films are indexed as (0006) and the weak peak at 37.7° does not belong either to GaN or sapphire.

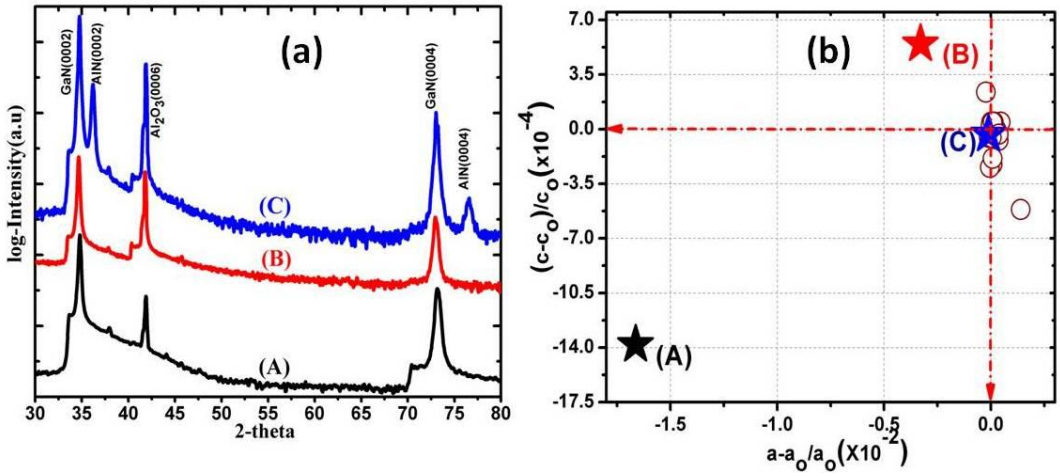

Fig.5.3: (a) *XRD patterns and* ***(b)*** *plots the strain along in-plane (a-axis) and out of plane (c-axis) for samples A, B and C. Open circles in* ***(b)*** *correspond to relative strains for GaN grown on different substrate from the literature.*

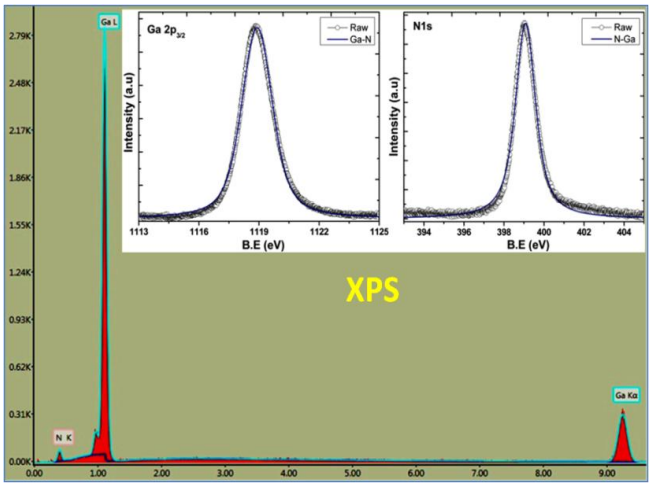

Fig.5.4: *EDAX and XPS spectra taken for sample (C) that confirms formation of GaN layer.*

We have also performed detailed XPS studies of the GaN surface. The spectra of Ga (2p) and N (1s) core level clearly provides evidence for stoichiometric GaN film formation as shown in **Fig. 5.4.** The additional XRD peaks observed at 2Θ =36.01°, 76.38° for sample C are indexed as originating due to (0002), (0004) planes of AlN. The absence of any other peaks confirms the single wurtzite phase of the films. ***Fig. 5.3*** **(b)** displays the c-plane strain ($\frac{c-c_o}{c_0}$), calculated for GaN films from (0002) reflection as -1.38x10^{-3}, 5.46x10^{-4} and -5.27x10^{-5} and in-plane strain ($\frac{a-a_o}{a_0}$) as -1.66x10^{-2},-3.29x10^{-3} and -9.06x10^{-5} for samples A, B and C respectively, with respect to the bulk a-and-c lattice parameters a = 3.18926 Å and c = 5.18523Å[22] . Open circles in inset (b) correspond to strain values that are calculated from a- and c-lattice parameters obtained from literatures[23,22]. Thus, the measured strain values for thick GaN film match[24] with that of our sample (C) with in-plane and out-of-plane values of -5.27x10^{-5} and -9.06x10^{-5}, respectively, indicating the presence of a compressive strain in the in-plane as well as out-of plane directions for film (A) grown on clean sapphire. Film (B) which consists of GaN petals formed on plasma nitrided substrate, shows compressive strain in the in-plane direction and tensile strain in the out-of plane direction, which can be originated from the crystallographic mosaicity due to anisotropic strain in film (B). Among all samples, sample C which comprises of 1-D nanostructures shows lowest compressive stress with high preferential orientation along c-direction, with GaN (0002) peak being the most intense.

After obtaining the structural and morphological information, we probe the optical properties of the formation. ***Fig. 5.5*** shows Cathodo-luminescence spectra obtained at room temperature for films A, B and C. Sample (A) grown on bare sapphire shows a less prominent band edge emission at 364nm and a strong defect luminescence in the 450-850nm range. The intensity ratio of yellow emission at (630nm) to band edge emission at 364nm is $I_y/I_b \approx 3.02$. Sample (B) where GaN is grown on nitrided Al_2O_3 substrate, shows a strong band edge emission and a reduced defect emission with the intensity ratio of $I_y/I_b \approx 0.85$, and sample (C) with an AlN intermediate layer shows a very strong band edge emission and almost negligible yellow emission with the intensity ratio of $I_y/I_b \approx 0.10$ (≈30 times lower than in sample A). We have measured the the ratio of yellow and band edge emissions values of I_y/I_b from the spectra of several recent reports[25–31] and best them in the right-panel of **Fig.5.5.**

It is clear from the best that the emission ratio value obtained in the present work better than the other results. It is clear from **Fig.5.5(a)** that the full width at half maximum (FWHM) ≈100.0 meV for band-edge peak for film (C) is lower than that for the other films (B is ≈140meV, A is ≈220meV) confirming again that the film is less strained. The band edge emission peak are red shifted towards bulk values of 3.39eV from sample A to C by 20meV, due to increased relaxation of the in-plane compressive strain[32]. The change in strain in the films can be estimated by using equation $\Delta E=0.141*\Delta\varepsilon_{c,}$ where ΔE is the shift in band-edge emission energy with respect to the bulk value[33]. Strain calculated along c-direction both by CL spectra and XRD data yield values of ≈-1.3x10^{-3} for sample (A**)** ≈-3.24x10^{-5} for sample (C), which also suggests that the formation of the nano-features is driven the interfacial dislocations[34].

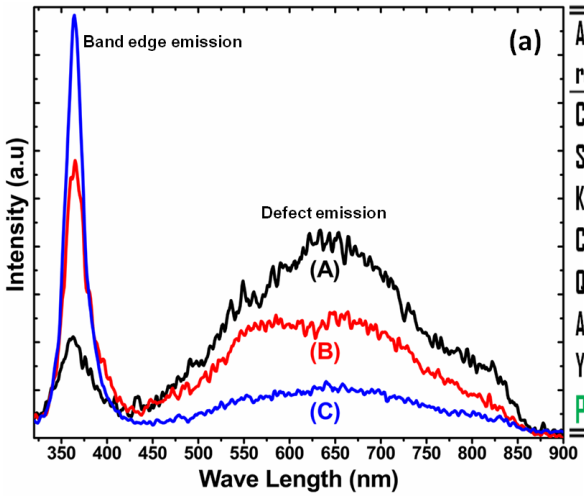

Author reference	The ratio of yellow to band edge emission (I_y/I_b)
Chen et al	0.51
Seo et al	0.30
Kisielowski et al	0.65
Chen et al	0.13
Qiming et al	0.33
Alan et al	0.25
Yang et al	0.31
Present work	0.10

Fig.5.5: *The room temperature CL spectra of samples A, B and C respectively. In the right panel corresponds to yellow to band edge emission ratio from the literature.*

To locate the presence of dislocations, HR-TEM measurements of these GaN nanostructures are performed and the images are shown in ***Fig. 5.6*** **(a-d).** ***Fig. 5.6*****(a)** is the cross-sectional bright-field image of sample (C), which shows 1-D nano-features with height of about 700-800 nm over the AlN columnar layer (≈460 nm). The Selected Area Electron Diffraction (SAED) pattern from individual GaN nano-structures along <2-1-10> zone axis confirms that the grown structures are single crystal wurtzite GaN and they are c- oriented (***Fig. 5.6*****a**-top dotted oval). The selected area diffraction of AlN nano-features in ***Fig. 5.6*****a (**-bottom dotted oval), shows spread in the electron diffraction pattern for (0002) spots for AlN nano-features of ≈8^{o} with respect to the specular (0, 0) reflection, and maintains the same

spread along the length of the nanocolumns which can be due to the out-of-plane mosaicity. We also observe an in-plane twist of nanocolumns (C) of about ~1-2degree along [0002] direction with respect to sapphire, which can be attributed to the mosaicity in the nanocolumns (to be extensively discussed in **Fig.5.7**).

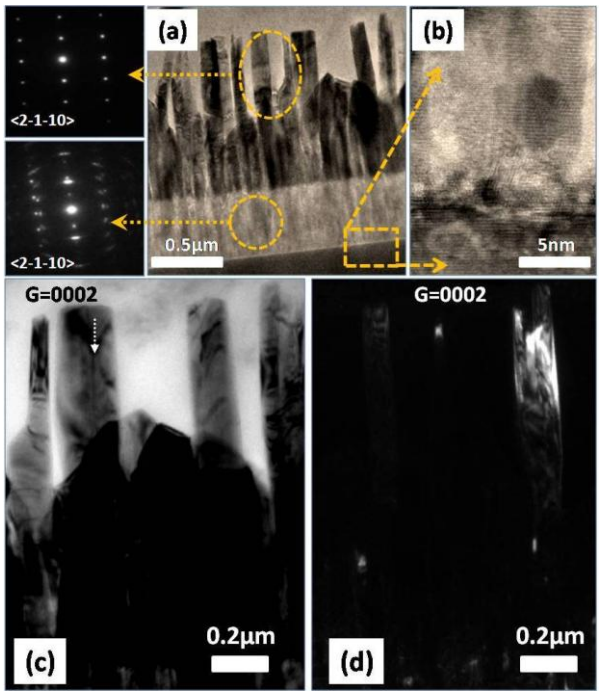

Fig.5.6: (a) *The low magnification cross-sectional TEM image of Sample C. Selected area diffraction patterns have been taken from GaN nano rod along <2-1-10> zone axis and interface of sapphire and AlN film along <01-10> and <2-1-10>, respectively.* ***(b)*** *HR-TEM image at the interface of sapphire and AlN film.* ***(c)*** *Cross-section TEM bright field with g=0002,* ***(d)*** *Cross-section TEM dark field with g=0002 for different rods showing screw dislocations.*

To understand this tilt, twist in relation to the mechanism involved of the nanostructure formation, we carefully look at the Al_2O_3/AlN interface by XTEM as shown in ***Fig. 5.6*****(b)**. The figure clearly shows that the AlN layer of nitrided surface of sapphire consists of inhomogeneous mounds of AlN layer and in regions of direct contact between AlN intermediate layer and the sapphire substrate, epitaxial growth is observed[35]. The plan view of FESEM of AlN intermediate layer illustrates the presence of two different but distinct shapes at the apex of AlN nano-features[7]. The origin of the shape evolution of the AlN nano-features can be explained via strain relaxation process induced shape transition. The shape transition from spherical to pyramidal shape[36] minimizes the elastic strain energy per unit volume. In this similar context, we suggest that the lattice mismatch induced elastic

strain relaxation pathway causes the change in shape of the islands from oval to partially and fully formed pyramid, and by creating misfit dislocations. The observed AlN (10-10)//Al_2O_3 (10-10) epitaxial relation is due to minimal azimuthal rotation of unit cell at the direct substrate/film contact regions. The observed pyramidal shape at the apex of AlN is {1-102}-r plane faceted with an angle of 57.35^o with respect to {1000} plane and the radial walls are m-faceted and c-oriented. We observe that growth mechanism of AlN nanocolumns with pyramidal apex was mediated by axial screw dislocation. However, the nanorods with oval apex do not show any dislocations inside them and so we consider this as a diffusion mediated growth in-between the dislocation mediated columns[7]. The similarity in density of such rods suggests that AlN intermediate layer having pyramidal nano-features (**section 4.4**) supports the formation of GaN nanocolumns. The density of GaN nanostructures (NTs NCT and NRs) is ≈5*10^9/cm^2 and the diameter of NRs, NTs, and c-shaped nanostructures is in the range of 80 to 120nm. Size distribution of AlN nanocolumns was found to be bimodal with oval apex nanocolumns of sizes ranging from 20-60nm and 80-120nm AlN nanocolumns with partially and fully formed pyramidal apex. The density of the oval apex mode is ≈2x10^9/cm^2, and that of the second faceted mode is ≈6x10^9/cm^2 (nanorods with pyramidal apex). It appears that those 1-D features of GaN are formed only on the larger diameter AlN columns with pyramidal apex, and the density and size of these GaN nano-features are similar to the density of larger sized AlN islands with pyramidal apex. To probe the reason for twist observed in nano-features, we have looked at the epitaxial relation between substrate and films. In general, for minimal lattice mismatch the AlN unit cell has to be rotated in-plane by 30^o. Our TEM results shows that the 30^o rotation has ~1^o off twist along the nanocolumn epitaxial to Al_2O_3 [0001] direction, with minimal azimuthal rotation by spontaneous nucleation due to strain in the axial screw dislocation mediated growth. Fig. 5.7 is the low magnification dark field image of GaN nanorods taken in g=0002 zone axis. The nanorod shown by dotted rectangle chosen for the selective area electron diffraction along the axis, to find dislocation induced twist in nanorod. ***Fig. 5.7*****(c)** shows the single nanorod marked by yellow spots indicates the representative point where we have taken selective area electron diffraction (SAED). Initially we have taken SAED at bottom of the nanorods and then middle of the rod. To have same pattern the sample was rotated to a beam direction of about 1^o off axis.

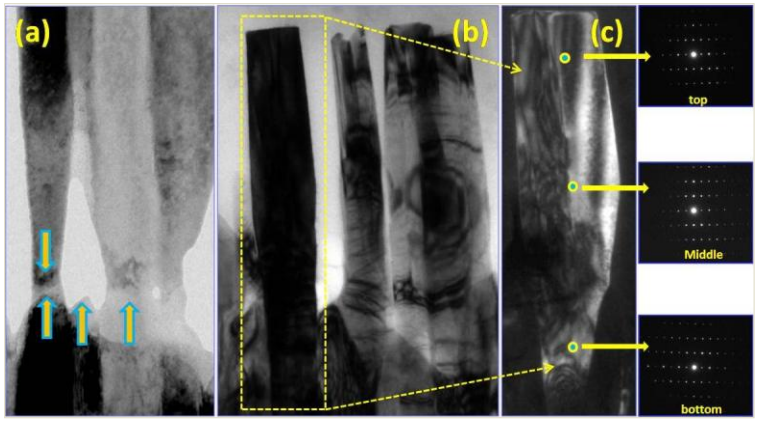

Fig.5.7: (a) *The low magnification cross-sectional TEM image of Sample C.* ***(b-c)*** *Selected area diffraction patterns have been taken from GaN nano rod along <2-1-10> zone axis.*

To understand the growth mechanism underlying the GaN nanostructure formation on top of AlN nanocolumns, we have performed two-beam bright field and dark field TEM imaging to identify the dislocations and identify their role in the formation of GaN 1-D features as shown in ***Fig. 5.6*****(c-d).** Interestingly, we observe a threading screw dislocation along the solid nanorod with g=0002, satisfying g.b≠0 where g-vector is perpendicular to burgers vector i.e. c/2[37]. ***Fig. 5.6*****(c)** is the two beam bright field image with g=0002, that confirms the presence of single axial screw dislocation with burger vector c/2 in the solid nanorods, (propagations of screw dislocation along the axis is marked by a white arrow) confirming that the growth mechanism was driven by axial screw dislocation. ***Fig. 5.6*****(d)** is the dark field image with g=0002 taken from the nanotubes, reveals the multiple screw dislocations with burger vector c/2. From this study, it clearly appears that the non-uniformity of shape and size of GaN nanocolumns is due to the nature of dislocation and propagation direction in the AlN intermediate layer. ***Fig. 5.6*****(c-d),** thus clearly shows that the solid m-faceted nanorods require only a single dislocation to provide the self perpetuating staircase for the spiral 1-D growth. However, nanotubes and c-shaped tubes that are a-plane bounded, require a critical local density of dislocations to overcome the surface energy required for the creation of a new inner surface in order to satisfy the Frank total energy minimization condition [9,38].

Fig. 5.8 is the plot of burgers vectors v/s r/R where r is the inner radius of dislocation core and R is the external radius of the nanorods. The plot suggests that the total elastic strain energy arises by screw dislocation, is dissipated for creating a hollow core and twist the

lattice along the axis. Depending upon the magnitude of the Burgers vector the inner core diameter and twist in nanorods is determined. Thus, total strain energy is relieved by the formation of hollow dislocation cores and twist in nanostructure is balances the energy contributions. Clearly for small b value the twist is less, because most of the strain energy is relieved through hollowing out the nanorod and for large b value more noticeable twist is observed.

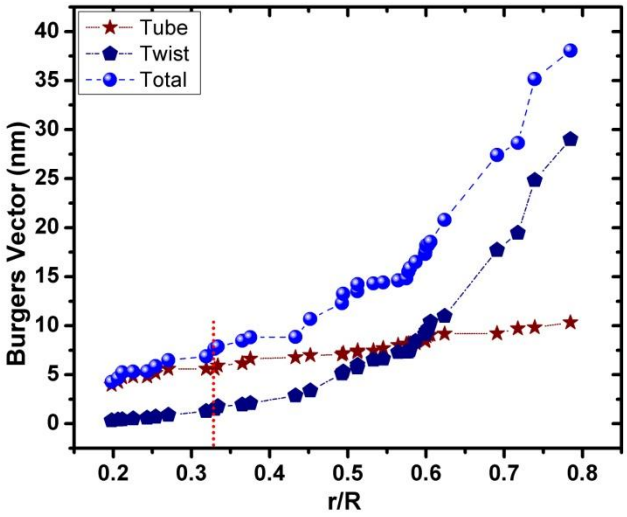

Fig.5.8: *The plot of burgers vectors V/s r/R ratio of GaN nanostructures.*

Thus we observe the spontaneous formation of ordered GaN 1-D nanostructures grown in nitrogen rich conditions on differently nitrided surfaces of c-plane sapphire. An insight into the dislocation mediated evolution of nanorod formation by several complementary characterization techniques is provided. For substrates nitrided by exposure to N_2^* plasma, we show that the dislocation proximity enables the step exchange induced evolution of nano-petal like features. For the substrate with an intermediate AlN layer, we observe bimodal distribution of AlN nanorods which are dislocation mediated and diffusion limited. We also show the need of direct contact between the nanocolumns and the substrate for epitaxial conformation and a dislocation that originated in the AlN intermediate layer for GaN nanocolumn formation. We confirm the epitaxial relation of the a- and m- plane faceted hexagonal GaN nanocolumns with respect to AlN(10-10)//Al_2O_3 (10-10) and AlN (10-10)//Al_2O_3 (11-20). The GaN nanostructures show high crystalline quality with enhanced optical emission as compared to GaN film on bare sapphire. This work shows the role of intermediate AlN layer and that the GaN morphology depends on the dislocations that

originate at the Al_2O_3/AlN interface and that enable self-perpetuating steps for GaN nanocolumn growth.

5.4 Role of intermediate layer on the evolution of 2-D GaN films on Si (111) surface:

GaN films were grown on nitrided surface of Si (111) substrate by using rf-plasma assisted molecular beam epitaxy the MBE system. **Fig. 5.9(a-d)** shows the scanning electron microscope (FESEM) image of GaN films grown on 15, 30, 45 and 60min. nitrided surface of Si (111) and corresponding RMS roughness data are shown as insets. The GaN film which were grown on 15 and 60min. nitrided surface of Si (111) show the least and highest RMS roughness, respectively.

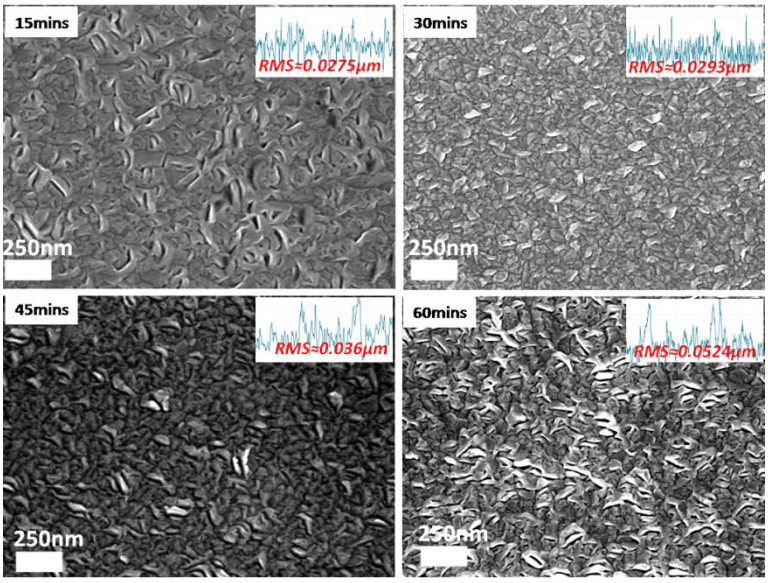

Fig.5.9: *Plan view FE-SEM image of GaN film grown on Si(111) surface after* ***a)*** *15mins* ***b)*** *30mins* ***c)*** *45mins and* ***d)*** *60mins of nitridation. Inset corresponds to RMS roughness.*

Crystal quality of the films was investigated by XRD. The entire XRD pattern (**Fig. 5.10(A)**) of GaN films grown on Si (111) surfaces nitrided for various durations show wurtzite structure. Sample (a) shows sharp reflection peaks at 2θ =34.1°, 72.5° corresponding to the (0002) and (0004) planes showing high quality single crystalline phase of wurtzite GaN. Upon increasing the nitridation time from 30 to 60 minutes, the corresponding samples (b), (c) and (d) show polycrystalline phase of wurtzite GaN films with prominent diffraction

peaks at 2θ=30.6°, 34.1°, 35.5° 62.9° and 68.6° which are assigned to the (10-10), (0002), (10-11), (10-13) and (11-22) planes. The first three planes are the well-known m, c and s planes of the wurtzite structure. No additional peaks were observed at 39.94° and 86.34° which correspond to diffraction from the (002) and (004) planes of the zinc blende phase of GaN. This again confirms the observation that there is no zinc blende phase in the GaN films grown in the present study. **Fig. 5.10(B)** shows the variation in strain field in the GaN thin films in both the horizontal as well as vertical directions of growth. The in-plane strain for samples a-d was measured to be -2.10×10^{-3}, -5.01×10^{-3}, -7.46×10^{-3}, and -9.82×10^{-3} respectively and the out of plane strain was -9.77×10^{-4}, -2.16×10^{-3}, -3.41×10^{-3}, and -5.44×10^{-3}. Among all the samples, (a) and (b) show highest quality of the wurtzite phase. This could be due to the crystallinity of the SiN_x intermediate layer. The samples (c) and (d) show poorer quality polycrystalline phase of GaN thin films, probably due to the amorphous nature of the SiN_x intermediate layer. Clearly, as nitridation time increases the subsequent growth leads to lowering in the quality of GaN films.

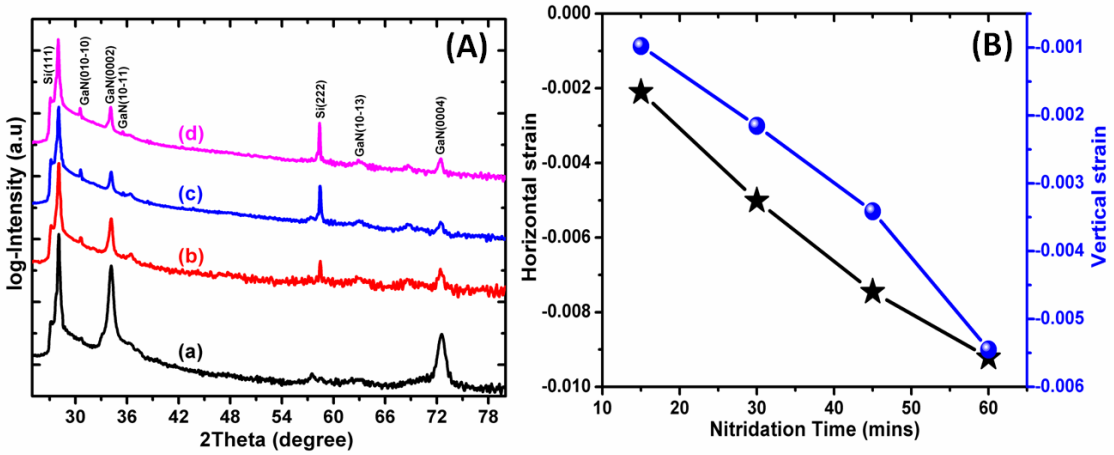

Fig.5.10: (A) *P-XRD patterns and* ***(B)*** *plot of strain along in-plane (a-axis) and out of plane (c-axis) of GaN film grown on Si(111) surface after* ***a)*** *15mins* ***b)*** *30mins* ***c)*** *45mins and* ***d)*** *60mins of nitridation, respectively.*

Fig. 5.11(A) displays the room temperature CL spectra of GaN grown on nitrided surface of Si (111) plane. For samples a and b, the spectra shows only a prominent band edge peak at 3.43eV and no observable defect peak, but for samples c and d multiple peaks were observed corresponding to the band edge emission at the same energy as for previous samples and an additional peak around 2-2.8eV, which was attributed to the emission from defect states[39].

The appearance of strong defect emission at 2.4eV in sample (c)-(d) could be attributed to polycrystalline nature of GaN as already revealed by XRD. The room temperature mobility measured using Hall apparatus for samples (a), b, c and d was 178, 140, 60 and 58 $cm^2/V.s$ respectively. Among all, samples (a) and (b) show high mobility, which could be because of their relatively higher quality having been grown on a crystalline SiN_x intermediate layer. The carrier concentrations were determined to be $1.2x10^{20}$, $1.3x10^{20}$, $1.75x10^{20}$ and $1.8x10^{20}/cm^3$ and relate inversely to the Hall mobilities measured, as seen in **Fig. 5.11(B).**

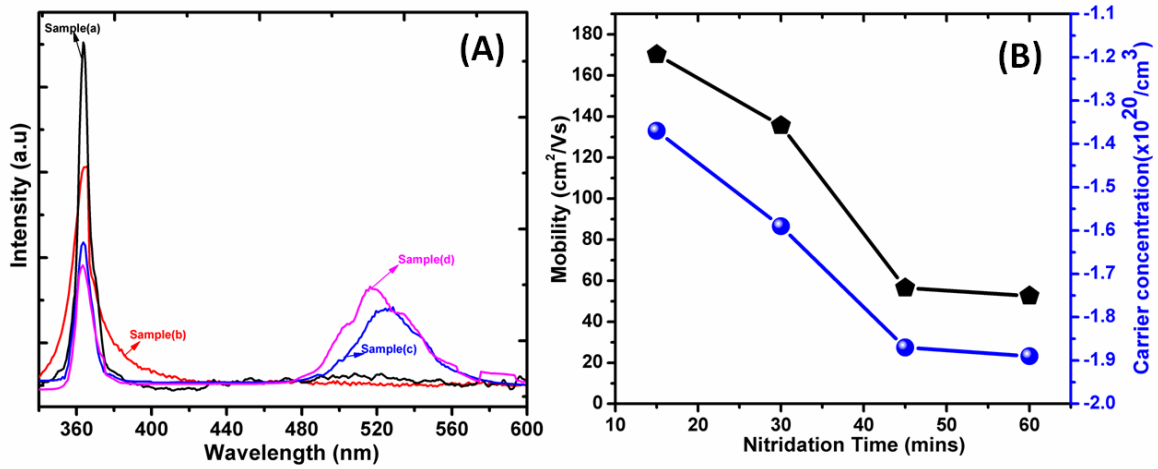

Fig.5.11: ***(A)*** *Room temperature CL spectra (B) variation in mobility and* carrier concentrations *of GaN film grown on a) after 15mins b) 30mins c) 45mins and d) 60mins nitrided surface of Si(111)plane, respectively.*

Fig. 5.12 shows the *I–V* characteristics of samples (a-d) done at room temperature represented in semi-logarithmic scale. The plot represents typical room temperature I-V characteristic of a Schottky diode showing rectifying behaviour. Clearly, the characteristics are that of a hetero-junction and on-off ratios were found to be 235, 26, 24 and 4 at 2V and reverse leakage currents were ~$1.6x10^{-4}$, $1.8x10^{-4}$, $8x10^{-3}$, and $1.6x10^{-3}$A for samples (a-d) at 2V respectively. The forward bias turn-on voltage was observed to be strongly correlated to nitridation time. In order to deduce an explanation for nitridation time dependence on turn-on voltage and on-off ratio, we relate it to the percentage ratio of N/Si of silicon nitride. The N/Si ratio starts to saturate after 30 minutes of nitridation, due to the difference in stoichiometry of SiN_x and its consequent change in thickness (crystallinity) leads to a change in the turn on voltage.

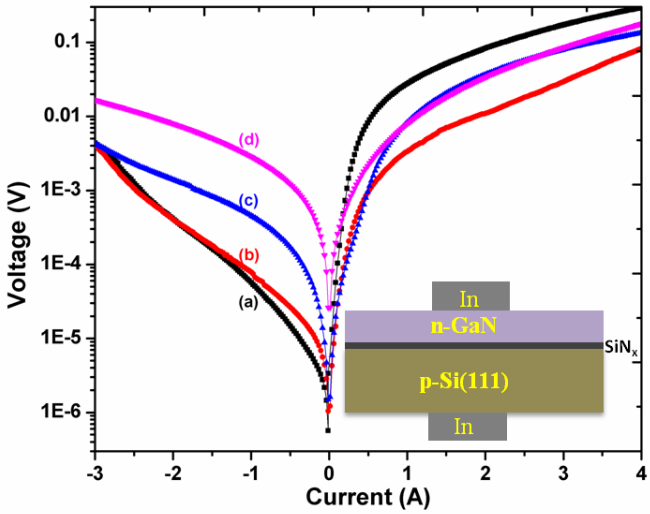

Fig.5.12: *Room temperature I-V characteristics of the GaN/p-Si(111) hetero-junctions grown on Si(111) surface after* ***a)*** *15mins* ***b)*** *30mins* ***c)*** *45mins and* ***d)*** *60mins of nitridation, respectively.*

The (I-V) characteristic was fitted by the standard diode equation: $I = I_s \exp\left[\frac{qV}{\eta KT} - 1\right]$---- (1), where I_s = reverse saturation current, V = applied voltage, q = electronic charge, k = Boltzmann constant and η = ideality factor. The ideality factors were found to be 1.4, 1.5, 1.7 and 2 for samples (a)-(d) respectively. The variation in ideality factors with respect to nitridation time was found to be interrelated with the stoichiometry of SiN_x as well as its thickness and crystal phase. The ideality factors are also known to be dependent on the defect states present at the interface. The deep level defects states seen in the CL spectra coincided well with the high values of ideality factors which also depend on the in-homogeneity of the barrier heights. The change in N/Ga ratio on the observed variation in ideality factors and barrier height depicts the change in stoichiometry. Among all the samples, (a) shows a good rectifying behaviour, with a low leakage current and an atomic percentage of 1:1. Other samples show considerably higher values of ideality factor with high leakage current which is related to high density of dislocations, known to produce a deep level energy path for electron conduction[40,41]. It is well known that high barrier height and low ideality factor represents good rectifying behaviour, as observed in sample (a). The barrier height (φ_b) is determined by fitting standard Richardson's equation. The relation between reverse saturation current and barrier height can be written as $I_s = AA^*T^2 \exp\left(\frac{-q\phi_B}{kT}\right)$----- (2), where

A is the area of the diode, A* is the effective Richardson constant (32 A $cm^{-2}K^{-2}$), *K* is the Boltzmann's constant, *q* is the electron charge, and T is the measurement temperature. The barrier heights were estimated to be ~0.74, 0.724, 0.7, and 0.65 for sample (a-d) as shown in **Fig. 5.13(B)**. The barrier height determined from our experiment is closely related to the difference in electron affinity of Si and GaN, matching closely with Si and GaN band offset which are calculated by using electron affinity of Si and GaN~0.95. Among all the samples, (a) shows that N/Ga ratio~1 and other samples show non-stoichiometry nature of GaN. The barrier height variation can be due to the in-homogenous interfaces, crystal phase and stoichiometry, while the reducing on/off ratio and large leakage currents indicate a defect mediated tunnelling which originate because of high density of defects and trap centre at interface[41–43].

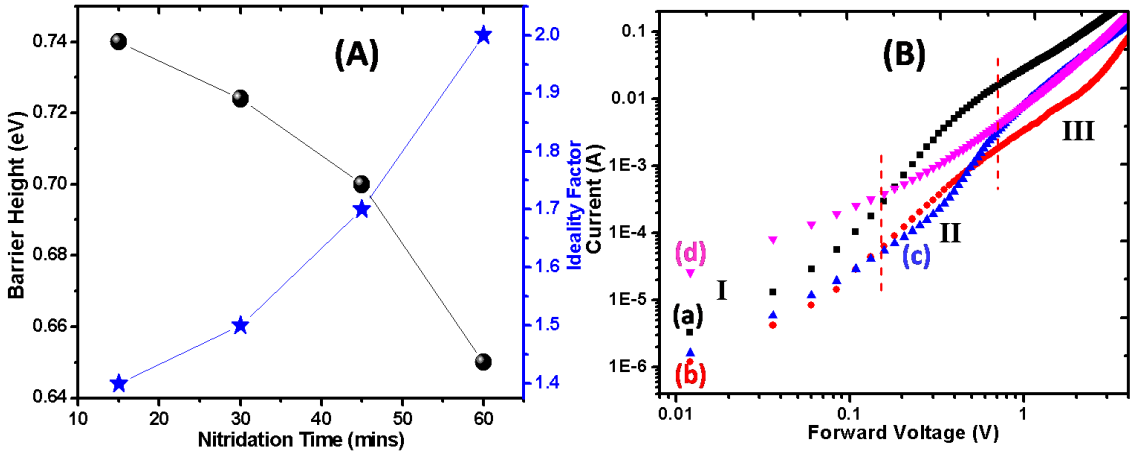

Fig.5.13: (A) *Plot of barrier height and ideality factor v/s nitridation time* ***(B)*** *Log-log plots of the current-voltage characteristic under forward bias for GaN/p-Si(111) hetero-junctions grown on Si(111) surface after* ***a)*** *15mins* ***b)*** *30mins* ***c)*** *45mins and* ***d)*** *60mins of nitridation, respectively.*

The log-log plots of *I* versus *V of sample (a-c) show* three district regions (***Fig.* 5.13(B)**). Sample (a) shows a very short region (I) at a low bias voltage of <0.2 V (region I) whereas sample (b-d) show relatively higher values of voltage. The high resistance is probably due to the superior crystal quality of SiN_x layer, which limits the current and hence the region (I) dominates in samples (c-d). For samples (a-c) the region (II) occurs within the voltage regime $0.2<V<0.8$ where the current exponentially increases and follows the equation $I \sim \exp(\alpha * V)$, which is usually observed in wide band gap semiconductor p-*n* diodes due to recombination-tunneling mechanism. In sample (d), we do not observe the region (II),

probably due to thermally generated carrier tunneling or defect induced current conducting path. Samples (a-d) show a prominent region (III) for V >0.9 V and the I-V characteristics almost obey the power law $I \sim V^2$ this kind of current conduction is attributed to the space charge limited current (SCLC) [44].

5.5 Role of intermediate layer on the evolution of GaN nanostructures on Si(111) surface:

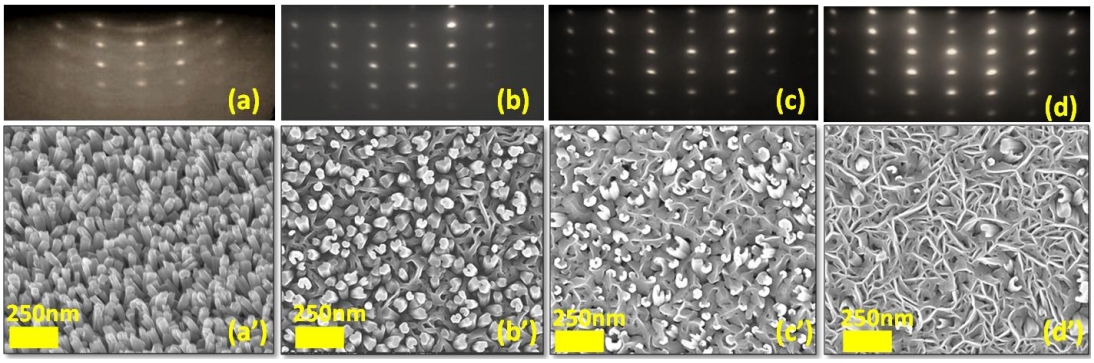

Fig.5.14: *FE-SEM images of GaN films grown on* ***(a)*** *10mins of Ga deposition and 10mins of nitridation on Si(111)7x7 surface,* ***(b)*** *after 10sec.* ***(c)*** *20sec.* ***(d)*** *30sec. nitrided surface of Si(111).*

Fig. 5.14(a) corresponds to the RHEED pattern taken along the <11-20> azimuth for the sample (i) where GaN film was grown after the following procedure: (I) Ga is initially deposited onto a clean Si(111)-7x7 surface for 10min. (II) Nitridation of the Ga layer is carried out for 10min. **Fig. 5.14(a)** is a typical spotty RHEED pattern which is characteristic for transmission of electrons through 3D-features. The spread in the RHEED spots indicates that these single-crystalline nanorods are tilted with respect to substrate normal. The spotty RHEED pattern are elongated in an arc along the horizontal direction for the nanorods, which shows anisotropy along [1-100] direction. The lattice periodicities as viewed along <11-20> and <1-100> projections are c and $c/2$ for axial, a and $a/\sqrt{3}$ for in-plane ordering. The ratio of spacing between RHEED spots in horizontal and vertical direction is $2a^*/\sqrt{3}c^* \approx 1.89$ for pattern viewed along <11-20> and $2a^*/2c^* \approx 1.63$ along <1-100> (where $a^* = \frac{\pi}{2a}$ and $c^* = \frac{\pi}{2c}$)[4,45]. This c/a ratio shows that the GaN nanorods grow epitaxially, are single crystalline and have a wurtzite crystal structure with c-axis perpendicular to the substrate surface**. Fig. 5.14(a')** is the corresponding plan view FESEM image of the GaN film. We believe that

these nanorods grow on GaN droplets which form prior to growth during the surface passivation of Ga metal and subsequent nitridation. The number density of nanorods was observed to be the same as that of GaN droplets; these droplets help in the nucleation of nanorods aligned along [0001] direction. The density of nanostructures is of the order of ~ $4x10^9 cm^{-2}$ and width ≈80-100nm. The RHEED pattern shown in **Fig. 5.14(b)** reveals the formation of 3-D GaN nanostructures. The spotty RHEED pattern without circular arcs is an indication of absence of misorientation in the film. The ratio of distance between spots in the horizontal and vertical direction is $5.7A^o/3.1A^o$=1.83, which is in good agreement with the calculated value $c/(\sqrt{3a/2})$ =1.87**. Fig. 5.14(b')** is the corresponding FESEM image of GaN nanowall network with randomly distributed nanorods which are grown on top of the 1sec. nitrided surface of Si (111) at 750°C. It is clear from the figure that the uneven distribution of strain leads to the formation of nanorods in order to reduce the excess strain generated due to the lattice and thermal expansion mismatch. **Fig. 5.14(c)** shows the RHEED patterns taken along the [11-20] azimuth for GaN film grown after 20sec. of Si(111) nitridation. The Bragg diffraction pattern appears to be spotty in nature indicating 3D growth. **Fig. 5.14(c')** is the corresponding FESEM image of GaN film grown at 750°C on 20sec. nitrided surface of Si. GaN nanostructures were observed to form in this case, the morphology of which was like tri-branched networks having a wedge-shaped blunt apex and a few tilted nanorods forming within the voids of the matrix. **Fig. 5.14(d)** shows spotty RHEED pattern and the c/a ratio calculated from the vertical and horizontal direction of RHEED spots was 1.63, showing that the nanowalls are wurtzite in structure. We have observed dominant spotty pattern which is an indication of the transmission through a nanowall. The absence of any circular arcs indicates absence of polycrystallinity or tilt in this sample. **Fig. 5.14(d')** is the FESEM image of the corresponding sample which clearly shows that densities of nanorods are drastically reduced and their morphology is dominated by tri-branched networks with sharp wedges.

Now we have discussed structural quality of films. **Fig. 5.15** shows the 2Θ-ω scan of XRD pattern obtained in range 20° to 100° for all films. The peaks observed at 2Θ = 34.34° and 72.98° corresponds to the Bragg reflection of (0002) and (0004) planes of GaN, respectively, and other peaks at 2Θ = 28.4° and 58.85° corresponds to Si(111) and Si(222) plane reflections. The Θ-2Θ scan re-confirms that the film is single-crystalline wurtzite GaN,

with three diffraction peaks observed at 2θ=31.08°, 37.19° and 63.5°, corresponding to the GaN (10-10) m-, (10-11) s- and (10-13) planes of GaN respectively. The GaN film which is grown after 30sec nitridation shows only symmetry reflection which indicates no misalignment with respect to the surface normal.

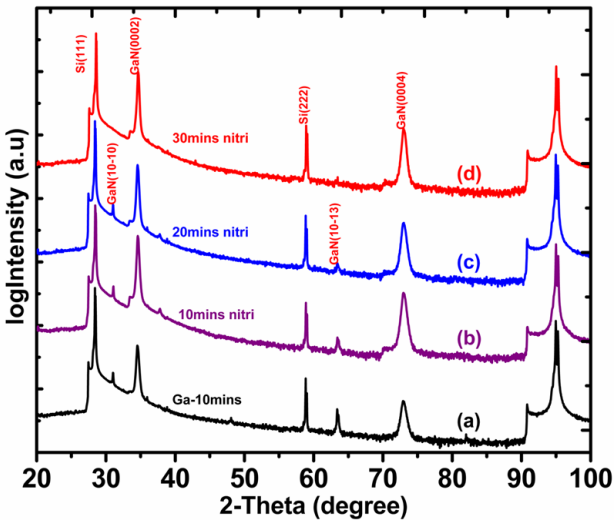

Fig.5.15: *P-XRD patterns of GaN films grown on* ***a)*** *10mins of Ga deposition and 10mins of nitridation on Si(111)7x7 surface,* ***b)*** *after 10sec* ***c)*** *20sec,* ***d)*** *30sec. nitrided surface of Si(111)plane, respectively.*

From the symmetric (0002) and asymmetric (10-10) reflections, the lattice constants are determined to be a=0.31nm and c=0.512nm, which is characteristic of a relaxed wurtzite GaN unit cell. The XRD again confirms that there is no evidence for zinc-blende GaN nanostructure formation on the triangular Si(111) surface. The presence of other reflections from off-axis planes of GaN is due to the presence of crystal mosaicity or due to misaligned of nanorod with respect to surface normal. We have seen peaks other than symmetric reflections in the samples (a-c) which indicates misalignment of nanorods. But sample (d) dominant nanowall network GaN morphology shows only symmetric reflection.

Now we discuss optical quality of the GaN nanorods and nanowall network grown on modified surface of Si(111) plane. The room temperature CL spectra of the nanorods and nanowall network are shown in **Fig. 5.16.** Sample (a) grown on GaN droplet template, shows band-edge luminescence at 364nm. The intensity ratio of yellow emission at (630nm) to band edge emission at 364nm is $I_y/I_b \approx 4.02$. Sample (b) where GaN is grown on nitrided 10sec nitrided surface shows a weak band edge emission and the intensity ratio of $I_y/I_b \approx 2.8$.

Sample (c) shows strong band edge emission and the intensity ratio is 1.2. But in case of sample (d), which shows nanowall like morphology shows strong band edge luminescence (BEL) peak ~3.42 eV and the intensity is two orders of magnitude higher than in the nanorods. The decrease in band edge emission intensity in case of (sample (**(a)**) nanorods is due to scattering and channeling of light along the nanorods from the quasi-aligned GaN nanorods.

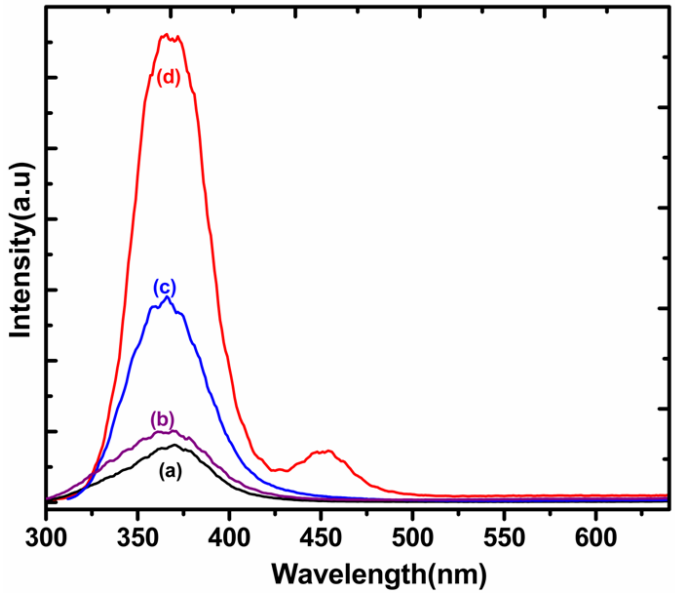

Fig.5.16: *Photoluminescence of GaN films grown on* ***a)*** *10mins of Ga deposition and 10mins of nitridation on Si(111)7x7 surface,* ***b)*** *after 10sec* ***c)*** *20sec and* ***d)*** *30sec nitrided surface of Si(111) plane, respectively.*

Raman spectra of samples (a-b) are shown in **Fig. 5.17**. It is well known that position of the strong E_2 (high) line is used to determine stress in epitaxial GaN. The three spectra (red–blue–black) were arbitrarily taken at different positions on the sample. Raman spectrum for the GaN nanorods **(Fig. 5.17(a))** shows a shift in the E_2 (high) mode at different positions on the sample. The non-uniform shift in position of E_2 (high) mode is the characteristic of the anisotropic distribution of strain in the film. The non-uniform strain distribution could be due to uneven distribution of GaN droplets in the case of sample (a). The E_2 (high) mode shifts to the low-frequency side due to tensile stress in the film. The line width of the E_2 (high) phonon mode for nanorods is $12cm^{-1}$ (sample a), the low value shows the high quality of the epitaxial GaN nano-features. **Fig. 5.17**(b) is the Raman spectra taken from the sample with morphology of GaN nanowalls and randomly distributed nanorods. A shift in the position of

E_2 (high) line, similar to the previous sample, was seen. The anisotropic distribution of stress in this case is probably due to the non uniform distribution of SiN_x layer. The line width of the E_2 (High) phonon for sample (b) is $18cm^{-1}$, which in this case is due to the film relaxation as observed from nano-feature formation. Raman spectra of sample (c) is from a morphology showing GaN nanowalls with few nanorods present in the void region of the nanowall network; a relatively smaller shift in the position of E_2 (high) line was seen in the film. The E_2 (high) peak position was ≈ $568.8cm^{-1}$ for this film, while a peak at $569.1cm^{-1}$ is expected for stress free GaN bulk powder sample[46,47]. We attribute that the relaxed film shows less stress when the surface is nitrided for about 20sec, due to the uniform growth of SiN_x layer which is responsible to obtain good quality GaN films. The low line width (10 cm^{-1}) of the peak indicates that the film is of high crystalline quality.

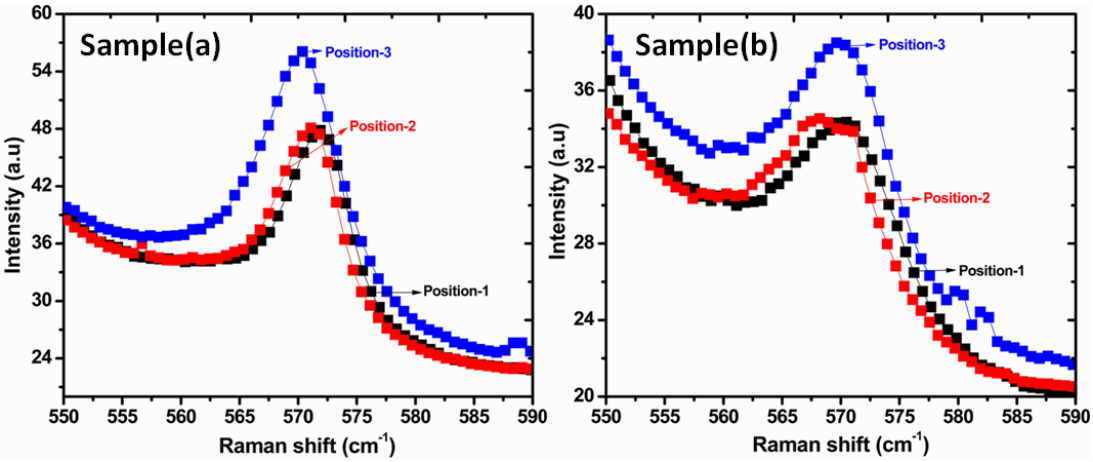

Fig.5.17: *Room temperature Raman spectra of GaN film grown on* ***a)*** *10min. of Ga deposition and 10min. of nitridation on Si(111)7x7 surface,* ***b)*** *after 10sec. nitrided surface of Si(111)plane, respectively.*

In Raman spectroscopy of sample (d), the E_2-high mode was observed at $570.3cm^{-1}$ as shown in **Fig. 5.18.** The Raman frequency shift of the E_2 (high) phonon mode is uniform all over the film and the value of E_2 high mode was almost the same as that of bulk GaN of about $569.1cm^{-1}$, which implies that stress free GaN nanowalls grew on 30sec. nitrided surface of Si (111). This again is probably due to the formation of uniform and high quality crystalline SiN_x by plasma nitridation of Si(111) surface, which consequently results in the formation of relaxed GaN nano-features.

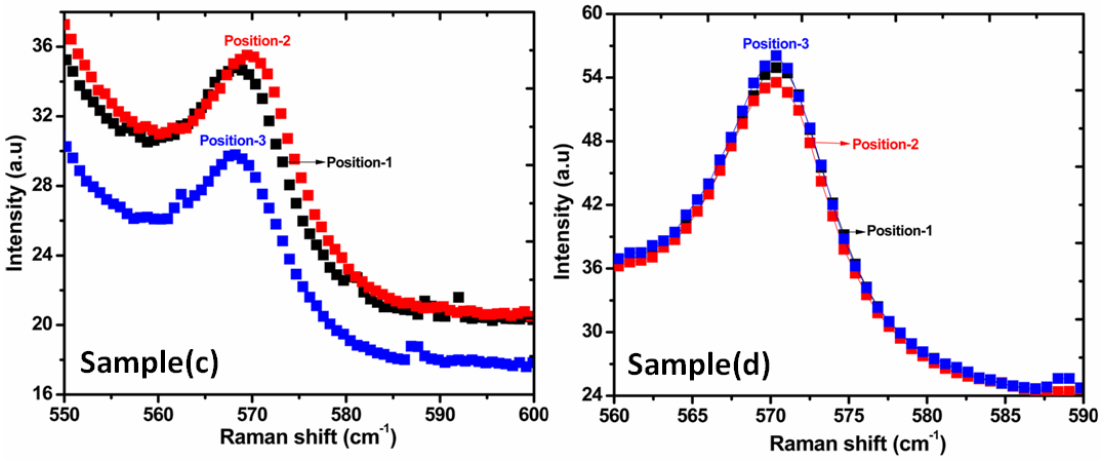

Fig.5.18: *Room temperature Raman spectra of GaN films grown on* ***c)*** *20sec,* ***d)*** *30sec nitrided surface of Si(111), respectively.*

Electric properties were measured for the films across the unintentionally doped *n*-GaN/highly doped *p*-Si hetero-junctions. The contacts were taken from the backside of Si substrate and front of GaN surface. I-V characteristics of these GaN films are shown in **Fig. 5.19**.

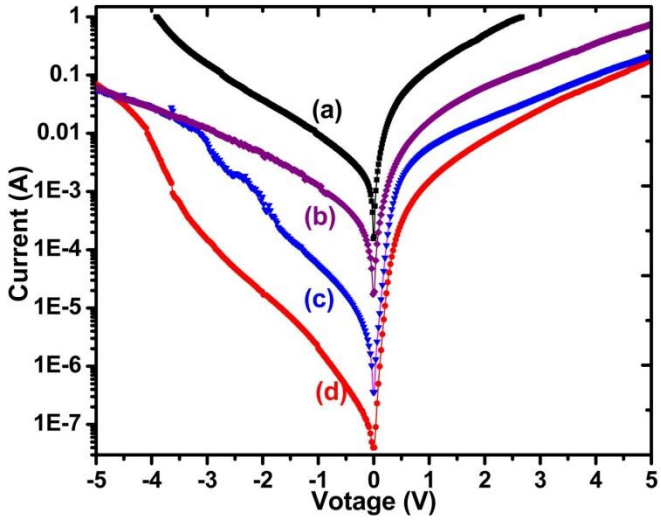

Fig.5.19: *Shows the I-V characteristics of GaN films grown on a) 10min. of Ga deposition and 10min. of nitridation on Si(111)7x7 surface, b) after 10sec. c) 20sec. and d) 30sec. nitrided Si(111) surface of hetero-junctions measured at room temperature.*

These devices show interesting rectification behavior with respect to thickness and uniformity of intermediate SiN_x layer employed during the growth. Knowing band gaps and electron affinities of Si and GaN, the valence band and conduction band offsets are calculated. The values of band gap and electron affinity of GaN and Si are 3.4eV, 1.12eV and

3.1eV, 4.05eV, respectively[48]. The calculated valence band offset is 0.95eV and corresponding conduction band offset is 1.33eV. **Fig. 5.19** shows the I-V characteristics of the GaN and Si (111) heterostructures. These four devices exhibit good rectifying behaviour and their forward bias turn-on voltage is about 0.3V. The turn-on voltage is observed to be strongly dependent on the thickness of the intermediate layer and crystalline quality of GaN films.

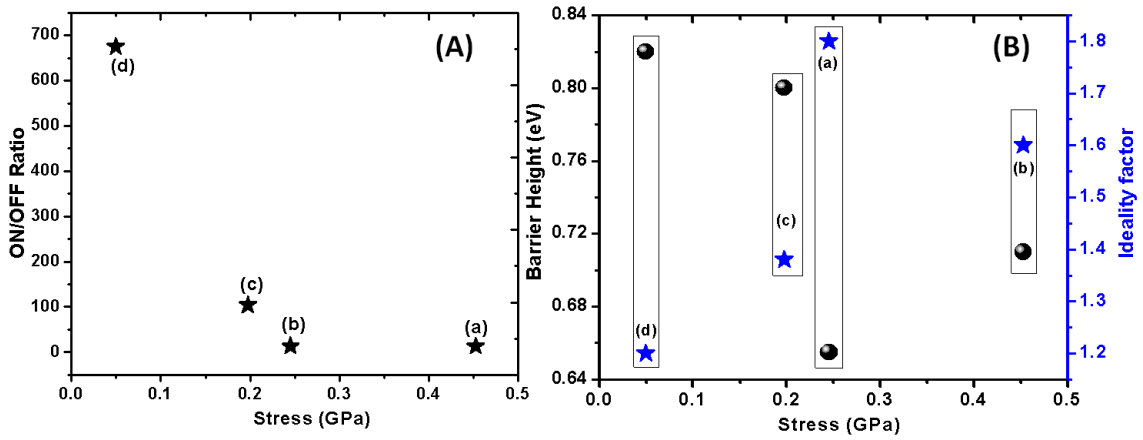

Fig.5.20: A) *Plot ON/OFF ratio versus stress* ***B)*** *variation of barrier heights and ideality factor versus stress of GaN films grown on* ***(a)*** *10min. of Ga deposition and 10mins of nitridation on Si(111)7x7 surface,* ***(b)*** *after 10sec.* ***(c)*** *20sec.* ***(d)*** *30sec. nitrided surface Si(111) plane, respectively.*

Fig. 5.20(A) is the plot of on/off ratio v/s stress in the film. Sample (a) shows very low on/off ratio that could be attributed to excess charge carries or nitrogen vacancies and a leakage current of order 10^{-2}A at turn-on voltage of 1V. The diode (sample (b)), which is grown at longer time of 10min. nitridation shows a low leakage current of 10^{-3}A at the turn-on voltage of 1V, while samples (c-d) show very low leakage current of about 10^{-5}A and 10^{-7}, respectively. The drastic reduction in leakage current and increase in on/off ratio indicates the low defect (dislocations) density and reduction in localized electronic state at the interface. We believe that with higher nitridation time, stoichiometric Si_3N_4 layer with completely relaxed GaN nanostructures form. The on/off ratios at 1V gradually increase from sample (a-d) as tensile stress decreases resulting in the increase in device performance. **Fig. 5.20(B)** shows the stress dependent ideality factor and barrier height of the GaN/Si hetero-junction at room temperature. The ideality factors and barrier heights are calculated by fitting the linear region of I-V curve using the standard diode equation described earlier. The sample (a) shows a high ideality factor; with increasing nitridation time the ideality factor

reduces to 1.2 for sample (d). The observed high barrier heights (φ_b) and ideality factors (η) for samples (a-c) are attributed in literature to defect states which cause deep level assisted tunneling and in-homogeneity at the interface[42,50]. **Fig. 5.20(B)** clearly shows that longer nitridation (sample (d)) yields higher barrier heights and almost agrees with the calculated valence band offset. We reason that the large lattice and thermal mismatch between GaN and Si generate high density of dislocations at the interface that can act as recombination (scattering) centres, resulting in a large ideality factor and low barrier height[51,52]. Thus, the presence of stoichiometric SiN_x intermediate layer yields high quality GaN films (sample (d)) with low ideality factor and high barrier height.

5.6 Summary:

In this chapter, we have discussed the role of intermediate layer on the epitaxy and orientation of GaN formation on sapphire and Si(111) substrate. First we have discussed the difference in the evolution of dislocation mediated low-dimensional GaN nanostructures on differently pre-nitrided c-plane sapphire surface. We show that when GaN grows on c-plane sapphire, after forming an AlN layer by exposure to N^*_2 plasma, leads to the formation of nano-petal-like 1-D GaN nanostructures. We observe that GaN grown on this AlN intermediate layer prefers to grow only on the single crystalline AlN nanocolumns of size in the range of 80-120nm. The threading screw dislocation is seen to propagate both through AlN and GaN, nanorods with its morphology depending on the proximity of the dislocations. Our results show that the shape, structure and mosaicity of GaN nano-features are dependent on the morphology of the AlN intermediate layer. We have also discussed the GaN 2-D nanorod formation on modified surface of Si(111). Resulting GaN nanostructures shows high quality single crystalline phase and optical emission properties. Formation of single crystalline GaN nanorods on GaN layer grown in nitrogen-rich condition has thus shown as a useful method to form dislocation free spontaneous growth of ordered and oriented GaN nanocolumns by PA-MBE, in a single growth process.

5.7 REFRENCES:

1. M. I. den Hertog, F. González-Posada, R. Songmuang, J. L. Rouviere, T. Fournier, B. Fernandez, and E. Monroy, *Nano Lett.*, 2012, **12**, 5691–6.

2. H. P. Bhasker, S. Dhar, A. Sain, M. Kesaria, and S. M. Shivaprasad, *Appl. Phys. Lett.*, 2012, **101**, 132109.

3. D. Cherns, L. Meshi, I. Griffiths, S. Khongphetsak, S. V. Novikov, N. Farley, R. P. Campion, and C. T. Foxon, *Appl. Phys. Lett.*, 2008, **92**, 121902.

4. M. Kesaria, S. Shetty, and S. M. Shivaprasad, *Cryst. Growth Des.*, 2011, **11**, 4900–4903.

5. M. Kesaria, S. Shetty, P. I. Cohen, and S. M. Shivaprasad, *Mater. Res. Bull.*, 2011, **46**, 1811–1813.

6. S. Shetty, J. Ghatak, and S. M. Shivaprasad, *CrystEngComm*, 2014, **16**, 3076.

7. S. Shetty, J. Ghatak, and S. M. Shivaprasad, *Solid State Commun.*, 2014, **180**, 7–10.

8. S. A Morin, M. J. Bierman, J. Tong, and S. Jin, *Science*, 2010, **328**, 476–80.

9. F. C. Frank, *Acta Crystallogr.*, 1951, **4**, 497–501.

10. M. Jamil, J. R. Grandusky, V. Jindal, N. Tripathi, and F. Shahedipour-Sandvik, *J. Appl. Phys.*, 2007, **102**, 023701.

11. K. Y. Zang, Y. D. Wang, L. S. Wang, S. Y. Chow, and S. J. Chua, *J. Appl. Phys.*, 2007, **101**, 093502.

12. M. Kim, Y. Bang, N.-M. Park, C. Choi, T. Seong, and S. Park, *Appl. Phys. Lett.*, 2001, **78**, 2858.

13. S. I. Molina, A. M. Sánchez, F. J. Pacheco, R. García, M. A. Sánchez-García, F. J. Sánchez, and E. Calleja, *Appl. Phys. Lett.*, 1999, **74**, 3362.

14. R. Songmuang, G. Katsaros, E. Monroy, P. Spathis, C. Bougerol, M. Mongillo, and S. De Franceschi, *Nano Lett.*, 2010, **10**, 3545–50.

15. M. S. Centre, 2004, **27**, 501–504.

16. C.-L. Wu, J.-C. Wang, M.-H. Chan, T. T. Chen, and S. Gwo, *Appl. Phys. Lett.*, 2003, **83**, 4530.

17. M. Kumar, M. K. Rajpalke, B. Roul, T. N. Bhat, N. Sinha, A. T. Kalghatgi, and S. B. Krupanidhi, *Appl. Surf. Sci.*, 2011, **257**, 2107–2110.

18. Y. Nakada, I. Aksenov, and H. Okumura, *Appl. Phys. Lett.*, 1998, **73**, 827.

19. A Wierzbicka, Z. R. Zytkiewicz, S. Kret, J. Borysiuk, P. Dluzewski, M. Sobanska, K. Klosek, A Reszka, G. Tchutchulashvili, A Cabaj, and E. Lusakowska, *Nanotechnology*, 2013, **24**, 035703.

20. P. Kumar, J. Kuyyalil, and S. M. Shivaprasad, *Appl. Phys. Lett.*, 2010, **97**, 221913.

21. N. H. Zhang, X. L. Wang, Y. P. Zeng, H. L. Xiao, J. X. Wang, H. X. Liu, and J. M. Li, *J. Phys. D. Appl. Phys.*, 2005, **38**, 1888–1891.

22. V. Darakchieva, B. Monemar, and A. Usui, *Appl. Phys. Lett.*, 2007, **91**, 031911.

23. M. A Moram and M. E. Vickers, *Reports Prog. Phys.*, 2009, **72**, 036502.

24. S. Porowski, *J. Cryst. Growth*, 1998, **189-190**, 153–158.

25. C. C. Chen, C. C. Yeh, C. H. Chen, M. Y. Yu, H. L. Liu, J. J. Wu, K. H. Chen, L. C. Chen, J. Y. Peng, and Y. F. Chen, *J. Am. Chem. Soc.*, 2001, **123**, 2791–8.

26. H. W. Seo, S. Y. Bae, J. Park, H. Yang, K. S. Park, and S. Kim, *J. Chem. Phys.*, 2002, **116**, 9492.

27. C. Kisielowski, J. Krüger, S. Ruvimov, T. Suski, J. Ager, E. Jones, Z. Liliental-Weber, M. Rubin, E. Weber, M. Bremser, and R. Davis, *Phys. Rev. B. Condens. Matter*, 1996, **54**, 17745–17753.

28. H.-Y. Chen, H.-W. Lin, C.-H. Shen, and S. Gwo, *Appl. Phys. Lett.*, 2006, **89**, 243105.

29. A. H. Chin, T. S. Ahn, H. Li, S. Vaddiraju, C. J. Bardeen, C.-Z. Ning, and M. K. Sunkara, *Nano Lett.*, 2007, **7**, 626–31.

30. B. Yang, A. Trampert, O. Brandt, B. Jenichen, and K. H. Ploog, *J. Appl. Phys.*, 1998, **83**, 3800.

31. Q. Li and G. T. Wang, *Nano Lett.*, 2010, **10**, 1554–1558.

32. M. A. Reshchikov and H. Morkoç, *J. Appl. Phys.*, 2005, **97**, 061301.

33. S. W. Lee, J.-S. Ha, H.-J. Lee, H.-J. Lee, H. Goto, T. Hanada, T. Goto, K. Fujii, M. W. Cho, and T. Yao, *Appl. Phys. Lett.*, 2009, **94**, 082105.

34. M. Kesaria and S. M. Shivaprasad, *Appl. Phys. Lett.*, 2011, **99**, 143105.

35. S. Shetty, M. Kesaria, J. Ghatak, and S. M. Shivaprasad, *Cryst. Growth Des.*, 2013, **13**, 2407–2412.

36. V. Consonni, M. Knelangen, L. Geelhaar, A. Trampert, and H. Riechert, *Phys. Rev. B*, 2010, **81**, 085310.

37. D. Cherns, L. Meshi, I. Griffiths, S. Khongphetsak, S. V Novikov, N. R. S. Farley, R. P. Campion, and C. T. Foxon, *Appl. Phys. Lett.*, 2008, **93**, 111911.

38. S. Jin, M. J. Bierman, and S. A. Morin, *J. Phys. Chem. Lett.*, 2010, **1**, 1472–1480.

39. M. a. Reshchikov and H. Morkoç, *J. Appl. Phys.*, 2005, **97**, 061301.

40. R. Ghosh and D. Basak, *Appl. Phys. Lett.*, 2007, **90**, 243106.

41. M. Dutta and D. Basak, *Appl. Phys. Lett.*, 2008, **92**, 212112.

42. S. Mridha and D. Basak, *J. Appl. Phys.*, 2007, **101**, 083102.

43. S.-Y. Liu, T. Chen, Y.-L. Jiang, G.-P. Ru, and X.-P. Qu, *J. Appl. Phys.*, 2009, **105**, 114504.

44. T. N. Bhat, M. K. Rajpalke, B. Roul, M. Kumar, and S. B. Krupanidhi, *J. Appl. Phys.*, 2011, **110**, 093718.

45. M. Kesaria and S. M. Shivaprasad, *Appl. Phys. Lett.*, 2011, **99**, 143105.

46. E. V. Konenkova, Y. V. Zhilyaev, V. A. Fedirko, and D. R. T. Zahn, *Appl. Phys. Lett.*, 2003, **83**, 629.

47. M. Kumar, B. Roul, T. N. Bhat, M. K. Rajpalke, P. Misra, L. M. Kukreja, N. Sinha, A. T. Kalghatgi, and S. B. Krupanidhi, *Mater. Res. Bull.*, 2010, **45**, 1581–1585.

48. T. N. Bhat, M. Kumar, M. K. Rajpalke, B. Roul, S. B. Krupanidhi, and N. Sinha, *J. Appl. Phys.*, 2011, **109**, 123707.

49. T. E. Cook, C. C. Fulton, W. J. Mecouch, R. F. Davis, and G. Lucovsky, 2003, **3949**.

50. B. Roul, M. K. Rajpalke, T. N. Bhat, M. Kumar, A. T. Kalghatgi, S. B. Krupanidhi, N. Kumar, and A. Sundaresan, 2011, **162512**, 3–5.

51. Y.-P. Chiu, B.-C. Chen, B.-C. Huang, M.-C. Shih, and L.-W. Tu, *Appl. Phys. Lett.*, 2010, **96**, 082107.

52. B. Roul, T. N. Bhat, M. Kumar, M. K. Rajpalke, N. Sinha, A. T. Kalghatgi, and S. B. Krupanidhi, *Solid State Commun.*, 2011, **151**, 1420–1423.

Chapter 6

GaN Nanostructures and 2-D Films on Si (111), (100) Surfaces

6. Growth of Epitaxial GaN Nanostructures and 2-D Films on Si (111) and Si(100) Surface:

6.1 Introduction:

The subtle interplay between substrate and overlayer structure, interface properties and kinetics of growth, determine the epitaxy and morphology of nanostructures[1]. Earlier optoelectronic devices such as laser diodes exhibited limited lifetimes due to large densities of extended defects. Of late, to mitigate deleterious effects of the high dislocation densities in 2D-films, nanostructures have started emerges as a building block in progress of electronic as well as optoelectronic devices. Novel alternate means to reduce threading dislocation densities by an order of magnitude has also been achieved by ELOG, ,Nano-ELOG, Domain and Super-lattice Matching Epitaxy [2–5]. An emerging alternative to conventional flat thin films, for high efficiency III-nitride devices, is the formation of nanostructures[6,7] on silicon substrates. These can accommodate the lattice mismatch at the hetero-interface by forming a network of columnar structures in which dislocations can terminate at their free side faces[8]. Once relaxed, these strain-free high aspect-ratio nanocolumns can be used for devices with efficient light extraction[9,10], while tuneability of band gap via nano-dimension variation is promising for monolithic integration of multicolor emission[11]. Since the first report by Cerutti et. al.,[12,13] on the formation of strain and defect-free, single crystalline wurtzite GaN nanocolumns on Si(001) by plasma assisted molecular beam epitaxy (PAMBE), a few reports on the formation of Ga(Al/In)N nanocolumnar LED structures on silicon[14,15] (111), (001) and Al_2O_3[16-17] substrates, have appeared, and a few[12,18] on the formation of wurtzite GaN nanowires on diamond cubic Si(001). As of now, many existing compound semiconductors nanowire based vertical and planar transistors have been fabricated on self assembled nanowires with the integration of well established silicon technology. Next generation self assembled nanostructures could be used for interlinking vertical nanorod based transistors, ultra bright and high resolution LED, high efficient tandem solar cell etc. by forming micro-structural array of self assembled (millions of) nanorods[19–22]. The complex interdependence needs to be understood at the atomistic level to tailor materials with desired properties arising due to the reduced dimension[23]. To elucidate on this we study a hetero-epitaxial system of interest to contemporary technology, by growing GaN nanostructure on silicon surface. In

this chapter we have discussed the growth phase diagram of GaN films on Si(111) and Si(100) surface, whose self assembly is controlled by strain engineering and kinetics of growth. However, the underlying mechanism of the spontaneous growth, structure and role of intermediate layer, orientation and assembly of the reduced-dimension features are still unclear in the literature. The aim of this work is to take advantage of III-nitride nanorods grown by plasma-assisted molecular beam epitaxy to form heterostructures that are difficult or impossible to achieve in traditional, thin films. To do this, it is first necessary to establish the growth phase diagrams of GaN nanostructures under MBE growth conditions. By using the information in these growth maps we can control growth by carefully tuning the growth parameter, without employing any catalyst, buffer layer or surface treatment. The effort in this part of the work is in understanding the role of diffusion, reaction rate and sticking coefficient on the formation of 2-D films and nanostructures of GaN on two surface (111) and Si(100) of Silicon, by plasma-assisted molecular beam epitaxy. This is followed by RHEED, XRD, CL and TEM characterization to model the evolving structure and morphology of the nanostructured GaN epitaxial overlayer and their properties at the atomistic level.

6.2 Experimental Section:

(A) The growth system used in this study was Plasma assisted Molecular Beam Epitaxy (PA-MBE) System equipped with a radio frequency (RF) plasma source with a base pressure of $5x10^{-11}$Torr. Prior to the growth, the Si(111) substrates were ultrasonically degreased in acetone for 10 min. and followed by degassing at 500^{o}C for 30 mins in the preparation chamber and then in the growth chamber the sample is repeatedly flashed at 900^{o}C for 10mins to get a clean Si(7x7) reconstruction. In the first set of experiment, Ga k-cell temperature was fixed to 1000^{o}C with a corresponding flux rate of $3.86x10^{14}$ atoms $cm^{-2}s^{-1}$ as measured by precision flux gauge, while the substrate temperature was varied from 450^{o}C to 680^{o}C, except for a substrate temperature of 650^{o}C for which the k-cell temperature was fixed to 1050^{o}C. The radio frequency plasma source was operated at a forward power of 375 W_f, and all the films were grown for 2 hrs with a nominal thickness of 0.6um. In second case, the nitrogen flow rate was varied from 2 sccm to 6 sccm by using high precision mass flow controller and the other parameters such as Ga effusion cell temperature of 1000^{o}C and

substrate temperature of 630^{o}C were maintained constant. In third case, the GaN growth is done by varying Ga k-cell temperature from 900^{o}C to 1100^{o}C at interval of 100^{o}C by maintaining the fixed substrate temperature of 650^{o}C and 4.5 sccm N_2 flow rate. The surface morphology and structure of these nanostructures are evaluated by a field-emission-scanning electron microscope (FE-SEM) in-situ reflection high energy electron diffraction (RHEED) and Raman spectroscopy. To determine structural quality of the GaN films, a four crystal high-resolution x-ray diffractometer and to probe optical emission properties the Photo-luminescence (PL) measurements are done at room temperature.

(B) Chemically cleaned Si(001) substrate is thermally degassed at 500^{o}C in ultra high vacuum for several hours, followed by the removal of the native SiO_2 layer by repeated flashing to 900^{o}C, to obtain an atomically clean (2X1) reconstructed Si(001) surface as visualized by *in-situ* RHEED. A 0.6μm GaN layer is grown at 700^{o}C, under nitrogen rich conditions (N/Ga BEP ratio 100), with Ga effusion cell temperature of 1000^{o}C and nitrogen flow rate of 4.5sccm. The obtained GaN films are characterized by several complementary techniques as described earlier.

6.3. Substrate temperature induced nanostructure formation on Si (111) surface:

Fig. 6.1 is the plan view of FE-SEM images of the GaN nanostructures with the corresponding RHEED pattern acquired along the [11-20] azimuth for individual films**. Fig. 6.1(a)** is the FE-SEM image of GaN film showing a highly defected 2-D flat morphology (**Sample A**) and corresponding RHEED pattern shown in **Fig. 6.1(a').** The spotty RHEED pattern observed is due to the transmission of electron beam due to rough surface or nano-features. The ratio of spacing between RHEED spots in horizontal and vertical direction is $2a^*/\sqrt{3}c^* \approx 1.89$ for a pattern viewed along <11-20> and $2a^*/2c^* \approx 1.63$ along <1-100> direction (where $a^*=\frac{\pi}{2a}$ and $c^*=\frac{\pi}{2c}$)[24]. **Fig. 6.1(b)** shows a random network of GaN with a porous structure consisting of wedge shaped tri-branched nanowalls oriented along the <11-20> and <1-100> directions with small misorientation **(Sample B**). The corresponding RHEED pattern (**Fig. 6.1(b'))** is bright and spotty, characteristic of transmission through the 3D-features. The ratio of spacing between RHEED spots in horizontal and vertical direction

is $2a^*/\sqrt{3}c^* \approx 1.89$ for this sample also. **Fig. 6.1(c)** depicts the FE-SEM image of randomly oriented GaN nanorods **(Sample C**) with a density of about $10^{10}/cm^2$. Among these nanorods, some of them are solid and some of them are c-shaped in the view. The corresponding RHEED pattern (**Fig. 6.1(c'))** shows a spacing between RHEED spots in horizontal and vertical direction of $1.88 \approx 2a^*/\sqrt{3}c^*$. In this RHEED pattern, the spots elongate as faint circular arcs indicating the polycrystallinity or random orientation of the features with respect to the surface normal (which is probed further by HR-XRD phi scans discussed in the next section). We believe that these nanorods are formed on top of GaN nanowall network, and their alignment will be discussed in detail later.

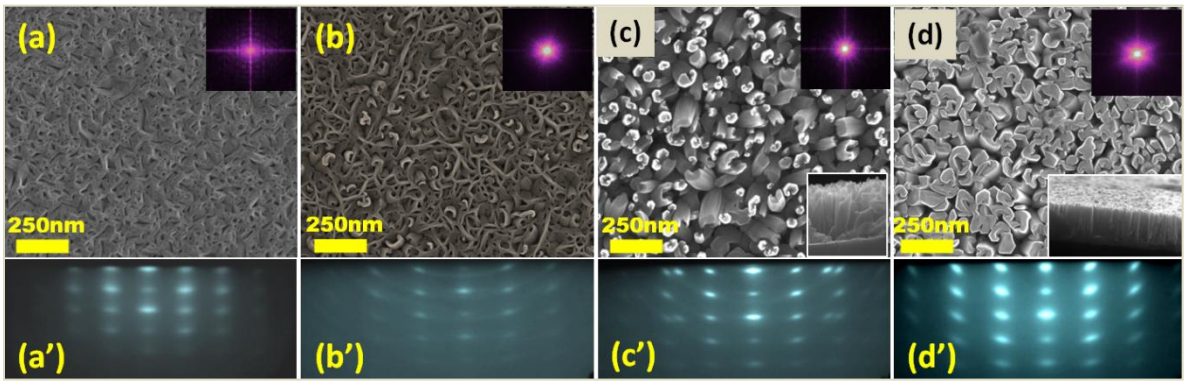

Fig.6.1: (a-b) *Plan view FE-SEM image and inset is the Fast Fourier Transform (FFT) with their corresponding RHEED pattern (a'-d') acquired along <11-20> direction of GaN film grown on Si(111) at (a) 450°C (Sample (A)) (b) 630°C (Sample (B)) (c) 680°C (Sample (C)) and (d) 650°C (Sample (D)) substrate temperature, respectively.*

Fig. 6.1(d) is the plan view FE-SEM image of (**sample D**) showing well aligned nanorods with a density ~10^{10} cm^{-2}. **Fig. 6.1(d)** shows spotty RHEED pattern and the ratio calculated from the vertical and horizontal direction of RHEED spots is also $2a^*/\sqrt{3}c \approx 1.88$ (c/a=1.63), showing that the nanorods possess wurtzite structure. The reduction of the length of the circular arcs indicates reduced polycrystallinity or tilt of the nano-features. High resolution cross-sectional view of FE-SEM (inset at the right bottom of **Fig. 6.1(d))** shows nanorods with an average length of 1um and average diameter of 100-140nm. Finally, The Fast Fourier Transform (FFT) shows a 3-fold symmetry[25] in the corresponding FESEM image as shown in inset of **Fig. 3.11(b-d)** except sample (A)**.**

To obtain information about crystal quality, phase and epitaxial relation we performed HR-XRD and by aligning with respect to the strong Si (111) reflection observed at 28.8° and

P-XRD measurements. **Fig. 6.2(a)** shows the typical 2-theta scans of the GaN grown on Si (111) surface. The observed sharp peaks at 34.34^{o} and 74.26^{o} are from the (0002) and (0004) symmetric reflection from wurtzite GaN and the other two peaks at 28.84^{o} and 58.34^{o} corresponds to Si (111) and (222) planes, respectively.

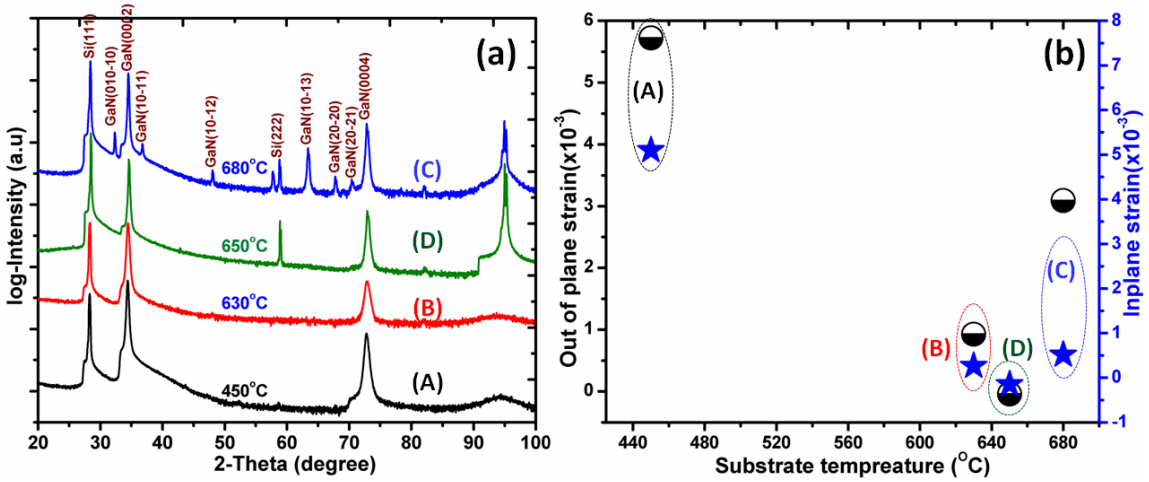

Fig.6.2: *(a) PXRD 2-theta scans of GaN films (b) plot of strain along in-plane (a-axis) and out of plane (c-axis) for samples A, B, C and D, respectively.*

No other diffraction peaks are observed, indicating the obtained GaN films are single crystalline and c-oriented. The intensity of (0002) peak in the case of the sample with GaN nanorods is dominant in comparison to the samples A and B. The multiple reflections observed in case of sample (C) is due to the tilt of the nano-features with respect to surface normal as also evident from ***Fig.6.1.*** **Fig. 6.2(b)** shows the plot of the calculated strain values vs. substrate temperature for these films. The strain is calculated with reference to bulk GaN lattice constants of a = 3.1907 Å and c = 5.1869 Å and for our samples we have calculated a- and c- lattice constant from asymmetric (11-24) and symmetric (0002) reflections respectively. Our results clearly suggest that, both the nanowall network and the aligned GaN nanorods are strain relaxed. The structural quality of the films was studied by obtaining rocking curves (**Fig. 6.3(a)**) around symmetric (0002) and asymmetric (10-21) reflections and looking at their full widths at half maximum (FWHM) values. The plot of these FWHM values as a function of the substrate temperature is shown in **Fig. 6.3(b)**. The nano-features of all the films resulted in FWHM higher than bulk values. Relatively, the samples which are grown at 630^{o}C and 650^{o}C (sample (C-D)) show much narrower FWHMs.

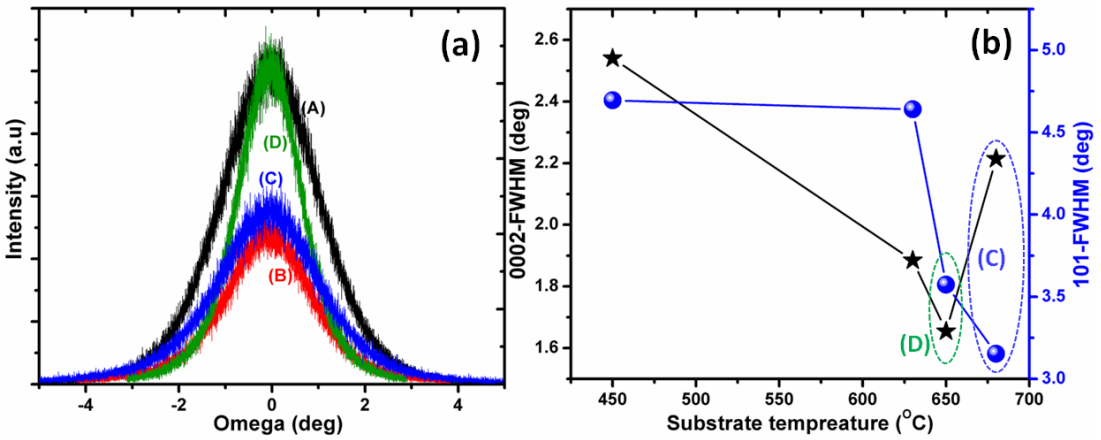

Fig.6.3: ***(a)*** *HR-XRD rocking curves of (0002) plane* ***(b)*** *FWHM of (0002) and (10-11) reflection for samples A, B, C and D, respectively.*

Furthermore, to determine the in-plane orientation of the GaN film with respect to the substrate, we have done HR-XRD Phi scan, for off-axis diffraction peaks. The sample rotations, ϕ and χ, were adjusted in order to get off-axis reflections into the scattering plane of the diffractometer. Here, ϕ is the angle of rotation about the surface normal and χ is the angle of the sample tilted about the axis formed by the intersection of the Bragg and scattering planes. After tilting the sample to the suitable χ for specific off-axis reflections, ϕ scans were performed to (10-11) plane of GaN and (1-11) plane of the Si substrate. **Fig. 6.4** shows a phi scan for the (10-11) planes of GaN and the corresponding diffraction peaks are observed at an interval 60^{o}, showing epitaxial growth

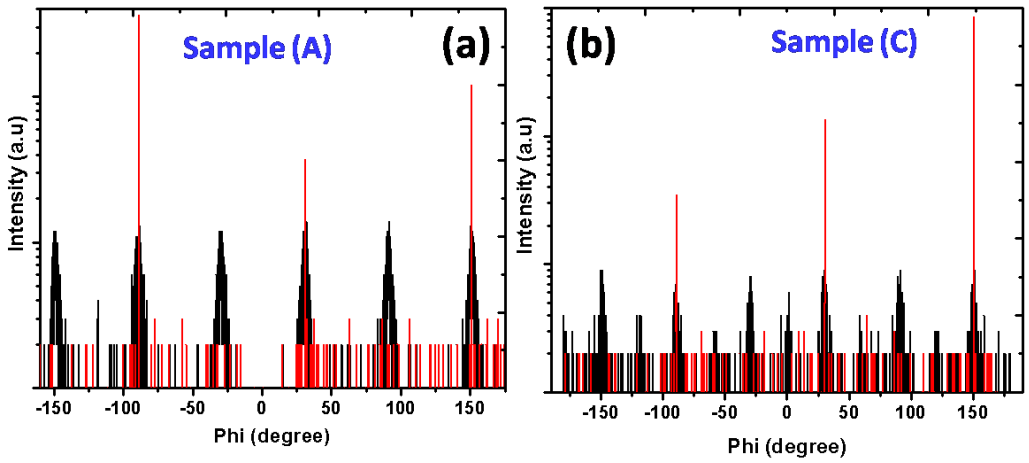

Fig.6.4: *Representative in-plane Phi-scan measured from GaN films grown at (a) $450^{o}C$ (Sample (A)) and (b) $680^{o}C$ substrate temperature (Sample (C)) on Si (111) substrate.*

The GaN film shows the six-fold azimuthal symmetry consistent with the wurtzite crystal structure[26,27]. The Si (1-11) planes show three fold symmetry with an interval of 120°. Thus, the growth direction of the GaN film of (0001) orientation is parallel to the (111) of silicon surface. The in-plane orientation of GaN on Si is GaN (11-20)//Si (1-10), indicates that the GaN films grow without any in-plane rotation with respect to substrate. The triangular lattice of Si (111) planes and triangular network hexagonal arrangement of atoms of the wurtzite GaN are in registry to the Si (111) plane.

After obtaining the structural and morphological information, we probe the optical properties. **Fig. 6.5** shows the room temperature photo-luminescence spectra of the samples A, B, C and D respectively. Sample (A) shows (the films grown at 450°C) less prominent band edge emission without any defect related emission. We attributed this to non-radiative recombination centres present in the sample. Samples A–D shows a clear band edge emission with slight blue shift with increasing substrate temperature from 450°C to 680°C. Among them, the sample D (oriented GaN nanorods) shows strong band to band emission but the sample (C) which has randomly oriented nanorods shows less intense emission due to the light emission from the tips of the nanorods. **Fig. 6.5(b)** presents the variation of band edge position and FWHM with respect to substrate temperature.

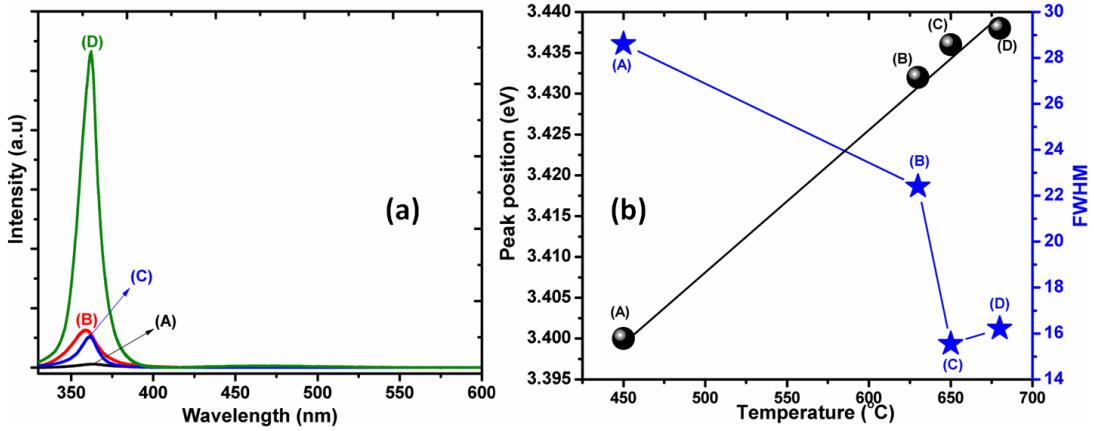

Fig.6.5: (a) *Room temperature CL spectra and* ***(b)*** *Band edge peak position (y-axis) and FWHM (y-axis) for samples A, B, C and D, respectively.*

The band edge emission peak is blue shifted towards bulk values of 3.43eV from sample A to D by 20meV, is attributed to strain relaxation. We do not observe any broad band emission near 2.2 eV, due to yellow luminescence, showing low non-radiative defect density in this low temperature growth films[28–33]. The **Fig. 6.5(b)** shows the variation in

band edge position with respect to growth temperature and it is clear that the PL peak position blue shifts in case of highly strained samples (sample (A)). Among all the samples, the sample (D) is close to the bulk value of band edge emission. The blue shift in the PL peak position in sample (B) may be due to the decrease in size at the apex of the network configuration where confinement of excitons could exist. With respect to the sample (D), sample (A) is red shifted which could be due to the presence of tensile stress in the 2-D films or due to point defects. **Fig. 6.5(b)** also shows the variation in FWHM of band-edge emission with respect to the growth temperature, and are found to be ≈28.6, 22.4, 15.5 and 16.2 meV for samples A, B, C and D, respectively. The decrease in FWHM with growth temperature is attributed to strain relaxation and formation of defect free GaN film.

To further understand the mechanism involved in the temperature dependent morphological evolution, we tried to look at on sticking coefficient of Ga adatoms on different substrate temperatures as shown in Fig.6**.6 (taken from ref 44, 45).**

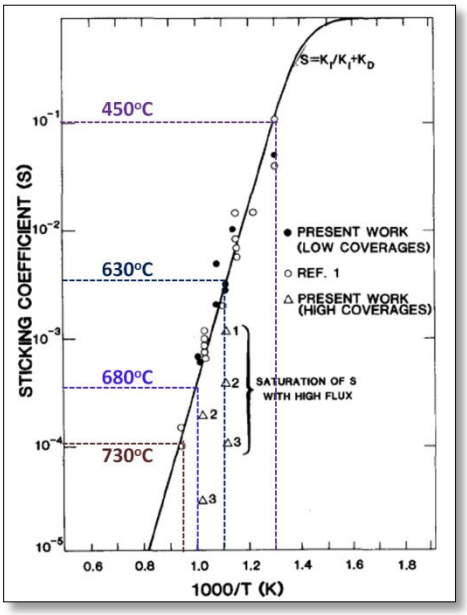

Fig.6.6: *Plot of sticking coefficient of Ga adatoms on Si(111) surface at different substrate temperature*[34,35].

The FE-SEM image corresponds to sample (**Fig 6.1A** for deposition at 450^{o}C) shows 2-D morphology with high dislocation density at nitrogen rich condition. To understand this formation which is contrary to our observation of GaN on Al_2O_3 (0001), we initially look at the elemental composition ratio of Ga to N in the film. It is found that the of Ga:N ratio is about 0.9 by EDAX studies, which indicates that in the nitrogen rich growth condition used,

results in a stoichiometric GaN formation on Si(111) surface at 450^{o}C. From **Fig.6.6**, it is clear that the Ga sticking coefficient at 730^{o}C on sapphire is same as that of the Si at the 450^{o}C, and thus a morphology close to 2-D films is possible on Si(111) substrate at 450^{o}C in nitrogen rich condition. Since the desorption rate of Ga is very high at higher substrate temperatures, the increase in the growth temperature will lead to relatively higher nitrogen rich condition resulting in the formation of nanostructures. Thus at relatively low temperatures we can get 2-D films with high dislocation density but without any cracks on silicon (111) substrate. Sample (B) shows network morphology along with the presence of nanorods, (**Fig. 6.1**) which is typically grown at nitrogen rich conditions whose origin is already explained in Chapter [3]. The sample (C) features show a six-fold symmetry as evident in the FFT of the image shown in inset of **Fig. 6.1**. The HR-XRD phi scan for the sample shows intense peaks at an interval of 60^{0} in addition to that less intense peaks observed at 30^{0} intervals. This observation indicates two sets of epitaxy that may be present in the sample due to the coexistence of both nanowalls and nanorods, with the nanowalls having epitaxial relation with (10-10)// (111) of Si while the nanorods shows (10-11)// (11-1) epitaxy. The nanorods are c-orientated with m-faceted side walls. Similar to the explanation provided earlier, due to the significantly higher sticking coefficient of Ga adatoms on the c-plane than on the m-plane, Ga adatoms diffuse from the m-plane to the c-plane leading to the growth of nanorods. In case of sample (D) which is grown at Ga rich condition, we believe that the Ga adatoms attain high supersaturation condition in Ga rich condition. The reduction in diffusivity significantly reduces the Ga adatoms mobility. As predicted theoretically that the shorter diffusion length eventually reduce the binding sites and results surface roughing. At low substrate temperature induces locally dominated GaN growth at Ga rich condition. We also suggest that the high reactive Si surface forms SiN_x islands locally and induces anisotropic strain on Si surface. Thus, the generation of local tensile strain field enhances the local nucleation. The local accumulation of strain and consequent relaxation enables the dislocations and these dislocations enable self induced driving force for nanorods or nanostructure formation[34]. The growth of well aligned nanorod is driven by minimization of the total surface and interface energies. Alternatively, the growth may exploit the anisotropy in the diffusion of surface adatoms on (110) surfaces, giving rise to the growth of 1D nanorods which are aligned along [110] direction.

Fig. 6.7 shows the room temperature I-V characteristic curves of un-intentional n-doped GaN/p-Si(111) heterojunction.

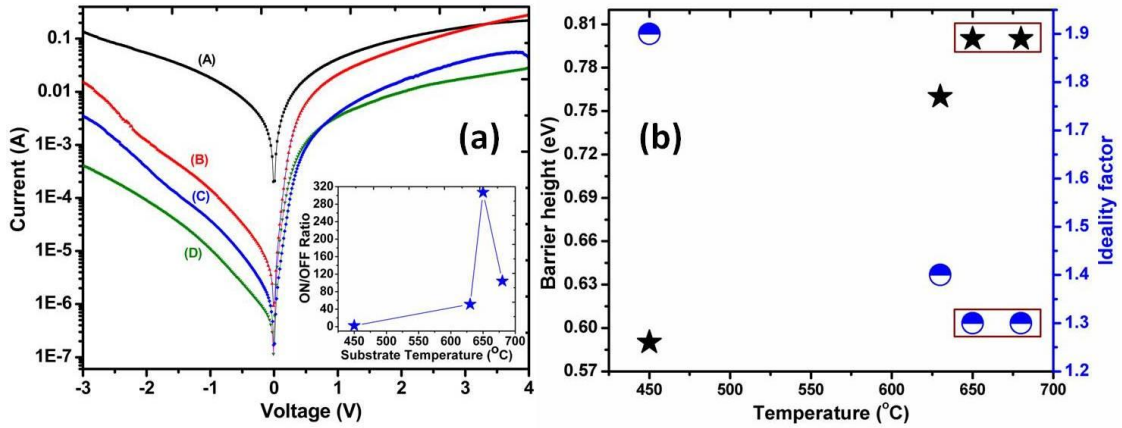

Fig.6.7: (a) *Shows the I-V characteristics (inset-on/off ratio w.r.t substrate temperature)* ***(b)*** *Plot of barrier height and ideality factor of GaN film grown at (a) 450^{o}C (b) 630^{o}C, (c) 680^{o}C and (d) 650^{o}C substrate temperature, respectively.*

The sample B, C and D show good rectifying behavior with the on/off ratio for sample (D) grown at 450^{o}C is observed to be very high and it is shown in **Fig. 6.7(a-inset).** The barrier height (φ_b) and the ideality factor (η) of this junction shown in **Fig. 6.7(b)** were calculated by fitting standard diode equation, for different growth temperatures. It very clear that, the sample (C and D) which has nanorod morphology shows low ideality factors and high barrier height, which could be due to reduced defect states and homogenous interface formation[39].

6.4 Nitrogen flux dependent GaN nanostructure formation:

We have studied nitrogen flux dependent morphological evolution of GaN films on Si(111) surface by varying the N_2 flow rate as 2, 4.5 and 6sccm, while maintaining the substrate and Ga k-cell temperature at 630^{o}C and 1000^{o}C respectively. The FE-SEM images of the films grown at nitrogen flow rates of 2, 4.5 and, 6 sccm are as shown in **Fig. 6.8(a-c).** The films which are grow with nitrogen flow rates of 2 and 4.5sccm show a mixture of nanowall network and randomly oriented nanorods (**Fig. 6.8(a-b)).** The partially formed nanorod density is ~10^{9}cm^{-2} for the films grown with 2 sccm N_2 flow rate, (**Fig.6.8a**) and their density reduces drastically for the films grown at 4.5 sccm N_2 flow rate (**Fig. 6.8b**), which may depend on sticking co-efficient of Ga adatoms. We believe that the network

forms due to open, screw dislocation and the nanorods nucleate in their voids. As nitrogen flux rates increases from 4.5 to 6 sccm, we have found clear nanowall network morphology. **Fig. 6.8(a')** is the corresponding RHEED pattern obtained along <11-20> azimuth with spots along circular arcs which can be due to the misalignment of nanorods, as evidenced by XRD and SAED studies. **Fig. 6.8(b')** is the spotty RHEED pattern with faint circular arcs.

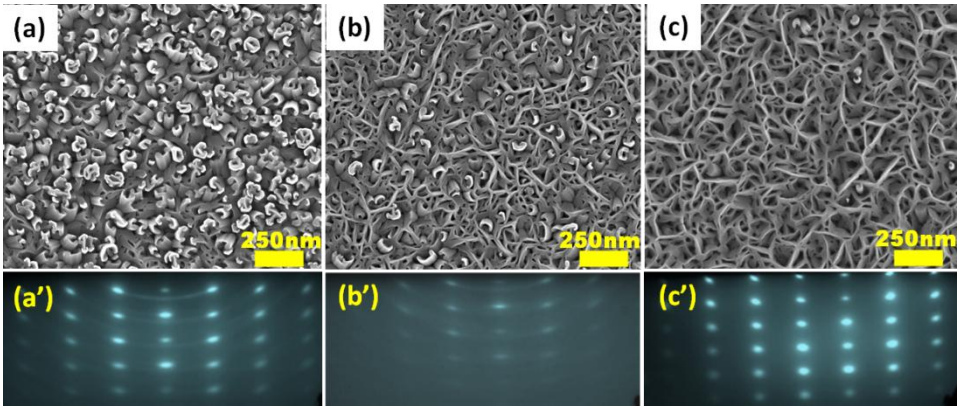

Fig.6.8: (a-b) *Plan view FE-SEM image with their corresponding RHEED pattern (a'-c') taken along the [11-20] zone axis of GaN film grown at* ***(a)*** *2sccm (Sample (A)) (**b**) 4.5sccm (Sample (B)) and* ***(c)*** *6sccm (Sample (C)) nitrogen flow rate at fixed substrate temperature and Ga k-cell temperature of 630^{o}C and 1000^{o}C, respectively.*

Fig. 6.8(c) shows a plan view FE-SEM image of GaN film formed at nitrogen flow rate of 6 sccm, with distinct nanowall network features. Thus, it appears that to obtain the nanowall network morphology, one has to maintain higher super saturation condition. Since high flow rates of nitrogen retard the diffusion of Ga adatoms, reducing the average diffusion length of Ga to the lateral growth of the walls, enabling wider and taller nanowall formation, without the nanorods formation. **Fig. 6.8(c')** shows a clear spotty RHEED pattern without any distinct circular arcs clearly suggesting the well oriented nanowalls tapering along (0001) direction.

To determine the crystal quality and orientation of the nano-features characterized HR-XRD was employed. **Fig. 6.9(a)** shows the intense symmetric reflection of GaN (0002), the GaN (0004) planes and the substrate Si(111) and Si(222) reflection peaks. We have not observed any peaks corresponding to cubic phase of GaN, indicating that the GaN epitaxial layers consist of wurtzite crystal phase and are c-axis oriented. To calculate the c- lattice parameter, by considering the Si (111) peak as the reference, the Bragg angle of GaN (0002) is determined. The out-of-plane lattice constants for the sample are determined by using

Theta values of symmetric reflection, and the in-plane lattice constant -a is obtained from asymmetric 2θ-ω scan in a skew symmetric geometry. The in-plane strain and out of plane strain are determined for sample A, B and C as shown in **Fig .6.9(b).** The film which is grown at 6 sccm nitrogen flow with nanowall morphology is observed to be strain free with bulk like GaN properties.

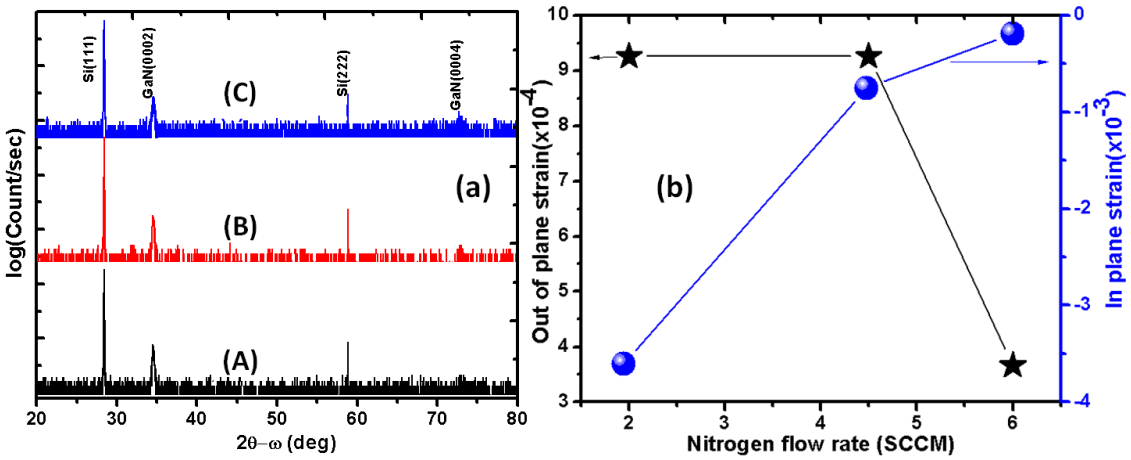

Fig.6.9: (a) *HR-XRD 2θ-ω scans* ***(b)*** *plot of strain along in-plane (a-axis) and out of plane (c-axis) of GaN film grown at (A) 2sccm (B) 4.5sccm and (C) 6sccm nitrogen flow rate at fixed substrate temperature and Ga k-cell temperature of 630^{o}C and 1000^{o}C, respectively.*

Fig. 6.10 shows results from CL measurements carried out on three samples grown at different nitrogen flow rate.

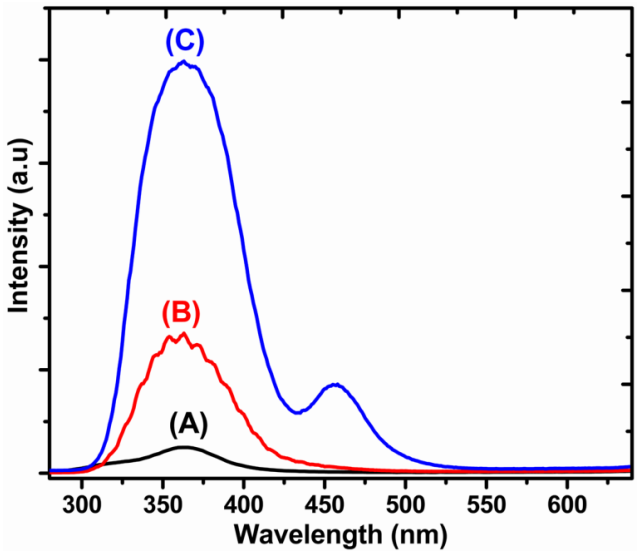

Fig.6.10: *Room temperature CL spectra of GaN film grown at (A) 2sccm (B) 4.5sccm and (C) 6sccm nitrogen flow rate at fixed substrate temperature and Ga k-cell temperature of 630^{o}C and 1000^{o}C, respectively.*

As can be seen, increasing nitrogen flow rate resulted in nanowalls that have less emission from defects and strong band edge emission. **Fig. 6.10** shows a direct comparison of the spectra of GaN films grown at different nitrogen flow rate. We clearly see that the band edge emission intensity of GaN grown on 6 sccm nitrogen flow is nearly an order of magnitude higher than in other sample. The intensity of the defect related emission at the yellow region is reduced in all the cases. Thus, films with nanowall network shows good optical properties as compared to other samples.

The electrical characteristics of all hetero-junctions of unintentionally doped n-GaN and doped p-Si are carried out. **Fig. 6.11(A)** shows the current-voltage (I-V) characteristics of the hetero-junctions of GaN films which are grown at 2, 4.5 and 6 sccm N_2 flow rate. The fabricated hetero-junctions exhibit a good rectifying behavior at 1V with I_F/ I_R~ 39, 155, 388 for the GaN layers grown at 2, 4.5 and 6 sccm sample, respectively. (I_F and I_R stand for the forward and reverse currents, respectively). The reverse leakage current values are found to be -1.2x10^{-3}, -2.6x10^{-4} and 9x10^{-6} A at −1V respectively for these junctions. The observed low reverse leakage current for GaN/Si heterojunction grown at 6sccm nitrogen flow can be attributed to the low defect density in this film. The barrier height (BH) φ_b and ideality factor is calculated by fitting standard diode equation. It can be seen that the BH large and ideality factor is low for the heterojunction grown at 6 sccm. The reduction in barrier height and high ideality factor observed (**Fig. 6.11 (b)**) for the films grown at 2 and 4.5 sccm nitrogen flow is due to dislocations and other defects[37–39].

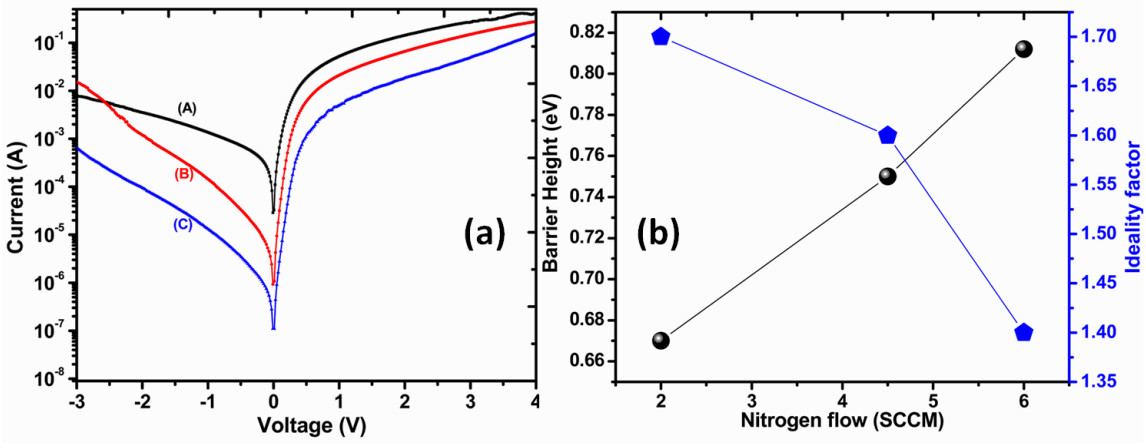

Fig.6.11: (a) *Shows the I-V characteristics* ***(b)*** *plot of Barrier height and ideality factor of GaN film grown at (A) 2sccm (B) 4.5sccm and (C) 6sccm nitrogen flow rate at fixed substrate temperature and Ga k-cell temperature of 630^{o}C and 1000^{o}C, respectively.*

The log-log plots of I-V in **Fig. 6.12** show three distinct voltage dependent denoted as I, II, III. At low forward bias voltage (<0.1V) (region I), the relation is linear and can be attributed to the thermally generated carrier tunneling. The observed high resistance at low voltage can be due to the presence of unintentionally formed thin SiN_x layer which limits the current **Fig. 6.12.** In region II, the voltage correspond to 0.08<V<0.8 the corresponding forward current increases exponentially following the equation I~exp(αV), which could be due to the recombination-tunneling mechanism[40–42]. The constant α has been evaluated by fitting the experimental data region II of log-log plot of I-V curve as shown in **Fig. 6.12**. At higher forward voltage i.e. V>1V (region III), the current is approximately square of the applied voltage ($I \sim V^2$) which suggests a space charge limited current conduction (SCLC)[40,46].

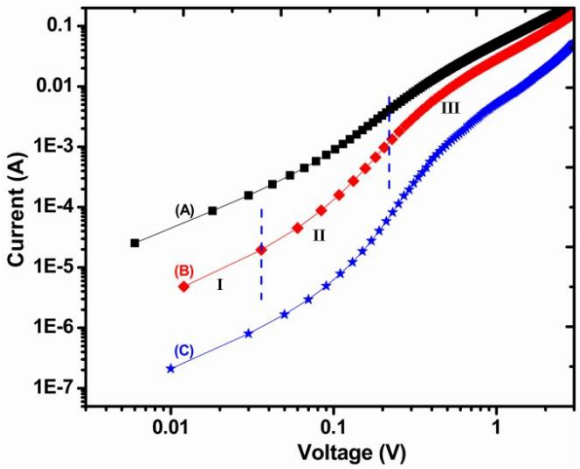

Fig.6.12: *Log-log plots of current-voltage characteristic under forward bias for GaN/p-Si(111) hetero-junctions grown at (A) 2sccm (B) 4.5sccm and (C) 6sccm nitrogen flow rate.*

6.5 Ga flux induced morphological evolution of GaN Nanostructure:

To study the Ga flux dependent morphological evolution, we have grown samples by varying the Ga k-cell temperature as 900, 1000 and 1100^{o}C while keeping the substrate temperature at 650^{o}C and N_2 flow rate as 4.5sccm. -**Fig. 6.13(a-c)** shows plan view FE-SEM images of the samples grown with different Ga fluxes. **Fig. 6.13 (a)** is the FE-SEM image for the sample grown at 900^{o}C k-cell temperature; which suggests morphology consists of quasi-aligned nanorods. The sample grown with Ga k-cell temperature of 1000^{o}C, the FE-SEM image and RHEED shown in **Fig. 6.13(b and b')** consists of both the nanowall network and tilted nanorods. **Fig. 6.13 (c)** shows the FE-SEM image of the GaN film grown at 1100^{o}C k-

cell temperature, and the morphology tends towards being a 2-D film formed by coalesced features. The corresponding RHEED pattern in **Fig. 6.13 (c')** is streaky indicating a 2-D growth mode.

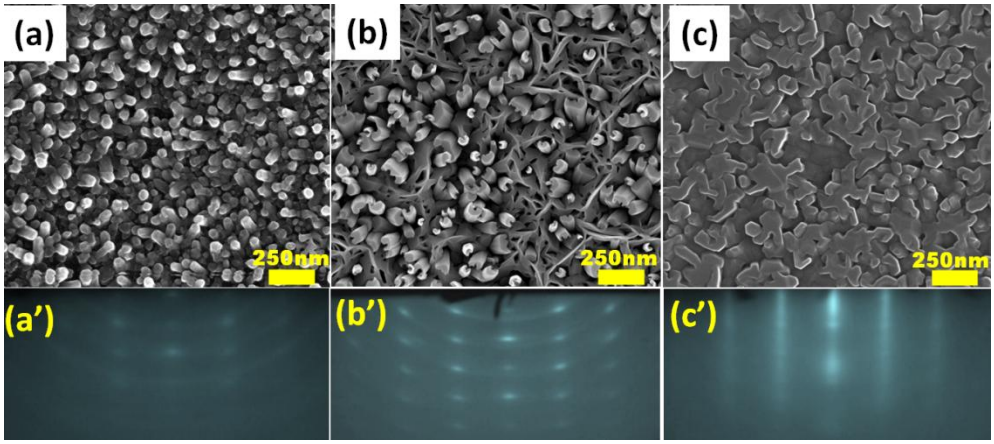

Fig.6.13(a-c): *Plan view of FE-SEM image with their respective RHEED pattern (a'-c') taken along the [11-20] zone axis of GaN film grown at Ga k-cell temperature (a) 900^{o}C (Sample (A)) (b) 1000^{o}C (Sample (B)) and (c) 1100^{o}C (Sample (C)) with fixed substrate temperature of 650^{o}C and nitrogen flow rate of 4.5sccm.*

To study crystal phase and quality, we have performed X-ray diffraction measurements and corresponding 2θ-ω scans are shown in **Fig. 6.14**(a) for GaN films grown with 900^{o}C, 1000^{o}C and 1100^{o}C k-cell temperature, respectively. As in RHEED, X-ray diffraction shows only (0002) and (0004) planes manifesting the formation of single crystalline Wurtzite GaN. The sample (A) grown at 900^{o}C k-cell temperature shows a high out-of-plane strain but no in-plane strain due to less thickness, off-axis reflection of crystal planes of wurtzite GaN is difficult to acquire as shown in **Fig. 6.14(a).** We observe that off-axis reflections are out of the detection limit of our instrument. For the film (sample -B) grown at 1000^{o}C k cell temperature (**Fig. 6.14(b)),** we observe that the in-plane strain of 2.1x10^{-3} and out plane strain is 4x10^{-4}, respectively while that at Ga k-cell temperature is 1100^{o}C shows relatively less in-plane and out of plane strains in the film of about 2.1x10^{-4} and 4x10^{-4} reiterating the high crystalline quality of the GaN films. **Fig. 6.15(a)** shows a phi scan for the (10-11) planes of a GaN film grown on a Si(111) substrate. It is clear from **Fig. 6.15(a)** that the GaN film shows the six-fold azimuthal symmetry consistent with the wurtzite crystal structure with the GaN film (0001) orientation parallel to the (111) of silicon.

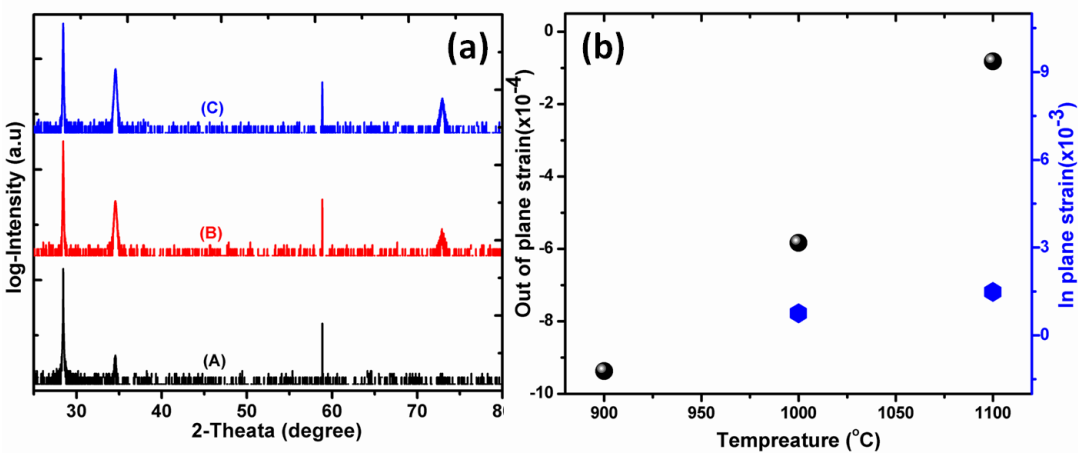

Fig.6.14: (a) *HR-XRD 2θ-ω scans* ***(b)*** *plot of strain along in-plane (a-axis) and out of plane (c-axis) of GaN film grown at (A) 900°C (B) 1000°C and (C) 1100°C Ga k-cell temperature.*

The optical properties of the samples were probed by Cathodo-luminescence (CL) measurements. **Fig. 6.15(b)** shows the room temperature CL spectra of the obtained GaN films (sample (A-C)). The samples (A and B) show near band emission (NBE) at 3.432 eV, which is slightly blue-shifted as compared to sample (C), suggesting that higher Ga flux results in films with tensile stress. The intensity of band edge in the sample (C) is nearly four times higher than that of sample (A-B), thus high optical quality.

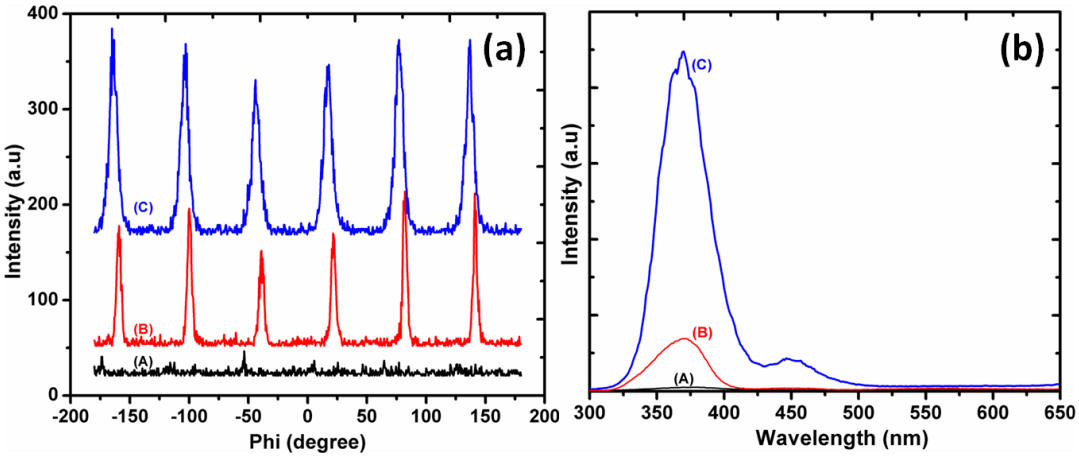

Fig.6.15: *(a) In-plane phi-scan (b) Room temperature CL spectra of GaN film grown at (A) 900°C (B) 1000°C and (C) 1100°C Ga k-cell temperature, respectively.*

Room temperature current-voltage (I-V) characteristics of this GaN/Si hetero-junction are shown in **Fig.6.16 (a).** The parameters barrier height (φ_b) and ideality factor (η) dependence on Ga flux are shown in **Fig. 6.16 (b)**. Schottky barrier height and ideality factor

depend on Ga k-cell temperature. The film which was grown at 1100^{o}C showed the best rectifying behaviour among all the films studied, while φ_b is increasing and η decreasing with increasing Ga flux. The low barrier heights and high ideality factors observed in sample (**A** and **B**) are probably due to structural defects at the interface.

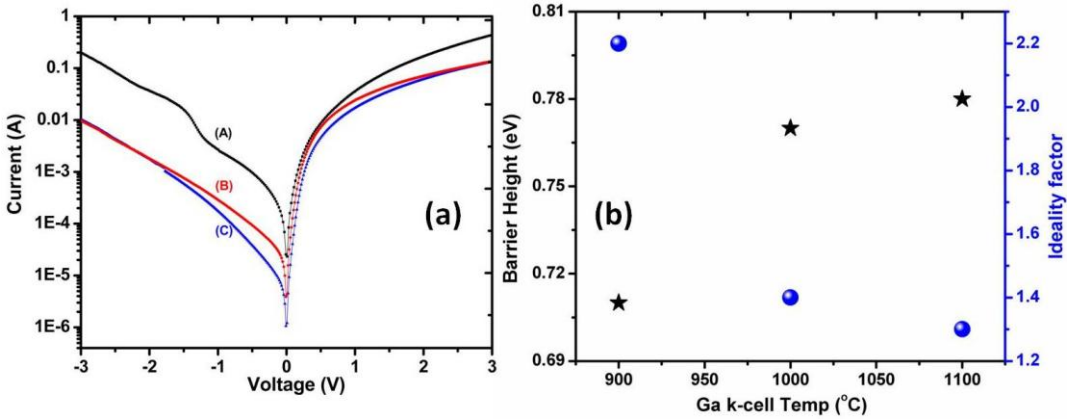

Fig.6.16: (a) *Shows the I-V characteristics* ***(b)*** *Plots of barrier height and ideality factor of GaN film grown at (A) 900^{o}C (B) 1000^{o}C and (C) 1100^{o}C Ga k-cell temperature.*

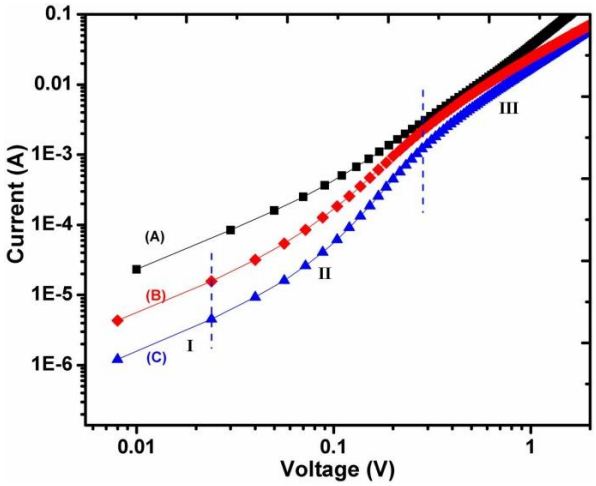

Fig.6.17: *Log-log plots of the current-voltage characteristic under forward bias for GaN/p-Si(111) hetero-junction grown at (A) 900^{o}C, (B) 1000^{o}C and (C) 1100^{o}C Ga k-cell temperature, respectively.*

The log-log plot of forward bias can be divided into three different regions depending on the applied voltage as shown in **Fig. 6.17**. For the first sample (A), the first region ($V <$ 0.05) showed a linear dependence of the current on the voltage ($I \alpha V$) while II and III are not observed probably due to the presence of a large density of trap states. For sample (**B** and **C**), all three regions were observed, indicating fewer trap states in this film. The first region

showed Ohmic behaviour the second exponential region ($0.05 < V < 0.5$) displaying a higher device quality, than the previous sample. In the third region ($0.5 < V < 1$), the *I-V* characteristics follows a power law ($I \sim V^n$) attributed to the space-charge-limited current (SCLC).

6.6 The origin of shape, orientation and structure of spontaneously formed wurtzite GaN-nanorods on cubic Si (001) surface:

The cubic atomic arrangement in the Si(100) surface can provide a template for the growth of Zinc-Blende GaN films. However the instability in the structure and the large mismatch discussed earlier, can lead to highly disordered and strained films. We have studied the evolution of a GaN films on the atomically clean Si(1000) surface sunder nitrogen rich condition (4.5sccm). **Fig. 6.18(a**) is the plan view FESEM image of the GaN film, which shows a high density of 1-D nanostructures of ≈ 80nm diameter and 500-600 nm height.

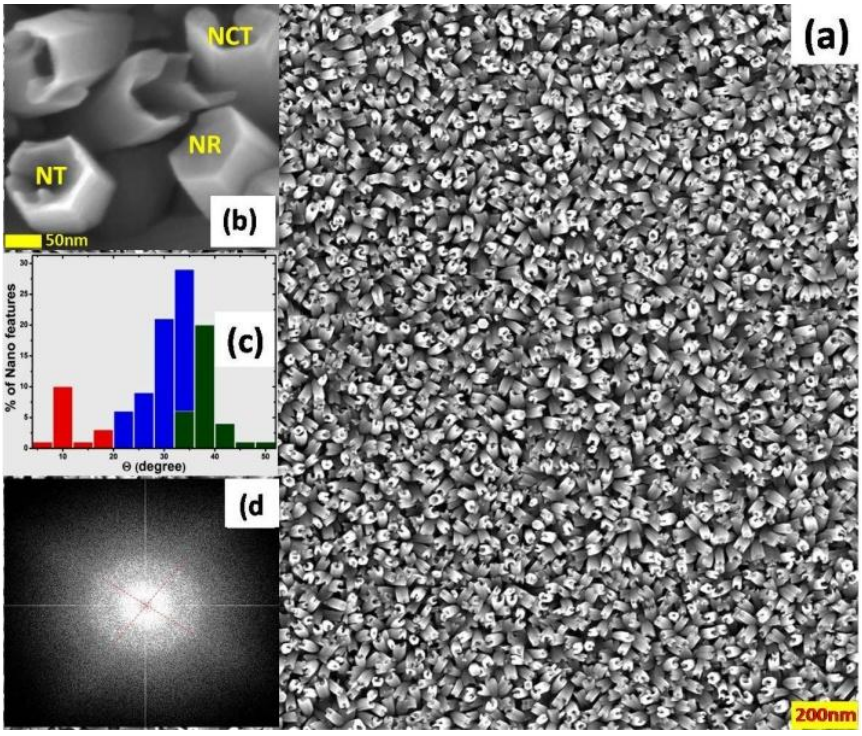

Fig. 6.18 *(a) Plan view FESEM image of the 1-D nanostructures grown on Si(001)-2×1, (b) Magnified region showing the morphology of rods (NR), tubes (NT) and sieves (NCT), (c) Histogram plot of angular tilt Θ of the three types 1D nanostructures with respect to surface normal (red-rods, green -tubes and blue is c-tubes) and (d) 2D FFT image acquired over plan view FESEM image, showing a 4-fold symmetry corresponds to the growth along Si(111) planes.*

Few of these are solid rods (NRs) (density ~$4X10^6$ cm^{-2}) but most of them are either nanotubes (NT) (~$2X10^9 cm^{-2}$) or nano C-tubes (NCT) (~$3X10^8 cm^{-2}$), whose morphology is clearly evident in **Fig. 6.18(b).** These columnar nanostructures are seen to be tilted with respect to substrate [0001] normal direction. To understand the orientation in the columnar nanostructures with respect to surface normal, we plot a histogram of the distribution of the angular spread of the rods, tubes and c-shaped sieves (in different colours) in **Fig. 6.18(c),** by estimating the tilt angle (Θ) from the projection of the 600 nm 1-D structures in the plan view FESEM image. The histogram clearly shows that the solid rods are tilted by about ≈ 10^o (red) with respect to surface normal while the tubes are tilted between 20-35^o (blue) and c-shaped tubes aligned with an angle of 30-45^o(green). We also present the two dimensional Fast Fourier Transform (2D FFT) on the plan view FESEM image as shown in **Fig. 6.18(d),** which shows a bright circular concentric region proximal to the centre, indicating randomness at longer length scales, and four mutually perpendicular faint lobes (lines are drawn to guide the eye), showing a fourfold symmetric arrangement of these tilted 1-D nanostructures. **Fig. 6.19** contains the diffraction pattern obtained by RHEED of the film and SAED of single rod.

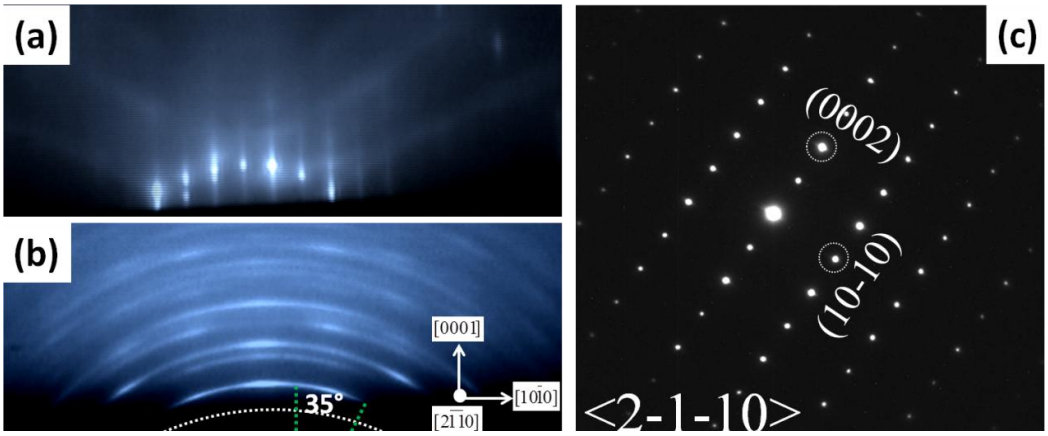

Fig. 6.19 *shows RHEED pattern acquired along <11-20> direction for (a) clean Si(001)-2×1,(b) GaN overlayer and (c) SAED pattern acquired from one of the nanorods along <2-1-10> zone axis. (0002) and (10-10) spots are marked with dashed circle.*

Fig. 6.19(a) shows a streaky RHEED pattern with faint Kikuchi lines acquired along the <2-1-10> direction for clean Si(001) (2X1) substrate, and **Fig. 6.19(b**) is obtained after 0.6μm GaN is grown on clean Si(001)-2X1. **Fig. 6.19**(b) displays anisotropic diffraction spots (transmission through 3D features) which have an angular spread upto 35° with respect to the specular(0, 0) reflection, which can originate either due to a polycrystalline film or an

orientational disorder of the 1-D formations. Due to the spread in the spot intensity, it is difficult to find the exact ratio of the inter–spacing between RHEED spots in [0001] and [10-10] direction, but considering the mid-point of these arcs, it roughly suggests that the features have wurtzite structure. To see the atomic structure in each 1-D feature, selected area electron diffraction (SAED) along the zone axis <2-1-10> obtained by TEM on one of these 1-D features, is shown in Fig.2c. This confirms that the observed 1-D nanostructures are single crystalline and wurtzite in structure with [0001] as the growth direction, with an orientational disorder which is also evident in **Fig. 6.18(a)**.

To further probe the crystal quality, structure and angular tilt, we present the x-ray diffraction pattern in **Fig. 6.20** which consists of Bragg reflection planes of the substrate (Si) and the GaN overlayer. The Θ-2Θ scan re-confirms that the film is single-crystalline wurtzite in structure, with three diffraction peaks at $2\theta=36.8^{o}$, 32.4^{o} and 34.5^{o}, corresponding to the GaN (10-11) s-, (10-10) m- and (0002) c- planes. The reflection from c-plane originates from the terraces of the solid nanorods (NRs). The intense peak is due to the (10-11) s- plane (28.6^{o} from surface normal) of the 1-D features that are close to being parallel to the substrate (001) plane confirming their tilt of about 30° to the substrate normal. The fact that the m-plane is the second most intense peak suggests that the 1-D formations are bound by the hexagonal facets and are exposed to XRD due to their tilt with respect to the substrate normal. Other reflections (10-12) and (10-13) at 42.8° and 31.7° with respect to the (0001) direction are also exposed because of the tilt in the 1-D features. From the symmetric (0002) and asymmetric (10-11) reflections, the lattice constants are determined to be a=0.32 nm and c=0.52 nm, which is characteristic of a relaxed wurtzite GaN unit cell. The other peaks at $2\theta=69.4^{o}$ and 48.3^{o} are from Si (400) and (220), and overlap with GaN (11-20) and (10-13) reflections. The XRD again provides no evidence for zinc blende GaN nanostructure formation on the cubic Si(001) surface. The inset of **Fig. 6.20** is the Cathodo-luminescence spectrum obtained for this film at room temperature at 9keV electron beam energy. The spectrum shows a strong band-edge emission at 3.4 eV with full width at half maximum (FWHM) ≈120.0 meV, and the absence of any defect related peaks in the 2.0 to 2.8 eV region, confirming that the GaN NR, NT, NCTs formed are relaxed with minimal extended defects. The 120.0 meV width of the band-edge emission which is an order higher than bulk value of ≈10meV may be a consequence of the tilt in the nanostructures, due to anisotropic

CL emission from different planes normal to the detector as seen in XRD results. Raman measurements at room temperature (not shown here) confirm the strain-free nature of the film, by the presence of only the characteristic E_2(high) Raman mode at 567 cm^{-1}, with FWHM of ≈6 cm^{-1}.

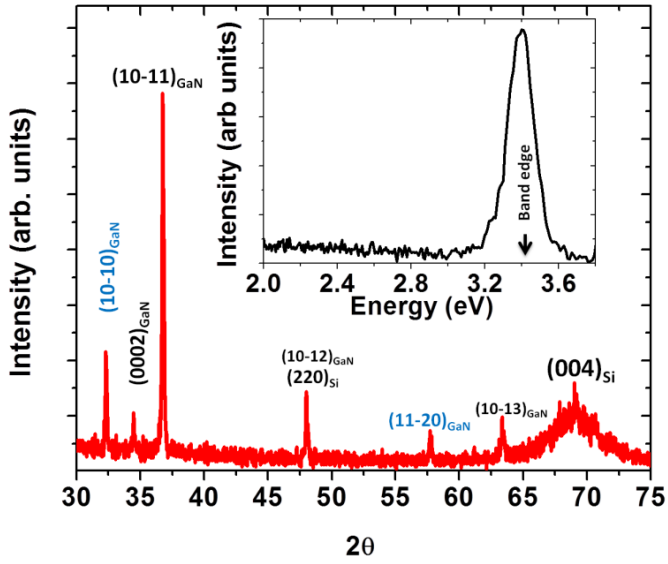

Fig. 6.20 the *XRD pattern of the wurtzite crystal with the inset showing the band-edge emission in the CL spectra acquired at room temperature.*

To probe the role of the interface in determining the epitaxy and morphology of the GaN overlayer feature on the Si(001) substrate, we have performed HR-TEM studies whose results are shown in **Fig. 6.21**. **Fig. 6.21**(a) is the low resolution cross-sectional bright-field image which shows that most of the 500-600nm long 1-D features seen are tilted by ≈35° with respect to the Si(001) surface normal as discussed earlier. **Fig. 6.21**(b) is the interfacial details of the 10° tilted GaN nanorod, with a ≈3nm thick unintentional amorphous silicon-nitride layer. We have confirmed the chemical composition of the layer by XPS (not shown here) in a separate experiment. It has been observed in the past[44] that when growth occurs in nitrogen rich condition by PA-MBE on Si(111) and Si(001) surface, since the Si-N bond (4.5eV/bond) is stronger than GaN (2.2eV/bond), an inhomogeneous SiN_x interfacial layer formation precedes the growth of GaN. We observe the atomic arrangement in the Si(111) (d_{111}≈0.313 nm) and GaN($d_{10\text{-}10}$ ≈0.274 nm, d_{0002}≈0.257 nm, $d_{10\text{-}11}$≈0.241 nm, $d_{11\text{-}20}$≈0.158 nm etc) planes. The absence of reflections like d_{101}≈0.431 nm, d_{200}≈0.335 nm, d_{201}≈0.288 nm planes rules out the presence of the crystalline α-Si_3N_4 phase, suggesting that the interfacial layer is an amorphous SiN_x phase. The inhomogeneous silicon nitride layer consists of

mounds, between which we observe regions of exposed Si(001) surface, where the epitaxial GaN (0001) oriented rods nucleate. These grow with their c- planes parallel to the Si(111) atomic planes, thus forming a tilt angle of $\approx 10^{o}$ w.r.t the Si(001) surface normal. **Fig. 6.21**(c) shows the digitally proceed IFFT image of the direct contact region marked in **Fig. 6.21**(b), clearly showing the misfit dislocation at the interface (shown by arrows). **Fig. 6.21**(b) also shows that though the nanorods nucleate at the area of direct contact, it later also grows laterally on the amorphous silicon-nitride mounds. **Fig. 6.21**(c) shows the high resolution XTEM image of the $\approx 35^{o}$ tilted nanotube and the Si(001) substrate, again formed at the region of direct contact. Here, we clearly observe that the Si(111) close packed planes align with GaN(01-01)planes, forming the m-faceted 1-D nanotubes with a tilt of $\approx 35^{o}$. This also explains the fourfold symmetry of the nanotubes observed in the FFT images in **Fig.6.18(d)**, since the top view of Si(001) surface consists of four perpendicular Si(111) planes.

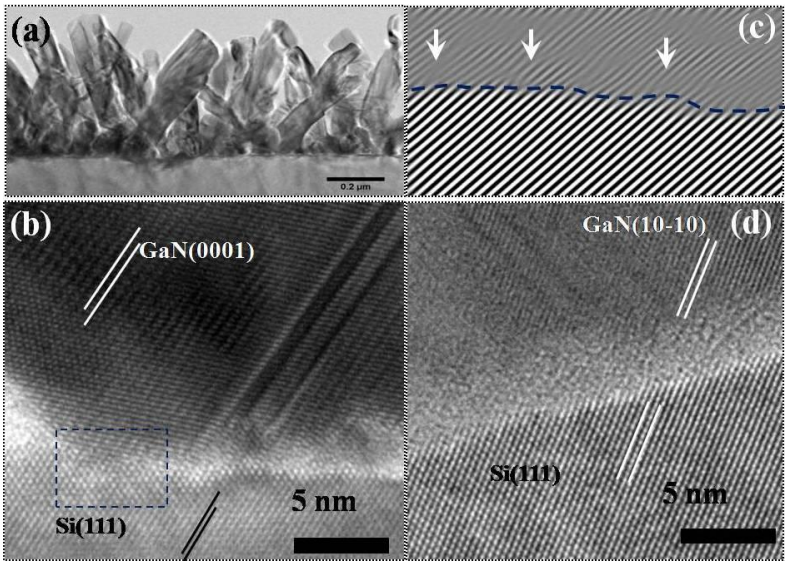

Fig. 6.21 *(a) Cross-section bright field TEM images showing the overall morphology of the 1-D features (b) High resolution XTEM images acquired at the GaN/Si(100) interface of a typical 10^{o} tilted nanorods (c) Inverse FFT of marked region in Fig.(b) where GaN nanotube is in contact with substrate, with misfit dislocations shown as arrows (d) Interface of the nanotubes with 35^{o} tilt with respect to substrate normal, shows that the GaN(10-10) planes are parallel to the Si(111) planes.*

To understand why the solid nanorods and the nanotubes have different tilt angles, we focus on the role of the threading dislocations formed at the respective interfaces due to differences in the epitaxial relations. We carried out two beam TEM diffraction contrast imaging whose results are, shown in **Fig. 6.22**. **Fig. 6.22**a and **Fig. 6.22** a' are the dark field

images acquired from one of the ≈10^{o} tilted nanorod. The arrows marked in **Fig. 6.22**a, show clearly the dislocation visible in the *g*=0002 condition, but not in the g=10-10 (**Fig. 6.22**a').

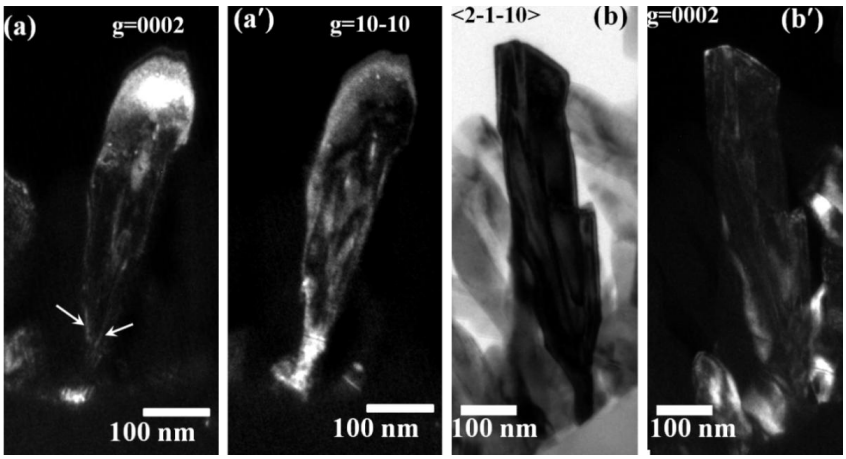

***Fig. 6.22 (a)** and **(a')** Dark field images of a nano-rod obtained at g=0002 and **g**=10-10. **(b)** XTEM bright field image a nano-tube acquired along zone axis <2-1-10> and **(b')** is the dark field image of the same rod obtained at **g**=0002.*

The disappearance of dislocations at g.b=0, suggests that the dislocations are of screw type with burger vector c/2[45–47], and it clearly shows that the dislocation emerge from the surface as Frank Partials in c-direction with the partials converging at the silicon surface at the direct contact interface region. If the dislocations are mutually far apart, we observe the branching and spiralling of the dislocations that thread through the 1-d features and is imaged in **Fig. 6.22(**b) as a bright field XTEM image taken along the <2-1-10> zone axis. Its corresponding dark field image with *g*=0002 (Fig.5b') shows that the screw dislocations may not converge to a common contact point and thus eventually can lead to the branching of the rods/tubes. The presence of several proximal dislocations appears to promote their merger, that provides the extra energy necessary to expel the dislocation and form the internal surfaces for the hollow tubular formations[48,49]. With the Si{111} and GaN{10-10} planes being parallel, makes the c-oriented tubes tilted by ≈35° with respect to the surface normal. Thus, the presence or absence of the threading dislocations determine the tilt of the 1-D features ranging from solid rods with less tilt (≈10^{o}) and tubes tilted upto ≈35^{o} and c-shaped tubes upto ≈45^{o}.

We now consolidate the results in the form of a schematic model in **Fig. 6.23**, to explain the origin of the morphology of the wurtzite 1-D nanostructures formed on the Si(001)

interface by PA-MBE, which shows the relation between the atomic planes and the tilt angles of the GaN 1-D features.

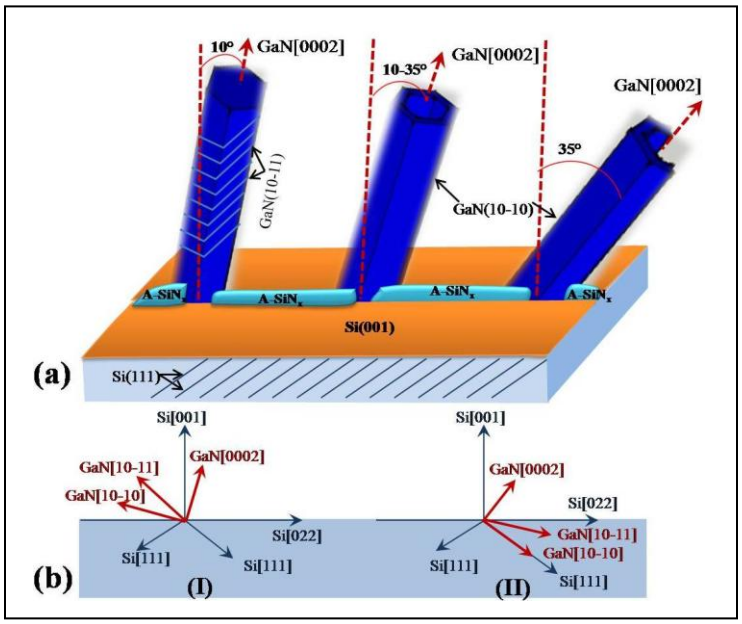

Fig. 6.23(a): S*chematic model of 1D nano-structure formation of rods, tubes and c-tubes with tilt angles of 10^o, 30^o and 45^o. (b) Cross-sectional view of the plane directions of GaN and Si at tilt angle of (I) ≈10^o and (II) ≈35^o.*

In the growth performed under nitrogen rich conditions the nitrogen plasma forms an instantaneous SiN_x layer on the Si(001) surface, whose in-homogeneity provides regions of direct contact for epitaxial growth of GaN on Si(001). The retardation of Ga adatoms by the collision of the N_2 molecules causes supersaturation at the interfacial misfit dislocations. This nucleates GaN around the interfacial screw dislocation and follows a Frank type of spiral growth[50] into 1-D nano-features. Since the surface free energy of Si(111) and GaN (10-10) are lowest and with the mismatch between Si(111)(d=0.313nm) and GaN(10-10)(d=0.273nm) planes being minimal it encourages the epitaxial growth of the majority of nanotubes that are tilted by ≈35^o. We also observe that the presence of the amorphous SiN_x layer around these direct contact regions enables a lateral growth of the rods without the epitaxial influence of the Si(001) substrate into their own hexagonal wurtzite equilibrium crystal structure. It can also be noted that since the d-spacing of GaN(11-20) is twice that of Si(111), there can be an azimuthal rotation of 30^o such that the GaN(11-20) planes are parallel to Si(111) planes as shown in Fig.6(b). Since Si(100) surface has four sets of Si(111) planes, a 4 fold symmetry of the nanostructure growth is observed in our studies. The next

preferred epitaxial relationship can be where Si(111) planes are parallel to the GaN(10-11) planes which results in our observation of a few solid hexagonal bounded (m-facet) nanorods that are tilted by ≈10^o with the surface normal. Our studies further show that the low tilted (≈10^o) compact nanorods consist of a single screw dislocation threading through them provides the nucleation steps for the spiral 1-D growth. However, if there is a local high dislocation density in the nanorods they can merge and expel the dislocation to overcome the surface energy required for the creation of a new inner surface. This promotes the formation of >25^o tilted nano-feature such as nanotubes and c-shaped tubes.

6.7 Summary:

In conclusion, in the present chapter we have proposed the phase diagram of GaN morphological evolution on Si(111) substrate is studied by varying a) substrate temperature, b) Ga flux and c) N_2 flux and is depicted in **Fig.6.24**.

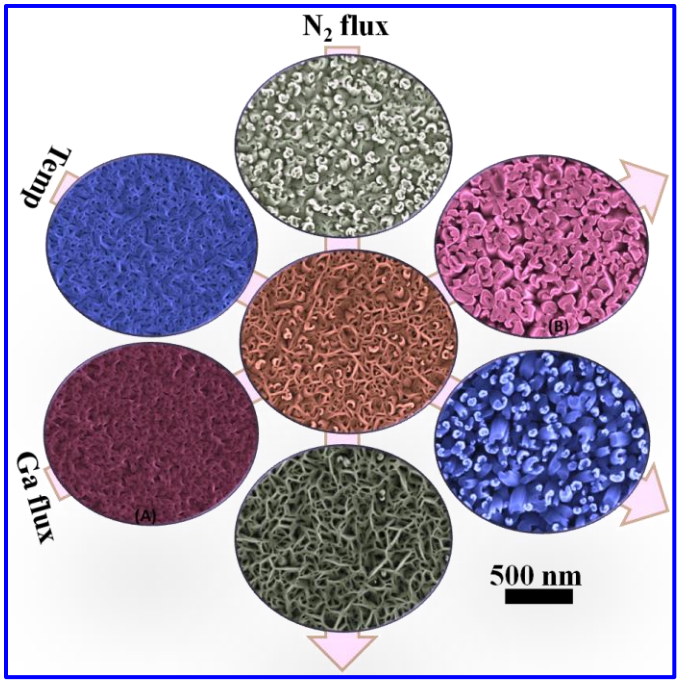

Fig. 6.24: *Plan view FESEM images of GaN films grown at three pathways by varying substrate temperature, nitrogen flux rate and gallium flux (marked A and B grown at 650^{o}C substrate temperatures) respectively.*

It is evident from the presented result that the morphological evolution of GaN films on Si(111) surface is strongly depends on sticking coefficient of Ga adatoms. The structural and optical properties of these films are investigated. The electrical properties of GaN/p-

Si(111) hetero-junctions were also studied and it shows inverted rectification behavior. The higher rectification ratio was observed in the case of GaN/p-Si(111) hetero-junction has aligned nanorods and nanowall morphology. The improved ideality factor and higher barrier height is observed in nanowall and nanorods is attributed to the decreased defect mediated tunneling nature. With a multi-technique approach, we have addressed and modelled the atomic details of 1-D nanostructures spontaneous formed at the GaN/Si (100) interface in nitrogen rich conditions. We show that the surface free energy and lattice mismatch determine the epitaxial relation between the columnar growth and the substrate atomic planes, which consequently influence the morphology and orientation of the nano-features. We demonstrate the dominant role of interfacial misfit induced dislocations and their merger in determining the morphology and tilt of the solid, tubes, c-tubes, and branched nanorods. We elucidate the influence of the interfacial SiN_x mounds on the structure and growth direction of the hexagonal wurtzite 1-D features on cubic Si(001) surface. We believe this study provides direct atomic evidence for the generic reasons that are involved in misfit dislocation mediated nanostructure formation. Such studies are essential in explaining the origin, orientation, shape and structural evolution, to identify the growth kinetic handles that can be tuned to tailor make desired self-assemblies of nanostructures with desired properties.

6.8 REFRENCES:

1. S. D. Carnevale, J. Yang, P. J. Phillips, M. J. Mills, and R. C. Myers, *Nano Lett.*, 2011, **11**, 866–71.

2. H. Baek, C.-H. Lee, K. Chung, and G.-C. Yi, *Nano Lett.*, 2013, **13**, 2782–5.

3. P. Kumar, J. Kuyyalil, and S. M. Shivaprasad, *Appl. Phys. Lett.*, 2010, **97**, 221913.

4. J. Narayan and B. C. Larson, *J. Appl. Phys.*, 2003, **93**, 278.

5. V. Lebedev, K. Tonisch, F. Niebelschutz, V. Cimalla, D. Cengher, I. Cimalla, C. Mauder, S. Hauguth, O. Ambacher, F. M. Morales, J. G. Lozano, and D. González, *J. Appl. Phys.*, 2007, **101**, 054906.

6. M. S. Kang, C.-H. Lee, J. B. Park, H. Yoo, and G.-C. Yi, *Nano Energy*, 2012, **1**, 391–400.

7. H. P. T. Nguyen, K. Cui, S. Zhang, M. Djavid, A. Korinek, G. A Botton, and Z. Mi, *Nano Lett.*, 2012, **12**, 1317–23.

8. K. D. Goodman, V. V. Protasenko, J. Verma, T. H. Kosel, H. G. Xing, and D. Jena, *J. Appl. Phys.*, 2011, **109**, 084336.

9. Q. Li and G. T. Wang, *Nano Lett.*, 2010, **10**, 1554–1558.

10. W. Guo, M. Zhang, A. Banerjee, and P. Bhattacharya, *Nano Lett.*, 2010, **10**, 3355–9.

11. H. P. T. Nguyen, K. Cui, S. Zhang, S. Fathololoumi, and Z. Mi, *Nanotechnology*, 2011, **22**, 445202.

12. L. Cerutti, J. Ristić, S. Fernández-Garrido, E. Calleja, A. Trampert, K. H. Ploog, S. Lazic, and J. M. Calleja, *Appl. Phys. Lett.*, 2006, **88**, 213114.

13. T. Kuykendall, P. Ulrich, S. Aloni, and P. Yang, *Nat. Mater.*, 2007, **6**, 951–6.

14. W. Guo, M. Zhang, P. Bhattacharya, and J. Heo, *Nano Lett.*, 2011, **11**, 1434–8.

15. P. Kumar, M. Tuteja, M. Kesaria, U. V. Waghmare, and S. M. Shivaprasad, *Appl. Phys. Lett.*, 2012, **101**, 131605.

16. T. Stoica, E. Sutter, R. J. Meijers, R. K. Debnath, R. Calarco, H. Lüth, and D. Grützmacher, *Small*, 2008, **4**, 751–4.

17. C. Hahn, Z. Zhang, A. Fu, C. H. Wu, Y. J. Hwang, D. J. Gargas, and P. Yang, *ACS Nano*, 2011, **5**, 3970–6.

18. S. Li and A. Waag, *J. Appl. Phys.*, 2012, **111**, 071101.

19. K.-Q. Peng, X. Wang, X.-L. Wu, and S.-T. Lee, *Nano Lett.*, 2009, **9**, 3704–9.

20. Y. Kuwahara, T. Fujii, T. Sugiyama, D. Iida, Y. Isobe, Y. Fujiyama, Y. Morita, M. Iwaya, T. Takeuchi, S. Kamiyama, I. Akasaki, and H. Amano, *Appl. Phys. Express*, 2011, **4**, 021001.

21. J. Wu, *J. Appl. Phys.*, 2009, **106**, 011101.

22. T. J. Kempa, B. Tian, D. R. Kim, J. Hu, X. Zheng, and C. M. Lieber, *Nano Lett.*, 2008, **8**, 3456–60.

23. M. I. den Hertog, F. González-Posada, R. Songmuang, J. L. Rouviere, T. Fournier, B. Fernandez, and E. Monroy, *Nano Lett.*, 2012, **12**, 5691–6.

24. M. Kesaria and S. M. Shivaprasad, *Appl. Phys. Lett.*, 2011, **99**, 143105.

25. P. Kumar, M. Tuteja, M. Kesaria, U. V. Waghmare, and S. M. Shivaprasad, *Appl. Phys. Lett.*, 2012, **101**, 131605.

26. M. K. Rajpalke, B. Roul, M. Kumar, T. N. Bhat, N. Sinha, and S. B. Krupanidhi, *Scr. Mater.*, 2011, **65**, 33–36.

27. W.-Y. Shiao, C.-Y. Chi, S.-C. Chin, C.-F. Huang, T.-Y. Tang, Y.-C. Lu, Y.-L. Lin, L. Hong, F.-Y. Jen, C. C. Yang, B.-P. Zhang, and Y. Segawa, *J. Appl. Phys.*, 2006, **99**, 054301.

28. F. Cheregi, A. Vinattieri, E. Feltin, D. Simeonov, J.-F. Carlin, R. Butté, N. Grandjean, and M. Gurioli, *Phys. Rev. B*, 2008, **77**, 125342.

29. S. D. Singh, S. Porwal, a. K. Srivastava, T. K. Sharma, and S. M. Oak, *J. Appl. Phys.*, 2011, **110**, 123523.

30. M. X. Feng, J. P. Liu, S. M. Zhang, D. S. Jiang, Z. C. Li, K. Zhou, D. Y. Li, L. Q. Zhang, F. Wang, H. Wang, P. Chen, Z. S. Liu, D. G. Zhao, Q. Sun, and H. Yang, *Appl. Phys. Lett.*, 2013, **103**, 043508.

31. I. Berishev, A. Bensaoula, I. Rusakova, A. Karabutov, M. Ugarov, and V. P. Ageev, *Appl. Phys. Lett.*, 1998, **73**, 1808.

32. M. A. Reshchikov, D. Huang, L. He, H. Morkoç, J. Jasinski, Z. Liliental-Weber, S. S. Park, and K. Y. Lee, *Phys. B Condens. Matter*, 2005, **367**, 35–39.

33. R. . Davis, S. Einfeldt, E. . Preble, A. . Roskowski, Z. . Reitmeier, and P. . Miraglia, *Acta Mater.*, 2003, **51**, 5961–5979.

34. F. Furtmayr, M. Vielemeyer, M. Stutzmann, J. Arbiol, S. Estradé, F. Peirò, J. R. Morante, and M. Eickhoff, *J. Appl. Phys.*, 2008, **104**, 034309.

35. S. S. Iyer, *J. Appl. Phys.*, 1981, **52**, 5608.

36. T. N. Bhat, M. K. Rajpalke, B. Roul, M. Kumar, and S. B. Krupanidhi, *J. Appl. Phys.*, 2011, **110**, 093718.

37. M. Dutta and D. Basak, *Appl. Phys. Lett.*, 2008, **92**, 212112.

38. S. Mridha and D. Basak, *J. Appl. Phys.*, 2007, **101**, 083102.

39. M. K. Rajpalke, T. N. Bhat, B. Roul, M. Kumar, P. Misra, L. M. Kukreja, N. Sinha, and S. B. Krupanidhi, *J. Cryst. Growth*, 2011, **314**, 5–8.

40. R. Ghosh and D. Basak, *Appl. Phys. Lett.*, 2007, **90**, 243106.

41. T. N. Bhat, M. K. Rajpalke, B. Roul, M. Kumar, and S. B. Krupanidhi, *J. Appl. Phys.*, 2011, **110**, 093718.

42. M. Kumar, B. Roul, T. N. Bhat, M. K. Rajpalke, A. T. Kalghatgi, and S. B. Krupanidhi, *J. Nanomater.*, 2011, **2011**, 1–7.

43. M. Kumar, T. N. Bhat, M. K. Rajpalke, B. Roul, A. T. Kalghatgi, and S. B. Krupanidhi, *Nanoscale Res. Lett.*, 2011, **6**, 609.

44. E. Calleja, J. Ristić, S. Fernández-Garrido, L. Cerutti, M. A. Sánchez-García, J. Grandal, A. Trampert, U. Jahn, G. Sánchez, A. Griol, and B. Sánchez, *Phys. Status Solidi*, 2007, **244**, 2816–2837.

45. D. Cherns, L. Meshi, I. Griffiths, S. Khongphetsak, S. V Novikov, N. R. S. Farley, R. P. Campion, and C. T. Foxon, *Appl. Phys. Lett.*, 2008, **93**, 111911.

46. C. T. Foxon, S. V. Novikov, J. L. Hall, R. P. Campion, D. Cherns, I. Griffiths, and S. Khongphetsak, *J. Cryst. Growth*, 2009, **311**, 3423–3427.

47. D. Cherns, L. Meshi, I. Griffiths, S. Khongphetsak, S. V Novikov, N. Farley, R. P. Campion, and C. T. Foxon, *Appl. Phys. Lett.*, 2008, **92**, 121902.

48. S. A Morin, M. J. Bierman, J. Tong, and S. Jin, *Science*, 2010, **328**, 476–80.

49. S. Jin, M. J. Bierman, and S. A. Morin, *J. Phys. Chem. Lett.*, 2010, **1**, 1472–1480.

50. F. C. Frank, *Acta Crystallogr.*, 1951, **4**, 497–501.

Chapter 7:

Summary, Conclusions and Future Outlook:

7. Summary, Conclusions and Future Outlook:

The fabrication of high efficiency optoelectronic devices made of III-nitrides based materials has been retarded due to non-availability of compatible [1–4] substrates. Among the available materials, sapphire and Si are the most appropriate compared to any other [5–7], though even they have significant lattice and thermal expansion coefficient mismatches that induce defects, which require removal. Current research in this area involves finding new growth strategies such as modification of substrate surfaces via nitridation, and formation of nanostructures for enhanced device performance[8–20]. In this dissertation we have explained alternative routes of growth of GaN films and demonstrate several paths to ascertain their high quality. Our aim in this work is to provide a complete phase diagram of morphological evolution of GaN on sapphire and Si substrates, and provide an insight into the underlying growth mechanisms of the different morphologies of GaN films and show the structure, morphology and properties relation. This work provides the first evidence of spontaneous formation of catalyst-free GaN nanowalls and nanocolumns on Al_2O_3(0001), Si(001) and Si(111) surfaces. This chapter provides a summary of the overall work presented in the thesis and the direction, future research can assume towards approaching the 'potential' these materials can offer.

7.1 Spontaneous growth of GaN nanostructures on Al_2O_3(0001):

In this section, we have demonstrated the spontaneous growth of GaN nanostructures by kinetic control nitrogen rich conditions. The formation of these nanostructures on Al_2O_3(0001) substrate is caused by a strain relaxation pathway resulting in defect free GaN films. There are a few reports on alternative ways to reduce dislocation density such as buffer layers, surfactants, super-lattice matching epitaxy and Epitaxial Lateral Overgrowth (ELOG) which have been successfully employed, though each suffers from serious limitations[21–25]. All these alternative techniques result in a reduction of dislocation density to certain extent. In order to further reduce the defect density to get efficient devices, nano-structuring of GaN, yields films with very low values of defect densities. Several issues in nanostructure growth formation using catalysts and performing selective area growth by lithography[21] can be mitigated modification of surfaces and employing kinetic control. In this direction, we have

chosen a low temperature regime which enables the growth of both epitaxial and defect and strain free films. In this work, we have demonstrated the spontaneous growth of self-aligned single crystalline GaN nanostructures by controlling the growth parameters, both on sapphire and Si surfaces by PA-MBE without the use of any external catalysts. In the first set of experiments, we have presented the formation and characterization of GaN nanostructures grown at low temperatures (480-630°C) in nitrogen rich (III:V=1:100) conditions. Hexagonal nanowall network of GaN which are open screw dislocation were observed to form in these conditions at low temperature and gallium flux. However in a very narrow growth parametric window to report the formation of self-aligned m-faceted GaN nanocolumns [26–29]. The formation of nanocolumns is shown to be driven by the size, shape and incline plane of apex of the nanowalls surrounding the voids. The wedge shaped hexagonal nanowall network is observed to cease to grow when its inclined face attains an r-plane (11-20) configuration and the arriving Ga adatoms funnel into the open void between the nanowalls causing a supersaturation in the voids. These voids being open screw dislocation provide the steps for nucleation of the nanocolumns spiral growth. The nanostructures formed are observed to possess a central dislocation-line and are self-assembled, c-oriented wurtzite films with high structural and optical quality. The results clearly show the dominant role of kinetics in determining the growth of nanostructures in such highly nitrogen rich conditions, which can be tuned to form a crystalline and ordered nanowall network and nanocolumn assembly. The investigation of structural and optical properties of these nanostructures reveals defect and strain free GaN nanostructures showing very sharp band edge emission and high structural quality.

7.2 Nitrogen plasma assisted surface modification of c-sapphire and Si(111) surface:

After investigation of the parametric dependence of kinetic controlled growth window of nanostructure formation on sapphire substrate, we have next carried out the nitridation studies of sapphire and Si (111) surfaces by Rf-plasma and its effect on the overgrown GaN films. We probe the parametric dependence of the nitridation mechanism of Al_2O_3 surface by radio frequency nitrogen plasma. Our analysis by XPS and RHEED shows that the chemical composition and structure varies with exposure time and is independent of nitrogen plasma fluence and substrate temperature. We also show that nitrogen incorporation into the

host material is diffusion limited process and involves the conversion of Al_2O_3 into AlN, which has a higher rate initially and then saturates after 6 hrs of nitrogen plasma exposure. We deposit a thin AlN layer on this saturated nitrided sapphire substrate, which was found to consist of nanorods with a bimodal diameter distribution and apex morphology. Upon growth of a thin layer of AlN on the nitrided sapphire substrate, bimodal c-oriented AlN nanocolumns are observed to be formed. The larger nanocolumns with pyramidal apex with axial screw dislocations are attributed to spiral growth that originate due to misfit at the interface. The smaller nanocolumns of AlN with oval apex are seen to be consequence of diffusion mediated nucleation growth, under N-rich conditions. However, both types of nanocolumns are seen to be single-crystalline, c–orientated and strain-relaxed with small difference in their in-plane rotation. By TEM studies we attribute that the faceted nanocolumns to be dislocation mediated, while the oval apexed features are diffusion limited. By RHEED we infer that the nano features having the pyramidal apex have the orientation relationship [11-20] $_{AlN}$// [1-100] $_{sapphire}$ with sapphire, while the oval shaped islands possess the epitaxial relation [0002] $_{AlN}$// [0002] $_{sapphire,}$ due to the difference in the mechanism involved in AlN formation at the interface.

We have also discussed the surface nitridation of the Si(111) plane by nitrogen plasma exposure. The study of Si (111) nitridation suggests that with exposure time, island density gradually increases and the Si^{4+} oxidation state increases monotonically with N_2^* exposure time and Si^{3+} and Si^{1+} decreases. The increase in Si^{4+} component with decrease in S^{3+} and S^{1+} suggests the conversion of S^{3+} to S^{4+} state, leading to the formation of the more stable stoichiometric β-Si_3N_4 (0001). Our AFM image reveals that the beyond 30mins of nitridation, newly formed islands coalesce to form a flat SiN_x. And also we have observed that the 2-D layer beneath and on top of that SiN_x triangular nano-crystals formed and theses islands are pinned at the triangular corner by dislocation which appears to be due to a dislocation mediated spiral growth due to changing g bonding configuration. Upon further nitridation, dislocations drive permanent new step edges for further crystal growth resulting in the SiN_x film growing laterally on the screw dislocation cores, and further the continuous growth loop bowing around the spiral steps due to higher coverage leads to 2-D morphology. The electrical properties of the interface yield a VBO (Valence Band Offset) around 1.8eV and CBO (Conduction Band Offset) around 2.4 eV are estimated for SiN_x/Si interface, which

is in agreement with literature values. The variation in VBO with nitrogen plasma exposure time is due to sub-stoichiometric interface and due to presence of oxidation state of Si^{4+} Si^{3+} and Si^{1+} followed by interfacial bond formation and band bending.

7.3 Role of intermediate layer on the evolution of GaN films:

The role of intermediate layer (nitrided layer) on the epitaxy and orientation of GaN formation on sapphire and Si (111) substrate show that when GaN grows on the nitrided c-plane surface of sapphire, a nano-petal-like morphology of GaN nanorods results. This morphology also suggests that the GaN features formed are due to nucleation at two proximal screw dislocations with similar Burger vectors that are pinned with opposite screw-sense aligning the atomic steps like in a Frank-Read mode that provide the nucleation steps that coalesce. The proximity between the dislocations appears to determine the different diameters of the nanopetals observed. In a similar experiment, we have observed that GaN overgrown on an AlN intermediate layer previously grown over Al_2O_3 prefers to grow only on the single crystalline AlN nanocolumns with sizes in the range of 80-120nm. The threading screw dislocations were seen to propagate both through AlN as well as the GaN nanorods. However, difference in morphology such as nanotubes and c-shaped tubes dependence on critical local density of dislocations to overcome the surface energy required for the creation of a new inner surface in order to satisfy the Frank total energy minimization condition[30]. The GaN nanostructures show high crystalline quality with enhanced optical emission as compared to GaN film on bare sapphire.

After realizing the growth of GaN nanocolumns on modified surface of sapphire, we looked into the effect of substrate type, surface modification etc, on the formation of GaN film morphology on silicon(111) substrate. Here we have shown GaN 2-D and nanorod formation on modified surfaces of Si (111). The film which is grown at 15mins nitrided surface enables single crystalline GaN film, whereas film which is grown at higher time nitrided surface yields poly-crystalline GaN films. We believe that lower nitridation time enables crystalline $SiN_{x,}$ whereas, increase in nitridation time leads to formation of amorphous phase of SiN_x. Resulting GaN 2-D films which are grown at 15mins nitrided surface of Si (111) surface show high quality single crystalline phase and optical emission properties. Secondly we have shown GaN nanostructure formation on 10, 20 and 30sec of

nitrided surface of Si(111) (low converge). We demonstrate the nitridation time controlled spontaneous formation of ordered nanowalls and GaN 1-D nanostructures on Silicon (111) substrates. Here we addressed the coverage and anisotropic strain distributions in SiN_x intermediate layer that decides the GaN nanostructure formation that show high quality single crystalline phase and enhanced optical emission properties.

7.4 Growth of epitaxial GaN nanostructures and 2-D films on Si (111) and Si(100) surfaces:

In this chapter, we have proposed the phase diagram of GaN morphological evolution on Si (111) substrate by varying a) substrate temperature, b) Ga flux and c) N_2 flux. It is evident from the presented results that the morphological evolution of GaN films on Si (111) surface strongly depends on the sticking coefficient of Ga adatoms. The electrical properties of GaN/p-Si (111) hetero-junctions were studied and a higher rectification ratio was observed in the case of GaN/p-Si (111) hetero-junction which had a combination of aligned nanorods and nanowalls. An improved ideality factor and a higher barrier height are attributed to the decreased defects in the system. On the other hand, we have addressed the growth of GaN nanostructure on square planar lattice of Si (100) surface under nitrogen rich condition. We model the atomic details of 1-D nanostructures spontaneous formed at the GaN/Si (100) interface in nitrogen rich conditions. We show that the surface free energy and lattice mismatch determine the epitaxial relation between the columnar growth and the substrate atomic planes, which consequently influence the morphology and orientation of the nano-features. We demonstrate the dominant role of interfacial misfit induced dislocations and their merger in determining the morphology and tilt of the solid, tubes, c-tubes, and branched nanorods. We elucidate the influence of the interfacial SiN_x mounds on the structure and growth direction of the hexagonal wurtzite 1-D features on cubic Si(001) surface. We believe this study provides direct atomic evidence for the generic reasons that are involved in misfit dislocation mediated nanostructure formation.

Highlights:

We list here some significant observations that have been reported in this work:

- Growth diagram for spontaneous formation of GaN nanocolumn, nanowalls, 2D film on bare c-plane sapphire without use of buffer layer and catalyst at nitrogen rich

condition. We identify a narrow growth parametric window of spontaneous nanocolumn formation on bare c-Al_2O_3surface.

- We have proposed and provide direct evidence for dislocation mediated growth mechanism of nanocolumnar formation via open screw dislocation mediated spiral growth. The proximity and number density of the dislocation is seen to morphological evolution, like Frank spiral or Frank-Read-Mill induced nanocolumnar growth.
- We probe the parametric dependence of the nitridation mechanism of Al_2O_3(0001) surface by radio frequency nitrogen plasma. Here we show that nitrogen incorporation into the host material is diffusion limited process and involves the conversion of Al_2O_3 into AlN, which has a higher rate initially and then saturates at 6 hrs of nitrogen plasma exposure. Depositing a thin AlN layer on this saturated nitrided sapphire substrate is seen to consist of nanorods with a bimodal diameter distribution and apex morphology.
- The difference in the evolution of dislocation mediated low-dimensional GaN nanostructures on differently pre-nitrided c-plane sapphire surface, is shown. We show that when GaN grows on c-plane sapphire, after forming an AlN layer by exposure to N^*_2 plasma, leads to the formation of GaN nanostructures that are epitaxial with high crystallinity and demonstrate a thirty times increase in band edge emission as compared to GaN film grown on bare sapphire.

- We elucidate the atomistic level details of the formation of 1-D GaN nanostructures on Si(001), and the role of the unintentional interfacial Si_{Nx} layer in determining the shape, structure and organization of the nano-features. The 1-D GaN features are seen to be m-faceted and grow along the Si(111) planes, and thus are tilted with a 4-fold symmetry on the cubic Si(100) surface, forming solid-rods, tubes or c-tubes.

7.5 Future Directions:

This work has modestly furthered research of the growth of GaN nanostructure on c-plane sapphire and Si(001) and Si(111) surfaces. Though we have shown the spontaneous formation of epitaxial self –aligned nanostructure with low defect and strain, to make them reliable enough for device application further optimization in terms of size orientation and

property is essential. Methods of forming dislocation free nanowire and rods are also to be identified by sheer kinetic control. Testing theses morphological evolution as active device components have to be fabricated and evaluated in device configuration. To understand the those of substrate atomic arrangement, polarity and electronic distribution on the evolving film structure, morphology and consequently their optoelectronic properties, such studies of determining the morphological phase-diagrams on other semi-polar and nano-polar sapphire substrate has to be extensively undertaken. The effect of reduced defects and strain in the films formed here on actual mobility in transistors and high brightness LEDS and high efficiency solar cell structure have to be evaluated. Optimizing condition to obtain In and Al alloying these nanostructures will be crucial in enhancing their applicability to a variety of device that span over a wide spectral range from deep UV and IR. The promise that the band-gap engineering of materials seem to offer should be exploited by determining methods to make appropriate electric contacts and doping control which may not be trivial. The nanostructure may offer a very conducive route for p-doping in these materials. The low defects in these systems prompt the need to study their performance at high frequency high current in harsh environmental conditions.

The fact that, these systems appears to provide high mobility. High efficiency transport and low phase separation possibilities have to be thoroughly and systemically studied. The fact that enhance performances are possible by these system that are formed by sheer kinetic control and in single-step growth process, should be attractive for mass and low cost production. However, these preliminary growth studied have shown attractive possibilities, but we realize that the need for several optimization before useful-devices technology are developed to exploit them.

7.6 REFRENCES:

1. N. A. Mahadik, S. B. Qadri, and M. V. Rao, *Appl. Phys. Lett.*, 2008, **93**, 222106.

2. M. Tangi, J. Kuyyalil, and S. M. Shivaprasad, *J. Appl. Phys.*, 2012, **112**, 073510.

3. D. Zhuang and J. H. Edgar, *Mater. Sci. Eng. R Reports*, 2005, **48**, 1–46.

4. B. Roul, M. Kumar, M. K. Rajpalke, T. N. Bhat, A. T. Kalghatgi, and S. B. Krupanidhi, *Solid State Commun.*, 2012, **152**, 1771–1775.

5. D. G. Zhao, S. J. Xu, M. H. Xie, S. Y. Tong, and H. Yang, *Appl. Phys. Lett.*, 2003, **83**, 677.

6. C. L. Hsiao, L. W. Tu, T. W. Chi, H. W. Seo, Q. Y. Chen, and W. K. Chu, *J. Vac. Sci. Technol. B Microelectron. Nanom. Struct.*, 2006, **24**, 845.

7. H. Ishikawa, B. Zhang, T. Egawa, and T. Jimbo, *Jpn. J. Appl. Phys.*, 2003, **42**, 6413–6414.

8. T. N. Bhat, M. K. Rajpalke, B. Roul, M. Kumar, and S. B. Krupanidhi, *J. Appl. Phys.*, 2011, **110**, 093718.

9. M. Yeadon, M. T. Marshall, F. Hamdani, S. Pekin, H. Morkoç, and J. M. Gibson, *J. Appl. Phys.*, 1998, **83**, 2847.

10. C. Heinlein, J. K. Grepstad, S. Einfeldt, D. Hommel, T. Berge, and A. P. Grande, *J. Appl. Phys.*, 1998, **83**, 6023.

11. A Wierzbicka, Z. R. Zytkiewicz, S. Kret, J. Borysiuk, P. Dluzewski, M. Sobanska, K. Klosek, A Reszka, G. Tchutchulashvili, A Cabaj, and E. Lusakowska, *Nanotechnology*, 2013, **24**, 035703.

12. A. Wierzbicka, Z. R. Zytkiewicz, S. Kret, J. Borysiuk, P. Dluzewski, M. Sobanska, K. Klosek, A. Reszka, G. Tchutchulashvili, A. Cabaj, and E. Lusakowska, 2013, **035703**.

13. H.-Y. Chen, H.-W. Lin, C.-H. Shen, and S. Gwo, *Appl. Phys. Lett.*, 2006, **89**, 243105.

14. Y. H. Kim, J. Y. Lee, S.-H. Lee, J.-E. Oh, and H. S. Lee, *Appl. Phys. A*, 2005, **80**, 1635–1639.

15. W. Bergbauer, M. Strassburg, C. Kölper, N. Linder, C. Roder, J. Lähnemann, a Trampert, S. Fündling, S. F. Li, H.-H. Wehmann, and a Waag, *Nanotechnology*, 2010, **21**, 305201.

16. K. Sebald, J. Kalden, T. Voss, J. Gutowski, T. Aschenbrenner, G. Kunert, C. Kruse, S. Figge, and D. Hommel, *Phys. Status Solidi*, 2009, **6**, S578–S581.

17. H.-M. Kim, D. S. Kim, D. Y. Kim, T. W. Kang, Y.-H. Cho, and K. S. Chung, *Appl. Phys. Lett.*, 2002, **81**, 2193.

18. I. H. Wildeson, D. A Ewoldt, R. Colby, E. A Stach, and T. D. Sands, *Nano Lett.*, 2011, **11**, 535–40.

19. C. Li, Y. Bando, and D. Golberg, *ACS Nano*, 2010, **4**, 2422–8.

20. C. H. Chiu, T. C. Lu, H. W. Huang, C. F. Lai, C. C. Kao, J. T. Chu, C. C. Yu, H. C. Kuo, S. C. Wang, C. F. Lin, and T. H. Hsueh, *Nanotechnology*, 2007, **18**, 445201.

21. S. Li and A. Waag, *J. Appl. Phys.*, 2012, **111**, 071101.

22. H.-C. Hsu, Y.-K. Su, S.-J. Huang, R. W. Chuang, S.-H. Cheng, and C.-Y. Cheng, *Appl. Phys. Express*, 2011, **4**, 035501.

23. S. Dassonneville, A. Amokrane, B. Sieber, J.-L. Farvacque, B. Beaumont, and P. Gibart, *J. Appl. Phys.*, 2001, **89**, 3736.

24. M. Kesaria, S. Shetty, and S. M. Shivaprasad, *Cryst. Growth Des.*, 2011, **11**, 4900–4903.

25. H. Wang, C. Chen, Z. Gong, J. Zhang, M. Gaevski, M. Su, J. Yang, and M. A. Khan, *Appl. Phys. Lett.*, 2004, **84**, 499.

26. M. Kesaria, S. Shetty, and S. M. Shivaprasad, *Cryst. Growth Des.*, 2011, **11**, 4900–4903.

27. S. Shetty, M. Kesaria, J. Ghatak, and S. M. Shivaprasad, *Cryst. Growth Des.*, 2013, **13**, 2407–2412.

28. M. Kesaria, S. Shetty, and S. M. Shivaprasad, *J. Cryst. Growth*, 2011, **326**, 191–194.

29. M. Kesaria, S. Shetty, P. I. Cohen, and S. M. Shivaprasad, *Mater. Res. Bull.*, 2011, **46**, 1811–1813.

30. S. Jin, M. J. Bierman, and S. A. Morin, *J. Phys. Chem. Lett.*, 2010, **1**, 1472–1480.

PAPERS PUBLISHED IN INTERNATIONAL JOURNALS:

(1) Shetty, S.; Kesaria, M.; Ghatak, J.; Shivaprasad, S. M. The Origin of Shape, Orientation, and Structure of Spontaneously Formed Wurtzite GaN Nanorods on Cubic Si(001) Surface. ***Cryst. Growth Des***. **2013**, *13*, 2407–2412.

(2) Shetty, S.; Ghatak, J.; Shivaprasad, S. M. Surface Nitridation Induced AlN Nano-Columnar Growth on c-Sapphire. ***Solid State Commun***. **2014**, *180*, 7–10.

(3) Shetty, S.; Ghatak, J.; Shivaprasad, S. M. Role of AlN Intermediate Layer in the Morphological Evolution of GaN Nanorods Grown on c-Plane Sapphire. ***CrystEngComm*** **2014**, *16*, 3076.

(4) Shetty, S.; Shivaprasad, S. M. Growth of High Quality GaN Nanowalls on Si (111) Surface. ***IEEE Electron Devices Letters.*** (Accepted)

(5) Kesaria, M.; Shetty, S.; Shivaprasad, S. M. Evidence for Dislocation Induced Spontaneous Formation of GaN Nanowalls and Nanocolumns on Bare C-Plane Sapphire. ***Cryst. Growth Des.*** **2011**, *11*, 4900–4903.

(6) Kesaria, M.; Shetty, S.; Cohen, P. I.; Shivaprasad, S. M. Transformation of c-Oriented Nanowall Network to a Flat Morphology in GaN Films on c-Plane Sapphire. ***Mater. Res. Bull***. **2011**, *46*, 1811–1813.

(7) Kesaria, M.; Shetty, S.; Shivaprasad, S. M. Spontaneous Formation of GaN Nanostructures by Molecular Beam Epitaxy. ***J. Cryst. Growth*** **2011**, *326*, 191–194.]

(8) P. Kumar.; M. Tangi.; Shetty, S.; Kesaria, M.; Shivaprasad, S. M. Growth of aligned wurtzite GaN nanorods on Si (111): Role of Silicon nitride intermediate layer" MRS Proceedings / Volume 1411 / 2012.

PAPERS PUBLISHED IN INTERNATIONAL JOURNALS (NOT INCLUDED IN THESIS):

(9) Aruna, S. T.; Kini, N. S.; Shetty, S.; Rajam, K. S. Synthesis of Nanocrystalline CeAlO3 by Solution-Combustion Route. ***Mater. Chem. Phys***. **2010**, *119*, 485–489.

(10) Negi, D. S.; Roy, A.; Loukya, B.; Dileep, K.; Shetty, S.; Kumar, N.; Kumar, P. S. A. Epitaxial Co Metal Thin Fi Lm Grown by Pulsed Laser Deposition Using Oxide Target. ***J. Cryst. Growth*** **2014**, *394*, 112–115.

(11) Negi, D. S.; Loukya, B.; Dileep, K.; Sahu, R.; Shetty, S.; Kumar, N.; Ghatak, J.;R.Datta. Structural and Magnetic Characterization of Mixed Valence Co (II,III)$_X$ Zn $_{1-X}$O Epitaxial Thin Films. ***Journal of Magnetism and Magnetic Materials*** **2014**, *354*, 39–43.

(12) Sahu,R.; Dileep,K.; Negi,D. S.; K.K. Nagaraja.; Shetty,S.; J.;R.Datta. Structural and Optical property Characterization of epitaxial ZnO:Te thin films grown by pulsed laser deposition, ***Journal of Crystal Growth*, (2014)**

PAPERS COMMUNICATED TO INTERNATIONAL JOURNALS:

(13) Shetty, S.; and Shivaprasad, S. M."Sticking Coefficient Dependent Morphological Evolution and Electrical, Optical Properties of the Constituent Morphology of GaN films on Si(111) Surfaces" (Communicated to Applied Physics Letters).

(14) Shetty, S.; and Shivaprasad, S. M. "Role of Intermediate Layer in the Evolution of High Quality 2-D GaN Films on Nitrided Si (111) Surface" (Communicated to Journal of Applied Physics).

(15) Shetty, S.; and Shivaprasad, S. M. "Single Crystalline 2-D Films and Nanostructure of Hexagonal β-Si_3N_4 (0001) on Si (111) Surface by rf-plasma Nitridation (Communicated to Journal of Applied Physics).